Applying NMR Relaxation Methods to the Study of Liquids in Porous Media

University of Cambridge

Department of Chemical Engineering and Biotechnology

Jordan Alexander Ward-Williams

Clare College

This thesis is submitted for the degree of Doctor of Philosophy

December 2019

Preface

The work presented in this dissertation has been carried out in the Department of Chemical Engineering and Biotechnology at the University of Cambridge between January 2016 and November 2019. This thesis is the result of my own work and includes nothing which is the outcome of work done in collaboration, except as declared in the Preface and specified in the text. It is not substantially the same as any that I have submitted, or, is being concurrently submitted for any such degree, diploma or other qualification at the University of Cambridge or any other University or similar institution except as declared in the Preface and specified in the text. I further state that no substantial part of my thesis has already been submitted or, is being concurrently submitted for any such degree, diploma or other qualification at the University of Cambridge or any other University or similar institution except as declared in the Preface and specified in the text. It does not exceed the prescribed word limit for the relevant degree committee. This dissertation contains fewer than 150 figures and 65,000 words, including appendices, bibliography, tables, and equations.

Applying NMR Relaxation Methods to the Study of Liquids in Porous Media

Jordan Alexander Ward-Williams

The work presented within this thesis focusses on the development of NMR relaxation techniques to unambiguously characterise the adsorption behaviour of liquids imbibed within catalytic materials. Principally, this study is centred on γ-alumina, which is used industrially as both a catalyst and a catalyst support. Ratios of fixed field T_1 and T_2 values were compared with fast field cycling (FFC-) NMR measurements. For each technique the relative advantages and disadvantages were explored, and methodologies allowing a robust implementation of these techniques to study the adsorption were presented.

Fixed field measurements of $T_{1,B}/T_{1,pore}$ and $e_{surf} = -T_2/T_1$ were used to compare the relative interaction strength for a range of liquids imbibed within γ-alumina. A strong correlation between the adsorbate polarity and the $T_{1,B}/T_{1,pore}$ ratio of rigid molecules showed the sensitivity of high field NMR to surface adsorption processes. However when flexible molecules were studied the presence of internal motions distorted the trends in the relaxation behaviour, making both the $T_{1,B}/T_{1,pore}$ and e_{surf} measurements unsuitable.

FFC-NMR was explored as an alternative to fixed field NMR. This allowed the measurement of relaxation behaviour over a range of low field strengths. The FFC-NMR data showed a clear ordering of the solid-liquid interaction strengths, which was more consistent with the predicted physical chemistry of the system than the order given by a fixed field analysis. For methanol and acetone imbibed within γ-alumina multicomponent relaxation behaviour was observed. The origin of this was shown to be functionality specific adsorption behaviour, and the presence of a stable reaction intermediate respectively. These observations led to a more granular understanding of the adsorption. A formal modelling approach was then applied to the FFC-NMR data in order to extract quantitative correlation times that described the dynamics of each adsorbate at the catalyst surface.

The sensitivity of FFC-NMR to coadsorption was further studied through the use of binary liquid mixtures. A model for the interpretation of the relaxation behaviour of each component in the binary mixture was proposed and used to demonstrate the liquid structuring and micro-phase separation that occurred during adsorption.

Acknowledgements

First and foremost I would like to thank my supervisor, Professor Lynn Gladden for the belief that she has shown in me throughout my research, and her constant support and encouragement. It has allowed me to turn my PhD into something truly worthwhile. I would also like to thank Andy Sederman and Mick Mantle, both of whom have provided invaluable advice and support, on topics ranging from hardware to fundamental theory.

I would also like to thank everyone I've had the pleasure of working with at the MRRC. Special mention must go to Markus Leutzsch and Michael Tayler, both of whom took a keen interest in my project and were the source of many interesting and valuable scientific discussions. Joe Cooper, Dan Hurst, Marian Bentley, and Adam Colbourne also played an important part in keeping me sane over the years, with a regular supply of coffee and crosswords. Finally, to Laura Rozing and Callum Penrose who have been great additions to our ever growing FFC-NMR community.

Thank you to everyone at Stelar, and in particular Gianni Ferante, Moreno Pasin, Rebecca Steele, and Matteo Polello. Stelar have played a big role in championing FFC-NMR globally, and have provided me with many opportunities to showcase my work internationally. It was also Stelar that introduced me to Professor Jean-Pierre Korb, whose extensive knowledge on the theory of FFC-NMR has been a valuable asset to my work. His enthusiasm and support really helped me to understand the complex world of FFC-NMR modelling.

Finally, I would like to thank my friends and family who have supported me over the years. In particular my partner, Georgie Field, who has had to put up with years of undoubtedly boring science talk and many a weekend lost to experiments. Her constant encouragement, support, and razor-sharp proofreading has made this experience a lot more manageable.

Contents

Chapter 1 : Introduction

Contents

1.1 Background and context to the work

The adsorption of liquids within porous materials is central to the understanding and optimization of a number of industrial processes, including chemical catalysis, separations technology, and oil recovery. Adsorption problems are often poorly understood, despite their prevalence. This is due to the difficulty associated with applying standard analytical measurements to liquids imbibed within porous materials. Porous systems are often studied indirectly, by flowing liquids through the porous material and measuring the concentrations of species in the inflow and outflow. This can result in a laborious optimization process, in which many experiments are required in order to select the optimal conditions or porous medium for a particular purpose.[1] Direct analysis techniques that allow a greater understanding of the adsorption therefore play an important role in streamlining this optimization process and reducing the associated costs. This thesis will explore the use of NMR relaxation measurements to better understand solid-liquid adsorption in porous materials. The techniques that are developed are highly general, but this thesis will focus on applications to the field of catalysis.

Nuclear magnetic resonance (NMR) is a powerful, non-invasive analysis tool that has successfully been applied to the study of catalytic materials in recent years. In particular, NMR relaxation analysis has been shown to probe the adsorption strength and the liquid dynamics at solid surfaces.[2,3] Often relaxation measurements are carried out at high magnetic field strengths due to equipment availability, however, many different dynamic modes contribute to the relaxation behaviour at high field strengths, meaning that a measurement of the adsorbate-surface interaction can be ambiguous and easily misinterpreted. The limitations that occur at high magnetic field strengths have prevented this technique from becoming widespread. The work presented within this thesis focusses on the application of variable field and low field NMR relaxation analysis to porous systems to overcome the key issues associated with conventionally used high field NMR relaxation analysis. By transitioning to low field analysis the NMR relaxometry experiment becomes sensitive to slow relaxation modes, and becomes a more robust analysis tool.

Catalysts are used to accelerate the rate of chemical reaction without altering the position of equilibrium or being used up during the reaction. Many different types of catalysis exist, and the main forms can be summarised as:

1) Heterogenous catalysis - the catalyst and reagents are different phases, often employing a solid catalyst and gaseous or liquid reagents. Heterogeneous catalysts benefit from low separations costs and long catalyst lifetimes, but the elementary steps in the reaction mechanism are poorly understood.
2) Homogeneous catalysis - the catalyst and reagents are the same phase, often liquids. Homogeneous catalysis is well understood and highly selective, but the catalyst is expensive to separate from the products post-reaction.
3) Biocatalysis - enzymes and associated biological species are used as catalysts. Biocatalysis is well understood and highly selective, but the catalysts have short lifetimes and a low thermal stability.

The vast majority of industrially implemented reactions use catalysts to promote reactions, and despite the complexity of heterogeneous catalysis it accounts for over 80% of all industrial catalytic processes.[4] The low separations cost and long lifetimes of solid heterogeneous catalysts make them economically favourable to the alternatives. Due to their industrial prevalence and the significant knowledge gap that exists for these materials this thesis will focus exclusively on heterogeneous catalysis.

Figure 1.1 shows the 7 elementary steps that are expected during a heterogeneous chemical reaction. These can be classified as:[5]

1) transport of reactants from the bulk to an external boundary layer,

2) transport of reactants through the catalyst pore network,

3) adsorption of reactants onto the catalyst surface,

4) chemical reaction at the catalyst surface,

5) desorption of products from the catalyst surface,

6) transport of products through the catalyst pore network,

7) transport of products away from the external boundary layer into the bulk phase.

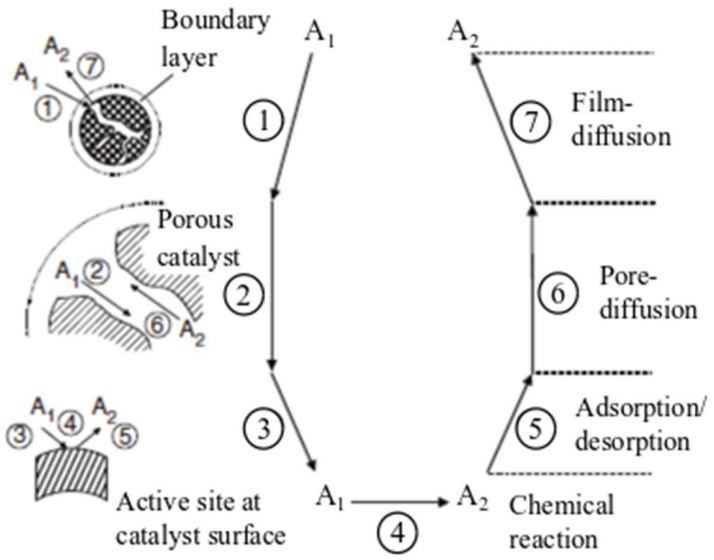

Figure 1.1: The stages of heterogeneous catalysis for the transformation of A_1 to A_2. Reproduced from Dittmeyer and Emig.[5]

Mass transport is classically considered as the dominant factor in steps 1, 2, 6, and 7, and adsorption dominates for steps 3-5. In mesoporous materials (where the pore size ranges from 2-50 nm) the adsorption interaction has also been shown to affect the intraparticle diffusivity of different liquids,[6] and therefore adsorption can play an important role in steps 2-6. Furthermore, the mass transport properties of a catalytic system can be improved with well-known methods such as changing the shape of the catalyst extrudate or increasing the reactor temperature. As a result, adsorption steps can become slower than mass transport. The slowest step in this reaction scheme acts as the rate determining step, and will control the kinetics of the reaction. Therefore, understanding how liquids interact with solid-surfaces is critically important when developing and optimizing new catalytic materials.

1.2 Objectives

The main objective of this thesis is to develop a robust methodology for measuring the solid-liquid interaction strength of liquids in porous media. This will be pursued through two approaches. Firstly, existing NMR relaxation techniques will be applied to porous systems, and the limits of their applicability will be tested. The second approach will be

to apply fast field cycling (a variable field NMR technique) to the study of liquids in porous media. Fast field cycling NMR is not yet fully established for investigating porous samples, and much theoretical and experimental work is required to demonstrate that it can be applied and interpreted reliably and accurately. The technique and methodology development will be carried out within this thesis using γ-alumina, which is both a widely used catalyst support, and an acid-base catalyst for a number of reactions.[7,8] This choice of porous material allows a simple system to be studied for validation of the NMR techniques, but also provides information that is directly relevant to the catalyst optimization process.

1.3 Outline of the thesis

Chapter 2 presents a summary of the key principles required to understand NMR measurements of liquids imbibed within porous materials.

Chapter 3 critically assesses the applications and limitations of both fixed field and fast field cycling NMR relaxometry approaches when applied to the study of liquids imbibed within porous materials.

Chapter 4 extends upon the arguments presented in chapter 3 through an experimental study of the fixed field relaxation behaviour of liquids imbibed within γ-alumina. The limits of the conventional metrics (T_1/T_2 and $T_{1,B}/T_{1,pore}$) are explored, and particular focus is paid to the relaxation behaviour of rigid and flexible molecules.

Chapter 5 introduces the fast field cycling NMR technique, and applies it to several liquids imbibed within γ-alumina. An initial analysis is performed based on a model-free interpretation of the data.

Chapter 6 extends the analysis performed in chapter 5 by focussing on minor features present in the adsorption data for methanol and acetone imbibed within γ-alumina. A thorough investigation of these features shows the sensitivity of fast field cycling NMR to functionality specific adsorption dynamics and the presence of stable reaction intermediates.

Chapter 7 combines the data presented in chapter 5 with a series of variable temperature measurements in order to apply a formal modelling procedure to the fast field cycling

NMR data obtained for liquids imbibed within γ-alumina. The modelling process allows the extraction of motional correlation times describing the adsorbate dynamics at the pore surface.

Chapter 8 presents a study on binary liquid mixtures imbibed within γ-alumina. The data are used to explore both the relative interaction strength of the two fluids as well as the liquid structuring phenomenon that occurs within the pore space.

Chapter 9 summarises the main conclusions of this work, and suggests the direction of future work based on the discoveries presented within this thesis.

1.4 References

(1) Hagen, J. Planning, Development, and Testing of Catalysts. In *Industrial Catalysis*; John Wiley & Sons, 2015; pp 395–432.

(2) D'Agostino, C.; Mitchell, J.; Mantle, M. D.; Gladden, L. F. Interpretation of NMR Relaxation as a Tool for Characterising the Adsorption Strength of Liquids inside Porous Materials. *Chem. A Eur. J.* **2014**, *20*, 13009–13015.

(3) Korb, J.-P. Multiscale Nuclear Magnetic Relaxation Dispersion of Complex Liquids in Bulk and Confinement. *Prog. Nucl. Magn. Reson. Spectrosc.* **2018**, *104*, 12–55.

(4) Wacławek, S.; Padil, V. V. T.; Černík, M. Major Advances and Challenges in Heterogeneous Catalysis for Environmental Applications: A Review. *Ecol. Chem. Eng. S* **2018**, *25*, 9-34.

(5) Dittmeyer, R.; Emig, G. Simultaneous Heat and Mass Transfer and Chemical Reaction. In *Handbook of Heterogeneous Catalysis*; American Cancer Society, 2008; pp 1727–1784.

(6) D'Agostino, C.; Mitchell, J.; Gladden, L. F.; Mantle, M. D. Hydrogen Bonding Network Disruption in Mesoporous Catalyst Supports Probed by PFG-NMR Diffusometry and NMR Relaxometry. *J. Phys. Chem. C* **2012**, *116*, 8975–8982.

(7) Trueba, M.; Trasatti, S. P. γ-Alumina as a Support for Catalysts: A Review of

Fundamental Aspects. *Eur. J. Inorg. Chem.* **2005**, 17, 3393–3403.

(8) Schiffino, R. S.; Merrill, R. P. A Mechanistic Study of the Methanol Dehydration Reaction on gamma-Alumina Catalyst. *J. Phys. Chem.* **1993**, *97*, 6425–6435.

Chapter 2 : Theory of Nuclear Magnetic Resonance

Contents

2.1 Introduction

This chapter outlines the key nuclear magnetic resonance (NMR) theory that is required to understand and contextualize the results presented within this thesis. This chapter presents an overview of the core concepts; a more detailed description of each concept can be found in texts by Keeler,[1] Levitt,[2] and Abragam.[3] The following discussion is based on these texts, and is supplemented by additional sources where relevant.

2.2 Basic principles of NMR

2.2.1 Nuclear spin

Nuclear spin, *I*, is an intrinsic form of angular momentum that describes the behaviour of a nucleus in the presence of a magnetic field. It is a fundamental property of the nucleus, which takes quantized values of $I \geq 0$ in half integer steps. Unlike classical angular momentum, the spin of a nucleus is not affected by its surroundings, which means that all nuclei of the same type have the same spin number. Many different values of *I* have been observed experimentally. By far the most commonly used nuclei for NMR studies are ^{1}H and ^{13}C, which both have values of $I = ½$. For a nucleus of spin *I*, there are (2*I*+1) associated spin states, m_I, where m_I takes values from –*I* to *I* in integer steps. These different spin states describe the different orientations of the nuclear spin. In the absence of a magnetic field the associated energy levels are degenerate, but when a magnetic field is applied the degeneracy of these states is lifted, and the energy of each state is given as:

$$E_{m_I} = -\gamma \hbar B_0 m_I \,, \tag{2.1}$$

where γ is the gyromagnetic ratio of the nucleus, $\hbar$ is the reduced Planck's constant, and B_0 is the applied magnetic field. The loss of degeneracy is known as the Zeeman splitting, and is shown schematically for a spin ½ nucleus in Figure 2.1.

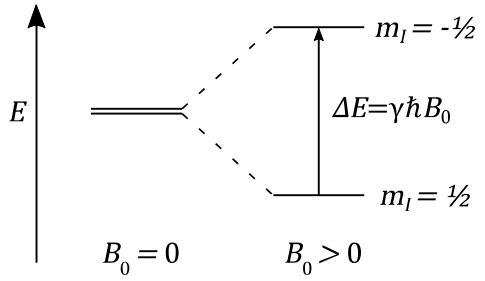

Figure 2.1: The energy level diagram for the spin states of a spin $I = ½$ nucleus in the absence, and presence of a magnetic field.

The population ratio between the two spin states is given as:

$$\frac{N_{-½}}{N_{½}} = \exp\left(\frac{-\Delta E}{kT}\right), \tag{2.2}$$

where N_{m_I} is the population of the m_I spin state, ΔE is the energy difference between the spin states, k is Boltzmann's constant and T is the temperature. The small deviations in the energy levels, and the populations of each spin state, are the origin of the NMR signal. Transitions between these levels are formally of a quantum mechanical nature, however, many of the core concepts of NMR can be justified in a more physical and conceptual fashion. This is through a model that is analogous to classical angular momentum, known as the vector model. The vector model will be applied throughout this chapter. For the following discussion a spin $I = ½$ nuclei is assumed.

2.2.2 The vector model

The nuclear spin phenomenon gives rise to a magnetic moment associated with each nucleus, **μ**. When a magnetic field is applied this causes a torque on the magnetic moment of each nucleus, given as:

$$\frac{d\mathbf{P}}{dt} = \boldsymbol{\mu} \times \mathbf{B}, \tag{2.3}$$

Where **P** is the angular momentum and **B** is the applied field. For generality the magnetization and applied field are expressed in vector notation.

The ensemble average of the individual magnetic moments is defined as the magnetization vector, **M**. In the absence of an applied field and at room temperature the direction of the individual magnetic moments is largely random due to thermal motion. However, in the presence of an external magnetic field there is a slight energetic preference for the magnetic moments to align with the applied magnetic field. The individual magnetic moments appear random, however, the ensemble average has a net alignment in the direction of the field. This net magnetization is defined as the equilibrium magnetization vector, M_0, which points in the direction of the applied field, B_0, as shown in Figure 2.2. At equilibrium, the magnetization vector is aligned with the external field and therefore the net torque is zero.

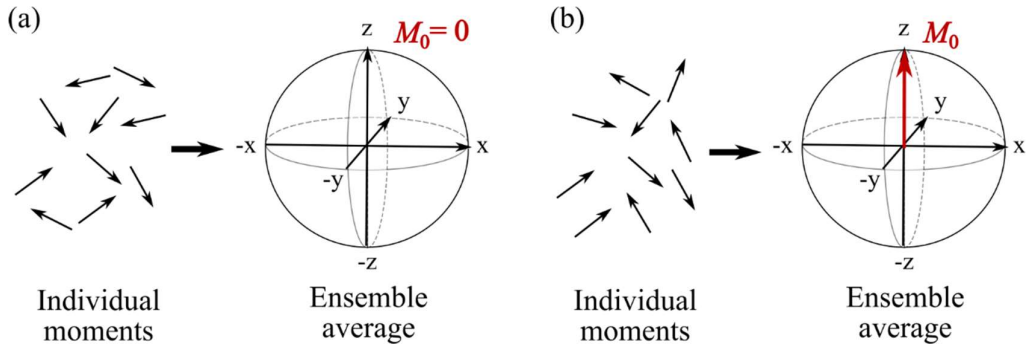

Figure 2.2: The individual magnetic moments of spins and the resultant ensemble average in the presence of (a) no magnetic field, and (b) a magnetic field in the z-direction.

Additional magnetic fields can be applied perpendicular to the background field through weak magnetic fields, B_1. These fields correspond to the radiofrequency section of the electromagnetic spectrum and are therefore known as RF pulses. The pulses are applied for durations of <1 ms, and rotate the magnetization vector away from its equilibrium position. The manipulation of the magnetization vector through a series of RF pulses is the basis of most NMR experiments.

If the magnetization is shifted away from the direction of the applied field, the torque causes a precession of the nuclear spins about the B_0 field, as shown in Figure 2.3.

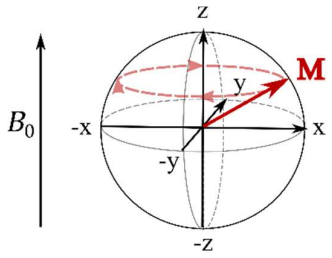

Figure 2.3: The Larmor precession of the magnetization vector, **M**, in the presence of a constant magnetic field, B_0. As **M** is time dependent it is no longer equivalent to the initial magnetization, M_0. Relaxation effects are omitted from this diagram.

This motion is known as a Larmor precession, ω_0, and for a static field in the z-direction can be described mathematically as:

$$\boldsymbol{\omega}_0 = -\gamma \boldsymbol{B}_0 \,. \tag{2.4}$$

The precession frequency is proportional to the frequency of the allowed quantum mechanical transition between spin states according to the Planck-Einstein relation.

2.2.3 The rotating frame

The effect of the Larmor precession and the application of RF pulses on the magnetization vector quickly become complex to follow in the laboratory reference frame. An important simplification can be made by considering the behaviour of the magnetization in a frame of reference that is rotating with an angular frequency, ω_{Rot}. From the perspective of the rotating frame the magnetization vector will precess at a reduced frequency:

$$\Omega = \omega_0 - \omega_{\mathrm{Rot}} \,, \tag{2.5}$$

where Ω is known as the offset. This corresponds to an effective Larmor precession of $\Omega = -\gamma \Delta B$, where ΔB is the effective field in the rotating frame. When $\Omega = 0$ the spins are 'on-resonance' and the magnetization vector becomes stationary in the rotating frame.

The fields used to perturb the spin system, B_1, are applied as linearly oscillating RF fields, typically along the x or y axis. These oscillating fields can be decomposed into two counter-rotating fields; one rotating at the same angular frequency as the Larmor frequency, ω_0, and one rotating in the opposite direction at an angular frequency of $-\omega_0$.

The component of the B_1 field rotating with a frequency of $-\omega_0$ has a negligible effect on the magnetization vector. The co-rotating component, however, has a much stronger effect. As this component of B_1 is rotating at the Larmor frequency it will appear static in the rotating frame. When perfectly on resonance, the magnitude of the B_1 field is large compared to the size of the effective background field, ΔB. This results in the precession of the magnetization vector occurring about the B_1 field, as shown in Figure 2.4b. The resonance phenomenon means that very weak RF pulses can be used to manipulate spins even though the magnitude of B_0 is much larger than that of B_1.

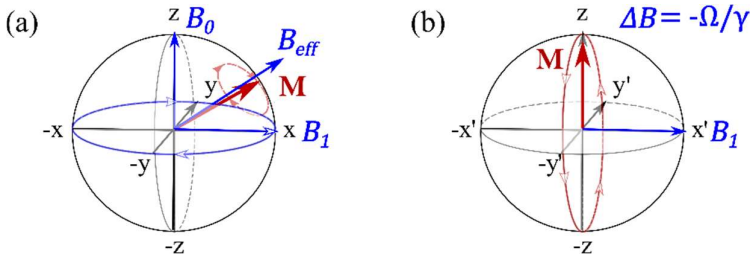

Figure 2.4: The effect of an RF pulse applied in (a) the stationary frame, and (b) the rotating frame where $\Omega = 0$. In the stationary frame, the B_1 field will also rotate, causing the precession of **M** to rotate with B_1.

By controlling the magnitude of the B_1 field, and the duration of its application, t_p, the degree of rotation, θ, can be chosen such that:

$$\theta = \omega_1 t_p = \gamma B_1 t_p \,. \tag{2.6}$$

Typically the strength of the B_1 field will be fixed, and differing degrees of rotation are selected by varying the duration of the pulse. The angle of rotation is used to define the pulse, with 90° and 180° pulses being by far the most commonly used.

2.2.4 Detection and signal processing

As shown in the previous section, when perturbed from equilibrium a spin system will precess about the B_0 field. This precession can be decomposed into a component in the z direction, and a component in the xy (transverse) plane. The transverse magnetization precesses at the Larmor frequency with a decreasing magnitude due to relaxation processes (which will be discussed further in section 2.3). By positioning detection coils in the xy plane a small current is induced when the transverse magnetization passes the coil. These currents are digitized and provide the NMR signal. To identify both the

magnitude and direction of the magnetization, both the x and y components of the magnetisation are required. It is rarely possible to position two isolated coils in the desired orientation to obtain these values, therefore an alternative approach known as quadrature detection is commonly employed. The detected signal is split into two equivalent parts, which are mixed independently with locally generated fields. By mixing in locally generated fields with a phase shift of 90°, the x and y components of the magnetization can be obtained without the need for challenging hardware. The signal, $S(\mathrm{t})$, is given as:

$$S(\mathrm{t}) = S_x(t) + iS_y(t)\,. \tag{2.7}$$

The measured time domain signal is referred to as the Free Induction Decay (FID). In practice, an exponential relaxation process occurs simultaneously with an oscillatory process caused by the Larmor precession, as shown in Figure 2.5. The Fourier transform of the time domain signal provides a frequency domain signal $S(\omega)$. The frequency domain signal is a complex number, and is separated into the real part (absorption lineshape) and the imaginary part (dispersion lineshape) as shown in Figure 2.5b. The absorption lineshape is a narrow and symmetrical peak that is conventionally reported in NMR spectroscopy experiments. The dispersion lineshape is much broader, and antisymmetric, which means it is used less frequently. Often a phase error will be introduced into the signal during the course of the experiment due to hardware imperfections. This distorts the pure absorption and dispersion lineshapes from those shown in Figure 2.5b. It is simple to account for such an error by applying a phase correction to the data. This can be performed during the post processing of the signal either manually, or through the use of algorithms that maximise the signal intensity of the absorption lineshape.

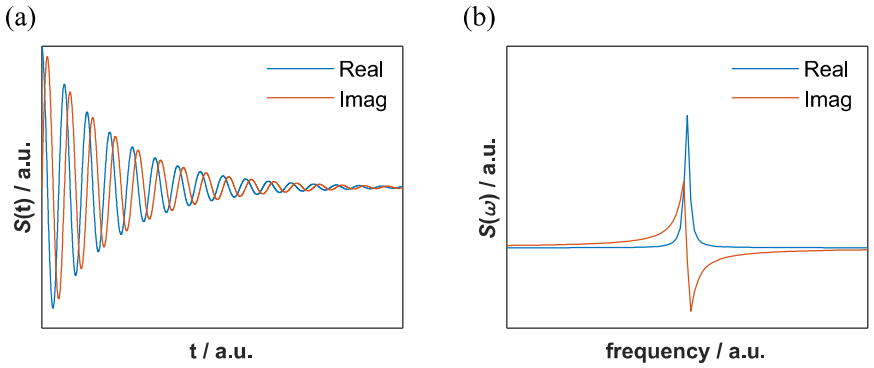

Figure 2.5: A typical example of the (a) time domain signal, $S(t)$, and (b) corresponding frequency domain signal, $S(\omega)$. $S(t)$ and $S(\omega)$ are related to one another through a Fourier transform. As $S(t)$ is complex, so too is $S(\omega)$. For both the time and frequency domain signals, the real part (absorption lineshape) and the imaginary part (dispersion lineshape) are shown.

2.2.5 Chemical shift

The Larmor frequency was shown to depend principally on the applied field (eq. (2.4)). However, if all spin active nuclei (all ^{1}H atoms for example) experienced the same effective field when subjected to a B_0 field, then the resultant NMR spectrum would be a single line of limited use. Instead, NMR is sufficiently sensitive to the local electronic structure of a nucleus that the ^{1}H species within different chemical functionalities precess at different Larmor frequencies. The electron cloud surrounding each nucleus creates a secondary field, opposing the B_0 field, which partially shields the nucleus from the applied field. A spin active nucleus therefore experiences a smaller local field, and precesses slightly slower than a non-shielded nucleus. The electron withdrawing and donating properties of different chemical functionalities are important in determining the degree of magnetic shielding experienced by the spin active nucleus, and the resonant frequency, $\nu = \omega/2\pi$, is given as:

$$\nu = \frac{-\gamma B_{\mathrm{Loc}}}{2\pi}, \tag{2.8}$$

where B_{Loc} is the local magnetic field strength. The local field can be approximated as $B_{\mathrm{Loc}} = B_0(1-\sigma)$, where σ is the shielding strength. The small shifts in the resonant frequency caused by shielding effects allow multiple chemical functionalities within the same molecule to be separated in the spectrum. For sufficiently sensitive experiments

hundreds or even thousands of peaks may occur, resulting in a large quantity of structural information encoded into a single experiment.[4]

To allow a comparison of NMR spectra obtained at different field strengths, a measurement of the local electronic shielding is used that is independent of applied B_0 field. This is known as the chemical shift, δ, and is given by:

$$\delta = \frac{\nu - \nu_{\mathrm{ref}}}{\nu_{\mathrm{ref}}} \times 10^6, \tag{2.9}$$

where ν_{ref} is the Larmor frequency obtained from a reference compound on the spectrometer. By convention, tetramethylsilane (TMS) is used as a reference compound, and therefore has a chemical shift of 0. For ^{1}H spectra the degree of shielding results in peaks between 0-10 ppm and for ^{13}C NMR spectra peaks appear between 0-200 ppm. The improved resolution of ^{13}C NMR experiments makes them a useful tool for structural elucidation, however the experiments are often far more time consuming than ^{1}H NMR due to the inherently low signal-to-noise ratio (^{13}C has a natural abundance of 1.1%) and long relaxation times.

2.2.6 *J*-coupling

J-coupling, or scalar coupling, is the indirect intramolecular interaction between neighbouring spin active nuclei through chemical bonds. The preferential orientation of the nuclear magnetic moment polarizes the electrons within a nucleus through a process known as a Fermi contact. The orientation of the electron is then transmitted through the molecule, and influences the magnetic field experienced by other spin active nuclei. This effect is shown schematically in Figure 2.6. The coupling is mediated through chemical bonds, and can readily extend over two or three bonds. For interacting nuclei a small perturbation of the energy levels of the spin system occurs, and causes the observed NMR signal to be split into multiple peaks. The number of peaks depends on the number and spin of all the interacting nuclei, making *J*-coupling a useful tool in structural elucidation. Both like nuclei (homonuclear) and unlike nuclei (heteronuclear) are subject to *J*-coupling effects.

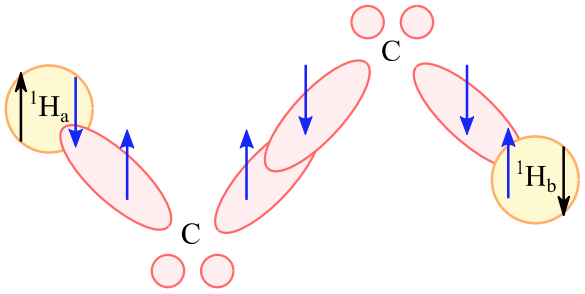

Figure 2.6: A schematic diagram of the J-coupling effect between two ^1H environments separated by 3 chemical bonds. The spin polarization (black) of H_a induces an electron polarization (blue) that is antiparallel. The ^1H electron has a well-defined orientation due to the nuclear spin. The electron on the carbon atom involved in the C-H_a σ-bond is polarized antiparallel to the hydrogen electron according to the Pauli principle. Electrons in adjacent p-orbitals on the carbon atom align parallel to according to Hund's rule. As a result of these interactions a polarization network forms, and the magnetic environment of H_b will be influenced by that of H_a.

2.3 NMR relaxation measurements

2.3.1 Relaxation

The presence of a background field, B_0, results in a slight energetic preference for the magnetization vector to be aligned with the field. When the alignment is at a maximum the system reaches an equilibrium position. If the magnetization is perturbed from its equilibrium position, the system will slowly return to equilibrium over the course of a few microseconds to several seconds through a process known as relaxation. This relaxation process can be monitored by the restoration of the magnetization in the z-direction, or the loss of magnetization in the xy plane. These processes are known as spin-lattice and spin-spin relaxation respectively.

2.3.1.1 Spin-lattice relaxation

When the magnetization of a sample is displaced from its equilibrium position the net magnetic moment of the sample is no longer optimally aligned with the external field, and the energy of the system is raised. This reduces the size of the z-component of the magnetization, as shown in Figure 2.7b. In order to return to equilibrium, the spins must transfer the additional energy to their surroundings through a process known as spin-

lattice relaxation. Energy transfer between the spin system and the environment is a stimulated process, which is controlled by local fluctuations in the magnetic field. These magnetic fluctuations are commonly caused by molecular motions, which reorient the local magnetic moments of the molecules with respect to the B_0 field. The reorientations cause the most efficient relaxation when the motional correlation time of the reorientation, τ_c, satisfies the criterion,

$$\omega_0 \tau_c = 1 \,. \tag{2.10}$$

The T_1 relaxation time can be measured through an inversion recovery pulse sequence, as shown in Figure 2.7a. A 180° pulse is applied to invert the magnetization, and a delay time, τ, is allowed so that the sample may recover towards equilibrium. After the delay a 90° pulse is used to tip the sample magnetization into the transverse plane for detection. Repeating this sequence many times with variable τ values allows the measurement of the T_1 relaxation process as a function of time.

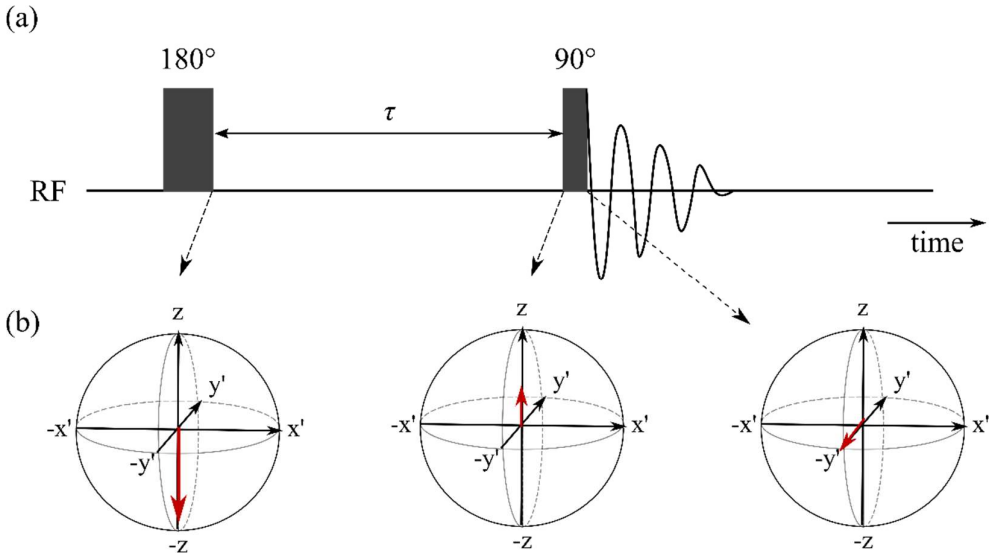

Figure 2.7: The (a) inversion recovery pulse sequence, and (b) vector model representations of the magnetization at key points of the sequence. The magnetization behaviour for a single τ value is shown for simplicity. The inversion recovery process is repeated for many values of τ in order to measure the T_1 relaxation. Schematics of the net magnetization are shown in the rotating frame.

According to the Bloch vector model of relaxation, the time dependent magnetization, $M_z(t)$, obeys the following relation:

$$\frac{dM_z(t)}{dt} = \frac{M_z(t) - M_0}{T_1}, \tag{2.11}$$

where M_0 is the equilibrium magnetization. For an inversion recovery experiment, the 180° pulse creates an initial magnetization of $-M_0$. The differential equation can be solved to give the magnetization of the inversion recovery experiment as:

$$M_z(t) = M_0\left(1 - 2\exp\left(-\frac{t}{T_1}\right)\right). \tag{2.12}$$

The measured signal follows the same functional form as the magnetization, allowing the measurement of the spin-lattice relaxation as a function of time. The extracted time constant, T_1, describes the speed of the relaxation process, and is highly sensitive to the local environment. Depending on the application, both the time constant, T_1, and the relaxation rate, $R_1 = 1/T_1$, are used to describe the spin-lattice relaxation behaviour.

2.3.1.2 Spin-spin relaxation

The same processes that contribute to spin-lattice relaxation are also found within spin-spin relaxation. Specifically, these processes make up the non-secular component of transverse relaxation. The difference between the two relaxation processes is the presence of a secular component of the relaxation, which is unique to T_2. This is caused by small variations in the z-component of the magnetic field across the sample. As the molecules tumble due to thermal motion the local fields experienced by each spin become dependent on the orientations of the adjacent spins. The small differences in B_{Loc} lead to variations in the precession frequencies of the spins, which causes dephasing and a loss of transverse magnetization. The dephasing process can be conceptualized by considering the time dependent precession of an ensemble of spins immediately after excitation with a 90° pulse. The Larmor precession for each spin is controlled by its local field, B_{Loc}, and is given as:

$$\omega_0 = \gamma B_{\mathrm{Loc}}. \tag{2.13}$$

After a short time delay, t_1, the spin components of the sample will not have significantly changed phase relative to one another, and only a small loss of magnetization in the transverse plane will be observed. If the spins are left for a longer period of time, t_2, the different precession frequencies of the spins leads to a greater variation in the position of

the magnetization vectors. In this scenario significant dephasing will have occurred, and the resultant transverse magnetization of the sample will be small. These different degrees of spin dephasing are shown in Figure 2.8.

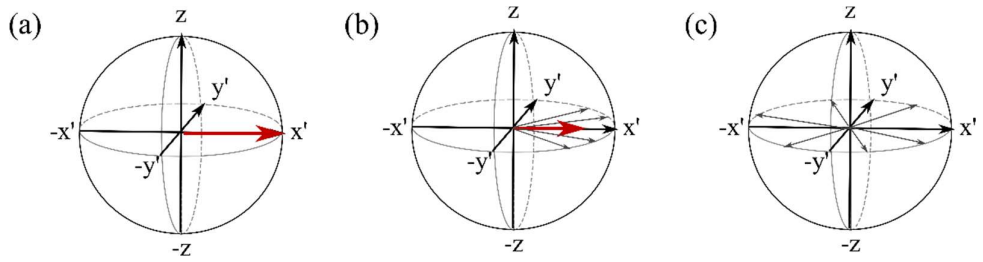

Figure 2.8: The spin dephasing observed (a) immediately after a 90° pulse, (b) after a short time delay, t_1, and (c) after a long time delay, t_2. The net transverse magnetization (red) and individual spin packets (black) are shown for clarity. The frame of reference is rotating at a frequency of γB_0, therefore some spins appear to precess anticlockwise if their Larmor frequency is smaller than γB_0. Schematics of the net magnetization are shown in the rotating frame.

Many contributions that lead to spin dephasing result from static spatial inhomogeneities in the magnetic field. In the presence of a static inhomogeneity the spin dephasing can be corrected for using a spin-echo as shown in Figure 2.9. For an ensemble of spins in the presence of a static field gradient, a delay of time τ is waited before a 180° pulse is applied to invert the spins. As the field is static the magnitude of the precession frequencies of each spin will be identical to those prior to inversion, but the direction will be reversed. This means that after a second delay of τ the magnetization vectors will refocus, and the true spin-spin relaxation can be measured. Static gradients can arise due to inhomogeneities in the applied B_0 field, or due to internal gradients that are intrinsic properties of the sample. If static gradient effects are not removed the apparent spin-spin relaxation time constant, known as T_2* is measured. Depending on the strength of the static gradients T_2* may limit the application of a range of pulse sequences even when T_2 is sufficiently long for their use.

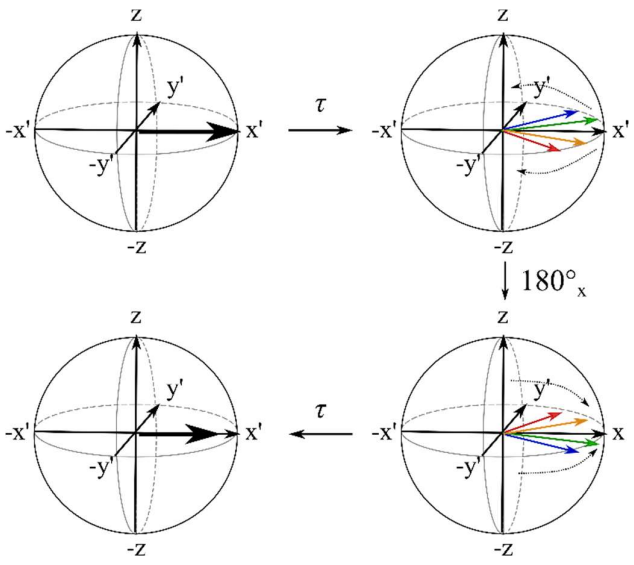

Figure 2.9: A schematic representation of the effects of a spin echo refocussing magnetization in the presence of a constant gradient field. Schematics of the net magnetization are shown in the rotating frame.

To measure the true T_2 decay of a sample spin echoes are looped one after another in a sequence known as a Carr-Purcell-Meiboon-Gill (CPMG) sequence,[5] which is shown in Figure 2.10.

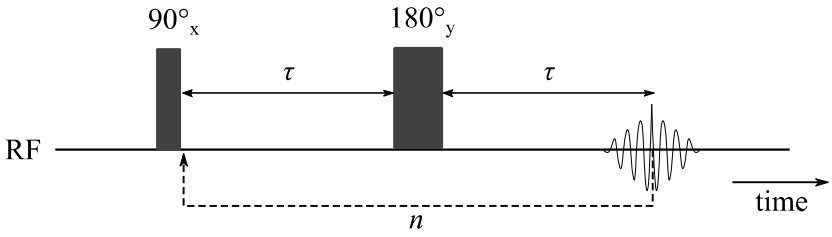

Figure 2.10: The CPMG pulse sequence. The spin echo component is repeated *n* times to allow sufficient sampling of the spin-spin relaxation behaviour as a function of time.

There are two possibilities for acquiring the magnetization data from a CPMG experiment. The first is to run the sequence for a fixed number of loops, *n*, and then acquire the full FID. This process is preferential to the use of a single spin echo with a variable value of τ when applied to samples that show a dependence of T_2 on the value of τ, such as liquids imbibed in porous media (as shown in section 2.4.2). This method allows spectral resolution to be obtained, but as the signal has decayed the sample must be left $5 \times T_1$ to return to equilibrium before another time point can be measured (i.e. with a different number of loops). As a result, the experiment is relatively slow. The

alternative is to sample only the top point of the echo each time the signal is refocussed. As no FID is recorded it is not possible to obtain spectral resolution, however the full T_2 decay can be sampled in a single scan. This rapid acquisition is referred to as a "one-shot" sequence.

The Bloch vector model states that the transverse magnetization, $M_{xy}(t)$, evolves as:

$$\frac{dM_{xy}(t)}{dt} = -\frac{M_{xy}(t)}{T_2}, \tag{2.14}$$

which has the general solution:

$$M_{xy}(t) = M_{xy}(0)\exp\left(-\frac{t}{T_2}\right). \tag{2.15}$$

As with the T_1 experiment, the magnetization will be proportional to the signal, and eq. (2.15) can be fitted to the data acquired from a CPMG experiment to extract the T_2 time constant. As T_2 is affected by both the secular and non-secular components of relaxation $T_2 \leq T_1$ for all practically encountered systems.

An important consideration for spin-spin relaxation is the presence of *J*-coupling. Whilst the spin echo is capable of refocussing the effects of static gradients it is not capable of refocussing spin-spin relaxation caused by *J*-couplings. To supress these effects very short echo times, or low field strengths can be used. However, these options are not always possible due to hardware or SNR limitations. A more general approach is to use a PROJECT sequence for the acquisition of T_2.[6] This sequence includes an additional 90° and 180° pulse within the echo train, which are used to supress the *J*-modulations.

2.3.2 Sources of relaxation

NMR relaxation mechanisms are caused by fluctuating magnetic fields, which generate magnetic noise. These fluctuations are predominantly modulated by molecular motions, and the main sources of relaxation are listed below.

Dipolar interactions: The local fields generated by two spin active nuclei will influence one another in a through-space interaction. For the simple case of two spins in a rotating homonuclear diatomic molecule, the magnetic field generated by spin 1 will vary as its magnetic moment changes orientation relative to the B_0 field. Spin 2 will experience these

fluctuating magnetic fields, which lead to relaxation. Spin 2 will influence spin 1 in the same manner. This effect is a through-space interaction, and is proportional to r^{-6}, where r is the internuclear distance.

Quadrupolar interactions: These act in a similar fashion to the dipolar interactions, however quadrupolar relaxation is much more efficient than dipolar relaxation. As a result, only intramolecular interactions (between spins within the molecule) contribute to the observed relaxation, and intermolecular interactions (between neighbouring molecules) can be neglected.

Paramagnetic interactions: Due to the large gyromagnetic ratio of paramagnetic species ($\gamma_S = 658\gamma_I$) the interaction of spins with paramagnetic impurities leads to very efficient relaxation. Often only a small quantity of paramagnetic impurity needs to be present to dominate the relaxation behaviour.[7,8] This effect is commonly observed for molecular oxygen within bulk liquids,[9] or paramagnetic impurities in porous media.

Scalar relaxation: Modulations of the scalar interaction can be classified separately from dipolar interactions as they are a through-bond interaction, rather than a through-space interaction.

For brevity, only the relaxation mechanisms that are most pertinent to the work contained within this thesis are described. Other relaxation mechanisms will occur concomitantly, such as chemical shift anisotropy or spin-rotation, and a fuller description of these phenomena can be found elsewhere.[10,11]

2.3.3 T_1-T_2 correlation experiments

Instead of measuring an individual T_1 or T_2 as a 1-dimensional (1D) experiment these measurements can be combined to allow the acquisition of both parameters from a single 2-dimensional (2D) experiment. By measuring both relaxation time constants simultaneously the measurement time is reduced, and the resolution of the experiment is vastly increased. A difference of approximately a factor of 3 in the relaxation times is required to distinguish between peaks in a 1D relaxation experiment.[12] The addition of the second dimension simplifies the data analysis, and allows a far greater separation of relaxation environments. Features with the same or similar T_1 values can also be resolved based on T_2 in a 2D experiment. The T_1-T_2 correlation experiment is performed by preconditioning spins with an inversion-recovery sequence, before using a CPMG

sequence for acquisition. This is shown schematically in Figure 2.11. The sequence can be performed with the acquisition of the full FID, however this becomes a 3-dimensional (3D) experiment and often has prohibitively long acquisition times. Instead, a one-shot CPMG acquisition is used, and the identification of features in the T_1-T_2 plots is performed by comparison between samples.

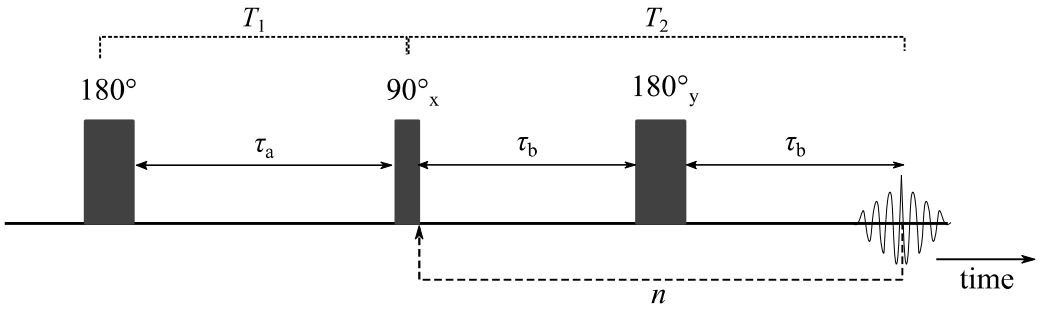

Figure 2.11: The pulse sequence used for a T_1-T_2 correlation experiment. The T_1 section is based on an inversion recovery experiment, and the T_2 section on a CPMG experiment.

The ratio T_1/T_2 can be directly extracted from these experiments, often as a modal value or a logarithmic average. The ratio has been widely used as a surface affinity metric for liquids imbibed within porous systems,[13,14] and will be discussed further in chapter 3.

2.3.4 Data processing

For samples with a single magnetic environment eqs. (2.12) and (2.15) can be applied directly to extract the T_1 and T_2 relaxation time constants respectively. Due to the linearity of these equations, n component systems can be measured using a multiexponetial approach. This method, however, is dependent on *a priori* knowledge of the value of n and is not well-suited to systems containing a distribution of relaxation time constants. To mitigate against these issues a common alternative is to apply an inverse Laplace transformation in order to obtain a probability distribution function of T_1 or T_2.[15] The observed NMR signal, $\underline{S}$, is decomposed into a kernel matrix describing the expected relaxation behaviour, $\underline{K}$, the true relaxation time distribution, $\underline{F}$, and the experimental noise, $\underline{E}$;

$$\underline{S} = \underline{KF} + \underline{E}\,. \tag{2.16}$$

Due to the ill-conditioned nature of the exponential kernel matrix, the solution to this equation is non-trivial. The standard methodology for obtaining $\underline{F}$ begins by assuming it

to be a continuous distribution. Tikhonov regularization can then be applied, and the minimisation problem is expressed as:[12]

$$\underline{F} = \arg\min_{\underline{F}\geq 0}\left(\frac{\alpha}{2}\left\|\underline{KF}-\underline{S}\right\|_2^2+\frac{1}{2}\left\|\underline{RF}\right\|_2^2\right), \tag{2.17}$$

where α is a regularization parameter and $\underline{R}$ is a matrix that acts upon $\underline{F}$ to give its second derivative. The regularization parameter is then optimised to strike a balance between the first (fidelity) and the second (penalty) terms. When properly optimised this method is robust and does not require *a priori* knowledge of the number of relaxation components within the system. The underlying assumption is that the distribution is smooth and continuous, which is observed experimentally for the majority of samples.

2.4 Relaxation in porous media

When a liquid is imbibed within a porous medium the sample is no longer uniform. The presence of the pore walls creates heterogeneities within the sample that can have a strong effect on the observed relaxation rate. In this section, the effects of surface relaxation and internal gradients will be discussed. A more detailed review on the application and interpretation of relaxation measurement for liquids imbibed within porous media systems is presented in chapter 3.

2.4.1 The two-phase fast exchange model

Within the pore space the imbibed liquids can be separated into two regions, the surface layer and a bulk pore volume, as shown in Figure 2.12. For liquids imbibed within small pores the diffusion coefficient is often sufficiently large that liquid reaches the pore surface many times during the measurement, and the surface properties control the relaxation behaviour. This is referred to as surface-limited relaxation. The presence of paramagnetic impurities, strong binding sites, and intrinsic gradients in the magnetic field at the pore surface contribute to the reduction of T_1 and T_2 for all adsorbates near the surface. The surface layer can therefore be defined as a finite volume, beyond which the enhanced relaxation effects are negligible. This is often assumed to be a single molecular thickness, but can be up to a 3 layers for small and highly structured adsorbates such as water.[16] The bulk pore fluid is minimally affected by the strong relaxation sinks present

at the pore surface, and the relaxation time constant of this region is similar to that of the bulk liquid.

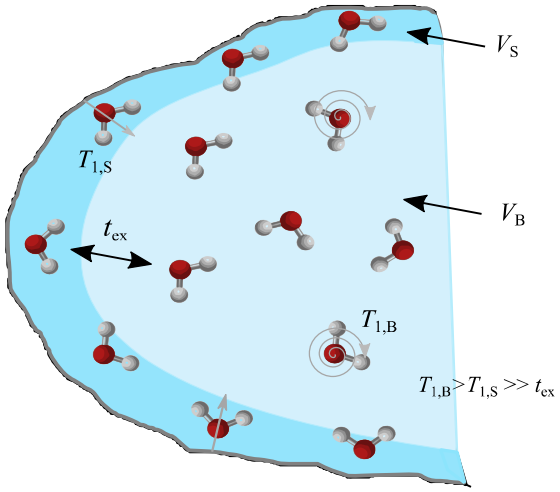

Figure 2.12: A schematic representation of the two-phase fast-exchange model of relaxation. The relaxation rates of molecules in the adsorbed phase, V_S, and the bulk pore space, V_B, are denoted as $T_{1,S}$ and $T_{1,B}$ respectively. Provided that the exchange time, t_{ex}, is much smaller than the $T_{1,S}$ and $T_{1,B}$ then the observed relaxation becomes a population weighted average of the two environments.

If the system were static then two relaxation environments would be expected; one corresponding to the surface layer (with a low T_1) and one corresponding to the bulk pore space (with a higher T_1). In reality the system is dynamic, and molecules at the surface exchange with the molecules in the bulk pore space sufficiently fast that only one relaxation environment is observed. This population weighted average, can be calculated from the two-phase fast exchange model as follows:

$$\frac{1}{T_{1,\mathrm{obs}}} = p\frac{1}{T_{i,\mathrm{S}}} + (1-p)\frac{1}{T_{i,\mathrm{B}}}, \tag{2.18}$$

where $i = 1, 2$. $T_{1,\mathrm{obs}}$ is the experimentally observed relaxation time constant, $T_{i,\mathrm{S}}$ and $T_{i,\mathrm{B}}$ are the surface and bulk relaxation time constants respectively, and p is the population fraction of spins in the surface layer. A commonly used rearrangement of eq. (2.18) is:

$$\frac{1}{T_{1,\mathrm{obs}}} = \frac{1}{T_{\mathrm{i,B}}} + p\left(\frac{1}{T_{\mathrm{i,S}}} - \frac{1}{T_{\mathrm{i,B}}}\right). \tag{2.19}$$

As the relaxation time constants are orders of magnitude smaller for spins at the surface compared to the bulk the assumption that $1/T_{1,S} >> 1/T_{1,B}$ is often valid. It is clear from eq. (2.19) that the observed relaxation rate of a liquid within a porous medium will be a function of the number of available binding sites at the surface, p, and the intrinsic surface relaxation rate. Therefore, the geometry of the porous medium, the surface chemistry, and the solid-liquid interactions all contribute to the relaxation behaviour of liquids imbibed within porous media.

2.4.2 Internal gradient effects

Within a porous medium there are a large number of solid-liquid interfaces, as shown in Figure 2.12. The magnetic susceptibility of the solid matrix and liquid can differ significantly. This means that in the presence of a magnetic field the solid and liquid are polarized to different extents, and an internal gradient is established at the interface. Diffusion of molecules through these gradients causes a significant increase in the degree of spin dephasing, and a shortening of T_2*. As the gradients are caused by susceptibility differences, the magnitude of B_0 will strongly influence the magnitude of the effective internal gradient, g_{eff}. The shortened values of T_2* result in a broadening of the NMR peak, and a corresponding increase in the full width half maximum (FWHM) from <0.01 ppm for bulk liquids to >1 ppm for liquids imbibed within porous media.[17] The exact effect of the gradient on T_2 is complex, and depends on three characteristic length scales:[18–20]

1. the distance the spins diffuse between echoes, l_e,
2. the pore diameter, l_s,
3. the distance a molecule must travel to dephase by 2π radians, l_g.

When one of these length scales is much shorter than the others it limits the motional behaviour and the relaxation behaviour can be classified into three asymptotic regimes, as shown in Figure 2.13. These regimes are defined as the short time (ST), motional averaging (MAV), and localized (LOC). The defining characteristics of each regime, and the dependence of the T_2 relaxation enhancement on the echo time, t_e, for spins in each of the regimes shown in Figure 2.13 can be summarised as:

1. *Short time limit* ($l_e << l_s, l_g$): this regime is observed for porous media with large pore spaces and weak internal gradients. The diffusion term of the relaxation is analogous to free diffusion in a constant field gradient, and is proportional to t_e^3.
2. *Motional averaging* ($l_s << l_e, l_g$): this regime is observed for porous media with very small pores. The gradient term varies with l_s^2 and t_e.
3. *Localization regime* ($l_g << l_s, l_e$): this regime is observed for porous media with strong and spatially variant internal gradients. The gradient term varies with t_e.

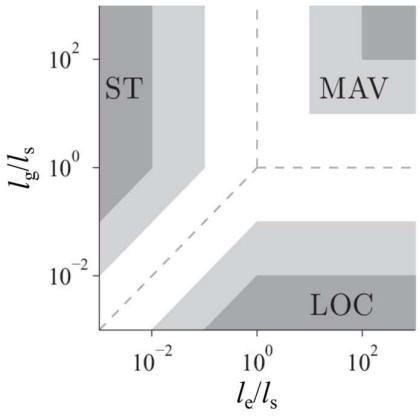

Figure 2.13: A schematic diagram of the diffusion regimes ST, MAV, and LOC as defined by the length scales l_e, l_s, and l_g. The limit of each regime is not well defined, and a pre-asymptotic regime exists outside of the shaded areas. Within the pre-asymptotic region an empirical correction to the T_2 decay can be applied. Reproduced from Mitchell et al.[20]

In these three limits analytical expressions exist to describe the diffusive contribution to T_2. The separation of internal gradient effects from the true T_2 value is only possible when the internal gradient component depends on the echo time, t_e, raised to a power greater than 1. This is because the true T_2 relaxation component depends on t_e^1. Therefore, if both the internal gradient component and the true T_2 have the same dependence on t_e they cannot be resolved experimentally. From a purely theoretical perspective, it would only be possible to remove the diffusive contribution to T_2 in the short time limit. However, in practice, liquids in porous media rarely reach the motional averaging or localization regimes, and often do not fulfil the criterion of the short time region either. Instead, the observed diffusive regime is an ill-defined pre-asymptotic regime where the diffusive contribution to T_2 varies as t_e^k, with $1 \leq k \leq 3$. In the pre-asymptotic regime the kernel function describing the empirical relaxation behaviour is given as:

$$K = \exp\left(-\frac{\mathrm{n}t_\mathrm{e}}{T_2}\right)\exp(-a\mathrm{n}{t_\mathrm{e}}^k)\,, \tag{2.20}$$

where n is the number of echoes in the CPMG experiment, a is a non-physical composite diffusion term, and $1 \leq k \leq 3$. By acquiring several CPMG experiments with different values of t_e a 2D data set is obtained. The data can be expressed as a 2D Fredholm integral:

$$\frac{S(\mathrm{n}, t_\mathrm{e})}{S(0,0)} = \int_{-\infty}^{\infty}\int_{-\infty}^{\infty} f(T_2, a)K\mathrm{d}(\log T_2)\mathrm{d}(\log a) + \varepsilon, \tag{2.21}$$

where $S(\mathrm{n}, t_\mathrm{e})$ is the observed signal, $S(0,0)$ is the initial signal at time $t = 0$, $f(T_2, a)$ is distribution of T_2 and a, K is the kernel function defined in eq. (2.20), and ε is the noise.

The solution to eq. (2.21) allows the extraction of the signal decay in the absence of diffusion effects, $S(\mathrm{n}, 0)$, from $f(T_2, a)$. The data $S(\mathrm{n}, t_\mathrm{e})/S(\mathrm{n}, 0)$ can then be plotted for all values of t_e over a constant time period. If the data collapse on to a single plot then the choice of k is valid, and the correction will remove the effects of diffusion in internal gradients from the value of T_2. The value of k can be optimised by hand iteration until a suitable collapse of the data is observed. If the optimal collapse occurs for $k = 1$ then it is not possible to separate the diffusive term from the true T_2 relaxation, and an internal gradient correction cannot be applied.

2.5 NMR relaxation formalisms

The discussion of relaxation that has been presented thus far has been focussed on the macroscopic measurement of T_1 and T_2. The theory that relaxation is caused by fluctuating magnetic fields, which are controlled by molecular motions, has also been discussed qualitatively. In this section the concepts required to quantitatively describe the relaxation behaviour of a system from the molecular level are presented. As an example of this methodology, the relaxation behaviour of a bulk liquid is discussed.

2.5.1 The autocorrelation function

The local field experienced by a nucleus will vary as a function of time, as shown in Figure 2.14. These variations are driven by random molecular motions, which in turn cause the magnetic field variations to be random. As a result, the long-time average of the fluctuations is zero. Due to the large number of spins within the system, the average over all spins at a given time is also zero. This is referred to as the ergodic hypothesis, and greatly simplifies the mathematics describing the relaxation behaviour.

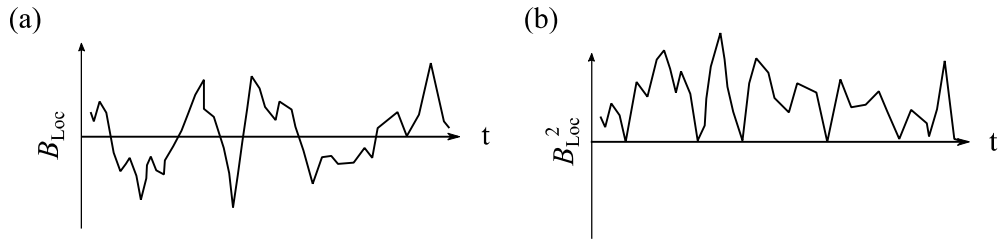

Figure 2.14: The fluctuations in the (a) local field, and (b) square of the local field experienced by a single spin. For illustrative purposes the local field represents the transverse component, such that the average field is centred about zero.

To describe the relaxation behaviour it is necessary to define the magnitude and rate of the fluctuations. As the average of the fluctuations is zero, this cannot be used to define the magnitude. Instead, a more meaningful value is the mean square fluctuating field, which is given as:

$$\langle B_{\mathrm{Loc}}^2(t)\rangle \neq 0\,, \tag{2.22}$$

where the angle brackets imply an ensemble average. The mean square fluctuating field is shown in Figure 2.14b. To describe the rate of fluctuations of the magnetic field it is common to consider the change in the local field between two time points separated by a delay of τ. This is measured by the correlation function, which is also known as the autocorrelation function, and is given by:

$$G(\tau) = \langle B_{\mathrm{Loc}}(t) B_{\mathrm{Loc}}(t+\tau)\rangle\,. \tag{2.23}$$

The autocorrelation function is a stationary function, which means that it is independent of the time, t, and varies only with τ. By definition, at $\tau = 0$ the correlation function converges to eq. (2.22), and at long times $G(\tau) \to 0$. The behaviour of $G(\tau)$ within these

limits depends on the rate of fluctuations of the magnetic field. The value of the correlation function is shown schematically in Figure 2.15 for slow fluctuations and fast fluctuations. In the case of slowly fluctuating fields the value of $B_{\mathrm{Loc}}(t)$ and $B_{\mathrm{Loc}}(t+\tau)$ are very similar up to large values of τ. As a result, the correlation function changes a small amount for low τ values, and decays slowly. In contrast, for a system experiencing much faster magnetic field fluctuations, the local fields can change significantly over short τ values. This results in a much faster loss of correlation, as is shown in Figure 2.15b.

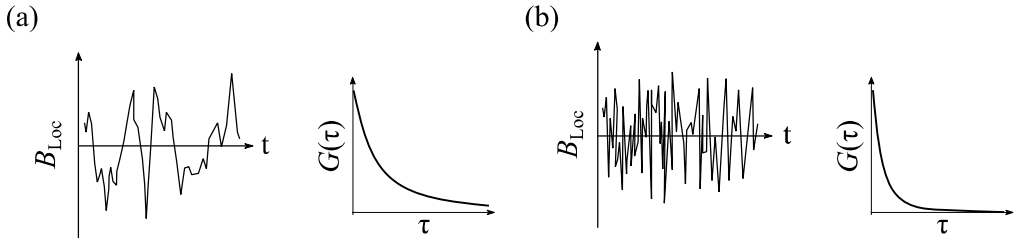

Figure 2.15: The local fields experienced by a single spin, and the corresponding correlation function for a system undergoing (a) slow, and (b) fast molecular fluctuations.

The correlation function can be separated into a time independent and time dependent contribution,

$$G(\tau) = \langle B_{\mathrm{Loc}}^2 \rangle g(\tau)\,. \tag{2.24}$$

The exact form of the time dependent component of the relaxation, $g(\tau)$, depends on the type of molecular motions that are occurring, and many different functions have been reported.[21–23] For the simplest case of isotropic rotational motion an exponential function is used:

$$G(\tau) = \langle B_{\mathrm{Loc}}^2 \rangle \exp\left(-\frac{|\tau|}{\tau_{\mathrm{c}}}\right), \tag{2.25}$$

where τ_{c} is the time taken for a molecule to rotate π radians, and is referred to as the correlation time of the molecular motion.

2.5.2 Spectral density function

The correlation function is a time domain representation of the magnetic fluctuations that induce relaxation. This can be converted into a frequency domain representation by taking the Fourier transform of the correlation function:

$$\mathcal{J}(\omega_0) = 2\int_0^\infty G(\tau)\exp\left(-i\omega_0\tau\right) d\tau\,. \tag{2.26}$$

For the case of an exponential correlation function as shown in eq. (2.25) the spectral density function is given as:

$$\mathcal{J}(\omega_0) = 2\langle B_{\mathrm{Loc}}^2\rangle \frac{\tau_c}{1+\omega_0^2\tau_c^2}\,. \tag{2.27}$$

For simplicity the reduced spectral density is often reported:

$$J(\omega_0) = \frac{\tau_c}{1+\omega_0^2\tau_c^2}\,. \tag{2.28}$$

As the reduced spectral density function is used preferentially within the literature, the term spectral density function (SDF) will be used to denote the reduced spectral density from here on.

The SDF corresponding to an exponential correlation function is a frequency dependent Lorentzian function. At high field strengths the function is frequency dependent, but below a value of $1/\tau_c$ the SDF reaches a frequency independent plateau. The frequency behaviour of the Lorentzian SDF for fast and slow correlation times is shown in Figure 2.16. The area under each curve is constant, however the height and width of the corresponding SDFs are very different. For fast motions a broad and low magnitude SDF is observed. This results in a small contribution to the relaxation behaviour over a large range of timescales. In contrast, for slow motions the SDF is large and narrow. This results in a strong contribution to the relaxation behaviour, but the relaxation enhancement only occurs at low frequencies. This means that slow molecular process can easily dominate the low field relaxation behaviour, even in the presence of other faster processes.

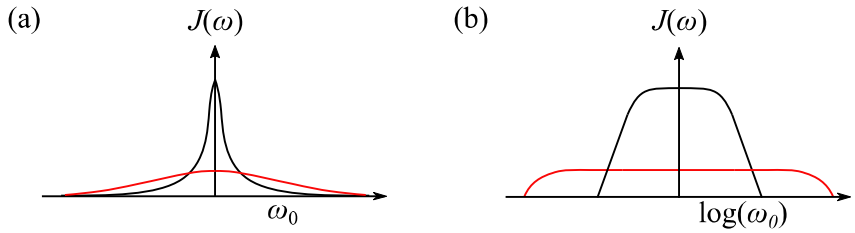

Figure 2.16: The spectral density function for a system characterised by a short (red), and long (black) correlation times. For clarity the data are shown on a (a) linear, and (b) log scale.

2.5.3 BPP theory

For simple liquids in their bulk state, the rotation of the molecule is known to dominate the overall relaxation behaviour. These rotations lead to a modulation of the dipole interactions between pairs of spins within the molecule, which is referred to as an intramolecular relaxation pathway. Bloembergen, Purcell and Pound (BPP) applied a Lorentzian SDF of the form of eq. (2.28) to describe this motion, and proposed the well-known expressions:

$$\frac{1}{T_{1,\text{intra}}} = \left(\frac{\mu_0}{4\pi}\right)^2 \frac{3\gamma^4\hbar^2}{10b^6}\left[J(\omega_0) + 4J(2\omega_0)\right], \tag{2.29}$$

$$\frac{1}{T_{2,\text{intra}}} = \left(\frac{\mu_0}{4\pi}\right)^2 \frac{3\gamma^4\hbar^2}{20b^6}\left[3J(0) + 5J(\omega_0) + 2J(2\omega_0)\right], \tag{2.30}$$

where μ_0 is the magnetic permeability constant, γ is the gyromagnetic ratio, $\hbar$ is Planck's constant divided by 2π, b is the internuclear separation of the spins (for rigid molecules this distance is constant), and $J(\omega_0)$ is given by eq. (2.28). The behaviour of T_1 and T_2 with respect to the frequency is the inverse of the behaviour of the SDF with respect to the frequency, as implied by eqs. (2.29) and (2.30). The T_1 and T_2 values as functions of the correlation time are more complex, and are shown in Figure 2.17. For T_1, the relaxation time constant decreases to a minimum when $\omega_0\tau_c = 1$. Close to the minimum there is little change in T_1 behaviour with respect to the molecular motions over an order of magnitude of correlation times. Either side of this region the T_1 increases steadily. The T_2 behaviour is identical to the T_1 behaviour for fast molecular motions, leading to the ratio of $T_1/T_2 \approx 1$ for motionally unhindered samples, such as simple bulk liquids. For samples exhibiting slower molecular motions ($\tau_c > 1/\omega_0$) the value of T_2 continues to

decrease in contrast to T_1. This means that for systems characterised by slow molecular motions the ratio of $T_1/T_2 > 1$. Such a situation is commonly observed for liquids imbibed within porous media,[13,24] where the surface binding reduces the mobility of the adsorbate.

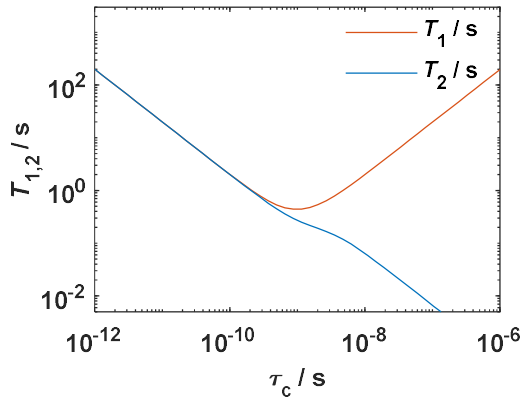

Figure 2.17: The T_1 and T_2 values according to BPP theory as a function of the molecular correlation time. The prefactor of eq. (2.29) was set to 1×10^9, and to 0.5×10^9 for eq. (2.30). For both relaxation time constants the frequency was set to $\omega_0 = 6.28\times10^8$.

2.5.4 Intermolecular relaxation

In addition to the relaxation caused by rotational motion, the dipolar interaction between spins on different molecules is modulated by translational diffusion, which changes the internuclear distance and orientations of the interacting spins. The correlation function describing the relevant magnetic fluctuations is well-known,[25–27] and the corresponding spectral density for this process, based on a hard sphere model,[22,25,26] is given as:

$$J(\omega_0) = \frac{(3/2)u^2 + (15/2)u + 12}{(1/8)u^6 + u^5 + 4u^4 + (27/2)u^3 + (81/2)u^2 + 81u + 81}, \tag{2.31}$$

where $u = \sqrt{2\omega_0\tau_t}$. This leads to the corresponding relaxation rate expressions:

$$\frac{1}{T_{1,\text{inter}}} = \left(\frac{\mu_0}{4\pi}\right)^2 \frac{6\pi}{5} N \frac{\gamma^4\hbar^2}{b^3}\tau_t[J(\omega_0) + 4J(2\omega_0)], \tag{2.32}$$

$$\frac{1}{T_{2,\text{inter}}} = \left(\frac{\mu_0}{4\pi}\right)^2 \frac{3\pi}{5} N \frac{\gamma^4\hbar^2}{b^3}\tau_t[3J(0) + 5J(\omega_0) + 2J(2\omega_0)], \tag{2.33}$$

where N is the number of spins per unit volume, and τ_t is a characteristic diffusion correlation time. $\tau_t = d/(2D)$ where d is one molecular diameter and D is the diffusion coefficient of the liquid.

2.5.5 Combining relaxation mechanisms

Multiple relaxation mechanisms may be occurring concurrently within the sample, caused by different types of molecular motion and relaxation sources. For k different relaxation mechanisms affecting all spins in the sample, the relaxation behaviour can be expressed as:

$$\frac{1}{T_i} = \sum_k \frac{1}{T_{i,k}} \quad \text{where } i = 1,2. \tag{2.34}$$

The wide array of observed relaxation processes means that theoretically there are many contributions to every measured relaxation rate. Fortunately, often only one or two relaxation mechanisms will dominate the relaxation behaviour, which simplifies eq. (2.34). For the case of bulk liquids presented in section 2.5.3 and 2.5.4 the relaxation rate can be written as:

$$\frac{1}{T_i} = \frac{1}{T_{i,\text{inter}}} + \frac{1}{T_{i,\text{intra}}} \quad \text{where } i = 1,2. \tag{2.35}$$

Eq. (2.35) is valid when the intermolecular (^{1}H-^{1}H) and intramolecular relaxation processes dominate the experimentally observed relaxation behaviour. The simplification allows the fitting of literature models to the data in order to extract physical constants that describe the behaviour of the system, such as τ_t and τ_c.

In summary, the methods presented within section 2.5 show the quantitative relationship between molecular motions and NMR relaxation behaviour. The process is general for all relaxation behaviour, and can be summarised as:

1. identify the relevant spin interaction(s), and molecular motion(s)
2. construct a suitable correlation function
3. Fourier transform the correlation function and construct the relaxation equations
4. fit the relaxation equations to the experimental data, and extract physical parameters.

The mathematical treatment of a wide variety of molecular motions has already been carried out within the literature.[21,22,26–33] This means that it is rarely necessary to perform steps 2 and 3 unless novel relaxation behaviour is being explored. Often the most important step is to ensure that the relaxation equations found in the literature are suitable for describing the molecular motions that occur within the sample. To do so, temperature dependent studies,[8] deuteration,[34] and material characterisation[35] can all be performed to ensure that the chosen relaxation model accurately describes the underlying molecular dynamics.

2.6 References

(1) Keeler, J. *Understanding NMR Spectroscopy*; John Wiley & Sons, 1999.

(2) Levitt, M. H. *Spin Dynamics: Basics of Nuclear Magnetic Resonance*; John Wiley & Sons, 2001.

(3) Abragam, A. *Principles of Nuclear Magnetism*; Oxford University Press, 1983.

(4) Barile, E.; Pellecchia, M. NMR-Based Approaches for the Identification and Optimization of Inhibitors of Protein-Protein Interactions. *Chem. Rev.* **2014**, *114*, 4749–4763.

(5) Meiboom, S.; Gill, D. Modified Spin Echo Method for Measuring Nuclear Relaxation Times. *Rev. Sci. Instrum.* **1958**, *29*, 688–691.

(6) Aguilar, J. A.; Nilsson, M.; Bodenhausen, G.; Morris, G. A. Spin Echo NMR Spectra without *J* Modulation. *Chem. Commun.* **2012**, *48*, 811–813.

(7) D'Agostino, C.; Bräuer, P.; Charoen-Rajapark, P.; Crouch, M. D.; Gladden, L. F. Effect of Paramagnetic Species on T_1, T_2 and T_1/T_2 NMR Relaxation Times of Liquids in Porous $CuSO_4/Al_2O_3$. *RSC Adv.* **2017**, *7*, 36163–36167.

(8) Korb, J. P.; Whaley Hodges, M.; Gobron, T.; Bryant, R. G. Anomalous Surface Diffusion of Water Compared to Aprotic Liquids in Nanopores. *Phys. Rev. E* **1999**, *60*, 3097–3106.

(9) Shikhov, I.; Arns, C. H. Temperature-Dependent Oxygen Effect on NMR D-T_2

Relaxation-Diffusion Correlation of *N* -Alkanes. *Appl. Magn. Reson.* **2016**, *47*, 1391–1408.

(10) Farrar, T. C.; Becker, E. D. Chapter 4 - Relaxation Mechanisms. In *Pulse and Fourier Transform NMR*; Academic Press, 1971; pp 46–65.

(11) Breitmaier, E.; Spohn, K.-H.; Berger, S. Spin-Lattice Relaxation Times and the Mobility of Organic Molecules in Solution. *Angew. Chem. Int. Ed.* **1975**, *14*, 144–159.

(12) Reci, A.; Sederman, A. J.; Gladden, L. F. Obtaining Sparse Distributions in 2D Inverse Problems. *J. Magn. Reson.* **2017**, *281*, 188–198.

(13) D'Agostino, C.; Mitchell, J.; Mantle, M. D.; Gladden, L. F. Interpretation of NMR Relaxation as a Tool for Characterising the Adsorption Strength of Liquids inside Porous Materials. *Chem. A Eur. J.* **2014**, *20*, 13009–13015.

(14) D'Agostino, C.; Brett, G. L.; Miedziak, P. J.; Knight, D. W.; Hutchings, G. J.; Gladden, L. F.; Mantle, M. D. Understanding the Solvent Effect on the Catalytic Oxidation of 1,4-Butanediol in Methanol over Au/TiO_2 Catalyst: NMR Diffusion and Relaxation Studies. *Chem. Eur. J.* **2012**, *18*, 14426–14433.

(15) Butler, J. P.; Reeds, J. A.; Dawson, S. J. Estimating Solutions of First Kind Integral Equations with Nonnegative Constraints and Optimal Smoothing. *J. Numer. Anal.* **1981**, *18*, 381–397.

(16) Fripiat, J.; Cases, J.; Francois, M.; Letellier, M. Thermodynamic and Microdynamic Behavior of Water in Clay Suspensions and Gels. *J. Colloid Interface Sci.* **1982**, *89*, 378–400.

(17) Chang, C. T. P.; Watson, A. T.; Edwards, C. M. NMR Imaging of Fluids and Flow in Porous Media. In *Methods in the Physics of Porous Media*; Academic Press, 1999; pp 387–423.

(18) Mitchell, J.; Chandrasekera, T. C.; Gladden, L. F. A General Approach to T_2 Measurements in the Presence of Internal Gradients. *Microporous Mesoporous Mater.* **2013**, *178*, 20–22.

(19) Mitchell, J.; Chandrasekera, T. C.; Gladden, L. F. Measurement of the True

Transverse Nuclear Magnetic Resonance Relaxation in the Presence of Field Gradients. *J. Chem. Phys.* **2013**, *139*, 74205.

(20) Mitchell, J.; Chandrasekera, T. C. Understanding Generalized Inversions of Nuclear Magnetic Resonance Transverse Relaxation Time in Porous Media. *J. Chem. Phys.* **2014**, *141*, 224201.

(21) Kimmich, R.; Anoardo, E. Field-Cycling NMR Relaxometry. *Prog. Nucl. Magn. Reson. Spectrosc.* **2004**, *44*, 257–320.

(22) Korb, J.-P. Multiscale Nuclear Magnetic Relaxation Dispersion of Complex Liquids in Bulk and Confinement. *Prog. Nucl. Magn. Reson. Spectrosc.* **2018**, *104*, 12–55.

(23) Kruk, D.; Herrmann, A.; Rössler, E. A. Field-Cycling NMR Relaxometry of Viscous Liquids and Polymers. *Prog. Nucl. Magn. Reson. Spectrosc.* **2012**, *63*, 33–64.

(24) Weber, D.; Mitchell, J.; McGregor, J.; Gladden, L. F. Comparing Strengths of Surface Interactions for Reactants and Solvents in Porous Catalysts Using Two-Dimensional NMR Relaxation Correlations. *J. Phys. Chem. C* **2009**, *113*, 6610–6615.

(25) Hwang, L.; Freed, J. H. Dynamic Effects of Pair Correlation Functions on Spin Relaxation by Translational Diffusion in Liquids. *J. Chem. Phys.* **1975**, *63*, 4017–4025.

(26) Ayant, Y.; Belorizky, E.; Aluzon, J.; Gallice, J. Calcul Des Densités Spectrales Résultant D'un Mouvement Aléatoire de Translation En Relaxation Par Interaction Dipolaire Magnétique Dans Les Liquides. *J. Phys. Fr.* **1975**, *36*, 991–1004.

(27) Kruk, D.; Meier, R.; Rössler, E. A. Translational and Rotational Diffusion of Glycerol by Means of Field Cycling ^{1}H NMR Relaxometry. *J. Phys. Chem. B* **2011**, *115*, 951–957.

(28) Godefroy, S.; Korb, J.-P.; Fleury, M.; Bryant, R. G. Surface Nuclear Magnetic Relaxation and Dynamics of Water and Oil in Macroporous Media. *Phys. Rev. E* **2001**, *64*, 1–13.

(29) Zavada, T.; Kimmich, R. The Anomalous Adsorbate Dynamics at Surfaces in Porous Media Studied by Nuclear Magnetic Resonance Methods. the Orientational Structure Factor and Lévy Walks. *J. Chem. Phys.* **1998**, *109*, 6929–6939.

(30) Singer, P. M.; Chen, Z.; Alemany, L. B.; Hirasaki, G. J.; Zhu, K.; Xie, Z. H.; Vo, T. D. Interpretation of NMR Relaxation in Bitumen and Organic Shale Using Polymer − Heptane Mixes. *energy Fuels* **2018**, *32*, 1534–1549.

(31) Korb, J.; Nicot, B.; Bubici, S.; Ferrante, G. Dynamics and Wettability of Oil and Water in Oil Shales. *J. Phys. Chem. C* **2014**, *118*, 23212–23218.

(32) Halle, B. Molecular Theory of Field-Dependent Proton Spin-Lattice Relaxation in Tissue. *Magn. Reson. Med.* **2006**, *56*, 60–72.

(33) Faux, D. A.; Cachia, S. H. P.; McDonald, P. J.; Bhatt, J. S.; Howlett, N. C.; Churakov, S. V. Model for the Interpretation of Nuclear Magnetic Resonance Relaxometry of Hydrated Porous Silicate Materials. *Phys. Rev. E* **2015**, *91*, 032311.

(34) Korb, J. -P.; Levitz, P. E. Direct Probing of the Wettability of Plaster Pastes at the Nanoscale by Proton Field Cycling Relaxometry. *AIP Conf. Proc.* **2008**, *1081*, 55–58.

(35) Korb, J. P.; Monteilhet, L.; McDonald, P. J.; Mitchell, J. Microstructure and Texture of Hydrated Cement-Based Materials: A Proton Field Cycling Relaxometry Approach. *Cem. Concr. Res.* **2007**, *37*, 295–302.

Chapter 3 : NMR relaxation methods for studying the solid-liquid interaction strength in mesoporous media

Contents

3.1 Introduction

A mesoporous material is defined as a medium containing pores with a diameter, d_p, of 2-50 nm. This is an intermediate size classification, between microporous materials (d_p <2 nm) and macroporous materials (d_p >50 nm).[1] Within a mesoporous medium the surface area to pore volume ratio of the material is large, meaning that when a liquid is imbibed within the material the surface is able to have a significant effect on all liquid molecules. Microporous materials also have a high surface area to pore volume ratio, but d_p is close to the molecular diameter, d_m, and this confinement results in anomalous physicochemical properties. Several molecular diameters can fit within the pore diameter in mesoporous materials, which limits the contribution of complex confinement effects to the molecular dynamics of the system. These effects are the source of the shape selective adsorption and reaction,[2,3] and highly reduced diffusion coefficients[4,5] that have been observed for liquids imbibed within microporous materials. Whilst there is no requirement for the pore size distribution of a mesoporous material to be narrow, these materials are often synthesised with uniform and monomodal pore size distributions to control the properties of the medium. Mesoporous materials have been extensively investigated as solutions to a range of industrial problems due to their strong adsorbate-surface interactions, high surface areas, and their ability to be readily modified.[6] These properties have resulted in successful applications of mesoporous materials in catalysis,[7,8] chemical separations,[9] gas sensing,[10] carbon dioxide sequestration,[11] drug delivery routes,[12] and energy storage.[13]

NMR relaxation is a powerful tool for the study of liquids (or gasses) confined within mesoporous media. In section 2.4.1 NMR relaxation measurements in the surface limited regime were shown to be sensitive to changes of molecular motions upon binding, and the surface to volume ratio of the porous medium. This can be demonstrated through the two-phase fast exchange model:

$$\frac{1}{T_1} = \frac{1}{T_{1,\mathrm{B}}} + \frac{\lambda S}{V}\left(\frac{1}{T_{1,\mathrm{S}}} - \frac{1}{T_{1,\mathrm{B}}}\right), \tag{3.1}$$

where T_1, $T_{1,S}$ and $T_{1,B}$ are the experimentally measured, surface, and bulk relaxation time constants respectively, λ is the surface layer thickness and is often assumed to be equal to d_m, and S/V is the surface to volume ratio of the porous medium. In addition, the non-

invasive nature of NMR measurements mean that they can be performed without disturbing a system from its true conditions. *In operando* NMR measurements have already been performed for heterogeneous chemical reactions at high temperatures and pressures,[14] fluid flow through metal pipes,[15] and, of course, within living organisms.[16,17] NMR experiments can be highly informative due to the large quantity of information that it is possible to encode within a single relaxation experiment, however, it is not always simple to interpret the adsorption information obtained. This chapter will focus on two principal methodologies that have been used to analyse liquids imbibed within porous media; and the applications, advantages, and limitations of these measurements will be discussed.

1) Fixed field measurements – relaxation measurements performed at a single field strength, which can be combined to create dimensionless ratios of T_1 and T_2. These ratios are often correlated with the solid-liquid interaction strength, and the experimentally observed properties of a system.
2) Variable field measurements – a series of relaxation measurements of the same sample performed over a wide range of magnetic field strengths. A fundamental model describing the molecular motions occurring within the sample is commonly used to describe the dynamics of the adsorbate. The parameters obtained from the model fitting are interpreted in terms of the solid-liquid interaction strength.

Fixed field measurements do not require specialist equipment, and the necessary pulse programs are commonplace on commercial NMR machines. Furthermore, the relaxation experiments can be combined with existing techniques in order to apply spectroscopic or diffusion weighting,[18] and spatial resolution[19] to better understand the system under study. As a result of the simplicity and versatility of its application, fixed field relaxation measurements are more commonly applied to the study of liquids imbibed within mesoporous materials than variable field techniques. In recent years, however, the development of commercial field cycling machines has increased the interest in variable field techniques.[20] By measuring the relaxation rate at a range of Larmor frequencies the relaxation behaviour can be probed over the corresponding range of timescales. The relaxation time constant is minimized when:

$$\omega_0 \tau_c = 1\,, \tag{3.2}$$

where ω_0 is the Larmor frequency, and τ_c is the correlation time of motion leading to the most effective relaxation. This clarifies the origin of the relaxation behaviour, and allows a formal modelling of the complex liquid dynamics that occur within porous media.

3.2 Fixed field measurements

From the discussion presented in sections 2.4 and 2.5 it follows that the relaxation rate of liquids imbibed within porous media depends on the material properties (i.e. the density of paramagnetic species and pore size), the liquid properties (i.e. dissolved oxygen content, interspin distance and molecular diameter), and the solid-liquid interaction strength. To facilitate the comparison of the relaxation data obtained from different samples with one another it is beneficial to simplify these contributions by taking a ratio of relaxation time constants. Depending on the chosen ratio, this method eliminates the contribution of the liquid and solid properties to the relaxation behaviour. In this section ratios of only the longitudinal, and the combined longitudinal and transverse relaxation time constants will be discussed.

3.2.1 Ratios of the longitudinal relaxation time constant, $T_{1,B}/T_{1,pore}$

3.2.1.1 Background

The relaxation contributions from the physical properties of the liquid can be removed by multiplying eq. (3.1) by the bulk liquid relaxation rate. Here the term $T_{1,pore}$ is used to indicate that it refers to the relaxation time constant of the liquid imbibed within a porous medium. This ratio can be written as:

$$\frac{T_{1,B}}{T_{1,pore}} = 1 + p\left(\frac{T_{1,B}}{T_{1,S}} - 1\right), \tag{3.3}$$

where $1/T_{1,B}$ is the bulk relaxation rate, $1/T_{1,S}$ is the surface relaxation rate, and p is the population fraction of spins in the surface layer. The strong effect of the surface on the relaxation rate means that $T_{1,S} \ll T_{1,B}$, which allows the relaxation rate ratio to be simplified to:

$$\frac{T_{1,\mathrm{B}}}{T_{1,\mathrm{pore}}} \approx 1 + p\left(\frac{T_{1,\mathrm{B}}}{T_{1,\mathrm{S}}}\right). \tag{3.4}$$

In addition, for mesoporous materials the value of p may be sufficiently large that $pT_{1,\mathrm{B}}/T_{1,\mathrm{S}} \gg 1$. In this limit the experimentally observed relaxation ratio, $T_{1,\mathrm{B}}/T_{1,\mathrm{pore}}$, becomes linearly proportional to the true surface relaxation ratio, $T_{1,\mathrm{B}}/T_{1,\mathrm{S}}$.

At a given measurement frequency, each individual relaxation time constant can be decomposed into a constant term and a correlation time dependent term. The constant term, A, is influenced by the physical parameters of the system, which include both liquid and solid properties where relevant. The correlation time dependent component, $f(\tau_{\mathrm{c}})$, is controlled solely by the molecular motions of the sample. The relaxation time constant is the product of these two terms:

$$\frac{1}{T_{1,i}} = Af(\tau_{\mathrm{c}}), \tag{3.5}$$

where τ_{c} is a characteristic motional correlation time of the system, and $i = \mathrm{S}, \mathrm{B}$. In many examples the surface-to-volume ratio is separated out instead of the correlation time dependent component, and a surface relaxivity parameter is defined as $\rho_1 S/V = Af(\tau_{\mathrm{c}})$.[21] The surface relaxivity parameter is often used when a continuous distribution of pore sizes is present,[21,22] where a single value of A is misleading. It follows from eqs. (3.4)-(3.5) that the relaxation ratio can be expressed as:

$$\frac{T_{1,\mathrm{B}}}{T_{1,\mathrm{pore}}} - 1 \approx p\frac{A_{\mathrm{S}} f_{\mathrm{S}}(\tau_{\mathrm{c,S}})}{A_{\mathrm{B}} f_{\mathrm{B}}(\tau_{\mathrm{c,B}})}. \tag{3.6}$$

The relaxation ratio $T_{1,\mathrm{B}}/T_{1,\mathrm{pore}}$ cancels out contributions to the prefactor, $A_{\mathrm{S}}/A_{\mathrm{B}}$, that are common for both the surface and bulk relaxation measurements. The motional terms, $f_{\mathrm{S}}/f_{\mathrm{B}}$, will only cancel out if the molecular motions do not change upon binding. Therefore $T_{1,\mathrm{B}}/T_{1,\mathrm{pore}}$ describes the changes in the molecular dynamics of the adsorbate upon binding, and does not depend on the physical constants associated with the liquid. This normalization approach has been used previously to correct for variations in the dipolar coupling constant between different liquids imbibed within porous glass.[23]

3.2.1.2 Applications

When comparing liquids imbibed within the same porous medium, larger ratios of $T_{1,B}/T_{1,pore}$ are indicative of a stronger interaction between the imbibed fluid and the pore surface. Stapf et al., measured this ratio for six different liquids imbibed within porous Bioran glass,[23] and found that it was possible to separate the interaction strength of the six liquids into the limits of strong and weak adsorption based on the polarity of the probe molecules. The non-polar species showed low $T_{1,B}/T_{1,pore}$ ratios, which at high field strengths did not exceed 2. In contrast, the polar species gave a ratio of ~5 at the same field strengths. When imbibed within Bioran glass the ratios were equal for the polar liquids; acetone, hexanol and ethanol. This indicated that the NMR relaxation measurements were not sensitive to the differences in the solid-liquid interaction strength between these adsorbates. D'Agostino et al. used the same approach to study the interaction strength of a wide range of different liquids imbibed within mesoporous catalyst supports, namely silica, titania, and γ-alumina.[24] The same distinction between strong (polar) and weak (non-polar) adsorption was observed, however there was greater variation in the $T_{1,B}/T_{1,pore}$ ratios of the polar species. Of the polar species ketones and aldehydes imbibed within the supports gave the largest ratios, followed by monoalcohols, and then polyols. The $T_{1,B}/T_{1,pore}$ ratios measured for polyols were lower than the ratios measured for alkanes imbibed within the supports. As alkanes were considered non-interacting, the lower ratio of $T_{1,B}/T_{1,pore}$ observed for polyols imbibed within the oxide supports indicated very little change in the molecular motions of the polyols upon binding. This was interpreted as a very weak interaction strength. It was argued that in solution the polyols formed extensive hydrogen bonded networks, which hindered their motion. When adsorbed on the surface the hydrogen bond network was disrupted, and the mobility of the adsorbed polyols was equal to or greater than it was for the bulk liquid. As a result, the ratio $T_{1,B}/T_{1,pore}$ decreased as low as 1.05 for 1,2-propandiol imbibed within silica. The ratio of $T_{1,pore}/T_{1,alkanes}$ was compared to the ratio of diffusion coefficients $D_{pores}/D_{alkanes}$ to confirm the enhanced mobility of the polyols, as shown in Figure 3.1. A clear trend can be seen between the two metrics, showing the correlation of self-diffusion and the molecular motions leading to T_1 relaxation for liquids imbibed within mesoporous oxides.

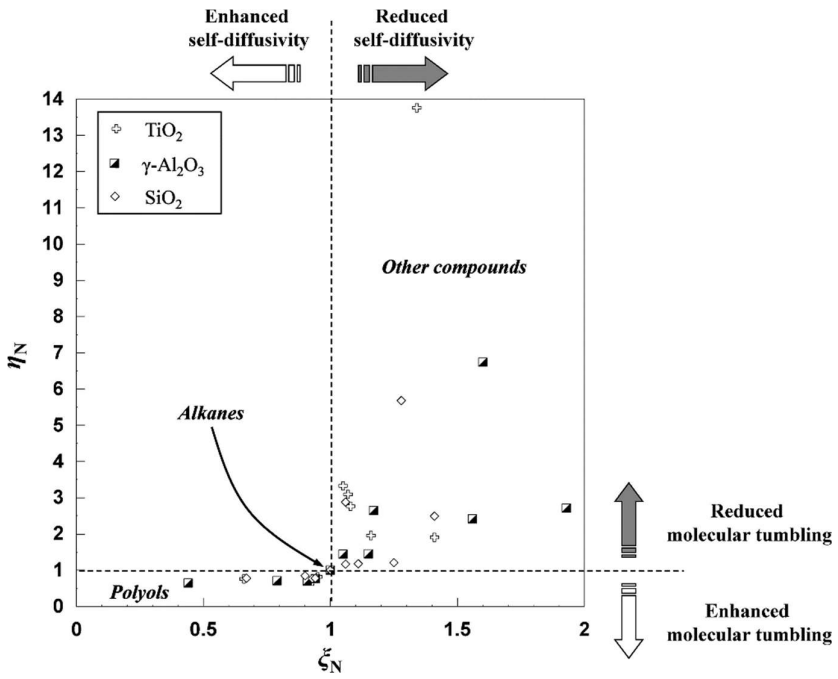

Figure 3.1: A comparison of the normalized diffusion coefficient, $\xi_{\mathrm{N}} = D_{\mathrm{pore}}/D_{\mathrm{alkane}}$, and the normalized T_1 correlation time, $\eta_{\mathrm{N}} = T_{1,\mathrm{pore}}/T_{1,\mathrm{alkane}}$ for a range of organic liquids imbibed within porous oxides of titania, γ-alumina, and silica. Reproduced from D'Agostino et al.[24]

T_1 experiments also allow spectral resolution as an additional discriminator for the analysis of complex samples. Robinson et al. used the chemical separation of the alkyl and hydroxyl group to measure the functionality-specific relaxation behaviour of both chemical environments for methanol imbibed within several porous oxides.[25] The T_1 value of the hydroxyl group was lower than that of the methyl group in all cases, which was consistent with previous observations of alcohol relaxation.[26,27] The authors explained the reduced hydroxyl T_1 values relative to that of the methyl group as originating from the motional restriction imposed on the hydroxyl functionality due to hydrogen bonding with the surface. The binding sites of the oxides were then blocked through passivation of the oxide with tetraethyl orthosilicate (TEOS). The absolute value of T_1 increased for both environments of methanol when imbibed within the passivated oxides.[25] In addition, the ratio of the hydroxyl and alkyl T_1 values, $T_{1,\mathrm{OH}}/T_{1,\mathrm{CH_3}}$, tended to 1 for all samples, which showed that the solid-liquid interactions of the hydroxyl and alkyl functionalities could no longer be differentiated after passivation. These observations were consistent with a weakening of the solid-liquid interaction strength after the TEOS treatment relative to the non-passivated supports.

Chemical separation is highly desirable when attempting to understand complex systems, however even at fixed fields chemical resolution is not always possible. Line broadening due to internal gradient effects can result in peak widths of 10^2-10^4 Hz,[28] and prevent chemical resolution even in simple systems. Robinson et al. were able to retain chemical selectivity in the aforementioned example by restricting the integration of the hydroxyl and alkyl peaks of methanol to narrow chemical shift regions.[25] This minimized the errors introduced by the overlap of peaks, as shown in Figure 3.2. If the number of peaks in the NMR spectrum is known then partial integration, peak fitting, or deconvolution methods[29,30] can be used to achieve chemical selectivity in the event of overlapping peaks. However, these methodologies often assume a symmetrical peak shape and can result in appreciable errors in the case of severe line broadening.

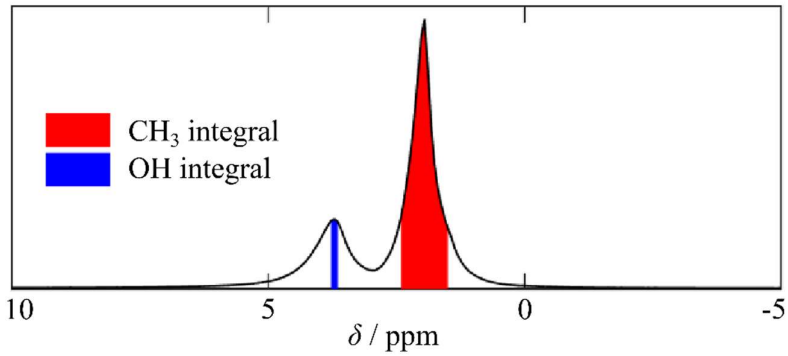

Figure 3.2: The NMR spectrum of methanol imbibed within γ-alumina. To minimize the effects of peak overlap on the measured T_1 relaxation time constant of each functionality only a small region of the spectrum was integrated for each environment. Reproduced from Robinson et al.[25]

A possible solution to the poor chemical separation observed for liquids imbibed within porous media is to use ^{13}C relaxation experiments. For ^{13}C NMR experiments the chemical shift range spans 200 ppm rather than 10 ppm observed for ^{1}H species. Therefore even in the presence of significant line broadening chemical selectivity can be obtained from ^{13}C NMR when it is not possible from ^{1}H NMR. Vecino et al. exploited this additional chemical separation when studying the adsorption behaviour of several alkenes and alkynes adsorbed on alumina surfaces.[31] By taking the individual $T_{1,B}/T_{1,pore}$ ratios for each carbon atom within the molecule the authors suggested the binding configuration of the adsorbates on the surface. A larger ratio implied that the atom was closer to the relaxation sinks on the catalyst surface. For both alkenes and alkynes the

adsorbate preferentially bound to the surface through the double bond functionality, and the alkynes showed a stronger interaction with the surface than the alkenes. The chemical specificity offered by ^{13}C NMR experiments allowed functionality-specific information to be extracted, and could equally be applied to the separation of the relaxation behaviour in multicomponent systems. However, ^{13}C relaxation experiments require additional equipment, and are difficult to implement. The low natural abundance of ^{13}C (1.1%), and the long relaxation times associated with ^{13}C relaxation mean that it can take >10 h to acquire a single measurement with a moderate SNR. Therefore, ^{13}C experiments are not a universal solution for measuring the relaxation behaviour of complex systems.

3.2.1.3 Limitations

A significant limitation of the $T_{1,B}/T_{1,pore}$ measurement is that two separate measurements are required, that of the bulk liquid and that of the liquid imbibed within the porous medium. This increases the experimental acquisition time, introduces more opportunity for error, and may not be physically possible in the case of species that are formed *in situ*. However, the main disadvantage of this methodology is that it is very complex to compare the behaviour of liquids imbibed within different porous media to one another. This is because the material properties of the support influence the relaxation rate. With an *a priori* knowledge of the number of spins in the adsorbed surface layer, *p,* it is possible to correct for the geometric differences between the $T_{1,B}/T_{1,pore}$ measurements for liquids imbibed within different supports. This does not, however, account for differences in the physical properties of the solid matrix that affect the efficacy of the relaxation. The latter changes the relaxation behaviour between samples without affecting the molecular dynamics or interaction strength,[32] as is shown in eq. (3.6). This is not corrected for within a $T_{1,B}/T_{1,pore}$ experiment and is a potential source of misinterpretation. When only a single porous medium is used, the efficacy of surface relaxation can be assumed to be constant for all imbibed liquids, and the relative differences in $T_{1,B}/T_{1,pore}$ will be related to the solid-liquid interaction strength.

3.2.2 Ratios of the longitudinal and transverse relaxation time constant, T_1/T_2

3.2.2.1 Background

T_1 and T_2 denote the observed longitudinal and transverse relaxation times respectively, and can be applied to bulk liquids or liquids imbibed within porous media. Within this

section the label 'pore' will no longer be used when referring to T_1 measurements to avoid overcomplicating notation.

Following the approach outlined in section 3.2.1 the experimentally observed T_1/T_2 ratio for a liquid imbibed within a porous medium can be written as:

$$\frac{T_1}{T_2} = \frac{\frac{1}{T_{2,\mathrm{B}}} + p\left(\frac{1}{T_{2,\mathrm{S}}} - \frac{1}{T_{2,\mathrm{B}}}\right)}{\frac{1}{T_{1,\mathrm{B}}} + p\left(\frac{1}{T_{1,\mathrm{S}}} - \frac{1}{T_{1,\mathrm{B}}}\right)}. \tag{3.7}$$

In the limit that $T_{i,\mathrm{S}} \ll T_{i,\mathrm{B}}$, where $i = 1, 2$, eq. (3.7) reduces to:

$$\frac{T_1}{T_2} \approx \frac{\frac{1}{T_{2,\mathrm{B}}} + p\left(\frac{1}{T_{2,\mathrm{S}}}\right)}{\frac{1}{T_{1,\mathrm{B}}} + p\left(\frac{1}{T_{1,\mathrm{S}}}\right)}. \tag{3.8}$$

This expression can be greatly simplified in the limit that $p/T_{i,\mathrm{S}} \gg 1/T_{i,\mathrm{B}}$ to give a population independent ratio of the surface relaxation rates:

$$\frac{T_1}{T_2} \approx \frac{T_{1,\mathrm{S}}}{T_{2,\mathrm{S}}} \approx \frac{f_2(\tau_\mathrm{c})}{f_1(\tau_\mathrm{c})}. \tag{3.9}$$

Assuming that the relaxation mechanisms dominating T_1 and T_2 relaxation are the same, the T_1/T_2 ratio will cancel out the physical constants arising from both the liquid and solid properties. This means that the T_1/T_2 ratio is sensitive only to the molecular motions, which are related to the interaction strength. The insensitivity of the T_1/T_2 ratio to the properties of the solid was demonstrated by D'Agostino et al. for 1-octanol imbibed within γ-alumina.[33] The alumina was impregnated with $CuSO_4$, at concentrations ranging from 8-3500 ppm, which created paramagnetic Cu^{2+} relaxation centres on the pore surface. Above a surface concentration of 100 ppm the individual T_1 and T_2 relaxation time constants became linearly proportional to the concentration of the paramagnetic species. Such behaviour was predicted by eq. (3.5) due to variations in A, and has been observed for Mn^{2+} and Fe^{3+} impregnated samples.[32,34] Despite the strong changes that were observed for the individual relaxation time constants, D'Agostino showed that the T_1/T_2 ratio stayed approximately constant by cancelling out the material properties (i.e. the effects of the concentration of paramagnetic species). The T_1, T_2 and T_1/T_2 values as

a function of Cu^{2+} loading are shown in Figure 3.3. According to eq. (3.9) the insensitivity of the observed T_1/T_2 ratio to the concentration of paramagnetic impurities showed that the surface motions that occurred for 1-octanol imbibed within γ-alumina were not affected by the concentration of paramagnetic impurities up to loadings of at least 3500 ppm.

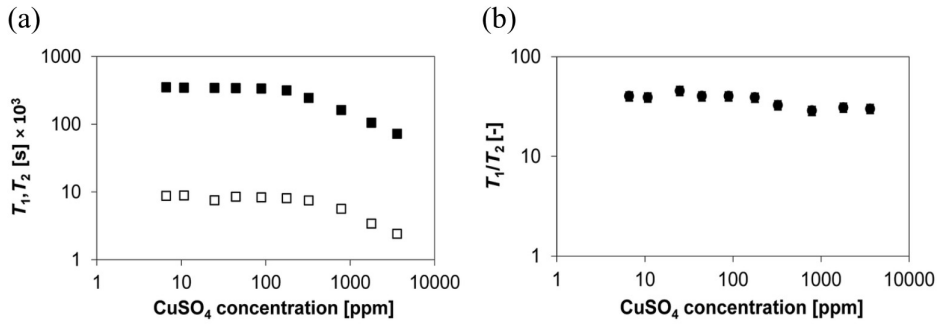

Figure 3.3: The (a) individual T_1 (■) and T_2 (□) values, and (b) T_1/T_2 ratios measured for 1-octanol imbibed within $CuSO_4/\gamma\text{-}Al_2O_3$ at a range of metal loadings. Reproduced from D'Agostino et al.[33]

3.2.2.2 Applications

The relationship between the T_1/T_2 ratio and the solid-liquid interaction strength has been widely explored, in both a theoretical and phenomenological manner.[35–37] From a theoretical perspective the relationship can be justified in the simplest form through Bloembergen-Purcell-Pound (BPP) theory. According to BPP theory the relaxation time constants vary with the motional correlation time, τ_c, as shown in Figure 3.4. This theory was explored in detail in section 2.5.3. The correlation time is defined as the time taken for a molecule to rotate through π radians, which is controlled by the solid-liquid interaction strength at the pore surface when a liquid is imbibed within a porous medium.[38] For a simple bulk liquid the molecular dynamics leading to relaxation are sufficiently fast and unrestricted that $T_1 \approx T_2$.[39] When the same liquid is imbibed within a porous medium the dynamics are slowed significantly, and $T_1 \neq T_2$. As the interaction strength between the solid surface and the imbibed liquid increases the associated correlation time of rotational motion increases, as does the T_1/T_2 ratio. Although BPP theory is not strictly valid for complex dynamic systems, such as liquid imbibed within porous media, it is often a useful starting point for discussing trends in the observed relaxation behaviour.[25,40]

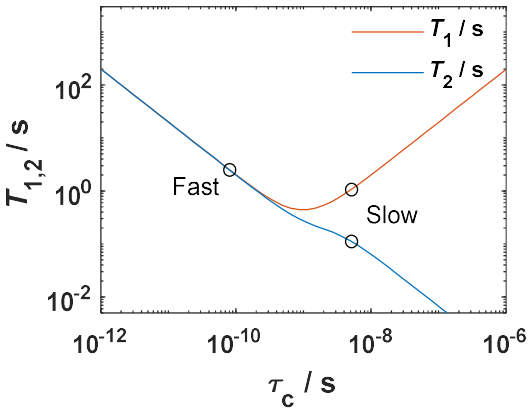

Figure 3.4: The T_1 and T_2 relaxation time constants as a function of rotational correlation time according to BPP theory. Correlation times typical of fast and slow motion are included for emphasis. The prefactor of eq. (2.29) was set to 1×10^9, and to 0.5×10^9 for eq. (2.30). For both relaxation time constants the frequency was set to $\omega_0 = 6.28\times10^8$, and the spectral density function was given by eq. (2.28).

McDonald et al. proposed an alternative explanation for the T_1/T_2 behaviour of liquids imbibed within porous media containing surface paramagnetic impurities. Within the framework of this model the T_1/T_2 ratio was given as:[37]

$$\frac{T_{1,s}}{T_{2,s}} = \frac{1}{2}\left\{\frac{4\ln\left(\left(\frac{\tau_m}{\tau_S}\right)^2\right) + 3\ln\left(\frac{1+\omega_I^2\tau_m^2}{\left(\tau_m/\tau_S\right)^2+\omega_I^2\tau_m^2}\right) + 13\ln\left(\frac{1+\omega_S^2\tau_m^2}{\left(\tau_m/\tau_S\right)^2+\omega_S^2\tau_m^2}\right)}{3\ln\left(\frac{1+\omega_I^2\tau_m^2}{\left(\tau_m/\tau_S\right)^2+\omega_I^2\tau_m^2}\right) + 7\ln\left(\frac{1+\omega_S^2\tau_m^2}{\left(\tau_m/\tau_S\right)^2+\omega_S^2\tau_m^2}\right)}\right\}, \quad (3.10)$$

where τ_m is a correlation time describing the time taken between successive hops of the adsorbate on the surface, τ_S is the surface residence correlation time, ω_I is the ^{1}H proton Larmor frequency, and $\omega_S = 658\omega_I$ is the electron Larmor frequency. Within this modelling approach the interaction strength can be described by the individual correlation times, or the surface affinity ratio, $A = \tau_S/\tau_m$. The latter describes the number of hops a molecule takes on the surface before desorbing. The surface affinity ratio has been theoretically likened to the wettability of a rock,[41] which is a macroscopic measurement of the surface interaction strength used commonly in the well logging industry.[42] The measurement and alteration of the wettability of rocks is of critical importance during the oil recovery process. McDonald et al. showed that as the value of A decreased, so too did the value of T_1/T_2 at any given field strength.[37] D'Agostino et al.

then further demonstrated that a like spin relaxation model based on eq. (3.10) can be simplified in the limit that $(\tau_m/\tau_S)^2 \ll (\omega_I\tau_m)^2 \ll 1$ to give:[35]

$$\frac{T_1}{T_2} \propto \frac{-\ln\left(\frac{\tau_S}{\tau_m}\right)}{\ln(\omega_I\tau_m)}. \tag{3.11}$$

It was then argued that the T_1/T_2 ratio was sensitive to changes in $\ln(\omega_I\tau_m)$, and somewhat insensitive to changes in $\ln(\tau_S/\tau_m)$, as τ_m and τ_S were correlated parameters. This meant that at a fixed field strength, the T_1/T_2 ratio was given as:[35]

$$\frac{T_1}{T_2} \propto \frac{-1}{\ln(\tau_m)}. \tag{3.12}$$

D'Agostino argued in parallel that the effective surface diffusion coefficient for the same process was:[35]

$$D_{eff}(T) = D_{eff,0}\exp\left[\frac{-\Delta E}{RT}\right], \tag{3.13}$$

where $D_{eff}(T)$ is the effective surface diffusion coefficient, $D_{eff,0}$ is the temperature independent contribution to the diffusion coefficient, T is the temperature, R is the gas constant, and ΔE is the activation energy for surface diffusion. The diffusion coefficient can be linked to the surface hopping correlation time via the relationship $D_{eff}(T) = \varepsilon^2/4\tau_m$. The correlation time can therefore be isolated as:

$$\frac{1}{\tau_m(T)} \propto \exp\left[\frac{E_a}{RT}\right]. \tag{3.14}$$

Eq. (3.14) can be substituted into eq. (3.12) at a fixed temperature and field strength:

$$\frac{T_1}{T_2} \propto \frac{-1}{\Delta E}. \tag{3.15}$$

Eq. (3.15) demonstrates a simple quantitative relationship between the surface interaction strength and the observed T_1/T_2 ratio. This relationship was experimentally verified by comparing $e_{surf} = -T_2/T_1$ to the activation energies obtained from temperature programmed desorption, which is a routinely used measurement in the characterisation of porous materials. Figure 3.5 shows the activation energy of the strongest adsorption

sites (calculated from temperature programmed desorption) plotted against e_{surf} for water imbibed within a range of porous oxide materials.[35] A linear relationship was obtained between the two measurements of surface interaction strength, as predicted by eq. (3.15). The e_{surf} parameter has also been shown to be directly proportional to the adsorption energy calculated by DFT for a range of alcohols and cyclohexane imbibed within an industrial silica support material.[36]

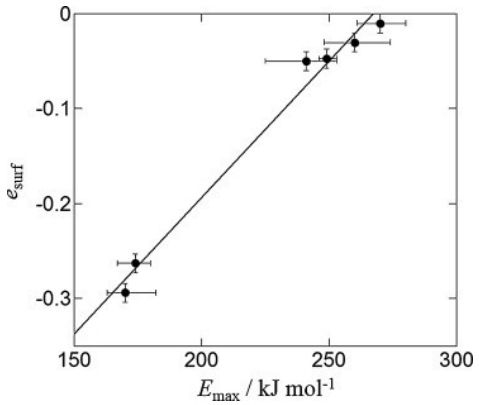

Figure 3.5: The experimentally observed relationship between e_{surf} and E_{max} (measured by temperature programmed desorption).[35] Data points correspond to water imbibed within (left to right) anatase TiO_2, rutile TiO_2, γ-Al_2O_3, SiO_2, θ-Al_2O_3, and ZrO_2. The linear relationship between e_{surf} and E_{max} is predicted by eq. (3.15). Reproduced from D'Agostino et al.[35]

Following a phenomenological approach Weber et al. measured the single component T_1/T_2 ratios of water, butanone and 2-propanol imbibed within Pd/Al_2O_3 and Ru/SiO_2 catalysts.[43] Identical trends were observed for both catalyst materials whereby the T_1/T_2 ratio was largest for water, and smallest for butanone. This meant that the solid-liquid interaction strength was given as water > 2-propanol > butanone. A series of displacement experiments were performed by adding a second liquid – referred to as the displacing liquid, to pellets that were already imbibed with a single liquid – referred to as the initial liquid. The signal intensity of each environment was monitored over time. If the T_1/T_2 ratio of the displacing liquid was larger than that of the initial liquid, then the displacement was fast, and almost full displacement was observed. In contrast, if the T_1/T_2 ratio of the displacing fluid was lower than that of the initial liquid then the displacement was far slower, and did not proceed to completion within the timescale of the measurement.[43] These observations were strong experimental evidence that the single

component T_1/T_2 ratios were an indicator of solid-liquid interaction strength, and a predictor of the behaviour of binary liquid mixtures.

The T_1/T_2 ratio has been applied widely to the study of the adsorption characteristics of mesoporous materials, with a strong focus on catalytic applications. Examples include the measurement of the interaction strength of liquids imbibed within metal supported catalytic materials[44] and different silica structures,[45] the determination of the degree of oxygenate inhibition during the oxidation of glycerol over an Au/TiO_2 catalyst,[46] and the control of adsorption properties during catalyst synthesis.[47] Of particular note was the use of the T_1/T_2 ratio in measuring the effect of the solvent inhibition during the oxidation of 1,4-butanediol over a range of precious metal catalysts.[48] T_1/T_2 ratios were measured for both the reactant (1,4-butanediol) and the solvent (methanol) and a dimensionless ratio, β, was defined as:[48]

$$\beta = \frac{[T_1/T_2]_R}{[T_1/T_2]_S}, \tag{3.16}$$

where $[T_1/T_2]_R$ is the relaxation ratio of the reactant, and $[T_1/T_2]_S$ is that of the solvent. The experimentally observed conversion plotted against the value of β is shown in Figure 3.6.

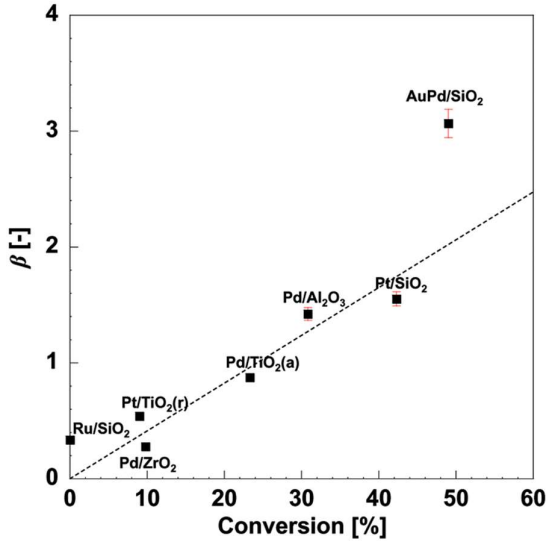

Figure 3.6: A comparison of β and the conversion of 1,4-butanediol after 48 h of reaction. The titanias were subcategorised as anatase (a) and rutile (r). Reproduced from D'Agostino et al.[48]

A clear linear trend was observed for all catalysts, with the exception of the bimetallic AuPd/SiO_2. Higher values of β showed a stronger reactant-surface interaction than a solvent-surface interaction, and would naturally lead to a faster relaxation rate for an adsorption limited reaction. The deviation of AuPd/SiO_2 from the trend indicated that the reaction was no longer solely adsorption limited, and that more complex factors were influencing the conversion. The linearity of the relationship between the conversion and β showed the predictive power of NMR relaxation measurements. Potential catalysts could be compared without the need to perform a full and time consuming catalytic measurement. This result demonstrated how relaxation ratio analysis can be employed as a quick and effective catalyst screening tool during the catalyst development process.

For the investigation of systems containing multiple components, the T_1-T_2 experiment can theoretically be acquired with spectral resolution, in the same manner as an individual T_1 or T_2 experiment. The downside of a chemically resolved T_1-T_2 measurement is that very long acquisition times are required, as both the T_1 and T_2 dimensions are incremented independently.[49] Instead, it is common to minimise the acquisition time of the T_1-T_2 experiment by acquiring T_2 with a single-shot CPMG echo train.[50] By doing so T_2 information can be extracted with an almost negligible increase in the experimental time relative to a single T_1 experiment, however, chemical shift information is lost. As a result, the only way to separate out relaxation environments is through multiexponential fittings or numerical inversions.[51] The separation of multiple components using T_1-T_2 correlation experiments has been widely reported, and this approach can be used to characterise a single liquid experiencing a range of different physical environments.[50] If the exchange between these environments is slow compared to the timescale of the measurement, multiple peaks or a continuous distribution of relaxation times is observed. Environments differing by only 10% have been separated out previously for mixtures of bulk and imbibed liquids.[52] The dynamic sensitivity is not accessible directly from chemical shift information, and it acts as an alternative approach for separating out signals from complex samples.

3.2.2.3 Limitations

Many advantages and successful applications of T_1/T_2 measurements have been discussed within this section, however there are three important considerations that must be taken into account to ensure a robust interpretation of the data. The first is the validity

of eq. (3.9), the second is the influence of internal gradient effects on the value of T_2, and the third is the assumption that the same relaxation mechanism occurs for all samples within a given study. The first of these assumptions can be tested by comparing eq. (3.7) and eq. (3.9) under idealised conditions, as is shown in Figure 3.7.

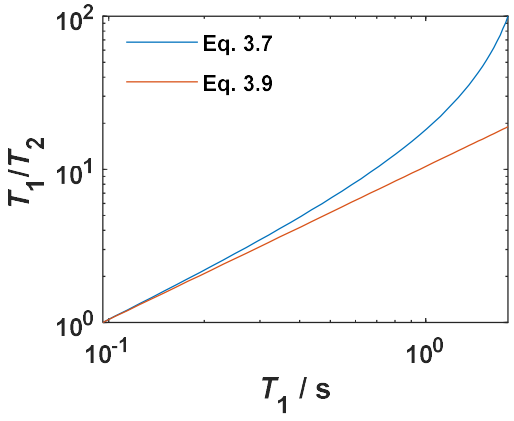

Figure 3.7: The T_1/T_2 ratio as a function of the observed T_1 values predicted by eqs. (3.7) and (3.9). Physical parameters were set as $p = 0.1$, $T_{1,B} = T_{2,B} = 2.5$ s, $T_{2,S} = 0.01$ s and $T_{1,S}$ was varied logarithmically from 0.01-1 s. The $T_{1,S}$ values used in the modelling were converted to the theoretically observed T_1 values plotted above using eq. (3.1).

The two equations are identical up to values of $T_1 \approx 200$ ms, however above this point the values given by eq. (3.7) and (3.9) begin to deviate. In the limit that the measurable T_1 value is similar to $T_{1,B}$, deviations of up to a factor of 4 were observed between T_1/T_2 and $T_{1,S}/T_{2,S}$. The extent of the deviation depends on the chosen values of $T_{1,B}$, $T_{2,B}$, $T_{2,S}$, and p. However the values used for Figure 3.7 are typical of liquids imbibed within mesoporous materials. This means that the direct interpretation of the measured T_1/T_2 ratio of weakly interacting species can be misleading. Robertson demonstrated this effect for water imbibed within a series of silica beads of varying pore sizes.[53] The different silicas were rehydroxylated to obtain a uniform surface chemistry, which was verified by ^{1}H MAS NMR, ^{29}Si MAS NMR and TPD. As the surface chemistry was uniform the only difference between the samples was the pore size, which ranged from 6-50 nm. According to eq. (3.9) the T_1/T_2 ratio should have been constant for all of the samples. Figure 3.8 shows that such behaviour was not observed, and the full form of the two-phase fast exchange model (eq. (3.7)) was required to explain the curvature in the trend of the observed T_1/T_2 values. It was noted that when each different size of silica was

imbibed with ethanol, diethyl ether, and cyclohexane, the observed T_1/T_2 ratios correlated with the expected interaction strength of the adsorbate. This means that qualitative trends may still be accessible from the observed T_1/T_2 ratios of weakly interacting species even if quantitative values require the data to be converted to $T_{1,S}/T_{2,S}$.

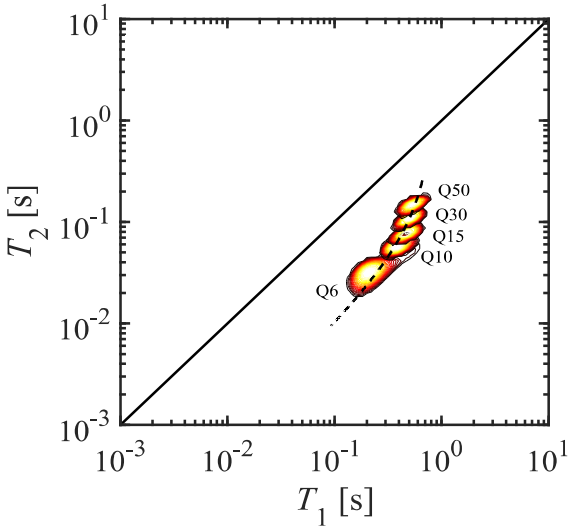

Figure 3.8: The T_1-T_2 correlation plots obtained for water imbibed within the Q-series silicas. The approximate pore size of each silica is included in the name, meaning Q6 has 6 nm pores and so on. The solid line shows $T_1/T_2 = 1$, and lines parallel to this signify a constant T_1/T_2 ratio. The dashed line shows a fit using eq. (3.7). Reproduced from Robertson.[53]

The second consideration is the influence of internal gradients (IG) on the T_2 relaxation time constant. As discussed in section 2.4.2, magnetic susceptibility differences between the solid and liquid phases can lead to the presence of strong gradient fields at the pore surface. The diffusion of spins through these internal gradients induces spin dephasing and enhances T_2 relaxation, but does not affect T_1.[54] In the simplest case that the IG effects may be approximated as a static gradient field, the relaxation rate can be expressed as:[55,56]

$$\frac{1}{T_2^*} = \frac{1}{T_2} + \frac{D\gamma^2 g_{\text{eff}}^2 t_{\text{e}}^2}{12}, \tag{3.17}$$

where T_2 is the true relaxation time constant, T_2^* is the effective relaxation time constant, D is the diffusion coefficient, γ is the gyromagnetic ratio, g_{eff} is the average gradient strength over the diffusion length scale, and t_{e} is the echo time of the CPMG experiment. Mitchell et al. demonstrated that for water imbibed within a Bentheimer sandstone

internal gradient effects led to an underestimate of T_2 of orders of magnitude at high field strengths.[57] The results of this experiment are shown in Figure 3.9. Even at low field strengths (10 MHz) the IG effects were appreciable, and would have led to an overestimate of T_1/T_2 and the solid-liquid interaction strength. Similar effects were also observed for cyclohexane imbibed within a Pt/TiO_2 catalyst.[57]

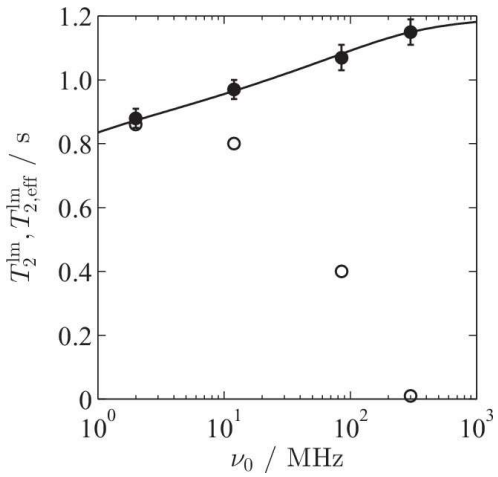

Figure 3.9: The true T_2 (●) and T_2^* (○) values obtained for water imbibed within Berea sandstone at a range of magnetic field strengths. Reproduced from Mitchell et al.[57]

To mitigate against IG effects the acquisition parameters can be optimised. Eq. (3.17) shows that relaxation enhancement due to IG effects depends on the effective gradient field strength, $g_{\rm eff}$, and the echo time, $t_{\rm e}$. The former is proportional to the magnetic field strength, and the latter can be varied freely. By performing T_2 experiments at low field strengths Kleinberg et al. observed that the T_2^* value of water imbibed within Berea sandstone reached a plateau equivalent to the true T_2 relaxation time constant.[58] However, it may not always be possible to reach the acquisition parameters necessary to eliminate the internal gradient effects. Very short echo times require specialist spectrometers, and can lead to spin-lock measurements instead of a CPMG measurement.[59] Similarly low field strengths lead to a poor SNR, and may obscure spectral resolution. An alternative when it is not possible to remove the IG effects during acquisition is to remove them in post processing, as discussed in detail in section 2.4.2. The T_2 relaxation is measured as a function of the echo spacing, and an empirical correction is applied to the data to remove the IG effects.[60,61] Multiple additional experiments are required, making this a time consuming solution. Furthermore, depending on the dynamic regime of the liquid it

may not be possible to separate the IG effects from the true relaxation rate.[61] As IG effects are not always immediately obvious and are difficult to remove, they represent a serious limitation of the interpretation of T_1/T_2 ratios as an analogue of the interaction strength.

The final consideration is whether the same relaxation mechanism occurs for all samples within the study. This is of particular importance when comparing liquids imbibed within a range of different porous media. At low field strengths (<40 MHz) polar liquids imbibed within porous glasses have been described by an intramolecular relaxation process,[23] whilst other authors have argued that an intermolecular relaxation process was dominant for different porous glasses.[62] Even for liquids imbibed within the same porous medium, the limits of strong and weak adsorption can be accounted for by different dynamical processes.[63] Furthermore, for weakly interacting species imbibed within small pores, the effects of pure confinement can become significant.[64] The T_1/T_2 ratio provides only a limited amount of information regarding the underlying relaxation mechanism, and distinguishing between relaxation mechanisms is rarely possible. Insights into the relaxation process can be obtained from detailed material characterisation,[65] variable temperature measurements,[66] and variable field strength measurements.[67,68] Coupling these techniques with T_1/T_2 studies therefore represents a powerful methodology for investigating solid-liquid interaction strengths in porous media.

3.3 Variable field measurements

3.3.1 Background

Variable field measurements are commonly carried out with a single spectrometer capable of varying the magnetic field experienced by the sample. To simplify the acquisition hardware, and to maximise the signal-to-noise ratio (SNR), the magnetic field is switched during the course of the experiment. The sample is initially polarized in a high a field, B_{pol}, to maximize the sample polarization. The magnetic field is then switched rapidly to the desired relaxation field, B_{rel}. The field switch is sufficiently fast (relative to the relaxation rate of the sample) that the initial sample polarization in the relaxation field is approximately equal to the polarization generated by B_{pol}. The sample is allowed to relax towards equilibrium for a duration, τ, before being switched back to a high field for detection, B_{det}. The experiment is repeated for varying values of τ and B_{rel}

in order to measure T_1 as a function of the ^{1}H Larmor frequency. A schematic of the field cycling experiment is shown in Figure 3.10. To achieve the field switching, sample shuttling techniques can be used to physically move the sample to and from a strong polarizing field to a secondary electromagnet or fringe fields of much lower amplitudes.[69,70] However, the need to physically move the sample imposes a lower limit on the field switching time of ~100 ms.[69] This limit means that the measurement of relaxation rates, $R_1 = 1/T_1$ greater than ~10 s^{-1} is unfeasible. An alternative methodology, known as fast field cycling (FFC)-NMR, uses a rapidly switching electromagnet to generate B_{pol}, B_{rel}, and B_{det} without the need to move the sample.[69] This reduces the field switching time to only a few ms and allows R_1 values of up to 1000 s^{-1} to be measured. These R_1 values can be typical of liquids imbibed within mesoporous systems.[44,71]

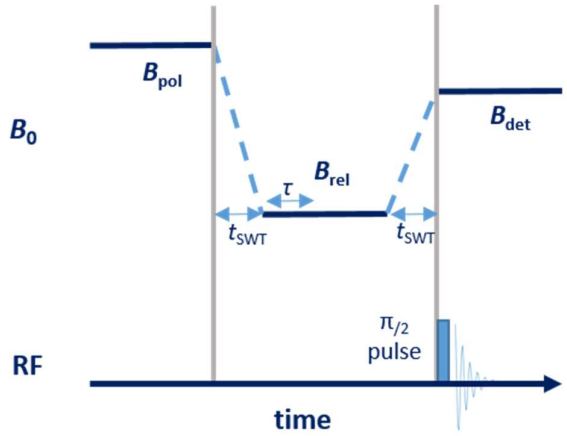

Figure 3.10: A schematic of the prepolarized FFC-NMR experiment. Magnetic fields used for polarization, B_{pol}, relaxation, B_{rel}, detection, B_{det}, and relaxation delays, τ, are optimized for each experiment. Switching times, t_{SWT}, are set to a few ms to avoid signal loss during the switching intervals. Reproduced from Ward-Williams et al.[27]

According to eq. (3.2) the variations of the ^{1}H Larmor frequency probed during an FFC-NMR experiment correspond to relaxation processes that occur over several orders of magnitude of timescale. A commercial FFC-NMR relaxometer can measure the T_1 relaxation between 10 kHz−40 MHz,[20] which is equivalent to molecular processes ranging from ~16 μs−4 ns. The resultant plot of relaxation rate versus the ^{1}H Larmor frequency is referred to as the nuclear magnetic relaxation dispersion (NMRD) profile. In contrast to fixed field T_1 or T_2 measurements, the NMRD profile is measured over such a wide range of frequencies that it is possible to fit the data with theoretical models

describing the molecular motions that lead to the dominant dipolar fluctuations. From these models motional correlation times are extracted, which contain information about the solid-liquid interaction strength.

3.3.2 Applications

The solid-liquid interactions in porous media are remarkably complex, and no single relaxation mechanism has been proposed to explain all systems. Without applying an *a priori* knowledge to the system it is possible to decompose the NMRD profile into a series of Lorentzian terms, given by:[72]

$$J(\omega_I) = \sum_i C_i \frac{1}{1 + \omega_I{}^2 \tau_{\mathrm{c,i}}^2}, \tag{3.18}$$

$$R_1(\omega_I) = A[J(\omega_I) + 4J(2\omega_I)], \tag{3.19}$$

where $J(\omega_I)$ is the spectral density function, C_i is a normalized scaling parameter, $\tau_{\mathrm{c},i}$ is the correlation time associated with environment i, and A is a scaling parameter. Hsu et al. argued that the relaxation of water imbibed within hierarchical H-ZSM-5 could be modelled with a three site approach ($i = 3$) based on eqs. (3.18)-(3.19).[73] The three sites corresponded to the three different pore sizes observed with nitrogen sorption measurements, which had average pore diameters of 0.5, 4.3, and >50 nm. The smaller pore sizes were associated with correlation times 2-3 orders of magnitude slower than water imbibed within the macropores. This was interpreted as a stronger interaction of water in the micro and mesopores of H-ZSM-5 than water in the macropores.

When more information is known about the system it is possible to derive a model that describes the relaxation behaviour based on a specific spin interaction. Notably, Korb et al. proposed a model of relaxation based on the fluctuating dipolar interaction between mobile ^{1}H spins on the adsorbate (*I* spins), and fixed paramagnetic impurities on the surface of the porous medium (*S* spins).[74] The adsorbed molecule diffused across a quasi 2D surface layer in a series of hops, characterised by the correlation time τ_m. After an average adsorption time, τ_S, the molecule desorbed from the surface and lost correlation. This process is shown schematically in Figure 3.11. As the gyromagnetic ratio of the paramagnetic species is much larger than that of the ^{1}H proton ($\gamma_\mathrm{S} = 658\gamma_\mathrm{I}$) only a small

number of paramagnetic impurities are required to dominate the observed relaxation behaviour.[62]

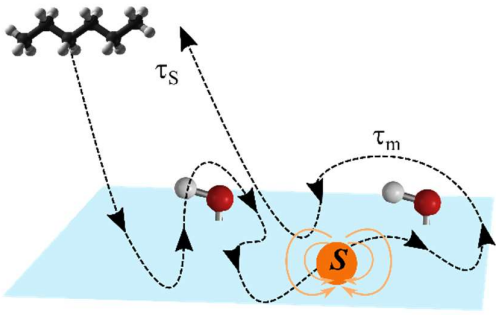

Figure 3.11: A schematic representation of the Korb model of NMR relaxation based on the transient binding of adsorbates in the presence of paramagnetic surface impurities. Fluctuations of the *I*-*S* dipolar interaction are modulated by a surface hopping mechanism, characterised by a hopping time, τ_{m}, and a surface residence time, τ_{S}.

The Korb model has been shown to have remarkable generality, and has been applied to the study of the adsorption properties of liquids imbibed within porous glasses,[62] metal oxide materials,[27,71] ceramics loaded with varying degrees of Fe_2O_3,[32] polar liquids imbibed within metal supported catalysts,[44] water dynamics during cement drying,[75] water in biochars,[76] and fluid typing and wettability estimation of oil and water imbibed within rock cores[41,77,78] and shales.[79] The model has been iterated over 20 years and, although minor changes in the form of the model occur depending on the exact application, the relaxation rate can be generally described as:

$$\frac{1}{T_1} = \frac{1}{T_{1,\mathrm{B}}} + \left(\frac{\mu_0}{4\pi}\right)^2 \frac{N_S}{N} \frac{\pi\sigma_S(\gamma_I\gamma_S\hbar)^2 S(S+1)}{15d^2\delta'^2}$$

$$\tau_{\mathrm{m}}\left(3\ln\left[\frac{1+\omega_I^2\tau_{\mathrm{m}}^2}{\tau_{\mathrm{m}}^2/\tau_{\mathrm{S}}^2 + \omega_I^2\tau_{\mathrm{m}}^2}\right] + 7\ln\left[\frac{1+\omega_S^2\tau_{\mathrm{m}}^2}{\tau_{\mathrm{m}}^2/\tau_{\mathrm{S}}^2 + \omega_S^2\tau_{\mathrm{m}}^2}\right]\right). \quad (3.20)$$

For these expressions μ_0 is the vacuum permittivity constant, $N_S/N = \lambda S/V_{\mathrm{P}}$ is the ratio of molecules at the pore surface to the total number of molecules, λ is the thickness of the adsorbed surface layer, S is the specific surface area, V_{P} is the pore volume, σ_S is the density of paramagnetic impurities on the surface, d is the molecular diameter, and δ' is

an effective distance of minimal approach between the I and S spins. For the case of acetone imbibed within chromatographic glass beads Korb et al. used eq. (3.20) to extract the values of τ_{m} describing the motion of the adsorbed water.[62] The data fitting performed for acetone imbibed within two porous glasses at a range of temperatures is shown in Figure 3.12. As the NMRD profile did not reach a plateau even at low frequencies $\tau_{\mathrm{S}} > 16\ \mu s$ for both samples. To interpret the solid interaction strength the extracted τ_{m} values were converted into effective diffusion coefficients, $D_{\mathrm{eff}}(T) = \varepsilon^2/4\tau_{\mathrm{m}}$ where ε is the molecular diameter. For both samples a significant decrease in the value of $D_{\mathrm{eff}}(T)$ was observed relative to the bulk diffusion coefficient of water, which was indicative of a strong solid-liquid interaction.

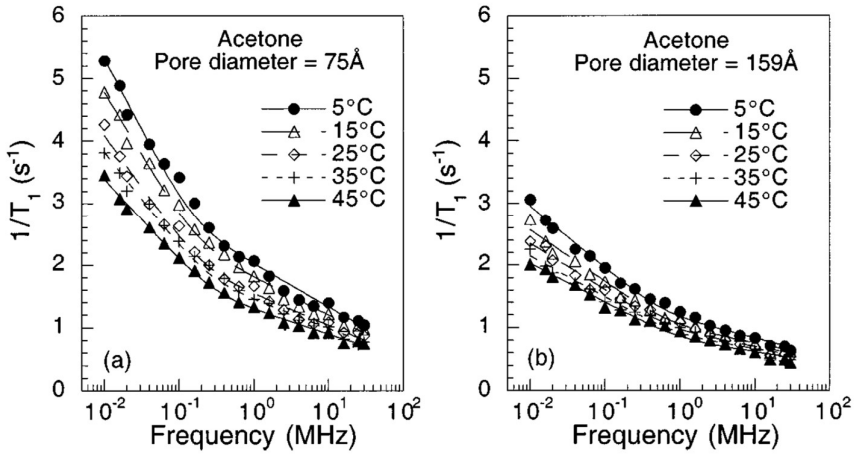

Figure 3.12: The NMRD profiles of acetone imbibed within porous glass beads of average diameter (a) 75 Å and (b) 159 Å. In each case experiments were performed at a range of temperatures, and were fitted with a Korb model to extract the associated diffusion coefficient. Reproduced from Korb et al.[62]

Despite the success of the Korb model in describing the relaxation behaviour of liquids imbibed within a wide range of porous media, alternative models coexist within the literature. Faux et al. argued that the ratios of $\tau_{\mathrm{S}}/\tau_{\mathrm{m}}$ commonly observed within the framework of the Korb model were unphysically large.[80] This ratio has been likened to a wettability measurement,[41] and is an expected measure of the solid-liquid interaction strength. To achieve a fully quantitative measurement of the interaction strength the correlation times must be free from any physical inconsistencies introduced during the modelling. Small changes to the assumptions used to formulate the correlation function were proposed,[80] and a new model, known as the 3τ model, was used to re-evaluate the

relaxation data of water imbibed in plaster pastes, clay, mortars, and shales.[81] Excellent fits were obtained for all experiments, and the analogous ratio to τ_S/τ_m was reduced from ~10,000 to <10. This means that molecules underwent fewer than 10 jumps on a catalyst surface before desorbing, which appeared more physically realistic than estimates obtained from the Korb model. The mathematical complexity of the 3τ model currently limits its application relative to the Korb model. The latter can be represented by simple closed form expressions for the spectral density function, and sufficiently captures the key features of paramagnetic surface relaxation.

A further class of models exist for systems where the dipolar interaction controlling the relaxation behaviour is not dominated by paramagnetic impurities. In these instances the directional binding of the adsorbate at the pore surface prevents the free rotation of the bound molecule. After a characteristic adsorption time, τ_A, the molecule desorbs from the surface. The molecule undergoes a bulk excursion of average time τ_B, before returning to the surface with a fixed orientation, and this process is shown schematically in Figure 3.13. This is referred to as bulk mediated surface diffusion (BMSD),[82] and allows the molecule to make jumps much larger than expected from a typical surface diffusion process. As the surface of the porous medium is not flat, the reorientations lead to a slow loss of the rotational correlation through a process known as reorientations mediated by translation diffusion (RMTD).[63,67] This process was used to explain why the relaxation rate behaviours of a range of polar liquids imbibed within a single porous glass were identical. It was argued that the NMRD behaviour was dominated by the curvature of the surface rather than specific solid-liquid interactions.[23,63] In contrast, in another example where the RMTD mechanism was shown to dominate the relaxation behaviour, the adsorption properties were important.[83] For water imbibed within cement, τ_A was seen to decrease dramatically when an adjuvant was added to modify the kinetics of the curing process.[83] This decrease in τ_A can be interpreted as a reduction in the solid-liquid interaction strength. Even though the two processes were both governed by RMTD relaxation mechanisms, the relaxation behaviour of the liquid within the cement sample was adsorption controlled and the liquids within the porous glass were geometry controlled.

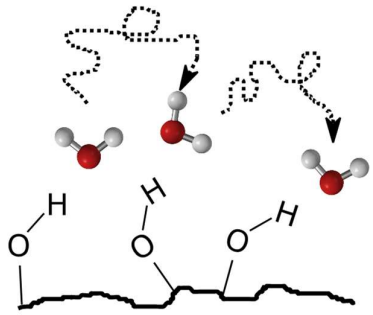

Figure 3.13: A schematic diagram of a molecule traversing the pore surface through a series of bulk excursions and binding events. The hydrogen bonding at the pore surface imposes a directionality on the binding.

The sample specific nature of the NMR relaxation behaviour of liquids imbibed within mesoporous media means that a single relaxation mechanism is not applicable to all systems. An understanding of the mechanism leading to NMR relaxation is important for the interpretation of the solid-liquid interaction strength of liquids imbibed within mesoporous materials. The limited information obtained from fixed field measurements is rarely sufficient to determine the relaxation mechanism, but this can often be deduced from variable field measurements.

3.3.3 Limitations

A distinct disadvantage of FFC-NMR is that it requires the acquisition of multiple T_1 experiments, which leads to long acquisition times relative to fixed field experiments. For fast relaxing samples with a high SNR, a full NMRD profile can be acquired in tens of minutes. However if the sample has a long T_1 and a low SNR, then the experiments can take over 24 h to acquire a full profile. This limits the use of FFC-NMR as a screening tool for high throughput experiments, and imposes a limit to the time resolution with which FFC-NMR can monitor kinetic processes. Barberon et al. presented one of the few kinetic studies that used FFC-NMR,[75] in which they monitored the water relaxation behaviour during cement drying.[75] Measurements of the cement hydration were taken at 30 min intervals, over the course of 12 h, to follow the change in surface area as a function of the hydration time. The temporal resolution was sufficient to track this relatively slow processes, but fast chemical reactions or physical processes are not compatible with FFC-NMR measurements.

The use of an electromagnet to switch the field during the experiment also imposes two further limitations on FFC-NMR measurements. The first is that the magnet switching times, t_{SWT}, are finite. This results in a lower limit on the measurable value of T_1. As $T_1 \rightarrow t_{SWT}$ the FFC-NMR signal will become greatly diminished due to relaxation effects, and the reliability of the relaxation time measurement will be reduced. This is particularly problematic when multiple relaxation environments exist within a single sample, as the relaxation weighting will be greatest for the fast relaxing components. The finite switching times could therefore cause fast relaxing environments to be missed, and would distort the relative populations of the different environments. The second issue introduced by the use of an electromagnet is that the magnetic field applied during the detection is not homogeneous enough to allow spectral resolution. Conventional FFC-NMR spectrometers provide a homogeneity of 10-100 ppm,[67,69,84] which is far poorer than the homogeneity obtained with a fixed field magnet (less than a few ppm). As a result, the linewidths obtained from FFC-NMR are too broad to distinguish between peaks in the ^{1}H spectra. Sample shuttling methods can be used to move the sample between weak relaxation fields (e.g. an electromagnet or fringe fields) and a homogeneous detection field (e.g. a fixed field magnet).[70,85] This methodology has been used to obtain spectrally resolved field cycling measurements for each of the 76 residues within the protein ubiquitin.[86] However, the use of a sample shuttling methodology has t_{SWT}~100 ms, and therefore sets an upper limit on R_1 of ~10 s^{-1}. As this limit is quite low, it prevents sample shuttling methods from being applicable to a number of porous media samples. In the absence of spectral resolution, some chemical resolution can still be obtained through multicomponent numerical inversions, but these methods begin to fail when applied to sparse distributions at low SNR.[87]

The final limitation of FFC-NMR is that the development of this technique is still in its infancy, both in terms of hardware and technique development. The application of stable and well controlled B_0 fields, RF pulses, and gradient fields is technically challenging for FFC-NMR. For example, fixed field relaxometry experiments are routinely combined with spatial resolution, diffusion experiments, or a second relaxation dimension. For FFC-NMR, only a few multidimensional sequences have thus far been implemented.[88] This limitation is not intrinsic, and is expected to lessen as new hardware becomes available and further research is carried out within the field.

3.4 Conclusions

Both fixed and variable field NMR relaxation methods have been shown to probe the solid-liquid interaction strength of liquids imbibed in mesoporous materials. Fixed field $T_{1,B}/T_{1,pore}$ and T_1/T_2 ratios benefit from a simple and robust implementation, and a straightforward interpretation. Numerous studies have taken advantage of these properties to correlate the physicochemical processes occurring within the samples to the fixed field relaxation ratios. These methods, however, rely on the assumption that the relaxation behaviour of each species is controlled by the same mechanism. In actuality internal gradient effects can distort T_2 values, and the type and strength of surface binding may fundamentally change the relaxation mechanism when comparing between different adsorbates on the same surface. The relaxation ratios will become distorted due to these effects, and may result in an erroneous interpretation. To further clarify the relaxation processes that are occurring, variable field measurements can be performed. By measuring the relaxation rate as a function of the ^{1}H Larmor frequency the relaxation behaviour is probed over a range of timescales, and theoretical models can be applied to explain the observed relaxation behaviour. Variable field measurements have been shown to provide sufficient information to identify the molecular motions that lead to relaxation in a diverse range of samples. Whilst field cycling methods provide more dynamic information, they are limited in terms of spectral resolution, and cannot yet be readily combined with spatial resolution (for mesoporous systems) or diffusion weighting. Therefore, the two techniques complement one another strongly when analysing heterogeneous samples such as liquids imbibed within porous media. The additional dynamic information provided by FFC-NMR allows the user to be confident in the interpretation of fixed field data, whilst the versatility of high field NMR allows relaxation data to be coupled to other sample discriminators for additional clarity.

In chapter 4 a fixed field analysis will be applied to study the solid-liquid interaction strength of a range of different liquids imbibed within γ-alumina. In chapters 5, 6, and 7 a FFC-NMR approach will be used for the same samples, and the information obtained from the two measurement techniques will be compared.

3.5 References

(1) Wilkinson, A. D. M. and A. *IUPAC. Compendium of Chemical Terminology*, 2nd ed. (t.; Wilkinson, A., D, M. A., Eds.; Blackwell Scientific Publications: Oxford, 1997.

(2) Davis, M. E. Zeolites and Molecular Sieves: Not Just Ordinary Catalysts. *Ind. Eng. Chem. Res.* **1991**, *30* (8), 1675–1683.

(3) Sastre, G.; Corma, A. The Confinement Effect in Zeolites. *J. Mol. Catal. A Chem.* **2009**, *305* (1), 3–7.

(4) Ruthven, D. M.; Post, M. F. M. Chapter 12 Diffusion in Zeolite Molecular Sieves. In *Introduction to Zeolite Science and Practice*; van Bekkum, H., Flanigen, E. M., Jacobs, P. A., Jansen, J. C., Eds.; Studies in Surface Science and Catalysis; Elsevier, 2001; Vol. 137, pp 525–577.

(5) Kärger, J.; Freude, D.; Haase, J. Diffusion in Nanoporous Materials: Novel Insights by Combining MAS and PFG NMR. *Processes* **2018**, *6* (9).

(6) Narayan, R.; Nayak, U. Y.; Raichur, A. M.; Garg, S. Mesoporous Silica Nanoparticles: A Comprehensive Review on Synthesis and Recent Advances. *Pharmaceutics* **2018**, *10* (3), 118.

(7) Martinez, A.; Lopez, C.; Marquez, F.; Diaz, I. Fischer-Tropsch Synthesis of Hydrocarbons over Mesoporous Co/SBA-15 Catalysts: The Influence of Metal Loading, Cobalt Precursor, and Promoters. *J. Catal.* **2003**, *220* (2), 486–499.

(8) Trueba, M.; Trasatti, S. P. γ-Alumina as a Support for Catalysts: A Review of Fundamental Aspects. *Eur. J. Inorg. Chem.* **2005**, No. 17, 3393–3403.

(9) Brady, R.; Woonton, B.; Gee, M. L.; O'Connor, A. J. Hierarchical Mesoporous Silica Materials for Separation of Functional Food Ingredients — A Review. *Innov. Food Sci. Emerg. Technol.* **2008**, *9* (2), 243–248.

(10) Wagner, T.; Haffer, S.; Weinberger, C.; Klaus, D.; Tiemann, M. Mesoporous Materials as Gas Sensors. *Chem. Soc. Rev.* **2013**, *42* (9), 4036–4053.

(11) Macario, A.; Katovic, A.; Giordano, G.; Iucolano, F.; Caputo, D. Synthesis of

Mesoporous Materials for Carbon Dioxide Sequestration. *Microporous Mesoporous Mater.* **2005**, *81* (1), 139–147.

(12) Vallet-Regí, M.; Colilla, M.; Izquierdo-Barba, I.; Manzano, M. Mesoporous Silica Nanoparticles for Drug Delivery: Current Insights. *Molecules* **2017**, *23* (1), 47.

(13) Mei, P.; Kim, J.; Kumar, N. A.; Pramanik, M.; Kobayashi, N.; Sugahara, Y.; Yamauchi, Y. Phosphorus-Based Mesoporous Materials for Energy Storage and Conversion. *Joule* **2018**, *2* (11), 2289–2306.

(14) Baker, L.; Renshaw, M. P.; Mantle, M. D.; Sederman, A. J.; Wain, A. J.; Gladden, L. F. Operando Magnetic Resonance Studies of Phase Behaviour and Oligomer Accumulation within Catalyst Pores during Heterogeneous Catalytic Ethene Oligomerization. *Appl. Catal. A, Gen.* **2018**, *557*, 125–134.

(15) Fridjonsson, E. O.; Stanwix, P. L.; Johns, M. L. Earth's Field NMR Flow Meter: Preliminary Quantitative Measurements. *J. Magn. Reson.* **2014**, *245*, 110–115.

(16) Zatorre, R. J.; Fields, R. D.; Johansen-Berg, H. Plasticity in Gray and White: Neuroimaging Changes in Brain Structure during Learning. *Nat. Neurosci.* **2012**, *15* (4), 528–536.

(17) Lurie, D. J.; Aime, S.; Baroni, S.; Booth, N. A.; Broche, L. M.; Choi, C. H.; Davies, G. R.; Ismail, S.; O'Hógáin, D.; Pine, K. J. Fast Field-Cycling Magnetic Resonance Imaging. *Comptes Rendus Phys.* **2010**, *11* (2), 136–148.

(18) Ahola, S.; Zhivonitko, V. V; Mankinen, O.; Zhang, G.; Kantola, A. M.; Chen, H.-Y.; Hilty, C.; Koptyug, I. V; Telkki, V.-V. Ultrafast Multidimensional Laplace NMR for a Rapid and Sensitive Chemical Analysis. *Nat. Commun.* **2015**, *6*, 8363.

(19) Hertel, S. A.; de Kort, D. W.; Bush, I.; Sederman, A. J.; Gladden, L. F.; Anger, B.; de Jong, H.; Appel, M. Fast Spatially-Resolved T2 Measurements with Constant-Gradient CPMG. *Magn. Reson. Imaging* **2019**, *56*, 70–76.

(20) Steele, R. M.; Korb, J.-P.; Ferrante, G.; Bubici, S. New Applications and Perspectives of Fast Field Cycling NMR Relaxometry. *Magn. Reson. Chem.* **2015**, No. 54, 502–509.

(21) Kleinberg, R. L. Utility of NMR T2 Distributions, Connection with Capillary Pressure, Clay Effect, and Determination of the Surface Relaxivity Parameter ρ2. *Magn. Reson. Imaging* **1996**, *14* (7), 761–767.

(22) Jaeger, F.; Bowe, S.; As, H. Van; Schaumann, G. E. Evaluation of 1H NMR Relaxometry for the Assessment of Pore-size Distribution in Soil Samples. *Eur. J. Soil Sci.* **2009**, *60* (6), 1052–1064.

(23) Stapf, S.; Kimmich, R.; Seitter, R. O.; Maklakov, A. I.; Skirda, V. D. Proton and Deuteron Field-Cycling NMR Relaxometry of Liquids Confined in Porous Glasses. *Phys. Rev. Lett.* **1996**, *115*, 107–114.

(24) D'Agostino, C.; Mitchell, J.; Gladden, L. F.; Mantle, M. D. Hydrogen Bonding Network Disruption in Mesoporous Catalyst Supports Probed by PFG-NMR Diffusometry and NMR Relaxometry. *J. Phys. Chem. C* **2012**, *116* (16), 8975–8982.

(25) Robinson, N.; Gladden, L. F.; Agostino, C. D. Exploring Catalyst Passivation with NMR Relaxation. *Faraday Discuss.* **2017**, 1–14.

(26) Stubner, B.; Knozinger, H.; Conard, J.; Fripiat J., J. Adsorption of Alcohols on Alumina. 2. Nuclear Magnetic Resonance Investigation. *J. Chem. Phys.* **1978**, *82* (16), 1811–1817.

(27) Ward-Williams, J.; Korb, J.-P.; Gladden, L. F. Insights into Functionality-Specific Adsorption Dynamics and Stable Reaction Intermediates Using Fast Field Cycling NMR. *J. Phys. Chem. C* **2018**, *122* (35), 20271–20278.

(28) Watson, A. T.; Chang, C. T. P. Characterizing Porous Media with NMR Methods. *Prog. Nucl. Magn. Reson. Spectrosc.* **1997**, *31* (4), 343–386.

(29) Li, X.; Hu, K. Chapter Three - Quantitative NMR Studies of Multiple Compound Mixtures; Webb, G. A., Ed.; Annual Reports on NMR Spectroscopy; Academic Press, 2017; Vol. 90, pp 85–143.

(30) Metz, K. R.; Lam, M. M.; Webb, A. G. Reference Deconvolution: A Simple and Effective Method for Resolution Enhancement in Nuclear Magnetic Resonance Spectroscopy. *Concepts Magn. Reson.* **2000**, *12* (1), 21–42.

(31) Vecino, P. A.; Huang, Z.; Mitchell, J.; McGregor, J.; Daly, H.; Hardacre, C.; Thomson, J. M.; Gladden, L. F. Determining Adsorbate Configuration on Alumina Surfaces with 13 C Nuclear Magnetic Resonance Relaxation Time Analysis. *Phys. Chem. Chem. Phys.* **2015**, *17* (32), 20830–20839.

(32) Muncaci, S.; Mattea, C.; Stapf, S.; Ardelean, I. Frequency-Dependent NMR Relaxation of Liquids Confined inside Porous Media Containing an Increased Amount of Magnetic Impurities. *Magn. Reson. Chem.* **2013**, *51* (2), 123–128.

(33) D'Agostino, C.; Bräuer, P.; Charoen-Rajapark, P.; Crouch, M. D.; Gladden, L. F. Effect of Paramagnetic Species on T1{,} T2 and T1/T2 NMR Relaxation Times of Liquids in Porous CuSO4/Al2O3. *RSC Adv.* **2017**, *7* (57), 36163–36167.

(34) Foley, I.; Farooqui, S. A.; Kleinberg, R. L. Effect of Paramagnetic Ions on NMR Relaxation of Fluids at Solid Surfaces. *J. Magn. Reson. Ser. A* **1996**, *123* (1), 95–104.

(35) D'Agostino, C.; Mitchell, J.; Mantle, M. D.; Gladden, L. F. Interpretation of NMR Relaxation as a Tool for Characterising the Adsorption Strength of Liquids inside Porous Materials. *Chem. A Eur. J.* **2014**, *20* (40), 13009–13015.

(36) Robinson, N.; Robertson, C.; Gladden, L. F.; Jenkins, S. J.; D'Agostino, C. Direct Correlation between Adsorption Energetics and Nuclear Spin Relaxation in a Liquid-Saturated Catalyst Material. *ChemPhysChem* **2018**, *19* (19), 2472–2479.

(37) McDonald, P. J.; Korb, J.-P.; Mitchell, J.; Monteilhet, L. Surface Relaxation and Chemical Exchange in Hydrating Cement Pastes: A Two-Dimensional NMR Relaxation Study. *Phys. Rev. E* **2005**, *72* (1), 11409.

(38) Faraone, A.; Liu, L.; Mou, C.-Y.; Shih, P.-C.; Copley, J. R. D.; Chen, S.-H. Translational and Rotational Dynamics of Water in Mesoporous Silica Materials: MCM-41-S and MCM-48-S. *J. Chem. Phys.* **2003**, *119* (7), 3963–3971.

(39) Keeler, J. *Understanding NMR Spectroscopy*; John Wiley & Sons, 1999.

(40) Espinat, D.; Gaulier, F.; Norrant, F.; Barbier, J.; Guichard, B.; Rivallan, M.; Levitz, P. Characterization of Asphaltenes in Solution and Inside the Pores of Catalysts by 1H NMR Relaxometry. *Energy & Fuels* **2017**, *31* (7), 7382–7395.

(41) Korb, J. P.; Freiman, G.; Nicot, B.; Ligneul, P. Dynamical Surface Affinity of Diphasic Liquids as a Probe of Wettability of Multimodal Porous Media. *Phys. Rev. E* **2009**, *80*, 61601-1–12.

(42) Anderson, W. G. Wettability Literature Survey- Part 1: Rock/Oil/Brine Interactions and the Effects of Core Handling on Wettability. *J. Pet. Technol.* **1986**, *38* (10), 1125–1144.

(43) Weber, D.; Mitchell, J.; McGregor, J.; Gladden, L. F. Comparing Strengths of Surface Interactions for Reactants and Solvents in Porous Catalysts Using Two-Dimensional NMR Relaxation Correlations. *J. Phys. Chem. C* **2009**, *113*, 6610–6615.

(44) Mitchell, J.; Broche, L. M.; Chandrasekera, T. C.; Lurie, D. J.; Gladden, L. F. Exploring Surface Interactions in Catalysts Using Low-Field Nuclear Magnetic Resonance. *J. Phys. Chem. C* **2013**, *117* (34), 17699–17706.

(45) Krzyżak, A. T.; Habina, I. Low Field 1H NMR Characterization of Mesoporous Silica MCM-41 and SBA-15 Filled with Different Amount of Water. *Microporous Mesoporous Mater.* **2016**, *231*, 230–239.

(46) D'Agostino, C.; Armstrong, R. D.; Hutchings, G. J.; Gladden, L. F. Product Inhibition in Glycerol Oxidation over Au/TiO2 Catalysts Quantified by NMR Relaxation. *ACS Catal.* **2018**, *8* (8), 7334–7339.

(47) D'Agostino, C.; Bräuer, P. Exploiting Enhanced Paramagnetic NMR Relaxation for Monitoring Catalyst Preparation Using T1–T2 NMR Correlation Maps. *React. Chem. Eng.* **2019**, *4* (2), 268–272.

(48) D'Agostino, C.; Feaviour, M. R.; Brett, G. L.; Mitchell, J.; York, A. P. E.; Hutchings, G. J.; Mantle, M. D.; Gladden, L. F. Solvent Inhibition in the Liquid-Phase Catalytic Oxidation of 1{,}4-Butanediol: Understanding the Catalyst Behaviour from NMR Relaxation Time Measurements. *Catal. Sci. Technol.* **2016**, *6* (21), 7896–7901.

(49) Gladden, L. F.; Mitchell, J. Measuring Adsorption, Diffusion and Flow in Chemical Engineering: Applications of Magnetic Resonance to Porous Media. *New J. Phys.* **2011**, *13* (3), 35001.

(50) Song, Y.-Q.; Venkataramanan, L.; Hürlimann, M. D.; Flaum, M.; Frulla, P.; Straley, C. T1–T2 Correlation Spectra Obtained Using a Fast Two-Dimensional Laplace Inversion. *J. Magn. Reson.* **2002**, *154* (2), 261–268.

(51) Mitchell, J.; Chandrasekera, T. C.; Gladden, L. F. Numerical Estimation of Relaxation and Diffusion Distributions in Two Dimensions. *Prog. Nucl. Magn. Reson. Spectrosc.* **2012**, *62*, 34–50.

(52) Reci, A.; Sederman, A. J.; Gladden, L. F. Obtaining Sparse Distributions in 2D Inverse Problems. *J. Magn. Reson.* **2017**, *281*, 188–198.

(53) Robertson, C. I. Characterising Adsorption and Mass Transfer in Porous Media (Doctoral Thesis)., 2018.

(54) Washburn, K. E.; Eccles, C. D.; Callaghan, P. T. The Dependence on Magnetic Field Strength of Correlated Internal Gradient Relaxation Time Distributions in Heterogeneous Materials. *J. Magn. Reson.* **2008**, *194* (1), 33–40.

(55) Torrey, H. C. Bloch Equations with Diffusion Terms. *Phys. Rev.* **1956**, *104* (3), 563–565.

(56) Mitchell, J.; Gladden, L. F.; Chandrasekera, T. C.; Fordham, E. J. Low-Field Permanent Magnets for Industrial Process and Quality Control. *Prog. Nucl. Magn. Reson. Spectrosc.* **2014**, *76*, 1–60.

(57) Mitchell, J.; Chandrasekera, T. C.; Gladden, L. F. Measurement of the True Transverse Nuclear Magnetic Resonance Relaxation in the Presence of Field Gradients. *J. Chem. Phys.* **2013**, *139* (7), 74205.

(58) Kleinberg, R. L.; Horsfield, M. A. Transverse Relaxation Processes in Porous Sedimentary Rock. *J. Magn. Reson.* **1990**, *88* (1), 9–19.

(59) Steiner, E.; Yemloul, M.; Guendouz, L.; Leclerc, S.; Robert, A.; Canet, D. NMR Relaxometry: Spin Lattice Relaxation Times in the Laboratory Frame versus Spin Lattice Relaxation Times in the Rotating Frame. *Chem. Phys. Lett.* **2010**, *495* (4), 287–291.

(60) Mitchell, J.; Chandrasekera, T. C.; Gladden, L. F. Obtaining True Transverse Relaxation Time Distributions in High-Field NMR Measurements of Saturated

Porous Media: Removing the Influence of Internal Gradients. *J. Chem. Phys.* **2010**, *132* (24), 1–10.

(61) Mitchell, J.; Chandrasekera, T. C.; Gladden, L. F. A General Approach to T2 Measurements in the Presence of Internal Gradients. *Microporous Mesoporous Mater.* **2013**, *178*, 20–22.

(62) Korb, J. P.; Whaley Hodges, M.; Gobron, T.; Bryant, R. G. Anomalous Surface Diffusion of Water Compared to Aprotic Liquids in Nanopores. *Phys. Rev. E* **1999**, *60*, 3097–3106.

(63) Zavada, T.; Kimmich, R. The Anomalous Adsorbate Dynamics at Surfaces in Porous Media Studied by Nuclear Magnetic Resonance Methods. the Orientational Structure Factor and Lévy Walks. *J. Chem. Phys.* **1998**, *109* (16), 6929–6939.

(64) Liu, G.; Li, Y.; Jonas, J. Confined Geometry Effects on Reorientational in Porous Silica Glasses. *J. Chem. Phys.* **1991**, *95* (9), 6892–6901.

(65) Plassais, A.; Lequeux, N.; Petit, D.; Barberon, F.; Bresson, B. Microstructure Evolution of Hydrated Cement Pastes. *Phys. Rev. E* **2005**, 1–8.

(66) Conte, P.; Loddo, V.; De Pasquale, C.; Marsala, V.; Alonzo, G.; Palmisano, L. Nature of Interactions at the Interface of Two Water-Saturated Commercial TiO2 Polymorphs. *J. Phys. Chem. C* **2013**, *117* (10), 5269–5273.

(67) Kimmich, R.; Anoardo, E. Field-Cycling NMR Relaxometry. *Prog. Nucl. Magn. Reson. Spectrosc.* **2004**, *44*, 257–320.

(68) Korb, J.-P. Multiscale Nuclear Magnetic Relaxation Dispersion of Complex Liquids in Bulk and Confinement. *Prog. Nucl. Magn. Reson. Spectrosc.* **2018**, *104*, 12–55.

(69) Ferrante, G.; Sykora, S. Technical Aspects of Fast Field Cycling. *Adv. Inorg. Chem.* **2005**, *57*, 405–470.

(70) Gossuin, Y.; Serhan, Z.; Sandiford, L.; Henrard, D.; Marquardsen, T.; de Rosales, R. T. M.; Sakellariou, D.; Ferrage, F. Sample Shuttling Relaxometry of Contrast Agents: NMRD Profiles above 1 T with a Single Device. *Appl. Magn.*

Reson. **2016**, *47* (3), 237–246.

(71) Chemmi, H.; Petit, D.; Levitz, P.; Denoyel, R.; Galarneau, A.; Korb, J.-P. Noninvasive Experimental Evidence of the Linear Pore Size Dependence of Water Diffusion in Nanoconfinement. *J. Phys. Chem. Lett.* **2016**, *7*, 393–398.

(72) De Pasquale, C.; Marsala, V.; Berns, A. E.; Valagussa, M.; Pozzi, A.; Alonzo, G.; Conte, P. Fast Field Cycling NMR Relaxometry Characterization of Biochars Obtained from an Industrial Thermochemical Process. *J. Soils Sediments* **2012**, *12*, 1211–1221.

(73) Hsu, C.; Chen, Y.; Rana, B. S.; Kumar, R.; Sinha, A. K.; Hwang, D. W. Dynamics of Water in Hierarchical Mesoporous H-ZSM 5 by Fast Field-Cycling. *J. Phys. Chem. C* **2014**, *118*, 20481–20487.

(74) Korb, J.-P.; Whaley-Hodges, M.; Bryant, R. G. Translational Diffusion of Liquids at Surfaces of Microporous Materials: Theoretical Analysis of Field-Cycling Magnetic Relaxation Measurements. *Phys. Rev. E* **1997**, *56* (2), 1934–1945.

(75) Barberon, F.; Korb, J.; Petit, D.; Morin, V.; Bermejo, E. Probing the Surface Area of a Cement-Based Material Ny Nuclear Magnetic Relaxation Dispersion. *Phys. Rev. Lett.* **2003**, *90*, 116103-1–4.

(76) Bubici, S.; Korb, J.-P.; Kučerik, J.; Conte, P. Evaluation of the Surface Affinity of Water in Three Biochars Using Fast Field Cycling NMR Relaxometry. *Magn. Reson. Chem.* **2016**, *54* (5), 365–370.

(77) Godefroy, S.; Fleury, M.; Deflandre, F.; Korb, J. P. Temperature Effect on NMR Surface Relaxation in Rocks for Well Logging Applications. *J. Phys. Chem. B* **2002**, *106* (43), 11183–11190.

(78) Korb, J. P.; Godefroy, S.; Fleury, M. Surface Nuclear Magnetic Relaxation and Dynamics of Water and Oil in Granular Packings and Rocks. *Magn. Reson. Imaging* **2003**, *21*, 193–199.

(79) Korb, J.; Nicot, B.; Bubici, S.; Ferrante, G. Dynamics and Wettability of Oil and Water in Oil Shales. *J. Phys. Chem. C* **2014**, *118*, 23212–23218.

(80) Faux, D. A.; Cachia, S. H. P.; McDonald, P. J.; Bhatt, J. S.; Howlett, N. C.; Churakov, S. V. Model for the Interpretation of Nuclear Magnetic Resonance Relaxometry of Hydrated Porous Silicate Materials. *Phys. Rev. E - Stat. Nonlinear, Soft Matter Phys.* **2015**, *91* (3), 1–11.

(81) Faux, D. A.; Mcdonald, P. J. Explicit Calculation of Nuclear-Magnetic-Resonance Relaxation Rates in Small Pores to Elucidate Molecular-Scale Fluid Dynamics. *Phys. Rev. E* **2017**, *95*, 1–16.

(82) Oleg V. Bychuk; Ben O'Shaughnessy. Anomalous Diffusion of Surface-Active Species at Liquid-Fluid and Liquid-Solid Interfaces. *J. Phys. II Fr.* **1994**, *4* (7), 1135–1156.

(83) Korb, J. -P.; Levitz, P. E. Direct Probing of the Wettability of Plaster Pastes at the Nanoscale by Proton Field Cycling Relaxometry. *AIP Conf. Proc.* **2008**, *1081* (1), 55–58.

(84) Lips, O.; Privalov, A. F.; Dvinskikh, S. V.; Fujara, F. Magnet Design with High B0 Homogeneity for Fast-Field-Cycling NMR Applications. *J. Magn. Reson.* **2001**, *149* (1), 22–28.

(85) Charlier, C.; Cousin, S. F.; Ferrage, F. Protein Dynamics from Nuclear Magnetic Relaxation. *Chem. Soc. Rev.* **2016**, *45* (9), 2410–2422.

(86) Charlier, C.; Khan, S. N.; Marquardsen, T.; Pelupessy, P.; Reiss, V.; Sakellariou, D.; Bodenhausen, G.; Engelke, F.; Ferrage, F. Nanosecond Time Scale Motions in Proteins Revealed by High-Resolution NMR Relaxometry. *J. Am. Chem. Soc.* **2013**, *135* (49), 18665–18672.

(87) Reci, A.; Sederman, A. J.; Gladden, L. F. Retaining Both Discrete and Smooth Features in 1D and 2D NMR Relaxation and Diffusion Experiments. *J. Magn. Reson.* **2017**, *284*, 39–47.

(88) Neudert, O.; Mattea, C.; Stapf, S. Application of CPMG Acquisition in Fast-Field-Cycling Relaxometry. *Microporous Mesoporous Mater.* **2018**, *269*, 103–108.

Chapter 4 : Fixed field NMR relaxation methods applied to liquids imbibed within γ-alumina

Contents

4.1 Introduction

In chapter 3 the use of fixed field NMR relaxation experiments was presented for a range of different liquids imbibed within mesoporous media. In these cases a relationship between the solid-liquid interaction strength and the fixed field relaxation ratios was demonstrated. However, these examples often focussed on a relatively small subset of fluids imbibed within a single porous medium, or a single fluid imbibed within a range of porous media, and as a result lacked generality. In this chapter conventional fixed field measurements of $T_{1,B}/T_{1,pore}$ and $e_{surf} = -T_2/T_1$ will be performed for an extensive range of liquids imbibed within γ-alumina. The range of liquids represent many of the key functionalities used in catalysis, and cover a wide range of solid-liquid interaction strengths. By restricting the analysis to a single porous medium the $T_{1,B}/T_{1,pore}$ ratio can be used to discriminate between different liquids. Furthermore, γ-alumina is known to have a strong surface relaxivity relative to other metal oxide supports.[1] Therefore, for liquids imbibed within γ-alumina the assumption that the bulk liquid relaxation behaviour does not strongly affect e_{surf} is valid. This makes e_{surf} a direct measure of the solid-liquid interaction strength, as discussed in section 3.2.2. In this chapter the robustness of these two metrics will be explored for adsorbates with a diverse range of physical and chemical properties.

4.2 Background

4.2.1 Chemistry of γ-alumina

γ-alumina was chosen for this study as it is used industrially as a catalyst support material, and has been used extensively as an acid-base catalyst itself. When used directly as a catalyst, the adsorption properties of the γ-alumina play an important role in controlling the activity of the catalyst.[2] Even when acting primarily as a support, the alumina properties have a strong influence on the activity and product distribution of a reaction.[3,4] Therefore, being able to reliably measure the solid-liquid interaction strength of liquids imbibed within γ-alumina is important for the understanding and the optimization of alumina based catalytic systems.

Alumina refers to a range of stable and metastable aluminium oxide phases, which differ in both their crystallographic structure and the amount of structural water present.[5] These phases are formed from the thermal dehydroxylation of aluminium hydroxides or oxyhydroxides, as shown in Figure 4.1. If the temperature is controlled the degree of dehydroxylation can be limited, and metastable alumina phases can be isolated. The dehydroxylation behaviour depends strongly on the precursor and the synthesis conditions.[6] This means that the isolation of a particular phase requires an optimization of the synthesis procedure rather than the use of a single set of conditions. The chemical properties of the alumina varies significantly between phases, with γ-alumina being a highly active acid-base catalyst with a strong adsorption capacity, and α-alumina being far more chemically inert.[7,8] Therefore the choice of an appropriate alumina phase depends on the intended application. High surface area and reactive phases such as γ-, η-, and θ-alumina are most commonly used for catalytic applications.

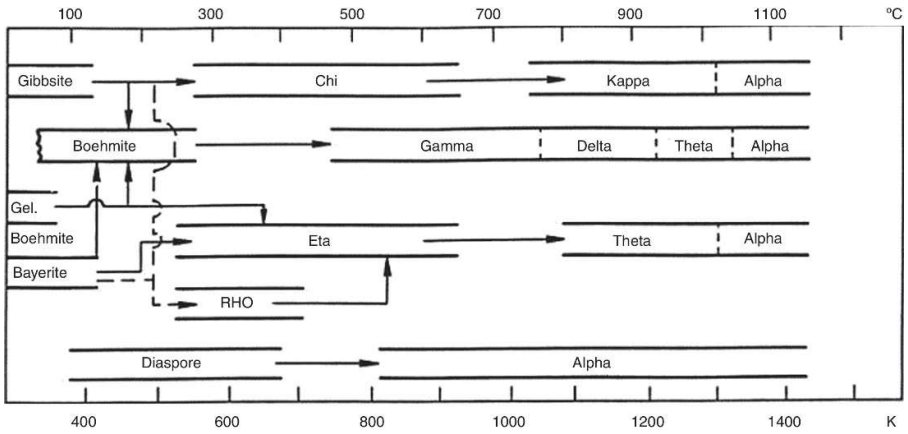

Figure 4.1: The temperature dependent phase diagram of alumina. Different alumina precursors lead to the formation of different metastable phases, but in all cases the thermodynamically stable alpha (α-) alumina phase was formed at high temperatures. Reproduced from Wefers et al.[6]

The crystal structure of γ-alumina is a cubic defect spinel structure with oxygen atoms forming cubic close packed layers, and aluminium atoms filling a stoichiometric fraction of the tetrahedral and octahedral sites, as shown in Figure 4.2. Depending on the nature of the γ-alumina precursor tetragonal distortions to the conventional cubic lattice have been reported, and in some studies the cubic phase is not observed at any temperature.[9]

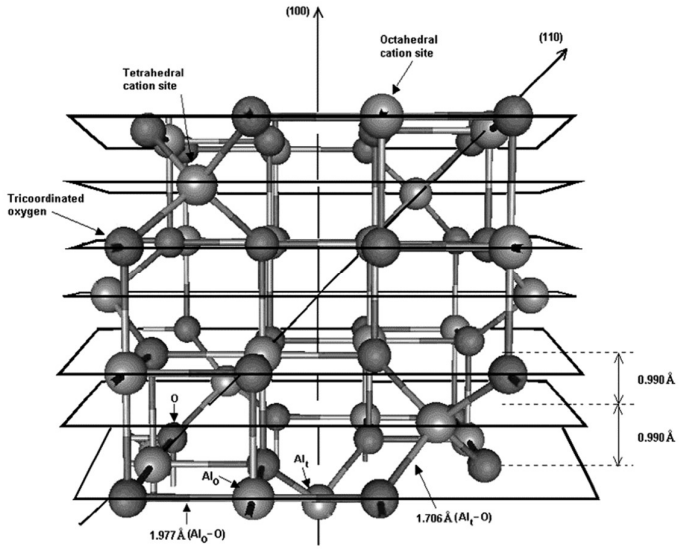

Figure 4.2:The cubic spinel lattice of γ-alumina. Reproduced from Ionesco et al.[10]

The adsorption behaviour of liquids imbibed within γ-alumina is expected to be dominated by the surface properties, and in particular the surface chemistry of the hydroxyl groups. Although there is some debate over the exact nature of the surface hydroxyl groups, the observation of several distinct hydroxyl stretching frequencies from IR measurements has proven the presence of different surface hydroxyl chemistries.[11] For γ-alumina 5 hydroxyl groups were proposed within the model of Knozinger and Ratnasamy, which differ in terms of their net electric charge, local atomic connectivity, and their acidity.[12] These are shown in Figure 4.3. The greater the net electric charge, σ, the more acidic the surface hydroxyl groups were considered to be, and it is due to this diverse surface chemistry that γ-alumina can act as both an acid and a base simultaneously. Whilst it is possible to separate out different hydroxyl functionalities with IR, for liquids imbibed within γ-alumina only a single peak is expected in the NMR relaxation experiments, as the adsorbate will rapidly exchange between different binding sites on the timescale of the experiment. This averages the relaxation effect and only a single dynamic environment is expected, which is consistent with previous NMR relaxation studies of liquids imbibed within γ-alumina.[13–15] The IR information provides a detailed structural characterisation of the alumina surface hydroxyl groups. An analysis of the solid-liquid interaction strength is not possible purely from IR characterisation, as the Knozinger and Ratnasamy model does not directly consider the surface hydroxyl density,[16] surface defects, or any species added to the catalyst surface, all of which are

expected to strongly affect the adsorption properties and the relaxation behaviour. NMR relaxation measurements probe the dynamics of the adsorbed molecule, and therefore act as a complementary technique to IR.

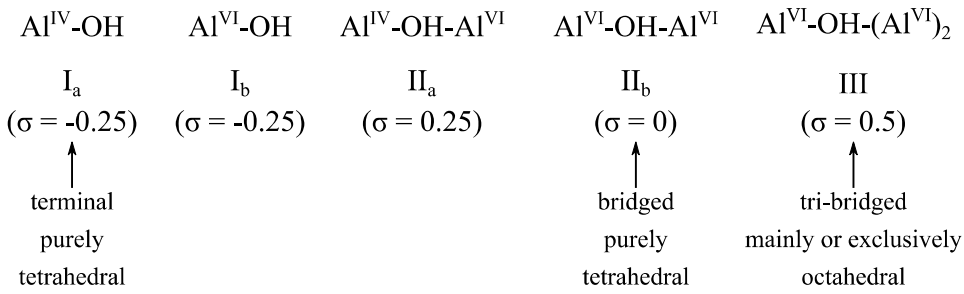

Figure 4.3: The Knozinger-Ratnasamy model for characterising the surface hydroxyl groups of γ-alumina acidity. The notation IV and VI refer to 4- and 6-coordinate aluminium sites respectively. The net electric charge of each hydroxyl group, σ, can be considered as a measure of the acidity. Within this model Al^{IV}-OH is the most acidic surface hydroxyl group. Reproduced from Trueba et al.[9]

4.2.2 Fixed field relaxation analysis

In chapter 3 a critical review was presented that covered the application, advantages, and disadvantages of fixed field NMR relaxation methods for studying the solid-liquid interaction strength of liquids imbibed within porous media. To avoid repetition, only the key theory required to interpret the results in this chapter will be presented. A particular focus will be placed on the difference in the relaxation behaviour of rigid and flexible molecules. The former have a fixed distance between hydrogen atoms within each molecule and the latter have variable interatomic distances, which can have a strong effect on the observed relaxation behaviour.

4.2.2.1 Approaches for measuring interaction strength

The results presented within this chapter explore the relaxation behaviour of several different liquids imbibed within γ-alumina. As a range of different liquids were imbibed within a single porous medium, fixed field relaxation ratios of $T_{1,\mathrm{B}}/T_{1,\mathrm{pore}}$ and T_1/T_2 were expected to correlate with the solid-liquid interaction strength.[1,15,17] The experimentally measured relaxation ratios are sensitive to the solid-liquid interaction strength as they directly probe the surface relaxation behaviour:

$$\frac{T_{1,\mathrm{B}}}{T_{1,\mathrm{pore}}} \approx 1 + p\left(\frac{T_{1,\mathrm{B}}}{T_{1,\mathrm{S}}}\right), \tag{4.1}$$

$$\frac{T_1}{T_2} \approx \frac{T_{1,\mathrm{S}}}{T_{2,\mathrm{S}}} \approx -\frac{1}{\Delta E}, \tag{4.2}$$

where p is population fraction of molecules in the surface layer, ΔE is the effective activation energy for translational diffusion, T_1 is the longitudinal relaxation time constant, and T_2 is the transverse relaxation time constant. More specifically, $T_{1,\mathrm{B}}$ refers to a bulk liquid, $T_{1,\mathrm{pore}}$ refers to a liquid imbibed within a porous medium, $T_{1,\mathrm{S}}$ and $T_{2,\mathrm{S}}$ are the surface relaxation time constants, and T_1 and T_2 are the experimentally measured values. When discussing the relaxation behaviour of liquids imbibed within a porous medium $T_{1,\mathrm{pore}}$ and T_1 are equivalent, however both forms of notation will be used within this chapter for consistency with the literature. Provided that the observed relaxation rate is reflective of the true surface relaxation ratio, fixed field relaxation methods have been shown to be a reliable metric for measuring solid-liquid interaction strengths. However, in the presence of internal gradients,[18] weak surface relaxivity,[19] or variations in the relaxation mechanism between samples, these metrics may become unreliable.

4.2.2.2 Rigid and flexible molecules

What constitutes a rigid or flexible molecule is not rigorously defined within the literature. In the extreme sense a rigid molecule can be defined as a molecule without the possibility of internal motions, and a flexible molecule can be defined as any molecule that possesses internal motions. As a result of the internal motions the distance between hydrogen atoms may change for a flexible molecule, but not for a rigid molecule, as shown in Figure 4.4.

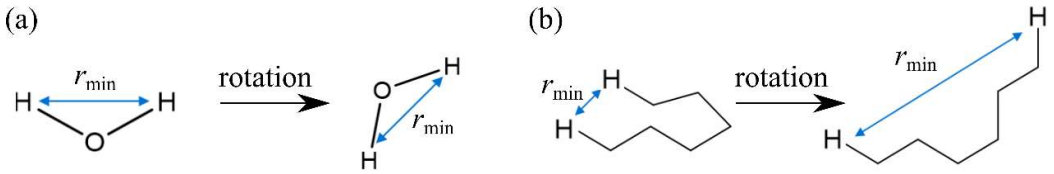

Figure 4.4: The minimum distance between two ^{1}H protons, r_{min}, before and after rotation for (a) water and (b) *n*-hexane. As water has a rigid structure r_{min} is constant. In contrast, as n-hexane is flexible r_{min} can vary significantly due to internal motions.

In practice, very few molecules are completely rigid. Therefore, within this chapter, the definition of rigid has been extended to include molecules with limited internal motions. This includes species with significant sp^2 hybridisation or small cyclic molecules, and the definition includes cyclohexane, cyclohexene, toluene, methyl acetate, methanol, 2-methyl-2-butene, and water.

Classical descriptions of NMR relaxation often use simplified models which make the assumption that molecules are rigid. The overall relaxation rate can be decomposed into an intramolecular and an intermolecular component as described in section 2.5.5. The intramolecular component of relaxation is commonly described by Bloemburgen Purcell and Pound (BPP) theory, which is based on the coupled motion of two spins held at a fixed distance from one another. The molecule undergoes rotational motion, with a characteristic correlation time of τ_c.[20] For the intermolecular component of relaxation, the translational diffusion of the molecule is considered. Ayant et al. proposed expressions to describe the intermolecular relaxation in bulk liquids based on the relative motion of spins at the surface of freely diffusing hard spheres.[21,22] The translational motion can be characterised by a correlation time, τ_D. The two correlation times are related by the Stokes-Einstein equation, which gives $\tau_D = 9\tau_c$ for spherical molecules.[23] The translational relaxation behaviour allows the variation of the interspin distance, but the hard sphere model does not allow for internal motions within the sample. Molecular dynamics (MD) simulations have recently shown the effect of the carbon chain length on the relaxation behaviour of a range of bulk liquid hydrocarbons.[23] The initial structures of the *n*-alkanes were optimised computationally, and MD simulations were performed to calculate the relaxation rate and motional correlation times in the absence of internal motions (rigid) and with internal motions (flexible). For the flexible molecules a systematic decrease in the ratio of τ_D/τ_c from approximately 7 for pentane down to 2 for heptadecane was observed. Small chain *n*-alkanes were a moderate approximation spherical molecules. As the carbon number increased the assumption that the molecules were spherical became poorer, and a more complex relationship between diffusion and rotational behaviour was observed. Furthermore, by allowing internal motions to occur, both the translational and rotational correlation time constants decreased for the *n*-alkanes.[23] As a result of this enhanced motion, the relaxation times decreased for flexible alkanes when compared to the rigid alkanes. The difference between the relaxation rates of the flexible and rigid molecules increased as the carbon chain length

increased, with *n*-decane relaxing 13 times faster when internal motions were removed. The effect of internal motions is well-known in NMR relaxation, with notable examples being bulk liquids,[24] and macromolecular structures such as proteins.[25] Phenomenological relaxation models of varying degrees of complexity are often employed to describe the complex relaxation behaviour caused by internal motions. These phenomenological models provide good fits to the experimental data, but have no rigorous theoretical basis in terms of the underlying molecular dynamics, and introduce additional variables into the relaxation equations.[26,27]

For rigid and flexible molecules imbibed within porous media, NMR relaxation ratios have been used as a model free methodology for the interpretation of the solid-liquid interaction strength.[1,17,28] However, these studies often only investigate a small subset of liquids. Within this chapter a large series of rigid and flexible molecules will be imbibed within γ-alumina to test the robustness of NMR relaxation ratios for measuring the solid-liquid interaction strength of these molecules.

4.2.3 Non-NMR methods for measuring interaction strength

In order to quantitatively demonstrate that differences in the fixed field relaxation ratios correlate with the solid-liquid interaction strength an independent measurement of the surface interaction strength is required. Conventional methods such as temperature programmed desorption (TPD), infrared (IR), and calorimetric studies[29] are not universally applicable to all liquids and porous media. For example, the high temperatures required for TPD experiments have been known to cause reactions to occur *in situ*,[30] and commonly used liquids, such as water, absorb IR radiation too efficiently to be studied by standard IR techniques.[31] Instead, within this chapter the interaction strength of each adsorbate was assumed to correlate directly with the polarity of the adsorbate. This assumption was valid for γ-alumina, as the support is highly polar, and therefore a significant contribution to the surface binding was electrostatic. Furthermore, the molecules were small in relation to the size of the pores, and therefore complex confinement effects would not have dominated the interaction. The solvent polarity values were taken from tabulated values of the Reichardt ET-30 values.[32] These values are a measure of the change in the UV-Vis transition energy of Reichardt's dye (Betanine 30) when dissolved in different solutions. The zwitterionic structure of Betanine 30 is shown in Figure 4.5. As Betanine 30 is a highly charged molecule, its solvation behaviour

is expected to be representative of surface binding of liquids imbibed within γ-alumina, and will therefore be a reliable measurement of the solid-liquid interaction strength.

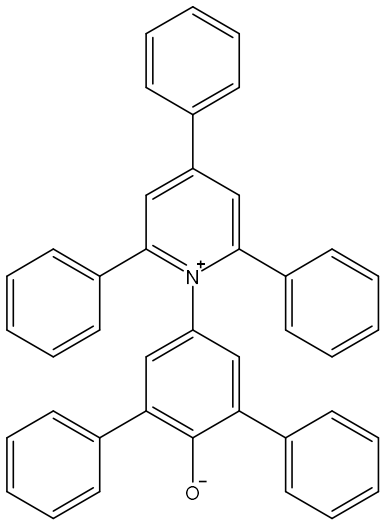

Figure 4.5: The chemical structure of Reichardt's dye, also known as Betanine 30.[32]

4.3 Materials and methods

4.3.1 Materials

The porous medium used was *γ*-alumina (BASF, catalogue number 43855) with a pore volume of 0.65 g ml^{-1}. Nitrogen Brunauer–Emmett–Teller (BET) and Barrett-Joyner-Halenda (BJH) measurements gave a surface area of 206 m^2 g^{-1} and a monomodal pore size distribution centred about a pore diameter of 9 nm (see appendix 1). Electron spin resonance (ESR) measurements were performed on a Bruker E500 X-band spectrometer with an ER 4122SHQE cavity at a microwave frequency of 9.385 GHz. Two features were observed for γ-alumina, a sharp paramagnetic resonance at 1600 G (6 ppm) ascribed to Fe^{3+} and a small broad feature centred about 3400 G which has previously been ascribed to superparamagnetic Fe^{3+} clusters within the framework[33] (see appendix 1). Deionised water was produced in-house using a Elga Purelab DV25 purification system. Cyclohexane, cyclohexene, 2-methyl-2-butene, toluene, DMSO, methanol (>99% purity) were obtained from Sigma Aldrich. Linear *n*-alkanes from hexane to tetradecane, and *n*-alcohols from methanol to decanol were obtained from Alfa Aesar (>98% purity).

4.3.2 Methods

4.3.2.1 Sample preparation

Samples were prepared by drying the alumina for 12 h at 120 °C to drive off physisorbed water, and then soaking the alumina for a further 12 h in the desired liquid. The sample was then poured onto filter paper and the extra pellet liquid was removed shortly prior to analysis. Between 30-50 pellets were used for each experiment, and the pellets were cylindrical extrudates with a diameter of 3 mm and ranged in length from 5-10 mm. Full saturation of the pore space with the liquid during the imbibition process was confirmed by gravimetric measurement of the pellets before and after liquid imbibition.[34]

4.3.2.2 Relaxation measurements

Unless otherwise stated experiments were carried out on a Bruker AV85 horizontal bore magnet (operating frequency of 85 MHz), with a 90 mm probe. Typical pulse lengths were 20 μs for a π/2 pulse. One-dimensional (1D) T_1 experiments were recorded with an inversion recovery pulse sequence, and two dimensional (2D) T_1-T_2 experiments were recorded with an inversion recovery pulse sequence followed by a PROJECT echo train. For molecules with only a single magnetic environment the PROJECT sequence was verified against a CPMG sequence. For each experiment 16 time delays were used for the T_1 experiment and 32-4096 echoes were used for the T_2 experiment. The time delays and echo trains were optimised for each sample in order to capture the key features of the relaxation curves. For each T_1-T_2 experiment 8 signal averages were acquired with phase cycling. Internal gradient corrections were performed by acquiring PROJECT experiments with an echo spacing that varied linearly from 2 – 18 ms in 32 increments. Chemical resolution was possible in only a few systems when using 1D T_1 methods and not possible when using 2D T_1-T_2 methods. To ensure a fair comparison between $T_{1,B}/T_{1,pore}$ and T_1/T_2 approaches applied to different samples, chemical resolution was not exploited within this chapter. Instead the NMR signal was taken as the total area of all peaks.

Exponential fittings as outlined in section 2.3.1 were used to extract the T_1 and T_2 time constants from 1D experiments. For the 2D T_1-T_2 experiment the data can be described by a Fredholm integral of the first kind:[1,35]

$$\frac{S(n,t_e)}{S(0,0)} = \int_{-\infty}^{\infty}\int_{-\infty}^{\infty} K(\tau_1,T_1,nt_e,T_2)f(T_1,T_2)\mathrm{d}(\log T_1)\mathrm{d}(\log T_2) + \varepsilon\,, \quad (4.3)$$

where S is the NMR signal, n is the number of echoes, t_e is the echo spacing, K is the Kernel matrix, τ_1 is the delay in the T_1 experiment, $f(T_1,T_2)$ is the true distribution of T_1 and T_2, and ε is the error term. Following the approach outlined in section 2.3.4 the data were inverted using an in-house Matlab script. A Tikhonov regularization was applied, and the magnitude of the smoothing parameter, α, was optimised through a generalized cross validation (GCV) method. Internal gradient corrections were applied using the procedure outlined in section 2.4.2. A series of T_2 measurements with different values of t_e were performed. The Kernel for these experiments is given as:

$$K = \exp\left(-\frac{nt_e}{T_2}\right)\exp(-ant_e{}^k)\,, \quad (4.4)$$

where a is an empirical constant and k is an empirical power law exponent. An in-house Matlab script was used to iterate through different values of the exponent k until the variable echo time T_2 data collapsed onto a single plot. Once the value of k was selected, this was used to remove the effects of internal gradients from the T_2 domain. k was incremented in steps of 0.05, and to ensure a robust collapse of the T_2 data the inversion was performed for the value of k either side of the selected value for comparison.

T_2 measurements acquired at different field strengths were measured with an Oxford instruments Geospec 2 MHz, a Bruker DMX300 (300 MHz), and a Bruker AV400 (400 MHz) magnet. All experimental delays were optimised using the procedure outlined for the AV85 magnet (85 MHz).

4.3.2.3 Displacement experiments

Displacement experiments were performed by preparing an alumina sample as outlined in section 4.3.2.1. For each displacement a single pellet was used, and the initial measurement (time $t = 0$) was recorded before the sample was exposed to the displacing liquid. The alumina sample was then immersed in a displacing fluid for a period of time, t, before being removed. The external surface of the pellet was dried, and the sample was measured by ^{1}H spectroscopy. The process was repeated to give displacement times of

0, 1, 5, 15, 30, 60, 120, and 720 min in order to monitor the concentration of both fluids as a function of time.

^{1}H NMR spectroscopy measurements were performed on Magritek Spinsolve 43 MHz permanent magnet, with a 5 mm coil. 16 scans were used to ensure a good signal-to-noise ratio, and the repetition time was set to 10 s to allow the sample to return to equilibrium between measurements. Liquid pairs were selected so that peaks could be spectroscopically resolved, even in the presence of line broadening due to internal gradients. When full spectral resolution was not possible, line fitting was applied using Mestrenova (Mestrelab S.L.) to decompose the spectrum into a series of Lorentzian-Gaussian peaks. For toluene-DMSO and DMSO-water two Lorentzian-Gaussian peaks were required to achieve a good fit to the data. When toluene-*n*-butanol was used a third peak was included to accurately capture the chemical shift of the ^{1}H species adjacent to the hydroxyl group in butanol.

The NMR signal for each region can be expressed as: [36]

$$S(\omega) = \left[\frac{\gamma \hbar^2 I(I+1)}{24\sqrt{k^3 \mu_0}}\right]\left[\frac{N\sqrt{\omega^3 T_2^*}}{\sqrt{T^3}}\right]\left[\frac{2\xi^2 \rho Q V_c}{\lambda F}\right]^{1/2} \sin\alpha\,, \tag{4.5}$$

where $S(\omega)$ is the voltage, γ is the gyromagnetic ratio of the nucleus, I is the nuclear spin, k is Boltzmann's constant, μ_0 is the vacuum permeability, N is the number of spins, ω is the Larmor frequency, T_2^* is the apparent transverse relaxation time constant, T is the temperature, ξ is filling factor of the receiver, ρ is the ratio of effective to total inductance, Q is the quality factor, V_c is the volume of the coil, λ is Nagaoka's constant, F is the noise factor, and α is the pulse angle. Measuring repeat experiments on the same sample and with the same experimental parameters simplified eq. (4.5) to:

$$S_i(\omega) = K_i N_i\,, \tag{4.6}$$

where $S_i(\omega)$ is the signal intensity of component i, K_i is a proportionality constant for component i, and N_i is the number of i spins. K_i can be assumed to be constant for all different chemical environments within a single sample, and peak areas obtained from the line fitting were converted to relative mole fractions, χ_i, using the expression:

$$\chi_i = \frac{S_i(\omega)/n_i}{\sum_i (S_i(\omega)/n_i)} = \frac{N_i/n_i}{\sum_i (N_i/n_i)}, \quad (4.7)$$

where n_i is the number of ^{1}H protons per molecule associated with each region of the NMR signal.

4.4 Results

Within this section the robustness of both $T_{1,B}/T_{1,pore}$ and T_1/T_2 ratios as a measure of the solid-liquid interaction strength for liquids imbibed within γ-alumina are explored. The section is separated into four parts;

- the intrinsic experimental error of each relaxation ratio is estimated,
- the relaxation ratios are applied to rigid molecules,
- the relaxation ratios are applied to flexible molecules,
- the relative interaction strengths obtained for rigid and flexible molecules are verified through displacement experiments.

4.4.1 Sample reproducibility

In order to compare between different samples the experimental error in the relaxation ratio of a given sample must be smaller than the differences between the samples. To estimate the error associated with each relaxation ratio, repeat measurements of T_1, T_2, and T_1/T_2 were recorded for three samples of water and heptane, both in bulk and imbibed within γ-alumina. The measured values are listed in Table 4.1.

Table 4.1: The 1D T_1 and T_2 values, and the 2D T_1/T_2 ratios obtained from 3 repeat samples of water and *n*-heptane. In both cases the data are shown for a bulk liquid and for liquid imbibed within pellets.

Fluid	Bulk/imbibed	T_1 / ms	T_2 / ms	T_1/T_2
water	bulk	2753	2134	1.3
water	bulk	2664	1956	1.4
water	bulk	2689	2012	1.3
water	imbibed	284	5	54.6
water	imbibed	259	5	49.8
water	imbibed	265	5	49.8
n-heptane	bulk	2320	2052	1.1
n-heptane	bulk	2215	2016	1.1
n-heptane	bulk	2170	1992	1.1

n-heptane	imbibed	1072	115	9.3
n-heptane	imbibed	1082	114	9.3
n-heptane	imbibed	1015	110	9.3

The percentage error associated with the T_1 measurements of the bulk liquids were relatively small, with water values consistent to within 3% and heptane values to within 7%. The magnitude of the error increased for water when the liquids were imbibed within γ-alumina, reaching 9%, but did not change significantly for *n*-heptane. The sample to sample variation was far larger than the numerical fitting errors, which were <1%. Further measurements were performed to explore the sensitivity of the relaxation data to likely sources of experimental error including; poor shimming, samples being placed outside the centre of the detection coil, and variable sample sizes. Negligible effects (<1%) on all relaxation time constants were observed. This suggested that the deviations observed between different water and heptane samples were due to physical changes between the samples. From the data shown in Table 4.1 a conservative estimate of the error in the ratio $T_{1,B}/T_{1,pore}$ can be given by summing the maximum percentage error in $T_{1,B}$ and $T_{1,pore}$. This gives a percentage error of $7\% + 9\% = 16\%$.

The T_1/T_2 ratio showed a smaller variation than the individual T_1 and T_2 values, and in most cases was identical across the repeated samples. This may be a true effect, due to the T_1 and T_2 values of the sample being correlated. As the T_1/T_2 ratio is measured from a single sample any heterogeneities in the sample will affect both T_1 and T_2 similarly. The variations can therefore be cancelled out when taking the ratio. However, the small sample-to-sample variation may also be caused by the data processing methodology. The 1D NMR experiments were fitted with an exponential function that allowed a continuous range of T_1 and T_2 values. In contrast, the 2D T_1-T_2 experiment required a discretised T_1 and T_2 list for the numerical inversion, and therefore only specific values of T_1 and T_2 (and hence T_1/T_2) were permitted. When the variations in T_1 and T_2 values were smaller than the step size in the allowed T_1 and T_2 lists the T_1/T_2 ratio would not change. In order to appropriately account for the effects of the data processing method, the percentage error was estimated from the maximum observed variation in the T_1/T_2 ratio obtained from 1D T_1 and T_2 measurements. This gave an error in the T_1/T_2 ratio of 10%, which was appreciably smaller than the error in the $T_{1,B}/T_{1,pore}$ ratio.

4.4.2 Rigid molecules

4.4.2.1 Direct measurements

The $T_{1,B}/T_{1,pore}$ and $e_{surf} = -T_2/T_1$ ratios measured for a range of liquids imbibed within γ-alumina were plotted as a function of the adsorbate polarity, as shown in Figure 4.6. As γ-alumina is a polar surface the polarity of the adsorbate was used as a proxy for the solid-liquid interaction strength. In cases where the polarity of the molecule was not reported in the literature, the polarity of an analogous molecule with similar chemical functionalities was chosen.

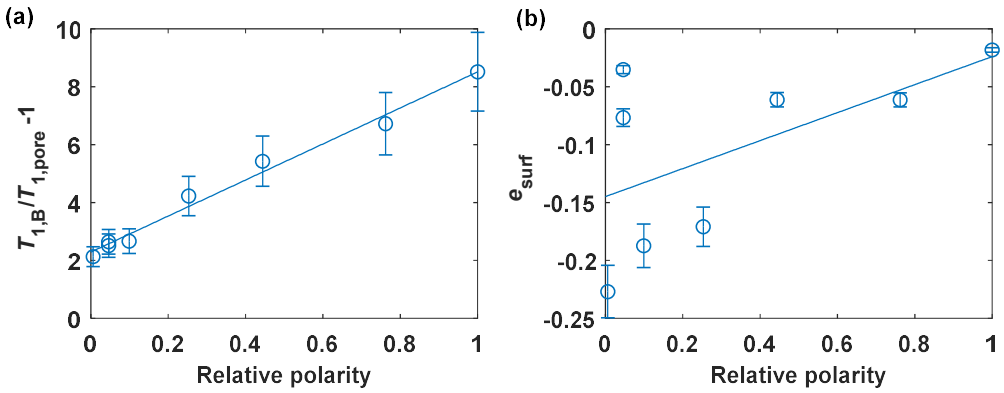

Figure 4.6: The (a) $T_{1,B}/T_{1,pore}$ -1 and (b) $e_{surf} = -T_2/T_1$ values as a function of polarity for a range of liquids imbibed within γ-alumina. The polarity range is normalized such that water has a polarity of 1. The symbols represent (from left to right) cyclohexane, cyclohexene, 2-methylbut-2-ene, toluene, methyl acetate, DMSO, methanol, and water. In each case a line of best fit is included to highlight the correlation between the polarity and the relaxation ratio.

For the $T_{1,B}/T_{1,pore}$ ratio a strong linear correlation was observed between the relaxation ratio and the liquid polarity for all adsorbates. As $T_{1,B}/T_{1,pore}$ -1 is proportional to $T_{1,B}/T_{1,S}$ this result demonstrated that the surface relaxation behaviour is sensitive to the solid-liquid interaction strength for a wide range of liquids imbibed within γ-alumina. For the e_{surf} parameter, a weaker correlation was observed. Cyclohexene, 2-methylbut-2-ene and DMSO appeared as outliers, even when using a conservative estimate of the experimental error. For these molecules the e_{surf} parameter predicted a strong interaction with the surface, and that the interaction of the alkenes was similar to that of methanol. The poorer quality of correlation suggested that the T_2 measurement was influenced by factors other than purely the solid-liquid interaction strength, and a more in depth analysis of this

relaxation ratio is presented in the following section. A common cause of enhanced T_2 relaxation for liquids imbibed in porous media is internal gradient effects. These effects are not directly controlled by the solid-liquid interaction strength, and only affect T_2 values rather than T_1.[37] The following section will explore whether internal gradient effects caused the significant outliers observed in Figure 4.6b.

4.4.2.2 Internal gradients effects

Internal gradients effects are caused by magnetic susceptibility differences that occur at the solid-liquid interface within porous media. The sensitivity of T_2 to the internal gradients is well-known[38] and a full theoretical description was presented in section 2.4.2. Evidence of internal gradients affecting the T_2 measurements of liquid imbibed within γ-alumina samples studied herein was observed as a stretching of the peak in the T_2 domain of the T_1-T_2 correlation plots, as shown in Figure 4.7. This effect appeared significant for the cyclohexane relaxation behaviour, with the peak being stretched by more than an order of magnitude in the T_2 domain. An additional minor feature was present at very low values of T_2, however the relaxation rate of this feature was too fast for it to have originated from the sample. For water imbibed in γ-alumina stretching in the T_2 domain was also visible, but extended over a much narrower range of T_2 values. A minor peak was also observed in this correlation plot at T_1~1 s and T_2~0.1 s, however the intensity of this peak was < 2% of the total signal intensity and therefore this feature was not considered in the analysis.

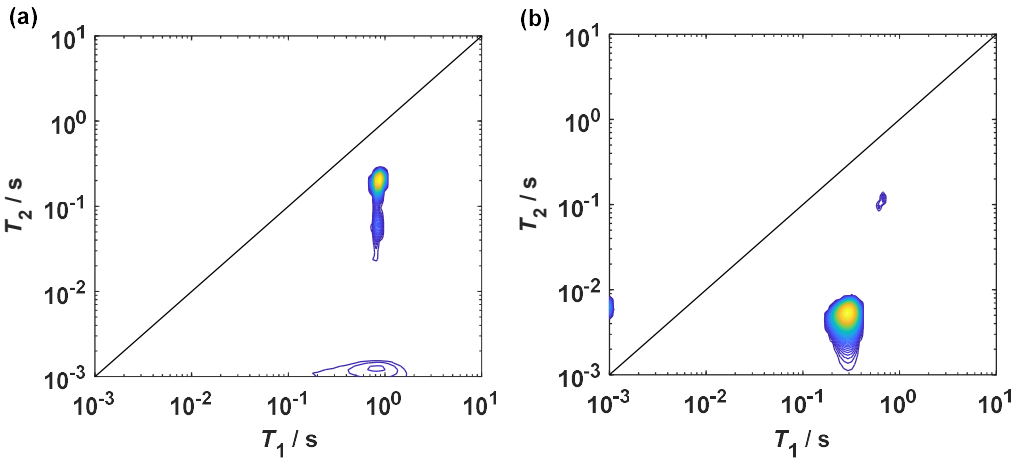

Figure 4.7: The 2D T_1-T_2 correlation plots obtained for (a) cyclohexane and (b) water imbibed within γ-alumina. The solid line represents $T_1/T_2 = 1$.

The magnitude of the internal gradients are known to scale with the applied magnetic field strength, whereas the true T_2 value is only weakly dependent on the magnetic field strength.[38] To confirm that the distortions in the T_2 domain of the T_1-T_2 correlation diagrams were due to internal gradient effects Figure 4.8 shows the T_2 values of 3 different liquids imbibed within γ-alumina measured at a range of magnetic field strengths. The relaxation time constant decreased as the field strength increased for all of the liquids imbibed within γ-alumina. For water and methanol a small change was observed in the value of T_2 as a function of the magnetic field strength, with the high field T_2 values being 1.1 and 1.7 times smaller than the low field values respectively. In contrast, for cyclohexane the T_2 value measured at 400 MHz was 31 times smaller than the value at 2 MHz. Furthermore, at low field strengths the T_2 value of cyclohexane was larger than that of methanol, but this was reversed at higher field strengths. The strong decrease in the cyclohexane relaxation time was consistent with a significant contribution to the observed value of T_2 due to internal gradient effects.

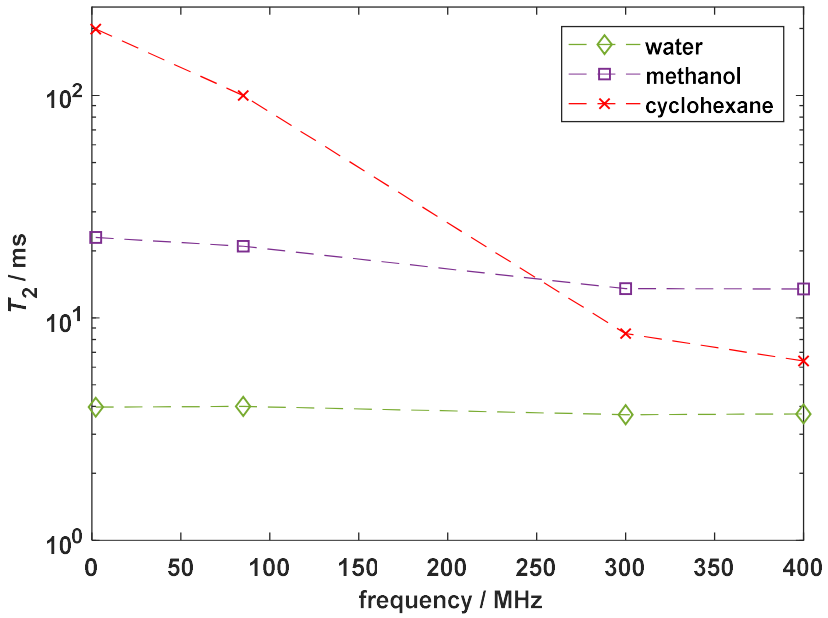

Figure 4.8: The transverse relaxation time constant, T_2, of water, methanol, and cyclohexane imbibed within γ-alumina as a function of the ^{1}H Larmor frequency.

The data in Figure 4.7 and Figure 4.8 suggested that internal gradient effects were contributing to the T_2 relaxation time constant for the samples measured at 85 MHz. In order to obtain the true T_2 value, and hence a true T_1/T_2 ratio, an internal gradient

correction was applied to several of the liquids presented in Figure 4.6. A comparison between the uncorrected and the corrected data is shown in Figure 4.9. For all liquids the e_{surf} parameter decreased after the correction, due to an increase in the value of T_2. Water and methanol were the least affected by the internal gradient correction, with the e_{surf} parameter decreasing by a factor of 1.3 and 1.7 respectively. The less polar species showed decreases in e_{surf} by a factor of 2.1-2.8, with the exception of toluene, which decreased by a factor of 4. The scatter in the relaxation data was not removed by applying the internal gradient correction, and a linear correlation has been included to highlight this in Figure 4.9.

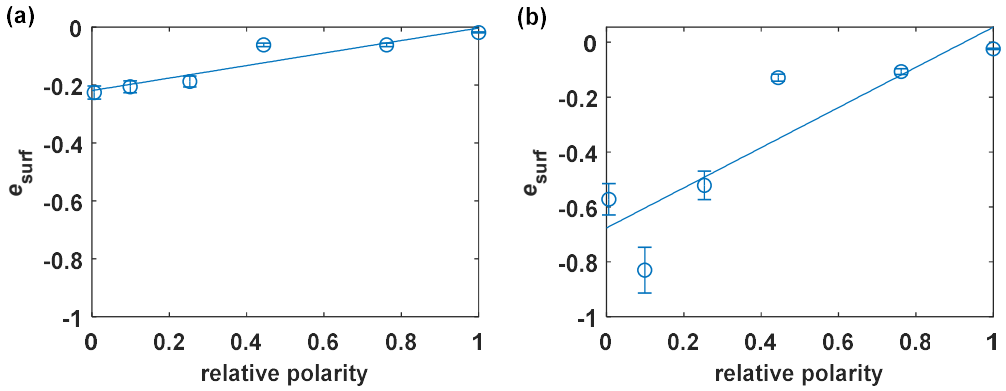

Figure 4.9: The (a) non-corrected and (b) internal gradient corrected $e_{\text{surf}} = -T_2/T_1$ values as a function of polarity for a range of liquids imbibed within γ-alumina. The polarity range is normalized such that water has a polarity of 1. The symbols represent (from left to right) cyclohexane, toluene, methyl acetate, DMSO, methanol, and water. In each case a line of best fit is included to highlight the correlation between the polarity and the relaxation ratio.

The application of an internal gradient correction required hand iteration of the time exponent, k, which is defined in eq. (4.4). This value was adjusted until the T_2 decay profiles measured with different inter-echo spacing collapsed to a single plot. For all liquids imbibed within γ-alumina the value of k was between 1.05-1.6, which is close to the theoretical limit of 1, at which point the gradient effects can no longer be separated from the true relaxation behaviour. Figure 4.10 shows the corrected T_1/T_2 ratios for cyclohexane imbibed within γ-alumina measured over the range of $k = 1.05 - 1.15$. The corrected data were highly sensitive to k. For $k = 1.05$ the correction resulted in a broad peak that stretched to very high values of T_2. Such a result was unphysical, and suggested an improper optimization of k. For $k = 1.1$ and 1.15 the corrected data showed a single

well resolved feature with values of T_1/T_2 of 1.7 and 2.3 respectively. Figure 4.10d-f shows the collapse plots used to obtain the value of k. Very little difference was seen between all of the plots, meaning that the optimization of k was non-trivial.

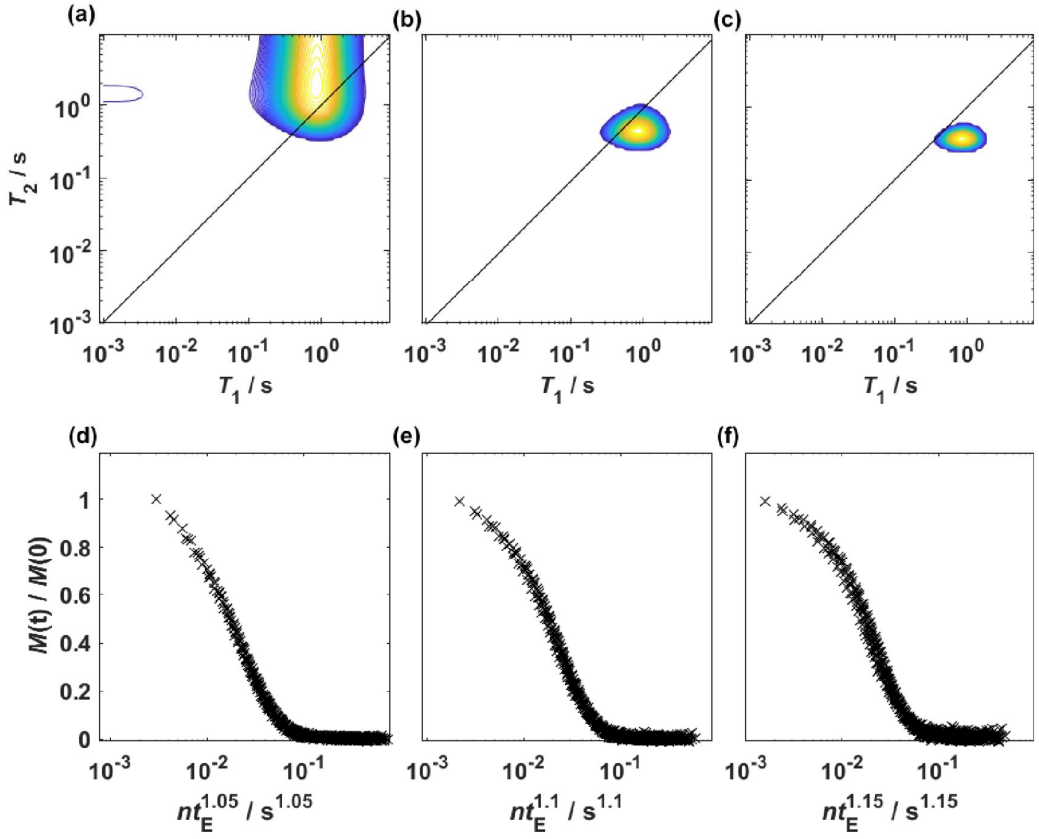

Figure 4.10: The internal gradient corrected T_1-T_2 plots of cyclohexane imbibed within γ-alumina obtained with correction factors of k = (a) 1.05, (b) 1.10, and (c) 1.15. The corresponding collapse plots are shown for k = (d) 1.05, (e) 1.10, and (f) 1.15.

4.4.3 Flexible molecules

For rigid molecules the intramolecular ^{1}H-^{1}H distances were constant throughout the experiment. The shape of the molecule deviated significantly from a perfect sphere, but the NMR relaxation ratios provided a useful tool for measuring the strength of the surface binding. In particular the $T_{1,B}/T_{1,pore}$ ratio showed an unambiguous correlation. In this section the same analyses are applied to flexible molecules, in which the minimum ^{1}H-^{1}H distance can vary. Figure 4.11 shows the relaxation rate data for a series of *n*-alkanes and primary alcohols imbibed within γ-alumina.

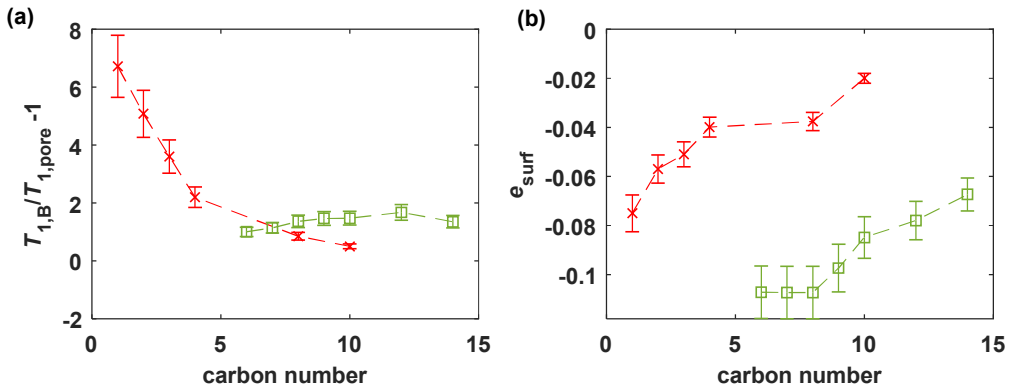

Figure 4.11: The (a) $T_{1,B}/T_{1,pore}$ -1 and (b) $e_{surf} = -T_2/T_1$ values as a function of carbon chain length for *n*-alcohols (*x*) and *n*-alkanes (□) imbibed within γ-alumina. The dashed lines are a guide to the eye, and show the trends in each relaxation ratio as a function of carbon chain length.

The $T_{1,B}/T_{1,pore}$ ratio of the alcohols decreased significantly as the carbon chain length increased. For *n*-octanol and *n*-decanol this ratio was lower than that of the *n*-alkanes imbibed within γ-alumina, and indicated a significant weakening of the solid-liquid interaction. The e_{surf} measurement showed the opposite trend, with a clear increase of the interaction strength as a function of the carbon chain length. Directly interpreting the two relaxation ratios as measurements of the interaction strength is therefore not possible for the *n*-alcohols. Similar behaviour was noted for the *n*-alkanes, which showed little change in interaction strength when measured with $T_{1,B}/T_{1,pore}$, but a significant increase in the interaction strength as the carbon chain length increased when measured by the e_{surf} parameter. The value of e_{surf} predicted a similar interaction strength for dodecane, tetradecane, and methanol imbibed within γ-alumina. Figure 4.12 shows a direct comparison of the flexible and rigid liquids imbibed within γ-alumina. The flexible molecules had values of $T_{1,B}/T_{1,pore}$ that systematically fell below the expected values for rigid molecules of the same polarity. As the chain length of the alcohols increased this deviation became larger, and *n*-octanol and *n*-decanol were predicted to be less strongly interacting than cyclohexane. A smaller deviation with alkyl chain length was observed for the *n*-alkanes relative to the $T_{1,B}/T_{1,pore}$ values measured for rigid molecules of the same polarity. From the e_{surf} data it was predicted that the *n*-alkanes were significantly more strongly interacting than cyclohexane, and that larger *n*-alkanes were similar to DMSO and methanol in terms of their interaction strength.

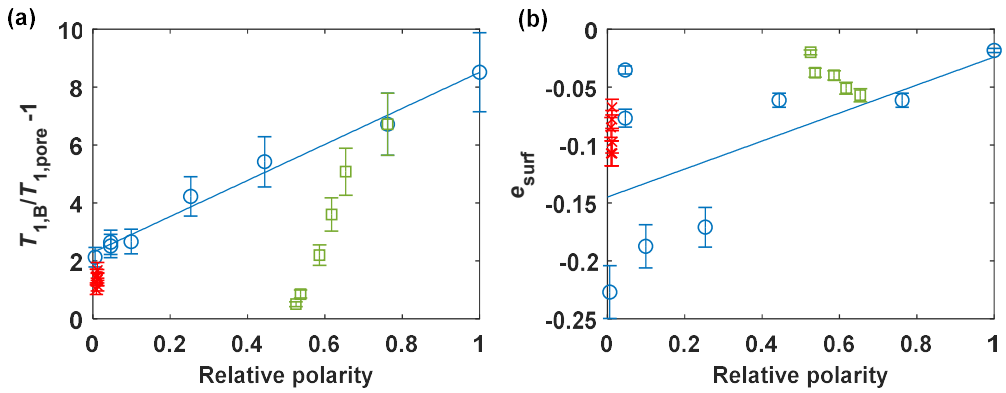

Figure 4.12: The (a) $T_{1,B}/T_{1,pore}$ -1 and (b) $e_{surf} = -T_2/T_1$ values as a function of polarity for a range of liquids imbibed within γ-alumina. The polarity range is normalized such that water has a polarity of 1. The rigid molecules (○) are those shown in Figure 4.6, and the flexible molecules represent the *n*-alkanes (*x*) and the *n*-alcohols (□). In each case a line of best fit is included to highlight the correlation between the polarity and the relaxation ratio of the rigid molecules.

4.4.4 Displacement experiments

Within this chapter relative polarity has been used as an analogue for interaction strength, and other contributions, such as the steric effects that occur during binding, may also affect the solid-liquid interaction strength within mesoporous materials. An independent measurement of the relative solid-liquid interaction strength was required to validate the results observed in Figure 4.6 and Figure 4.12, and to confirm that relaxation ratios could be used to measure the relative interaction strength of different adsorbates with a surface. A series of displacement experiments were performed on a Magritek Spinsolve 43 MHz magnet to study the relative solid-liquid interaction strengths of different pairs of liquids. A single pellet of γ-alumina was saturated with one liquid (the imbibed liquid) and the pellet was then immersed in a second liquid (the displacing liquid). The ingress of the displacing liquid was measured as a function of time using ^{1}H spectroscopy. Significant line broadening was observed for liquids imbibed within γ-alumina, which limited the spectroscopic resolution of this measurement. To mitigate against this issue, samples were chosen to maximise the chemical shift differences between the imbibed and displacing liquids. In cases where complete resolution was not possible, line fitting was used to separate out the two liquids. Figure 4.13 shows the ^{1}H NMR spectra for the displacements of toluene by DMSO, toluene by *n*-butanol, and DMSO by water within γ-alumina.

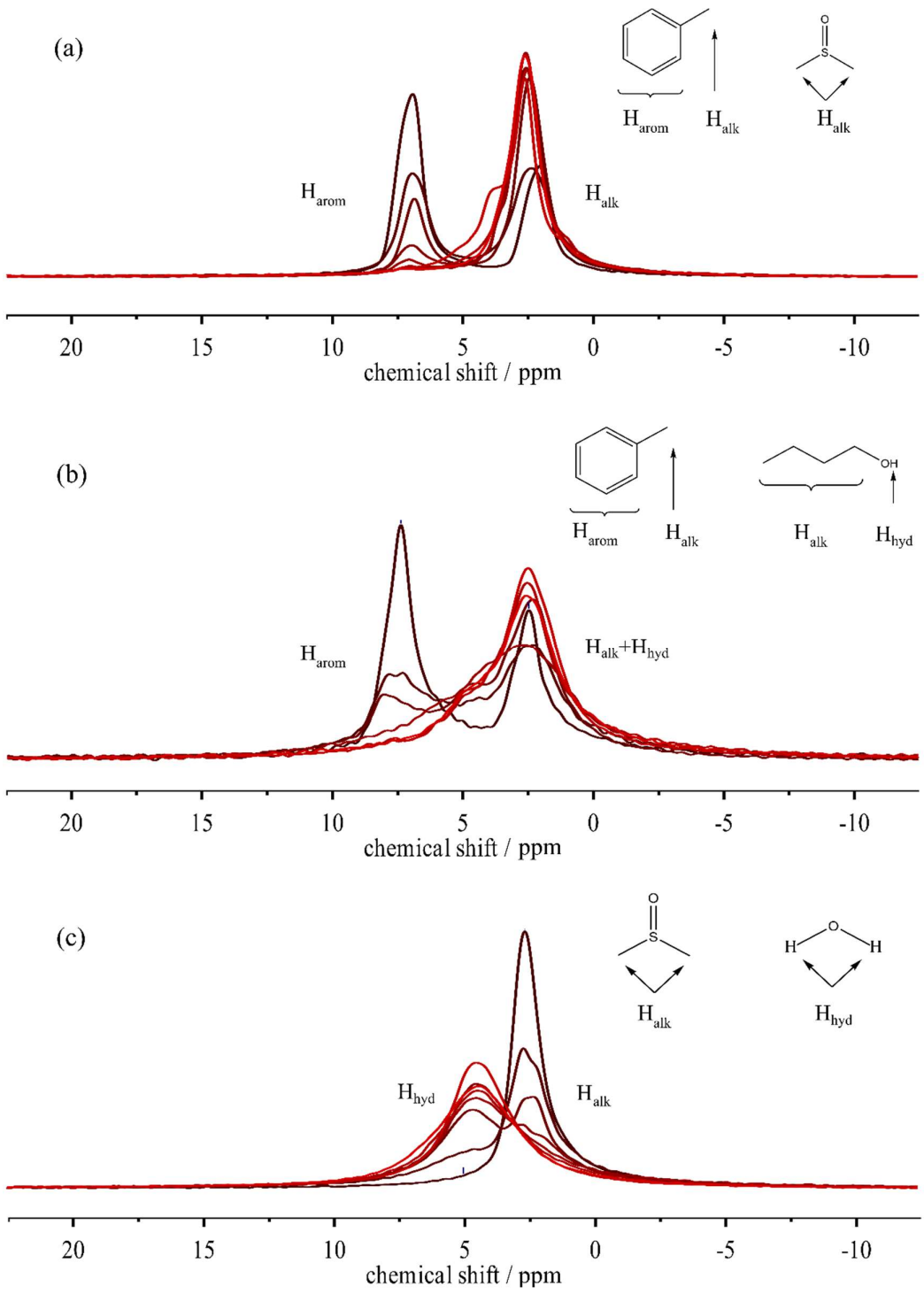

Figure 4.13: ^{1}H NMR spectra recorded as a function of time for the displacements of (a) toluene by DMSO, (b) toluene by *n*-butanol, and (c) DMSO by water within γ-alumina. In each case the spectra are plotted on a colour gradient from a displacement time of 0 min (dark brown) to 120 min (red). The chemical structures of each pair of molecules is shown to clarify the assignment of each peak. Experiments were performed on a Magritek Spinsolve 43 MHz magnet.

For all pairs of liquids two distinct peaks were visible, with a full width half maximum (FWHM) of approximately 1 ppm. When high concentrations of *n*-butanol were present a third peak was included in the deconvolution at a chemical shift of $\delta = 3.6$ ppm to achieve a good deconvolution. This was consistent with the chemical shift of the alkyl group adjacent to the hydroxyl group in butanol.[39] For DMSO-toluene and *n*-butanol-toluene imbibed within γ-alumina the chemical shift difference was large enough for the peaks to be almost fully resolved. In both cases it was clear that the toluene was completely displaced over the course of the experiment. The separation was poorer for the mixture of water-DMSO imbibed within γ-alumina due to the smaller chemical shift difference between the two species. Two peaks were still observed, but it was not possible to state definitively that all of the DMSO was displaced, as the water peak could have obscured a small DMSO peak. To confirm that water fully displaced DMSO on the timescale of the experiment the water-DMSO experiment was repeated with D_2O. The D_2O acted identically to H_2O in terms of its surface interactions, but was not visible in the ^1H spectra. Figure 4.14 shows that within the first 30 min of the displacement experiment the DMSO was almost fully displaced, and that the remaining DMSO signal was comparable to the residual H_2O peak present in the D_2O due to incomplete deuteration.

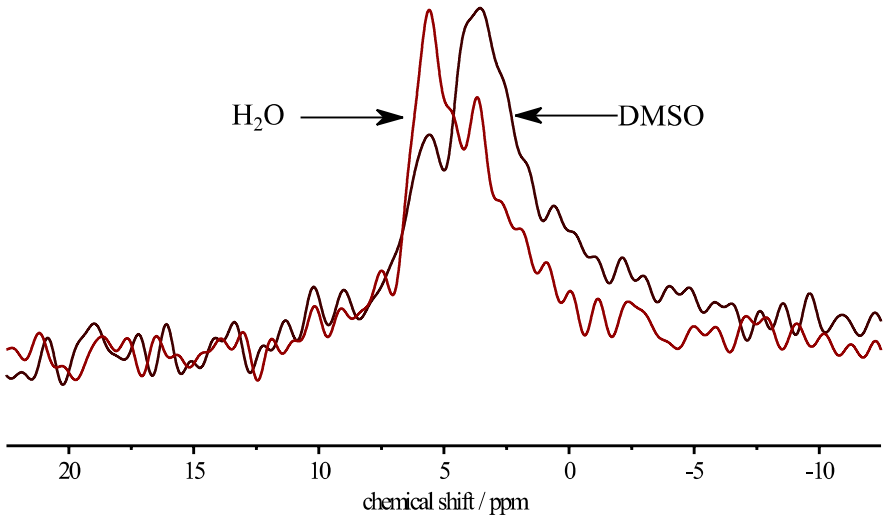

Figure 4.14: The ^1H NMR spectra obtained from the displacement of DMSO by D_2O after 30 min (black) and 60 min (red). The water peak corresponds to the residual H_2O peak of the D_2O sample due to imperfect deuteration.

The DMSO peak area was two orders of magnitude smaller than the value measured at $t = 0$. This confirmed that very little DMSO remained within the γ-alumina after 30 min of water immersion, and that the signal present after 30 min in Figure 4.13c was due solely to water.

The deconvolution of peaks can introduce significant error into the quantitative measurement of the peak areas. To estimate the lower limit of the error resulting from the deconvolution pure toluene was imbibed within γ-alumina. The deconvolution method was used to separate the aromatic and alkyl peaks. A ratio of 5:3 was expected based on the number of protons present in each environment, and ratios of 5:3.1 and 5:3.1 were measured for two different samples. This represented an overestimate of the alkyl environment by approximately 5%, and suggested that the deconvolution methods were reliable and accurate.

Figure 4.15 shows the time dependent populations of each pair of liquids during displacement experiments within γ-alumina. For each pair of liquids the experiment was repeated in reverse, so that both liquids in the pair could act as the displacing liquid. For the DMSO-toluene experiments Figure 4.15 shows that DMSO was able to fully displace toluene from the pore space within the first 60-100 min of the experiment. The displacement of DMSO by toluene progressed much slower, and the population fraction of DMSO did not fall below 31 mol%. Similar results were observed for *n*-butanol-toluene mixtures, which showed that toluene was rapidly and completely displaced by *n*-butanol. In contrast, when toluene was used to displace *n*-butanol 15 mol% could not be displaced, and the overall displacement process occurred much slower. For the water-DMSO system, DMSO was rapidly and completely displaced by water within the first 30 min of the experiment. Due to the similar chemical shifts of DMSO and water it was not possible to reliably separate the two peaks. D_2O-DMSO measurements confirmed that the DMSO was fully displaced when D_2O was added, and this was likely to have been the case when H_2O was added as well. This allowed the displacement of DMSO by water to be tracked spectroscopically. The fluctuations in the absolute intensity of the DMSO peak were too large to reliably follow DMSO intrusion in the D_2O-DMSO system. As only a single peak was present in this system eq. (4.7) could not be used to normalise the data, and it was not possible to compensate for the differences in the signal response between each time point.

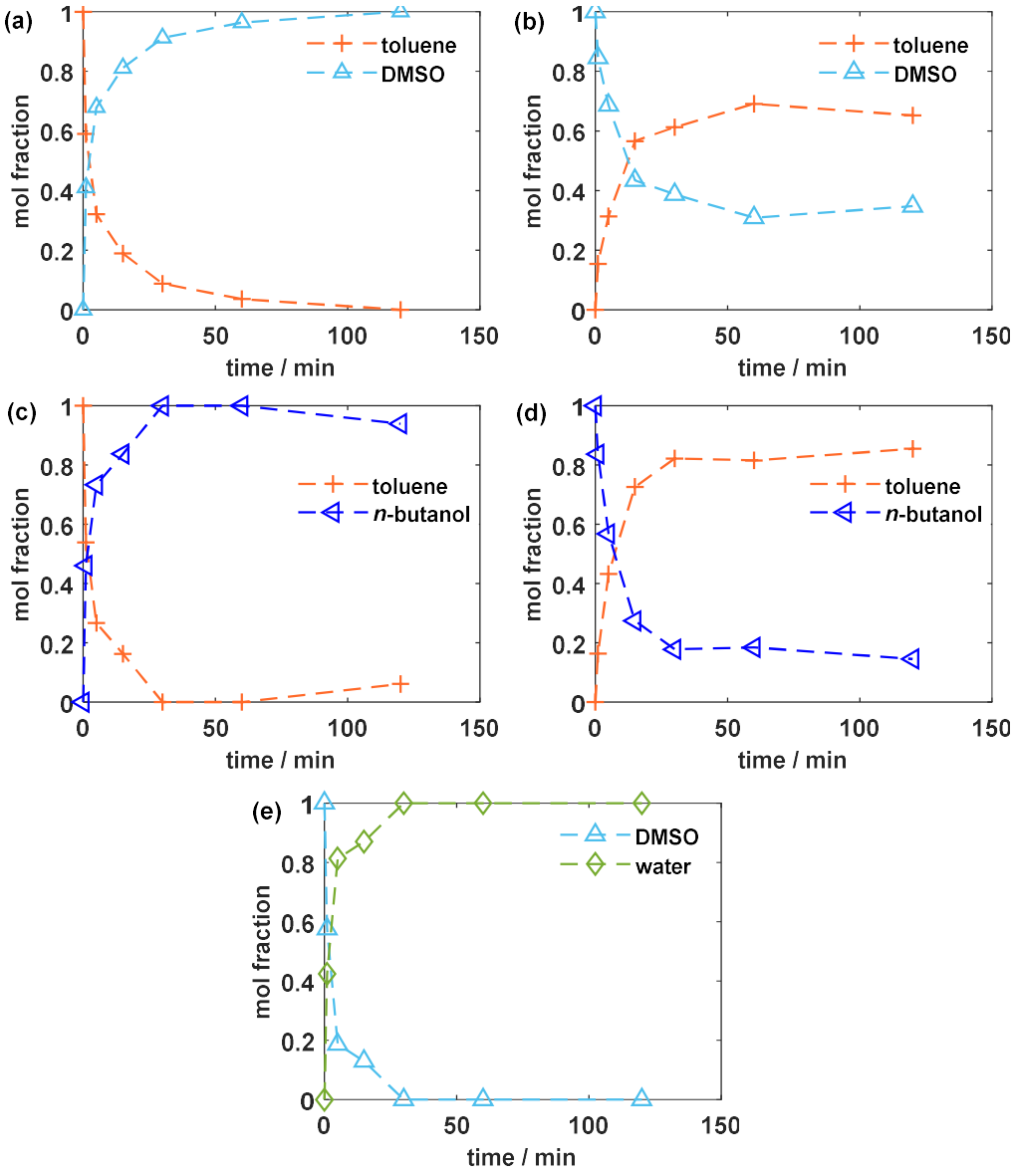

Figure 4.15: The intrapellet compositions measured by ^{1}H spectroscopy as a function of time for a series of displacement experiments within γ-alumina. Data are shown for the displacements of (a) toluene by DMSO, (b) DMSO by toluene, (c) toluene by *n*-butanol, (d) *n*-butanol by toluene, and (e) DMSO by water.

Finally, to confirm that the equilibrium concentrations obtained from the displacement experiments were consistent with the kinetic measurements shown in Figure 4.15, the samples were measured again after 12 h of soaking. The results of the long-time displacement experiments are shown in Table 4.2. For most samples the data point at long times was within experimental error of the data point obtained after 120 min. The only exception to this was the toluene displacement of DMSO, which showed a decrease in the mole fraction of toluene by 16 mol% between 2-12 h of soaking.

Table 4.2: The mole fraction of the imbibed fluid remaining within the γ-alumina pellet after 12 h of soaking in the displacing fluid.

imbibed fluid	displacing fluid	imbibed fluid left after 12 h / mol%
toluene	DMSO	2
DMSO	toluene	51
toluene	*n*-butanol	0
n-butanol	toluene	15
DMSO	water	0

4.5 Discussion

In this section the results presented in section 4.4 are explored in the context of previous studies and the underlying physical chemistry of the system. The validity of the $T_{1,B}/T_{1,pore}$ and e_{surf} parameters as measures of the solid-liquid interaction strength for both rigid and flexible molecules imbibed within γ-alumina is discussed.

4.5.1 NMR relaxation ratios of rigid molecules

For rigid molecules imbibed within a polar γ-alumina material Figure 4.6 shows that both $T_{1,B}/T_{1,pore}$ and e_{surf} measurements followed a general trend that the more polar an adsorbate was the greater its interaction strength with the surface. This is a well-known effect in surface adsorption, and has been used to optimise the extraction and isolation of chemical compounds through a range of chromatographic methods.[40,41] A strong linear trend was observed between the $T_{1,B}/T_{1,pore}$ ratio and the polarity of the adsorbate for a wide range of rigid molecules, which allowed a clear ranking of the adsorbate surface interaction strengths. This ordering was confirmed by the displacement experiments carried out using water-DMSO and DMSO-toluene mixtures. In each case the more polar species was able to fully displace the less polar species from the pore space within 120 min. In contrast, the less polar species was unable to fully displace the more polar liquid. These results were consistent with previous displacement experiments performed within Ru/SiO_2 and Pd/Al_2O_3,[15] and confirmed the ordering of the solid-liquid interaction strength obtained from the $T_{1,B}/T_{1,pore}$ ratio. The strong correlation showed that the error bars associated with each measurement were an overestimate of the true experimental

error. The chosen error bars represented a worst case scenario based on the experimental error of a subset of bulk and adsorbed measurements. For investigating adsorbates with much more similar polarities multiple repeat experiments could be performed to further reduce the experimental error and provide a clearer assessment of the solid-liquid interaction strength. $T_{1,B}/T_{1,pore}$ ratios show great application to the study of different liquids imbibed in a single porous medium, however, it cannot be used to study liquids across different porous media as the ratio does not correct for differences in the population of surface spins or the efficacy of surface relaxation as mentioned in section 3.2.1.1.

A much weaker correlation was observed between the e_{surf} parameter and the adsorbate polarity. The alkenes, cyclohexene and 2-methylbut-2-ene, were strongly anomalous, and showed solid-liquid interaction strengths comparable to water and methanol respectively. This is unlikely to be a true effect, as the presence of water is known to poison γ-alumina alkene oxidation catalysts by strongly outcompeting the alkene for surface binding sites.[42] Instead, this result implies that the e_{surf} parameter was distorted for alkenes. The $T_{1,B}/T_{1,pore}$ behaviour of the alkenes was consistent with the polarity of the molecules, which shows that the anomalous e_{surf} behaviour originated from uncharacteristically low T_2 values. For other unsaturated molecules imbibed in γ-alumina, such as DMSO, the e_{surf} value also over predicted the interaction strength. However, for toluene imbibed within γ-alumina the T_2 value was much larger than those of the alkenes, and the e_{surf} value was close to that of cyclohexane. An additional relaxation mechanism affecting T_2 specifically appears to be active for unsaturated molecules of low symmetry. This suggests that the e_{surf} approach can only be used to measure the interaction strength for saturated rigid molecules within γ-alumina. Measuring the T_2 value with CPMG and PROJECT sequences, and applying internal gradient corrections did not result in an improvement of the correlation between e_{surf} and the polarity of the adsorbates.

4.5.2 NMR relaxation ratios of flexible molecules

For flexible molecules, increasing the carbon chain length of the molecule increases the number of degrees of freedom of the molecule, and hence the degree of internal motions. From Figure 4.11 the $T_{1,B}/T_{1,pore}$ ratio showed that an increase in carbon chain length resulted in a weakening of the solid-liquid interaction strength for the *n*-alcohols, and little change in the interaction strength of the *n*-alkanes. This was not consistent with the

trends observed in the e_{surf} parameter measured for the same adsorbates. The latter showed a strong increase in the surface interaction strength of both the *n*-alkanes and the *n*-alcohols. Considering the adsorption strength purely from a polarity perspective the $T_{1,\mathrm{B}}/T_{1,\mathrm{pore}}$ measurements were consistent with the trends in the polarity. This was not, however, consistent with previous observations. For example, for *n*-alkanes temperature programmed desorption (TPD) measurements have shown that the increase in chain length has resulted in an increase in the adsorbate-surface interaction strength for a range of oxide surfaces.[40,43] The increase in interaction strength is commonly attributed to an increase in the Van der Waals interaction between the molecule and the surface as the chain length increases. Similar increases in the interaction strength have been observed for *n*-alcohols as the carbon chain length increased.[28,40,44] For *n*-alcohols on a titania surface it was argued that the monotonic increase in the interaction strength with chain length was dominated by the increase in Van der Waals forces in an analogous fashion to the *n*-alkanes.[40] This is consistent with the increase in the e_{surf} parameter observed within this chapter being a similar magnitude for the *n*-alkanes and the *n*-alcohols. All of these observations suggest that the e_{surf} parameter may be a reasonable metric for comparing liquid adsorption within a homologous series of flexible molecules, however the $T_{1,\mathrm{B}}/T_{1,\mathrm{pore}}$ ratio is not suitable.

Comparing the absolute values of the rigid and flexible molecule raised further questions about the validity of each relaxation ratio when applied to flexible molecules. The $T_{1,\mathrm{B}}/T_{1,\mathrm{pore}}$ ratio predicted a significant weakening of the alcohol-surface interaction strength as the carbon chain length increased, and *n*-alcohols larger than propanol were predicted to be less strongly interacting than toluene. This result was not supported by the displacement experiments performed for the *n*-butanol-toluene system imbibed within γ-alumina, as shown in Figure 4.15. *n*-butanol was able to fully displace toluene within the first 30 min of the experiment, but even after 12 h the toluene was unable to fully displace *n*-butanol. This was clear evidence that *n*-butanol was interacting more strongly with the surface than toluene, despite the values predicted by the $T_{1,\mathrm{B}}/T_{1,\mathrm{pore}}$ ratio. Neutron diffraction studies of a similar *tert*-butanol-toluene binary liquid mixtures imbibed within SBA-15 also showed that the more polar species preferentially occupied surface binding sites, and that toluene was forced into the bulk pore space.[45]

The e_{surf} parameter predicted a strong interaction of the *n*-alkanes with the catalyst surface. This interaction was much larger than that of cyclohexane, toluene, and methyl acetate, and approached that of methanol for larger *n*-alkanes. Although TPD studies have shown that the desorption energy of large alkanes can be similar to that of short chain alcohols on polar surfaces,[40] these experiments probe the relaxation behaviour as a function of the pore saturation. In fully liquid saturated pores the interactions between molecules also contribute to the relaxation behaviour, and these are not fully captured in a TPD measurement. The effects of liquid-liquid interactions has been shown by previous NMR studies, where tetradecane interacted less strongly with a Bioran glass surface than acetone or methanol.[46] Based on these results it is unlikely that the strong interaction of hexane relative to cyclohexane, and the greater interaction strength of tetradecane relative to methanol predicted in Figure 4.12b are realistic. Instead, the internal motion of the molecules prevents e_{surf} measurements from being used to quantitatively compare both rigid and flexible molecules imbibed within γ-alumina to one another.

4.6 Conclusions

The $T_{1,\mathrm{B}}/T_{1,\mathrm{pore}}$ and $e_{\mathrm{surf}} = -T_2/T_1$ values were measured for a wide range of liquids imbibed within γ-alumina. The experimental error for each measurement was shown to be sufficiently small that these relaxation ratios could be used to rank the relative solid-liquid interaction strengths of each liquid. The ranking obtained from this methodology was compared to the Reichardt polarity values which, for liquids imbibed within a polar porous medium, were expected to be an analogue for interaction strength. For rigid molecules the $T_{1,\mathrm{B}}/T_{1,\mathrm{pore}}$ ratio correlated very strongly with the polarity, which showed the robustness of this simple metric for measuring the interaction strength. The e_{surf} parameter was less strongly correlated, and showed highly anomalous results for unsaturated, non-aromatic liquids. Internal gradient corrections were applied to a subset of the T_1-T_2 data, but this did not improve the quality of the correlation between e_{surf} and the polarity.

For flexible molecules, internal motions further complicated the relationship between the relaxation ratios and the solid-liquid interaction strength. An increase in the chain length of *n*-alcohols and *n*-alkanes imbibed within γ-alumina led to inconsistent changes in the

interaction strength as predicted by the two relaxation ratios. The $T_{1,B}/T_{1,pore}$ ratio suggested a significant weakening of the solid liquid interaction strength, whereas e_{surf} values showed a clear increase. The latter was consistent with trends observed previously, but both ratios were poorly comparable between rigid and flexible molecules. This raised serious questions over the robustness of the relaxation ratios as a measure of the solid-liquid interaction strength for flexible molecules.

A series of displacement experiments were performed to confirm the ordering of interaction strengths predicted from the relaxation ratios. ^{1}H spectroscopy was used to track the first 2 h of the displacements of; toluene by DMSO, DMSO by toluene, toluene by *n*-butanol, *n*-butanol by toluene, and DMSO by water within γ-alumina. In all cases the more polar species rapidly, and fully, displaced the weakly interacting species within the timescale of the experiment. In contrast, the weakly interacting species were unable to fully displace the strongly interacting fluid. These measurements were used to support the ranking of interaction strength obtained for the rigid molecules, and to show that the ranking of flexible molecules was not consistent with the true physical chemistry of the system.

Relaxation ratios are robust measures of the solid-liquid interaction strength only when a number of caveats are applied to the analysis. This severely limits the application of these methods to a wide range of adsorption problems, and makes the likelihood of misinterpretation high. In chapter 5 an alternative relaxometry technique known as fast field cycling will be applied to study the adsorption of liquids within γ-alumina. This technique allows the measurement of T_1 at a range of magnetic field strengths, and provides far more information about the adsorption process than can be obtained from fixed field relaxation ratios. This additional information allows a more detailed understanding of the adsorption process and is used in chapter 6 to explore functionality specific adsorption and competitive adsorption, and in chapter 7 to directly model the molecular dynamics processes leading to relaxation.

4.7 References

(1) D'Agostino, C.; Mitchell, J.; Mantle, M. D.; Gladden, L. F. Interpretation of NMR Relaxation as a Tool for Characterising the Adsorption Strength of Liquids inside

Porous Materials. *Chemistry* **2014**, *20*, 13009–13015.

(2) Schiffino, R. S.; Merrill, R. P. A Mechanistic Study of the Methanol Dehydration Reaction on gamma-Alumina Catalyst. *J. Phys. Chem.* **1993**, *97*, 6425–6435.

(3) Reddy, B. M.; Lakshmanan, P.; Bharali, P.; Saikia, P.; Thrimurthulu, G.; Muhler, M.; Grünert, W. Influence of Alumina, Silica, and Titania Supports on the Structure and CO Oxidation Activity of $Ce_xZr_{1-x}O_2$ Nanocomposite Oxides. *J. Phys. Chem. C* **2007**, *111*, 10478–10483.

(4) Ovoshchnikov, D. S.; Donoeva, B. G.; Williamson, B. E.; Golovko, V. B. Tuning the Selectivity of a Supported Gold Catalyst in Solvent- and Radical Initiator-Free Aerobic Oxidation of Cyclohexene. *Catal. Sci. Technol.* **2014**, *4*, 752–757.

(5) Lamouri, S.; Hamidouche, M.; Bouaouadja, N.; Belhouchet, H.; Garnier, V.; Fantozzi, G.; Trelkat, J. F. Control of the γ-Alumina to α-Alumina Phase Transformation for an Optimized Alumina Densification. *Boletín la Soc. Española Cerámica y Vidr.* **2017**, *56*, 47–54.

(6) Wefers, K.; Misra, C. *Oxides and Hydroxides of Aluminum; Alcoa Technical Paper No. 19;* Aluminum Company of America, 1987.

(7) Brey, W. S.; Krieger, K. A. The Surface Area and Catalytic Activity of Aluminum Oxide. *J. Am. Chem. Soc.* **1949**, *71*, 3637–3641.

(8) Xie, Y.; Kocaefe, D.; Kocaefe, Y.; Cheng, J.; Liu, W. The Effect of Novel Synthetic Methods and Parameters Control on Morphology of Nano-Alumina Particles. *Nanoscale Res. Lett.* **2016**, *11*, 259.

(9) Trueba, M.; Trasatti, S. P. γ-Alumina as a Support for Catalysts: A Review of Fundamental Aspects. *Eur. J. Inorg. Chem.* **2005**, *17*, 3393–3403.

(10) Ionescu, A.; Allouche, A.; Aycard, J.-P.; Rajzmann, M.; Hutschka, F. Study of γ-Alumina Surface Reactivity: Adsorption of Water and Hydrogen Sulfide on Octahedral Aluminum Sites. *J. Phys. Chem. B* **2002**, *106*, 9359–9366.

(11) Sohlberg, K; Pennycook, S. J.; Pantelides, S. T. The Bulk and Surface Structure of γ-Alumina. *Chem. Eng. Commun.* **2000**, *181*, 107–135.

(12) Knözinger, H.; Ratnasamy, P. Catalytic Aluminas: Surface Models and

Characterization of Surface Sites. *Catal. Rev.* **1978**, *17*, 31–70.

(13) Stapf, S.; Ren, X.; Talnishnikh, E.; Blümich, B. Spatial Distribution of Coke Residues in Porous Catalyst Pellets Analyzed by Field-Cycling Relaxometry and Parameter Imaging. *Magn. Reson. Imaging* **2005**, *23*, 383–386.

(14) D'Agostino, C.; Bräuer, P.; Charoen-Rajapark, P.; Crouch, M. D.; Gladden, L. F. Effect of Paramagnetic Species on T_1, T_2 and T_1/T_2 NMR Relaxation Times of Liquids in Porous $CuSO_4/Al_2O_3$. *RSC Adv.* **2017**, *7*, 36163–36167.

(15) Weber, D.; Mitchell, J.; McGregor, J.; Gladden, L. F. Comparing Strengths of Surface Interactions for Reactants and Solvents in Porous Catalysts Using Two-Dimensional NMR Relaxation Correlations. *J. Phys. Chem. C* **2009**, *113*, 6610–6615.

(16) Digne, M.; Sautet, P.; Raybaud, P.; Euzen, P.; Toulhoat, H. Hydroxyl Groups on γ-Alumina Surfaces: A DFT Study. *J. Catal.* **2002**, *211*, 1–5.

(17) D'Agostino, C.; Mitchell, J.; Gladden, L. F.; Mantle, M. D. Hydrogen Bonding Network Disruption in Mesoporous Catalyst Supports Probed by PFG-NMR Diffusometry and NMR Relaxometry. *J. Phys. Chem. C* **2012**, *116*, 8975–8982.

(18) Mitchell, J.; Chandrasekera, T. C.; Gladden, L. F. Obtaining True Transverse Relaxation Time Distributions in High-Field NMR Measurements of Saturated Porous Media: Removing the Influence of Internal Gradients. *J. Chem. Phys.* **2010**, *132*, 244705.

(19) Robertson, C. I. Characterising Adsorption and Mass Transfer in Porous Media (Doctoral Thesis)., 2018.

(20) Bloembergen, N.; Purcell, E. M.; Pound, R. V. Relaxation Effects in Nuclear in Nuclear Magnetic Resonance Absorption. *Phys. Rev.* **1948**, *73*, 679–712.

(21) Ayant, Y.; Belorizky, E.; Aluzon, J.; Gallice, J. Calcul Des Densités Spectrales Résultant D'un Mouvement Aléatoire de Translation En Relaxation Par Interaction Dipolaire Magnétique Dans Les Liquides. *J. Phys. Fr.* **1975**, *36*, 991–1004.

(22) Korb, J.-P. Multiscale Nuclear Magnetic Relaxation Dispersion of Complex

Liquids in Bulk and Confinement. *Prog. Nucl. Magn. Reson. Spectrosc.* **2018**, *104*, 12–55.

(23) Singer, P. M.; Asthagiri, D.; Chen, Z.; Valiya Parambathu, A.; Hirasaki, G. J.; Chapman, W. G. Role of Internal Motions and Molecular Geometry on the NMR Relaxation of Hydrocarbons. *J. Chem. Phys.* **2018**, *148*, 164507.

(24) Freed, D. E. Dependence on Chain Length of NMR Relaxation Times in Mixtures of Alkanes. *J. Chem. Phys.* **2007**, *126*, 174502.

(25) Lipari, G.; Szabo, A. Model-Free Approach to the Interpretation of Nuclear Magnetic Resonance Relaxation in Macromolecules. 1. Theory and Range of Validity. *J. Am. Chem. Soc.* **1982**, *104*, 4546–4559.

(26) Bormuth, A.; Hofmann, M.; Henritzi, P.; Vogel, M.; Rössler, E. A. Chain-Length Dependence of Polymer Dynamics: A Comparison of Results from Molecular Dynamics Simulations and Field-Cycling ^{1}H NMR. *Macromolecules* **2013**, *46*, 7805–7811.

(27) Singer, P. M.; Chen, Z.; Alemany, L. B.; Hirasaki, G. J.; Zhu, K.; Xie, Z. H.; Vo, T. D. Interpretation of NMR Relaxation in Bitumen and Organic Shale Using Polymer − Heptane Mixes. *energy Fuels* **2018**, *32*, 1534–1549.

(28) Robinson, N.; Robertson, C.; Gladden, L. F.; Jenkins, S. J.; D'Agostino, C. Direct Correlation between Adsorption Energetics and Nuclear Spin Relaxation in a Liquid-Saturated Catalyst Material. *ChemPhysChem* **2018**, *19*, 2472–2479.

(29) Hattori, H. Heterogeneous Basic Catalysis. *Chem. Rev.* **1995**, *95*, 537–558.

(30) Carrizosa, I.; Munuera, G. Study of the Interaction of Aliphatic Alcohols with TiO_2. *J. Catal.* **1977**, *49*, 174–188.

(31) Mudunkotuwa, I. A.; Minshid, A. Al; Grassian, V. H. ATR-FTIR Spectroscopy as a Tool to Probe Surface Adsorption on Nanoparticles at the Liquid–solid Interface in Environmentally and Biologically Relevant Media. *Analyst* **2014**, *139*, 870–881.

(32) Reichardt, C. *Solvents and Solvent Effects in Organic Chemistry*; Wiley-VCH Publishers, 2003.

(33) Djemai, A.; Balan, E.; Morin, G.; Labbe, J. C.; Pierre, J. Behaviour of Paramagnetic Iron during the Thermal Transformations of Kaolinite. *J. Am. Ceram. Soc* **2001**, *84*, 1017–1024.

(34) Hollewand, M. P.; Gladden, L. F. Transport Heterogeneity in Porous pellets—I. PGSE NMR Studies. *Chem. Eng. Sci.* **1995**, *50*, 309–326.

(35) Mitchell, J.; Chandrasekera, T. C.; Gladden, L. F. Numerical Estimation of Relaxation and Diffusion Distributions in Two Dimensions. *Prog. Nucl. Magn. Reson. Spectrosc.* **2012**, *62*, 34–50.

(36) Jancke, H.; Malz, F.; Haesselbarth, W. Structure Analytical Methods for Quantitative Reference Applications. *Accredit. Qual. Assur.* **2005**, *10*, 421–429.

(37) Washburn, K. E.; Eccles, C. D.; Callaghan, P. T. The Dependence on Magnetic Field Strength of Correlated Internal Gradient Relaxation Time Distributions in Heterogeneous Materials. *J. Magn. Reson.* **2008**, *194*, 33–40.

(38) Mitchell, J.; Chandrasekera, T. C.; Gladden, L. F. Measurement of the True Transverse Nuclear Magnetic Resonance Relaxation in the Presence of Field Gradients. *J. Chem. Phys.* **2013**, *139*, 74205.

(39) SDBSWeb: https://sdbs.db.aist.go.jp (National Institute of Advanced Industrial Science and Technology, 23rd October 2019).

(40) Campbell, C. T.; Sellers, J. R. V. Enthalpies and Entropies of Adsorption on Well-Defined Oxide Surfaces: Experimental Measurements. *Chem. Rev.* **2013**, *113*, 4106–4135.

(41) Berger, T. A. Separation of Polar Solutes by Packed Column Supercritical Fluid Chromatography. *J. Chromatogr. A* **1997**, *785*, 3–33.

(42) Lueangchaichaweng, W.; Singh, B.; Mandelli, D.; Carvalho, W. A.; Fiorilli, S.; Pescarmona, P. P. High Surface Area, Nanostructured Boehmite and Alumina Catalysts: Synthesis and Application in the Sustainable Epoxidation of Alkenes. *Appl. Catal. A Gen.* **2019**, *571*, 180–187.

(43) Chen, L.; Smith, R. S.; Kay, B. D.; Dohnálek, Z. Adsorption of Small Hydrocarbons on Rutile TiO_2(110). *Surf. Sci.* **2016**, *650*, 83–92.

(44) Natal-Santiago, M. A.; Dumesic, J. A. Microcalorimetric, FTIR, and DFT Studies of the Adsorption of Methanol, Ethanol, and 2,2,2-Trifluoroethanol on Silica. *J. Catal.* **1998**, *175*, 252–268.

(45) Mhanna, R.; Razzak, A.; Hamid, A.; Dutta, S.; Lefort, R.; Noirez, L.; Frick, B.; Morineau, D. More Room for Microphase Separation : An Extended Study on Binary Liquids Confined in SBA-15 Cylindrical Pores. *J. Chem. Educ.* **2017**, *146*, 24501.

(46) Stapf, S.; Kimmich, R.; Seitter, R. O.; Maklakov, A. I.; Skirda, V. D. Proton and Deuteron Field-Cycling NMR Relaxometry of Liquids Confined in Porous Glasses. *Phys. Rev. Lett.* **1996**, *115*, 107–114.

Chapter 5 : Fast field cycling of liquids imbibed within γ-alumina

The work contained within this chapter forms part of the publication: Ward-Williams, J.; Korb, J.-P.; Gladden, L. F. Insights into Functionality-Specific Adsorption Dynamics and Stable Reaction Intermediates Using Fast Field Cycling NMR. *J. Phys. Chem. C* **2018**, *122*, 20271–20278.

Contents

5.1 Introduction

In instances where the relaxation behaviour of a system is not simple or well-defined the application of standard fixed field relaxation measurements can result in a misinterpretation of the physical chemistry that occurs, as was discussed in chapter 4. In these instances the available relaxation information is limited to only a single frequency, and therefore probes motion over a narrow range of relatively fast molecular dynamics. To increase the amount of available information fast field cycling (FFC)-NMR techniques can be used to measure the T_1 relaxation time constants as a function of the applied magnetic field strength.[1] This allows the measurement of T_1 over several orders of magnitude, and probes relaxation on the nanosecond to microsecond timescale. Rapidly occurring processes, such as bulk motions of small molecules, do not contribute to the change in relaxation rate[2] and instead any changes in relaxation behaviour are ascribed to slower surface diffusive processes.[1,3,4] The dominance of these relaxation processes at low fields means that, to a good approximation, molecule specific or competing relaxation mechanisms are insignificant, and the interpretation of the data can be made less ambiguous.

In this chapter the use of FFC-NMR is explored to characterise the relative interaction strengths of a range of organic liquids and water imbibed within a γ-alumina system of catalytic interest. By considering the effects of the physical properties of each adsorbate on the relaxation behaviour, the principal source of relaxation is identified for both bulk liquids and liquids imbibed within γ-alumina. This procedure allows a decoupling of the adsorption strength from other physical properties that influence the relaxation behaviour. Therefore FFC-NMR measurements allow a more robust quantitative ranking of the interaction strength of the adsorbates studied within this chapter.

5.2 Background and literature review

In this section the FFC-NMR technique is introduced and the theoretical framework used to analyse FFC-NMR experiments is discussed. A literature review is then presented to show the existing applications of FFC-NMR experiments to porous media systems.

5.2.1 The FFC-NMR technique

The FFC-NMR technique differs from conventional fixed field NMR approaches as the magnetic field, B_0, is varied during the course of an FFC-NMR experiment. This allows relaxation data to be obtained at a range of different magnetic field strengths from ~1 T to ~0.25 mT. For lower field strengths a prepolarized sequence is used to ensure a sufficiently high signal-to-noise ratio is achieved, and for higher field strengths a non-polarized sequence is used to ensure sufficient resolution of the magnetization decay. A typical prepolarized FFC-NMR experiment consists of three steps; polarisation, relaxation, and detection. During each of these steps a different magnetic field strength is applied to the sample. During the polarisation step a field, B_{pol}, is applied for a sufficient period (~5 T_1) to allow the sample to reach equilibrium magnetisation. The field is then rapidly switched to a relaxation field, B_{rel}, and the magnetisation is allowed to develop for a period, τ. Finally the field is switched to a detection field, B_{det}, and any remaining magnetisation is transferred into the transverse plane for detection using a π/2 pulse (Figure 5.1). Repeating the experiments for a range of τ values allows the extraction of the longitudinal relaxation rate constant, $R_1(B_{rel}) = 1/T_1(B_{rel})$, that depends only on the strength of the relaxation field. The experiment is then repeated for a series of different relaxation fields in order to construct a nuclear magnetic relaxation dispersion (NMRD) profile.

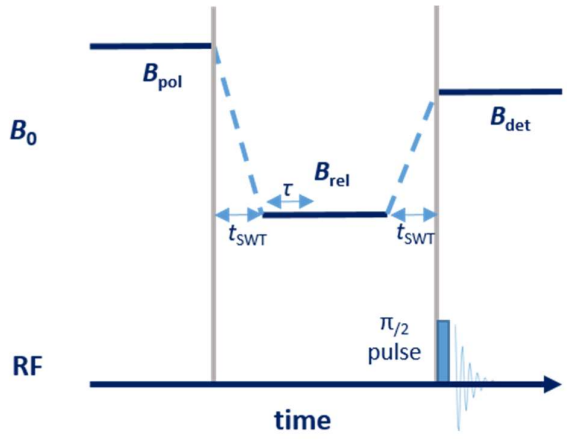

Figure 5.1: A schematic of the prepolarized FFC-NMR experiment. Magnetic fields used for polarization, B_{pol}, relaxation, B_{rel}, detection, B_{det}, and relaxation delays, τ, are optimized for each experiment. Switching times, t_{SWT}, are set to a few ms to avoid signal loss during the switching intervals. Reproduced from Ward-Williams et al.[5]

The magnetisation, M_z, of a spin system returning to its equilibrium value, M_{eq}, can be described by a first-order differential equation. The Bloch equation describing this process can be written as:

$$\frac{dM_z}{d\tau} = -R_1\left(M_z - M_{eq}\right). \tag{5.1}$$

In the case of a fast field cycling experiment with instantaneous switching times the solution to this differential equation is given by:[6]

$$M_z(\tau) = M_0(B_{rel}) + \left[M_0\left(B_{pol}\right) - M_0(B_{rel})\right]\exp\{-\tau/T_1(B_{rel})\}. \tag{5.2}$$

This means that high polarisation fields can be used to greatly increase the signal-to-noise ratio (SNR) when measuring the relaxation rates at Larmor frequencies several orders of magnitude lower than conventional spectrometer frequencies. In reality, hardware limitations impose a finite switching time for field cycling experiments of a few milliseconds when changing between magnetic fields. This leads to an irrecoverable loss of signal during the switching intervals, which reduces the sensitivity of the experiment, but does not affect the accuracy of the T_1 measurement.[1,7] Instead, the effects of the switching interval can be incorporated into the constant terms in eq. (5.2) to give the magnetisation of a true FFC-NMR experiment as:

$$M_z(\tau) = M_z^{\infty} + \Delta M_z^{eff}\exp\{-\tau/T_1(B_{rel})\}, \tag{5.3}$$

where M_z^{∞} is the effective long-time observed magnetisation and ΔM_z^{eff} is the difference between the initial magnetisation and the long-time magnetisation. Experimentally these values can be estimated as the first and last points of the relaxation curve, provided that suitable delay times are chosen for the experiment. In the case of a sample which contains multiple relaxation environments the linearity of eq. (5.1) in terms of $M_z(\tau)$ means that each relaxation component can be treated independently with a monoexponential procedure as outlined above. According to eq. (5.3) this approach will result in an accurate measurement of the relaxation rate of each component, but signal losses due to the finite switching times may lead to errors in the relative populations. This effect is likely to be most significant for species which have relaxation time constants that approach the experimental switching time.

For high field relaxation experiments prepolarization would lead to a small dynamic range of signal decay according to eq. (5.2). To circumvent this issue the sequence is modified by setting B_{pol} to zero and the magnetisation build-up during the relaxation interval is monitored in the non-polarized sequence.

5.2.2 Interpretation of FFC-NMR data

The ability of FFC-NMR to probe the relaxation behaviour at a range of magnetic field strengths means that it is sensitive to molecular motions occurring over a wide range of timescales. Relaxation is most efficient when:

$$\omega_0 \tau_c = 1, \tag{5.4}$$

where $\omega_0 = \gamma_H B_0$ is the Larmor frequency of the ^{1}H protons and τ_c is the correlation time of the molecular motions. This allows the FFC-NMR technique to probe relaxation processes corresponding to molecular motions up to tens of μs. In this section the FFC-NMR interpretation of fast and slow dynamical processes are discussed for bulk liquids and adsorbed liquids respectively.

5.2.2.1 Bulk liquids

The relaxation behaviour of bulk liquids is governed by bulk rotational and translational processes. These molecular motions are very fast, with correlation times on the ps timescale.[8] As a result, there is no change in the relaxation rate with respect to frequency, known as dispersion, observed for bulk liquids below approximately 10 MHz.[9] The exception to this is very viscous fluids.[10] For bulk liquids containing dissolved oxygen, which is a paramagnetic relaxation source, a high field relaxation feature has previously been observed.[2] This is caused by a dipolar interaction between the paramagnetic moment of molecular oxygen and the ^{1}H spins of the bulk liquid. The molecular motions of the sample will also contribute to the relaxation behaviour, but the paramagnetic relaxation is much more effective than diamagnetic relaxation ($\omega_S = 658\omega_I$). As a result, the relaxation behaviour of bulk liquids can be expressed as a single Lorentzian curve following the theory outlined previously:[2]

$$R_{1,\mathrm{obs}}(\omega) = A\left[\frac{\tau}{1 + (\omega_S \tau)^2}\right] + B\,, \tag{5.5}$$

where A and B are constants, τ is an effective correlation time combining the electron spin-lattice relaxation time and the translational diffusion of the liquid, and ω_S is the electron Larmor frequency.

5.2.2.2 Adsorbed liquids

For liquids imbibed within porous media the molecular motions controlling the relaxation behaviour are far slower than they are in bulk, with surface diffusional processes used to justify such slow motion.[1,4,11] This results in dispersion behaviour being observed down to very low Larmor frequencies. A separation of all of the factors contributing to the relaxation behaviour is complex, and requires an array of detailed experiments as well as a characterisation of the porous medium. This will be further pursued in Chapter 7 along with a discussion of the underlying relaxation mechanisms. For the analysis presented within this chapter the relaxation behaviour can be described by a phenomenological power law model of the form:

$$R_{1,S}(\omega) = \alpha\omega^{-\beta}\,, \tag{5.6}$$

where α is a scaling factor dependent on both the properties of the adsorbate and the porous medium, and β is a power law exponent that depends strongly on the molecular motions of the adsorbate. Power law relationships of this nature are well-documented[1,12,13] and serve as a valuable tool for the initial comparison of experimental data. Naturally the validity of this approach requires greater consideration when comparing liquids imbibed within a range of different porous materials, as the properties of the porous medium itself may contribute to the value of β as well as the value of α. Within this work the issue is avoided by keeping the porous surface constant across all samples.

The contribution of the bulk relaxation rate can also be included through the use of the two phase fast exchange model (eq. (2.19)). However, for relaxation profiles which show even modest dispersions, the surface relaxation rates is far in excess of the bulk relaxation rate ($p\,R_{1,S} >> (1\text{-}p)\,R_{1,B}$), meaning that the NMRD profiles can be well represented by eq. (5.6).

5.2.3 Applications of FFC-NMR to porous media systems

Fast field cycling instruments have only been commercially available for the last 20 years[14] and as a result of this only a few catalytic systems have thus far been studied using FFC-NMR. These include the role of coke on the relaxation behaviour of water, DMSO and heptane imbibed within Al_2O_3 and $PtRe/Al_2O_3$,[15] water on titania polymorphs,[16] and water on highly structured silica surfaces.[17] In the first of these examples the relative differences in the phenomenological power laws of three different liquids imbibed within a porous alumina were demonstrated. Very different behaviour was observed for each liquid, but only a few liquids were studied. This meant that it was only possible to clarify the adsorption as strong or weak, and it was not obvious if FFC-NMR could be used to rank surface-adsorbate interactions further within each classification. For water imbibed within titania polymorphs the temperature dependent relaxation behaviour was used to show that water wetted an anatase surface, but not a rutile surface.[16] The distinction between wetting and non-wetting interactions was a binary classification analogous to the strong and weak adsorption limits that were shown for alumina.[15] The third study investigated water on silica surfaces and applied a formal modelling approach in order to extract surface correlation times, which could in turn be used to show that the binding of water reduced its effective diffusion coefficient by two orders of magnitude.[17] In order to do so the authors assumed an intramolecular relaxation mechanism that was decomposed into two features, a 2D surface diffusion term that dominated at high field strengths, and an intermittent binding mechanism that dominated at low field strengths. Previously the Gladden group has also investigated the intermolecular relaxation of liquids imbibed within catalytically relevant materials and found similar two-component behaviour for water. The relative interaction strengths of butanone, 2-propanol and water on a Pd/Al_2O_3 catalyst were also inferred from an ordering of their respective surface correlation times, and this ordering was compared to the use of conventional fixed field measurements of T_1/T_2 as a probe of surface interaction strength.[18] Collectively, all of these results show that FFC-NMR can be used to monitor solid-liquid interaction strengths, but they do not demonstrate the degree of resolution it is possible to obtain within the strong and weak adsorption limits.

In a more general sense, FFC-NMR has also been applied successfully to study surface interactions in a range of porous media including silica glasses,[19–21] cement pastes,[22,23] rock cores,[3,24,25] and granular packings.[5,26] Often in the case of naturally occurring

materials, such as rock cores or the components of cement, there is a significant presence of paramagnetic impurities, which act as an effective source of intermolecular relaxation. In these cases relaxation can be well described by literature models, and surface correlation times can easily be accessed.[3,22–25] Because of the efficacy of paramagnetic relaxation only a small number of spin active impurities are required to dominate the observed relaxation behaviour, with as few as 36 ppm of Fe^{3+} impurities being argued to dominate the relaxation of polar liquids imbibed within silica.[20] In contrast, in man-made samples the degree of paramagnetic impurities is often much lower than the limit of detection. In these cases intramolecular pathways can dominate the observed NMRD profiles. Zavada and Kimmich demonstrated that for DMSO imbibed within a porous glass the undeuterated and partially deuterated NMRD profiles were identical, and that no paramagnetic impurities were present in the ESR.[27] The relaxation behaviour could be well described by an intramolecular process for many adsorbates. Catalytic material and oxide supports represent an interesting middle ground as they are highly refined materials with low level paramagnetic impurities, which would favour an intramolecular relaxation pathway. However, the large scale synthesis and shaping of catalysts, as well as loading of metal salts, will introduce paramagnetic impurities. This means that both inter and intramolecular relaxation mechanisms are important for catalytic materials, and it is not possible to define the strongest contribution *a priori*.

5.3 Materials and methods

5.3.1 Materials

The porous medium used was *γ*-alumina (BASF, catalogue number 43855) with a pore volume of 0.65 g ml^{-1}. Nitrogen BET/BJH measurements gave a surface area of 206 m^2 g^{-1} and a monomodal pore size distribution centred about a pore diameter of 9 nm (see appendix 1). Electron spin resonance (ESR) measurements were performed on a Bruker E500 X-band spectrometer with an ER 4122SHQE cavity at a microwave frequency of 9.385 GHz. Two features were observed for γ-alumina, a sharp paramagnetic resonance at 1600 G (6 ppm) ascribed to Fe^{3+} and a small broad feature centred about 3400 G which has previously been ascribed to superparamagnetic Fe^{3+} clusters within the framework[28] (see appendix 1). Deionised water was produced in-

house using a Elga Purelab DV25 purification system. Cyclohexane, *n*-heptane, toluene, DMSO, THF, acetone and methanol (>99% purity) were obtained from Sigma Aldrich. All deuterated variants of all compounds were obtained from Fluorochem at a purity of >98%.

Samples were prepared by drying the alumina for 12 h at 120 °C to drive off physisorbed water, and then soaking the alumina for a further 12 h in the desired liquid. The sample was then poured onto filter paper and the extra pellet liquid was removed shortly prior to analysis, resulting in a sample as shown in Figure 5.2. Full saturation of the pore space with the liquid during the imbibition process was confirmed by gravimetric measurement of the pellets before and after liquid imbibition.[29] For degassed samples, three freeze-pump-thaw cycles were performed before flame sealing to minimise the oxygen content.

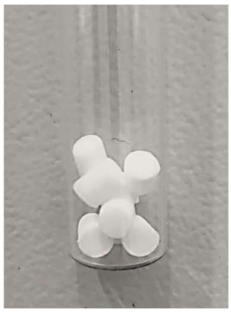

Figure 5.2: A typical sample of liquid imbibed within γ-alumina pellets. The pellets were cylindrical extrudates with a diameter of 3 mm and ranged in length from 5-10 mm. The sample was measured in a 10 mm NMR tube as shown.

Physical properties of each adsorbate were taken from a single source where possible in order to ensure that these parameters were comparable. The molecular diameter of each species was taken from previous FFC-NMR studies where possible, or otherwise calculated as the diameter of the sphere which had the same volume as the smallest ellipsoid required to encapsulate the molecule.

5.3.2 FFC-NMR methods

FFC-NMR experiments were performed on a Stelar Spinmaster Duo relaxometer. For each NMRD profile between 10 and 30 ^{1}H Larmor frequencies were analysed, logarithmically spaced between 10 kHz and 40 MHz. A pre-polarized sequence was used for field strengths below 10 MHz and a non-polarized sequence was used for measurements above 10 MHz. For each T_1 experiment 32 delay times were used with

relaxation delays that were logarithmically spaced between 1 ms and 6 x T_1. A detection frequency of 16.3 MHz was used for all experiments. Following the definitions outlined in eq. (5.3), M_z^0 was estimated as the observed magnetisation after 1 ms of relaxation delay and M_z^∞ was taken as the average of the magnitude measured after the longest two relaxation delays. In all cases only a single scan was required to achieve a good SNR unless otherwise specified. The raw FFC-NMR data were renormalized such that the signal in each dataset decayed from 1 to 0.[1] Unless otherwise stated the T_1 distribution at each field strength was obtained via an Inverse Laplace transformation using Tikhonov regularization.[30] The relaxation rate, $\langle R_1 \rangle = \langle 1/T_1 \rangle$, was calculated by taking the logarithmic average of the T_1 distribution at each field strength,[31]

$$\langle R_1 \rangle = \exp\left[-\sum_{i=1}^{n} f_i \ln\left(T_{1,i}\right)\right], \tag{5.7}$$

where f_i is the i^{th} value of the discretized T_1 distribution at a given field strength. The relative intensity of each peak could also be extracted directly from the regularised data. The results of the inverse Laplace transformations were validated against a mono or multiexponential function using NNLS regression. The difference in relaxation rates between 10 kHz and 10 MHz is defined as the total observable dispersion, TOD, for comparison purposes.

5.3.3 High field NMR methods

T_1 relaxation measurements at 400 MHz were performed using a Bruker AV400 superconducting magnet equipped with a Diff30 probe and a 5 mm ^{1}H coil. An inversion recovery sequence was used with 16 logarithmically spaced delay times between 1 ms and 25 s in order to estimate T_1 at high field strengths. For T_1 measurement at fixed field strengths an Oxford instruments 2 MHz, Xigo Nanotools 13 MHz and a Magritek 23 MHz spectrometer were used. For each experiment 32 logarithmically spaced delay times were used between 1 ms and 10 x T_1. Even in cases where spectroscopic resolution was possible the relaxation time constant was measured by integrating over all peaks in order to maintain consistency with the FFC-NMR experiments.

5.4 Results

5.4.1 Bulk liquid relaxation

Figure 5.3 shows the logarithmic average NMRD profiles, obtained for *n*-heptane, cyclohexane, toluene, THF, acetone, DMSO, methanol and water in their bulk liquid state. All 8 liquids showed the same general features in their dispersion profiles, where $\langle R_1 \rangle$ initially increased as the ^{1}H Larmor frequency was decreased, before reaching a plateau at 10 MHz. The position of the inflection point was almost identical for all liquids, despite the molecules being significantly different in terms of their physical properties, intermolecular interactions, and dissolved oxygen content. The size of the dispersion was small in all cases, with the largest dispersion measured by FFC-NMR being 0.12 s^{-1} for cyclohexane and n-heptane. The data were fitted using eq. (5.5) and the fitting parameters are listed in Table 5.1.

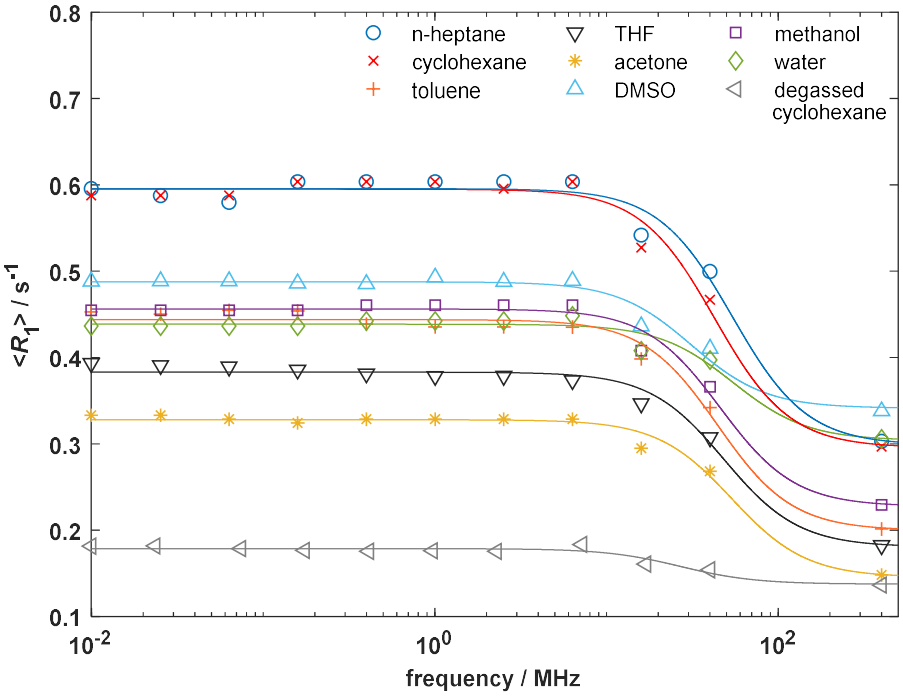

Figure 5.3: The NMRD profiles of the eight different liquids studied in their bulk state and cyclohexane after degassing. Solid lines represent the best fits of each dataset using eq. (5.5).

The shape of the NMRD profile suggested that a high frequency plateau of the relaxation behaviour had not been reached by 40 MHz. This resulted in a poorly defined model fit and unreliable estimates of the correlation times. To allow a better estimate of the bulk liquid correlation times, additional data were acquired on a 400 MHz spectrometer to capture the high field molecular dynamics. At these high field strengths the relaxation behaviour of all liquids approached a plateau, which allowed a more robust model fitting.

Table 5.1: The model parameter used to fit the data shown in Figure 5.3. Data were fit using eq. (5.5) and errors represent a 95% confidence interval in the fitting parameter.

Adsorbate	A / 10^{10} s^{-2}	τ / ps	B / s^{-1}
n-heptane	6.7 ± 3.0	4.5 ± 1.5	0.30 ± 0.05
cyclohexane	5.3 ± 1.6	5.7 ± 1.6	0.30 ± 0.04
Toluene	4.5 ± 2.0	5.5 ± 1.9	0.20 ± 0.04
THF	4.1 ± 1.1	5.0 ± 1.1	0.18 ± 0.02
acetone	4.0 ± 1.1	4.5 ± 1.0	0.15 ± 0.02
DMSO	1.9 ± 0.8	7.7 ± 2.5	0.34 ± 0.02
methanol	4.3 ± 1.2	5.3 ± 1.1	0.23 ± 0.02
water	3.0 ± 1.3	4.4 ± 1.6	0.30 ± 0.02
cyclohexane (degassed)	0.4 ± 0.25	9.0 ± 4.5	0.14 ± 0.01

Paramagnetic relaxation due to interactions between the ^{1}H spins and molecular oxygen dissolved within the bulk liquid have previously been cited as the origin of the frequency dispersion seen above 10 MHz.[2] To confirm this hypothesis in this study a sample of cyclohexane was degassed and a repeat measurement was performed. This resulted in a decrease of an order of magnitude in the size of the dispersion of cyclohexane, despite there having been no change in the molecular dynamics. This shifted the NMRD profile of cyclohexane from showing the largest dispersion to the smallest dispersion, and a lower absolute value of $<R_1>$. The degassed cyclohexane data is also shown in Figure 5.3.

5.4.2 Liquids imbibed within γ-alumina

Figure 5.4 shows the logarithmic average NMRD profiles for the eight liquids imbibed within γ-alumina as a function of the ^{1}H Larmor frequency. For methanol and acetone imbibed within γ-alumina two relaxation environments were observed in the T_1 distributions at each field strength. The presence of an additional component will be

explored in further detail in chapter 6, and in this chapter the logarithmic average relaxation rate, $\langle R_1 \rangle$, is reported.

For bulk liquids no change in $\langle R_1 \rangle$ was observed for any species below a ^{1}H Larmor frequency of 10 MHz, therefore the rate of change of $\langle R_1 \rangle$ below 10 MHz was expected to correlate with the interaction strength between the adsorbate and the surface for liquids imbibed within γ-alumina. All eight of the NMRD profiles showed similar trends in their relaxation behaviour, with the relaxation rate increasing steadily as the ^{1}H Larmor frequency decreased. This could be described well by a single power law that showed no evidence of reaching a plateau even at the lowest fields studied. Whilst the shape of the dispersion curves were similar, the magnitude of the dispersion were very different. Non-polar species, such as alkanes, showed a maximum relaxation rate between 1-3 s^{-1}, whereas polar species, such as methanol and water, showed relaxation rates of 100-300 s^{-1}. In the bulk state the difference between the polar and non-polar species was <0.15 s^{-1}, therefore the large differences that were observed for polar and non-polar adsorption can be used to justify strong and weak adsorption limits. For the weakly interacting species the discontinuity in $\langle R_1 \rangle$ behaviour above 10 MHz was clear, but this was less apparent for the strongly interacting species.

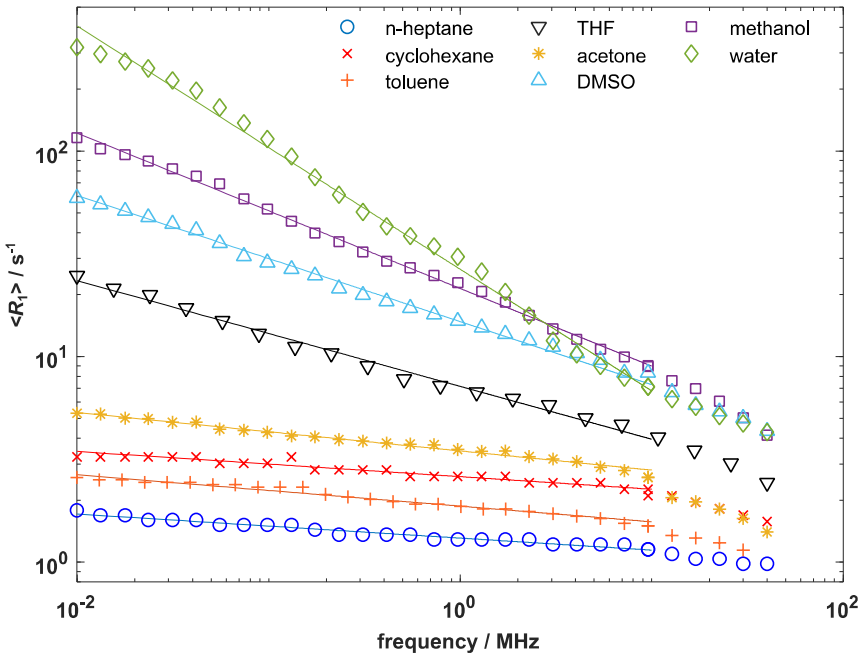

Figure 5.4: The NMRD profiles of *n*-heptane, cyclohexane, toluene, THF, acetone, DMSO, methanol and water imbibed within porous γ-alumina pellets. Solid lines represent the best fits of each dataset with eq. (5.6).

The data in Figure 5.4 were fitted with eq. (5.6) and the fitting parameters used to model each imbibed liquid are listed in Table 5.2. The total observable relaxation dispersion, defined as the difference in $<R_1>$ measured at 10 kHz and 10 MHz, is also reported. In almost all cases the dispersion profiles were well separated from one another, and the larger power law exponents were associated with greater absolute magnitudes of $<R_1>$. The exceptions to these trends were toluene (which had a greater power law exponent than cyclohexane but lower absolute values of $<R_1>$) and water (which crossed over with the methanol profile at a ^{1}H Larmor frequency value of approximately 2.5 MHz). There was also some evidence for the water relaxation behaviour reaching a plateau at low field strengths, and showing a small increase in $<R_1>$ at a frequency of approximately 0.2 MHz, though these features do not alter the underlying power law exponent significantly.

Table 5.2: The total observable dispersion (TOD) and power law exponent of the model shown in eq. (5.6) for each of the adsorbates imbibed within γ-alumina. The quoted error represents a 95% confidence interval for the parameter β from the model fitting procedure.

Adsorbate	**TOD / s^{-1}**	**α / s^{-1}**	**β**
water	310	$(2.8 \pm 0.8) \times 10^5$	0.592 ± 0.020
methanol	100	$(7.9 \pm 1.00) \times 10^4$	0.378 ± 0.008
DMSO	55	$(1.8 \pm 0.20) \times 10^3$	0.307 ± 0.008
acetone	2.1	15.0 ± 1.0	0.093 ± 0.005
THF	23	$(4.0 \pm 0.8) \times 10^2$	0.257 ± 0.012
toluene	1.1	6.2 ± 0.5	0.076 ± 0.004
cyclohexane	1.0	6.8 ± 0.4	0.061 ± 0.004
n-heptane	0.6	3.3 ± 0.1	0.058 ± 0.003

Qualitatively both metrics show a clear and consistent ordering, implying that the interaction can be ranked as water > methanol > DMSO > THF > acetone > toluene > cyclohexane ≈ n-heptane.

A series of fixed field measurements of a strongly (water) and a weakly (cyclohexane) interacting liquid imbibed within γ-alumina were performed to confirm that the relaxation behaviour obtained from the FFC-NMR study of the liquids imbibed in γ-alumina were consistent with fixed field experiments. These data are shown in Figure 5.5. Both water and cyclohexane imbibed within γ-alumina showed a good agreement between the two measurement techniques, with an average difference of <10%, and a maximum difference of 25% for cyclohexane imbibed within γ-alumina measured at

13 MHz. FFC-NMR measurements of water showed a slight overestimate, and cyclohexane showed a slight underestimate in terms of the relaxation rate relative to the fixed field instruments. These differences, however, were small and could be accounted for in terms of the different pulse sequences, sample sizes, magnet temperatures and spectrometers that were used. Considering all of these factors, the agreement between fixed and variable field relaxation measurements was good, and hence the FFC-NMR data were considered reliable.

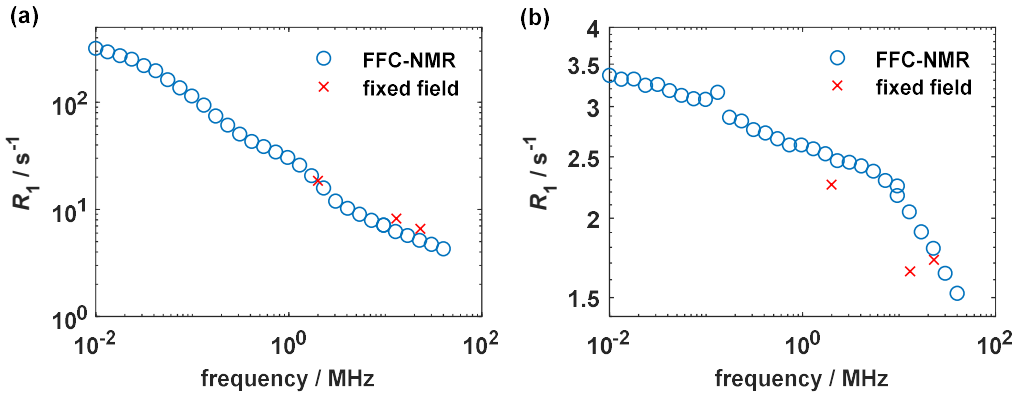

Figure 5.5: A comparison between the FFC-NMR experiments and a conventional fixed field R_1 measurement for a) water and b) cyclohexane imbibed within γ-alumina.

For the FFC-NMR experiments the monoexponential fitting error associated with the T_1 measurements at each field strength were <1% for all adsorbates that exhibited single component relaxation behaviour. This was, however, not the only source of experimental error that needed consideration when comparing across samples. The sample-to-sample variation has been shown to dominate the measurement error in chapter 4. To test the largest source of error in the FFC-NMR measurements three repeat experiments were performed with fresh samples for each of water, methanol and cyclohexane imbibed within γ-alumina, the results of which are shown in Figure 5.6. In each case the repeat experiments overlapped well with one another, suggesting a good degree of sample reproducibility. For cyclohexane, where the total observable dispersion is small, the percentage difference between the largest and smallest recorded values at a given field strength was approximately 10%, with higher deviations (up to 18%) observed at higher field strengths. A similar trend was observed for methanol and water, with greater deviations at high field strengths, and low field deviations of 12% and 6% respectively.

As the TOD was much greater for methanol and water imbibed within γ-alumina the repeat experiments on these systems visually appeared to coincide more closely than the cyclohexane repeats, despite all three imbibed liquids showing errors of the same order of magnitude. Based on these results an intrinsic sample-to-sample variation of approximately 10% can be assumed for FFC-NMR measurements, which far exceeds the measurement error. The inclusion of sample to sample variation had no effect on the ordering of the strongly interacting species proposed earlier, as all power law exponents and TOD were well resolved. The weakly interacting species (toluene, cyclohexane and *n*-heptane) were much closer in terms of relaxation behaviour and the experimental error made it difficult to differentiate between them.

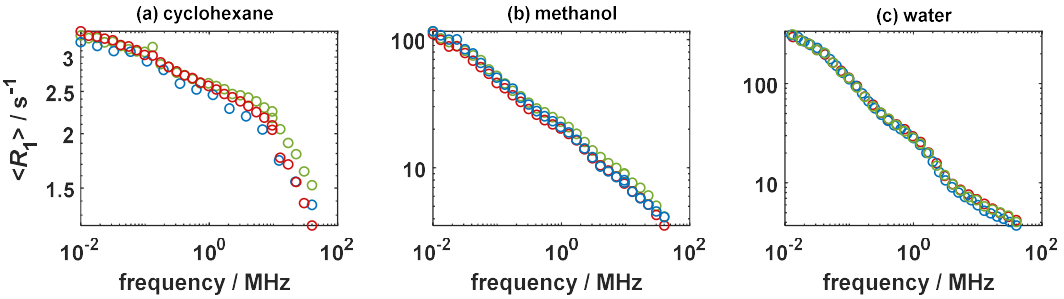

Figure 5.6: Repeat experiments showing the NMRD profiles of a) cyclohexane, b) methanol and c) water imbibed within three different samples of γ-alumina.

5.5 Discussion

A wide range of liquids in their bulk state, and imbibed within γ-alumina, have been studied using FFC-NMR. The relaxation behaviour of each liquid will now be discussed in terms of the most dominant contributions to the relaxation behaviour.

5.5.1 Contributions to bulk liquid relaxation behaviour

The absolute magnitude of the apparent correlation times reported in Table 5.1 are consistent within error to those obtained in a previous FFC-NMR study of bulk liquid relaxation.[2] From the values in Table 5.1 it was clear that the values of the correlation time, τ, did not vary significantly across all of the adsorbates that were studied, regardless of their physical properties. The insensitivity of τ to the physical properties of the system suggested that observed value of τ was not dominated by molecular motions causing fluctuations in the dipolar interaction. Instead the relaxation must have been principally

caused by a process that would be universal across all solvents. In the case of bulk liquids this behaviour has previously been attributed to the rapid electron spin-lattice relaxation of molecular oxygen, $T_{1,e}$.[2] If this effect were the only contribution to the observed relaxation rate then the NMRD profiles of all liquids would be identical. Such behaviour was not observed, and therefore this suggested that there was some degree of molecular motion information encoded into the observed relaxation behaviour. The effective correlation time, τ, can be considered as the reciprocal sum of the electronic relaxation time and the correlation time describing molecular rotation, τ_{Rot}:

$$\frac{1}{\tau} = \frac{1}{T_{1,e}} + \frac{1}{\tau_{\mathrm{Rot}}}. \tag{5.8}$$

The non-negligible contribution to the relaxation behaviour provided by the molecular motions was corroborated by the largest values of τ being measured for the most viscous liquids, DMSO and cyclohexane. In these viscous liquids the barrier to rotational motion is expected to be larger than in low viscosity liquids, resulting in a larger value of τ_{Rot}. A more detailed analysis of the correlation times of each liquid is not applicable here due the relatively large errors associated with the estimation of τ. More detailed experiments to reduce the magnitude of the error were not pursued, as the long relaxation delays associated with bulk liquid samples are experimentally taxing for FFC-NMR methods. The long polarization times that are required cause significant Joule heating of the magnet and associated electronics. For very slow relaxing samples shuttling techniques can be used to avoid excess heating.[2,32] However, the experiments presented in Figure 5.3 were sufficient to show that there was little difference in the value of τ obtained for all eight bulk liquids.

Table 5.1 showed that the prefactor, A, was a far greater discriminator between the bulk liquid relaxation behaviour. This was expected to correlate with oxygen solubility, which is inversely correlated to polarity.[33] The least polar bulk liquids, heptane and cyclohexane, had larger A values than the most polar species, methanol and water. This result was consistent with the expected order of oxygen solubility. The differences between A values were of similar size to the estimated uncertainties in each parameter, however strong evidence that this correlation was valid was obtained by degassing a sample of cyclohexane, which reduced the A value from 5.3 x 10^{10} s^{-2} to 0.4 x 10^{10} s^{-2}. The degassing procedure reduced the A value of cyclohexane by over an order of

magnitude and resulted in the lowest recorded A value of all adsorbates. As the molecular motions of the degassed sample were unchanged relative to the air equilibrated sample, the reduction in the A value was directly linked to the dissolved oxygen content.

The results presented in section 5.4.1 were consistent with the small dispersions seen for bulk liquids in Figure 5.3 being dominated by the effects of dissolved oxygen rather than any molecule specific relaxation processes. No change in the relaxation rate was observed below 10 MHz for any sample, therefore it follows that any differences in the NMRD profiles for liquids imbibed within porous media below 10 MHz can be unambiguously associated with the interaction of the adsorbate with the surface, even in the presence of dissolved oxygen.

5.5.2 Contributions to adsorbed liquid relaxation behaviour

The imbibed liquid data in Figure 5.4 showed a clear ordering of the relaxation behaviour, which suggested that the ordering of interaction strength was given as: water > methanol > DMSO > THF > acetone > toluene > cyclohexane ≈ *n*-heptane. However, the largest dispersion or largest relaxation rate may not imply the strongest interaction. The relaxation behaviour of a liquid imbibed within a porous medium has been shown to depend on the properties of the porous medium,[17] viscosity of the adsorbate,[34] the number of molecules in the adsorbed and bulk phases (in turn related to the molar volume and molecular size),[9] the intrinsic dipolar interaction, as well as the interactions between the adsorbate and surface.[35] The relaxation behaviour becomes a complex function of these parameters, any of which may dominate the observed relaxation trends. In this section each of these effects will be considered individually, and their implications on the relaxation behaviour of different adsorbates will be commented on. The relevant physical properties for each liquid are listed in Table 5.3. An estimate of the interaction strength between the adsorbate and the surface is not facile to obtain, therefore this property is assumed to trend with polarity given the highly polar nature of the alumina surface. The polarity of each adsorbate is given as the Reichardt polarity index relative to the polarity of water.[36]

Table 5.3: The key physical properties of the eight different liquids studied that are likely to contribute to the relaxation behaviour of the system.

adsorbate	*d* / Å[37]	viscosity / cP[38]	Molar volume / cm^3 mol^{-1}	relative polarity[36]
water	3.3	0.89	18	1.00
methanol	3.6[39]	0.60	41	0.76
DMSO	7.1	2.00	71	0.44
acetone	5.2	0.33	74	0.36
THF	6.3	0.55	82	0.21
toluene	6.0	0.59	107	0.10
cyclohexane	6.2	0.98	109	0.01
n-heptane	5.9	0.41	147	0.01

5.5.2.1 Surface variation effects

The comparison of different liquids imbibed within a single support greatly simplifies the interpretation of the NMRD profiles as the solid surface can be taken as constant for each experiment. This removes the effects of the geometry or differences in surface chemistry that may occur when comparing liquids imbibed in different porous media. The experiments presented within this thesis were performed on a single batch of γ-alumina to avoid batch-to-batch variation in surface chemistry and physical properties. This assumption of a constant surface chemistry was validated by repeat measurements on different samples with the same adsorbate showing an error in $<R_1>$ of approximately 10%, as is shown in Figure 5.6. This level of deviation was far lower than the differences between samples imbibed with different liquids, which confirmed that surface variations were not dominating the observed trends in relaxation behaviour.

5.5.2.2 Viscosity effects

There was no clear correlation between the viscosity of the adsorbate and the power law exponents of each liquid imbibed within γ-alumina, given in Table 5.3. DMSO and cyclohexane (the most viscous liquids) showed power law exponents of 0.31 and 0.06 respectively. Acetone and *n*-heptane (the least viscous liquids) also showed power law exponents of 0.09 and 0.06 respectively. A correlation between the solvent viscosity and the T_1 relaxation rate is well-known to occur for light oils and heavy crude oils below a critical value of viscosity, η_c,[9,34] which is often orders of magnitude larger than the viscosities of the solvent molecules used herein. Below this critical value molecular motions are sufficiently fast that the dipolar coupling between neighbouring spins is fully

averaged, hence the system is in the extreme narrowing limit ($T_1 \approx T_2 \propto \sqrt{\eta}$). The data shown in Table 5.1 and Table 5.3 suggest that this limit was not achieved in the current experiments. Instead, the molecular dynamics were dominated by the confinement of each species rather than their bulk viscosities, leading to a more complicated modulation of the dipolar coupling – as was previously observed for the crude oils in the presence of asphaltenes.[34] From the above discussion it follows that the viscosity of the adsorbate does not dominate the relaxation behaviour in the experiments shown in Figure 5.4.

5.5.2.3 Molecular size and molar volume effects

The influence of the molecular size and molar volume on the relaxation rates can be conceptualised in terms of the two-phase fast exchange model introduced in section 2.4.1 and reproduced in Figure 5.7. The surface layer consists of a finite volume beyond which relaxation effects are negligible. This is often assumed to be a single molecular thickness, but can be up to a 3 layers for small and highly structured adsorbates such as water.[40]

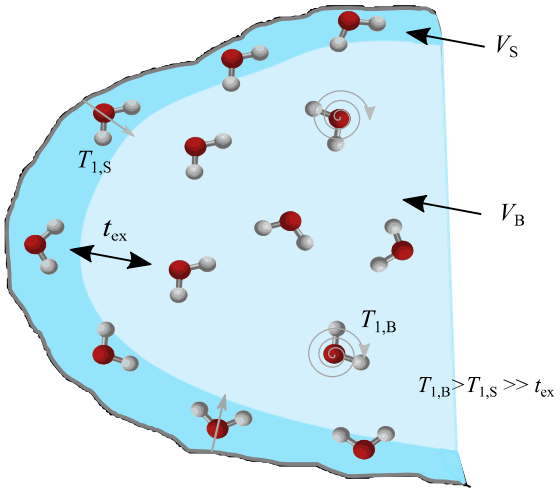

Figure 5.7: A schematic representation of the two-phase fast-exchange model of relaxation. The relaxation rates of molecules in the adsorbed phase and the bulk pore space are denoted as $T_{1,S}$ and $T_{1,B}$ respectively. Provided that the exchange time, t_{ex}, is much smaller than the $T_{1,S}$ and $T_{1,B}$ then the observed relaxation becomes a population weighted average of the two environments.

This finite volume, V_S, can therefore be occupied by n_S molecules (dependent on molecular size). Likewise, the centre of the pore space will consist of n_B molecules (dependent on the molar volume of the fluid) in a bulk-like volume, V_B. The expected relaxation behaviour can be expressed as:

$$\frac{1}{T_{1,\mathrm{obs}}} \approx \frac{1}{T_{1,\mathrm{B}}} + \frac{n_\mathrm{S}}{n_\mathrm{S} + n_\mathrm{B}} \frac{1}{T_{1,\mathrm{S}}}, \tag{5.9}$$

$$\frac{1}{T_{1,\mathrm{S}}} \approx \frac{n_\mathrm{S} + n_\mathrm{B}}{n_\mathrm{S}} \frac{1}{T_{1,\mathrm{obs}}} \qquad \text{where} \quad \frac{1}{T_{1,\mathrm{obs}}} \gg \frac{1}{T_{1,\mathrm{B}}}. \tag{5.10}$$

The differing molecular size and molar volume of each imbibed liquid will affect the relative weighting of the bulk and surface relaxation rates, but it is not obvious whether such an effect will outweigh any changes in $1/T_{1,\mathrm{S}}$. The data shown in Table 5.3 suggested no trend between the molecular size and the observed relaxation rate, and a potential inverse relationship between molar volume and the observed relaxation rate. The latter is coincidental as an increase in the molar volume would decrease n_B. According to eq. (5.9) decreasing n_B would increase the observed relaxation rate, in contradiction to the observed trend.

To explore the effects of variations in the molar volume and molecular diameter on the term $(n_\mathrm{S}+n_\mathrm{B})/\, n_\mathrm{S}$ for the γ-alumina studied herein water, methanol, and cyclohexane were considered in more detail. These three fluids represented some of the smallest and largest molecules studied, and would therefore highlight any contributions to the relaxation trends caused by the $(n_\mathrm{S}+n_\mathrm{B})/\, n_\mathrm{S}$ term. A structural characterisation of the alumina was required for this analysis. The pore volume and surface area were measured using gravimetric methods and nitrogen BET (Brunauer–Emmett–Teller), giving values of 0.65 mL g^{-1} and 206 m^2 g^{-1} respectively. In the case of non-specific surface binding, as depicted in Figure 5.7, a surface layer of one molecular diameter, λ, was assumed for water, methanol and cyclohexane. The volume of the surface fluid, V_S, and the bulk fluid, V_B, for a mass of m grams are given as:

$$V_\mathrm{S} = 206\, \lambda\, m, \tag{5.11}$$

$$V_\mathrm{B} = 6.5\, \times 10^{-7} m - V_\mathrm{S}\,. \tag{5.12}$$

Assuming that the density of the bulk and surface environments were the same, then each volume was proportional to the number of molecules within that volume. This gave $(n_\mathrm{S}+n_\mathrm{B})/\, n_\mathrm{S}$ as 9.6, 8.8, and 5.3 for water, methanol, and cyclohexane respectively. The differences in these ratios were far smaller than the observed differences in the relaxation

rates between each of the liquids, which suggested that the molar volume and molecular size were not dominating the relaxation behaviour of the γ-alumina system under the assumption of non-specific binding.

The previous assumption of non-specific binding has been widely used in NMR relaxation analyses for both strongly and weakly adsorbed species, but may be an oversimplification in the case of highly polar species capable of hydrogen bonding. In these cases the adsorbate will bind exclusively to a surface hydroxyl group. As such, the number of surface hydroxyl groups becomes important, particularly if this number is lower than the number of molecules of adsorbate that would fit within a surface monolayer. Using the same geometrical arguments as presented in eqs. (5.11) and (5.12) the number of molecules in the surface layer, N_{surf}, can be given as:

$$N_{\mathrm{surf}} = \frac{206\lambda m N_{\mathrm{A}}}{V_{\mathrm{m}}}, \tag{5.13}$$

where N_{A} is Avogadro's constant and V_{m} is the molar volume of the imbibed liquid. Similarly, the number of available surface hydroxyl groups, N_{OH}, is given as:

$$N_{\mathrm{OH}} = 206\lambda m \alpha_{\mathrm{OH}}, \tag{5.14}$$

where α_{OH} is the surface density of hydroxyl groups. If the number of hydroxyl groups that are available exceeds the number of molecules that can fit into the surface layer then n_{S} is given by eq. (5.13). If the number of available hydroxyl groups is smaller than the number of molecules within the surface layer then the hydroxyl group density will limit the surface adsorption and n_{S} will be given by eq. (5.14). The ratio $(n_{\mathrm{S}}+n_{\mathrm{B}})/\, n_{\mathrm{S}}$ for water and methanol as a function of the surface hydroxyl density was calculated, as shown in Figure 5.8.

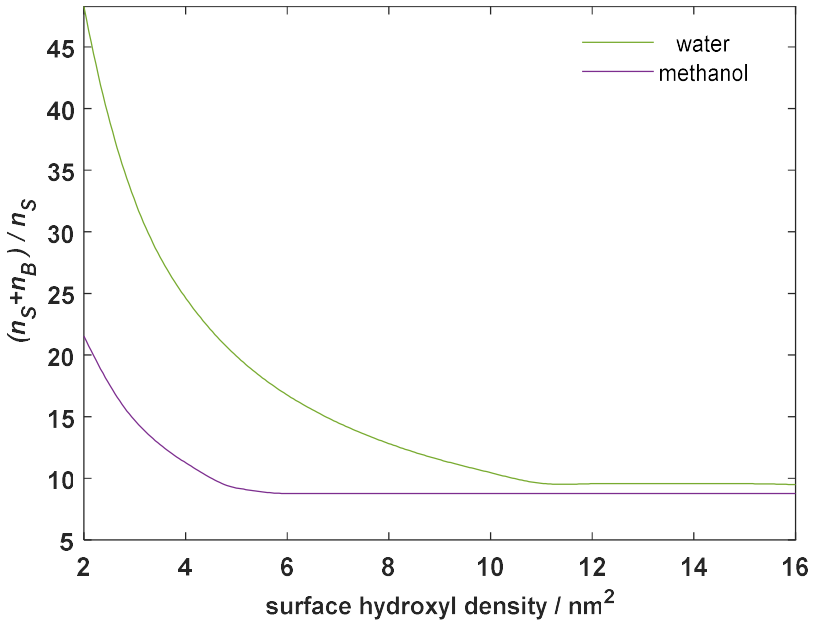

Figure 5.8: The population weighted adjustment as defined in eq. (5.10) for water and methanol imbibed within γ-alumina as a function of the surface hydroxyl density of the alumina.

As seen from Figure 5.8, at lower hydroxyl coverages the difference between $(n_S+n_B)/\,n_S$ for water and methanol was a factor of 2.2. This was a significantly larger difference than under the assumption of non-specific binding. In the limit that there are sufficient surface hydroxyls for each adsorbate to form a full surface layer, the population adjustment becomes identical to that obtained from a non-specific surface binding approach. An explicit consideration of the number of surface binding sites is therefore important when measuring small and dense adsorbates, such as water, on surfaces with a low to moderate surface hydroxyl density. For adsorbates equal in size to, or larger than, methanol the non-specific surface binding approach accurately described the relaxation behaviour.

γ-alumina has been reported in the literature as having a wide range of surface hydroxyl densities. This means that the lower values presented in Figure 5.8 were reasonable, and could be used to justify the unusual crossover behaviour observed in the methanol and water NMRD profiles. Figure 5.9 shows the $R_{1,S}$ data assuming surface hydroxyl densities of 5 and 10 nm^{-2}. After this correction has been applied, the water surface relaxation is seen to be equal to or greater than that of methanol relaxation rate at all field strengths studied. The absence of a crossover helped to remove any ambiguity about the

relative interaction strengths of these two adsorbates, and highlighted how a fixed field T_1 measurement alone may lead to an erroneous interpretation of the system. The observation of a crossover point in the methanol and water NMRD profiles also allowed an estimate of the upper limit of the surface hydroxyl density for the γ-alumina studied herein as <10 nm^{-2}.

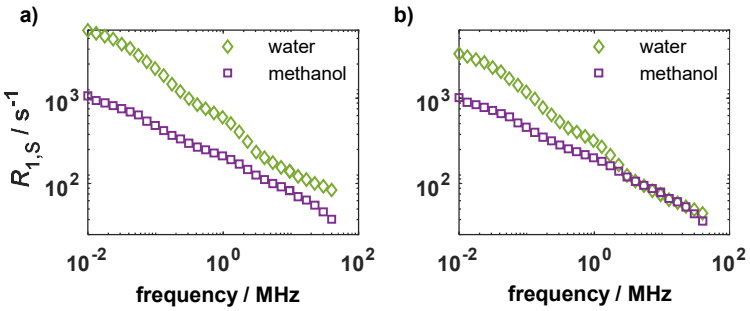

Figure 5.9: The surface relaxation rate of water and methanol imbibed within γ-alumina. An adjustment has been applied using the data from Figure 5.8 and eq. (5.10) assuming surface hydroxyl densities of a) 5 nm^{-2} and b) 10 nm^{-2}.

In summary, in the case of non-specific surface binding the molecular size and molar volumes of the adsorbates had a very small effect on the observed relaxation rate. When the relaxation process was dominated by a specific binding process, such as hydrogen bonding to surface hydroxyl groups, this affected the observed relaxation rate more strongly. In the limit of low hydroxyl densities and for small adsorbates, a factor of 2.2 was estimated as the difference between the expected relaxation rates of water and methanol imbibed within γ-alumina. This factor was not insignificant and could be used to explain the crossover that occurred between the methanol and water datasets. In this particular case the molecular sizes and molar volumes did influence the observed relaxation rates, but not the power law exponent, β, of the NMRD profile. This parameter remained a robust metric for understanding the interaction behaviour of different liquids imbibed within a porous medium, even when comparing across adsorbates of different sizes.

5.5.2.4 Intrinsic dipolar interaction

The dipolar interaction that dominates the relaxation behaviour of spin ½ species is a through space interaction, which occurs between a pair of spin active nuclei. It is, therefore, reasonable to expect the number of adjacent nuclei and the distance between

^{1}H protons to have an effect on the relaxation rate of a liquid imbibed within a porous medium. The differences between adsorbates have previously been accounted for by dividing the relaxation rate of the adsorbed species by that of the corresponding bulk fluid.[19,41] In the case of the experiments presented in this chapter the largest difference between two bulk liquid relaxation rates was a factor of 1.8, which was far too small to account for any of the differences observed for the different liquids imbibed within γ-alumina. Furthermore, the difference was smaller between the bulk liquid relaxation rates of species which showed similar dispersion profiles when imbibed within γ-alumina. For example, the low field plateaus of water and methanol, and *n*-heptane and cyclohexane were identical within experimental error. The similarity of all of the bulk liquid NMRD profiles showed that the magnitude of the intrinsic dipolar interaction was not dominating the relaxation trends observed in Figure 5.4.

5.5.2.5 Solid-liquid interaction strength

Figure 5.10 shows the correlation between the polarity of each adsorbate and the power law exponent obtained from the NMRD profile of each liquid imbibed within γ-alumina. With the exception of acetone, the complex dynamic chemistry of which will be discussed in greater detail in chapter 6, this metric correlated well with the values of polarity predicted from Reichardt analysis. The Reichardt values were taken as a measure of interaction strength for molecules interacting with a polar surface. The correlation therefore showed that the dominant effect controlling the relaxation rate of a liquid imbibed within γ-alumina was the solid-liquid interaction strength. An analogous trend can be obtained from the TOD data, but for reasons outlined within this discussion the power law exponent was expected to be the most quantitative measure of interaction strength. Deviations from a simple linear trend were observed. For example, THF interacted more strongly with the alumina surface than expected, which may have resulted from additional adsorbate-surface interactions that are not captured in a simple measurement of the adsorbate polarity. Furthermore, the effect of hydrogen bonding for polar species would have allowed a subtly different relaxation mechanism to occur for polar species compared to non-polar species, and the effect this would have on the power law exponent is not clear. Despite these possible sources of deviation from linearity, the data presented in Figure 5.10 showed that for liquids imbibed within a mesoporous catalytic support, FFC-NMR was primarily sensitive to the changes in molecular motions resulting from the strength of the adsorbate-surface interaction. The ordering of

interaction strength derived from FFC-NMR relaxation showed a better agreement with the polarity values compared to the fixed field relaxation analysis performed in chapter 4, particularly in the case of large and or flexible molecules. The insensitivity of T_1 at low field strengths to molecule specific relaxation mechanisms allowed FFC-NMR to serve as a reliable alternative in instances where T_1/T_2 ratios were no longer informative.

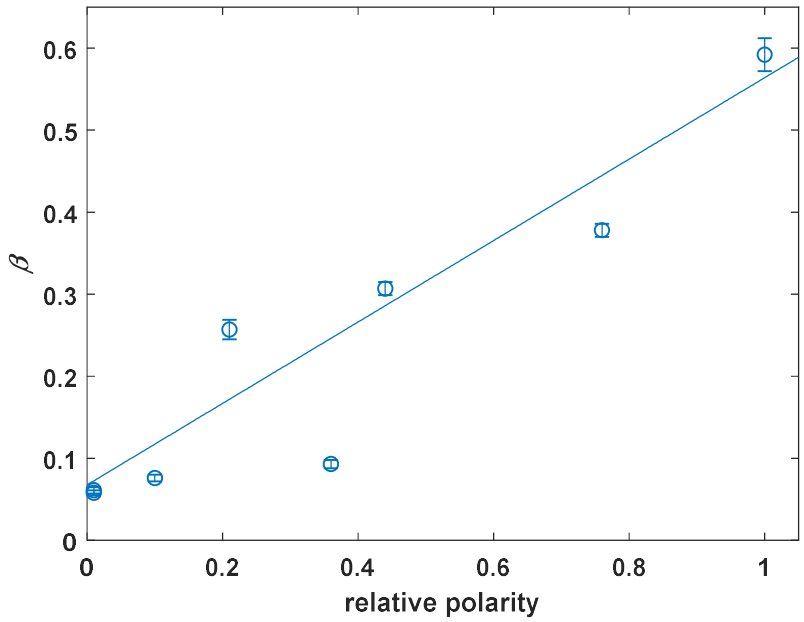

Figure 5.10: A comparison of the relative polarity of eight liquids imbibed within γ-alumina and the power law exponent, β, obtained by fitting eq. (5.6) to the observed NMRD profiles.

5.6 Conclusions

FFC-NMR data were presented for a variety of organic liquids and water in their bulk liquid state, and imbibed within γ-alumina. These data were validated against fixed field measurements, and the differences between samples were shown to be significant when compared to the sample to sample variation. For bulk liquids there was little variation in the relaxation behaviour of all eight liquids, with a maximum relaxation rate for any species of 0.6 s^{-1}. The relaxation behaviour was only weakly dependent on the ^1H Larmor frequency, and any dispersion behaviour that occurred was limited to a high field region (>10 MHz), which showed that the relaxation was caused by a fast motional process. The

principal source of this relaxation was the presence of molecular oxygen dissolved within the liquid, and a secondary effect was observed due to the rate of molecular rotation.

In contrast, the relaxation behaviour of liquids imbibed within a porous γ-alumina system showed vastly different behaviour for each liquid. When imbibed within γ-alumina the dispersion behaviour was seen to extend to the lowest measurable fields for all adsorbates, which demonstrated that much slower motions were controlling the relaxation. For weakly interacting species the total observable dispersion was as low as 0.6 s^{-1}, but for strongly interacting species this rose almost three orders of magnitude to 310 s^{-1}. A phenomenological power law model was applied to the data to describe the relaxation behaviour. Comparing the exponents of the power law allowed a quantitative ranking of all of the adsorbates, which trended well with polarity of the adsorbate. Other possible contributions to the relaxation behaviour were considered. In particular, the molecular size and molar volumes were shown to have a significant effect on the absolute value of the relaxation rate, but not the power law exponent. Therefore the power law exponent was used as a robust metric to rank the adsorbate-surface interaction strengths for each liquid within γ-alumina. This produced a more physically reasonable ordering than that suggested by a conventional T_1/T_2 analysis.

The data presented in this chapter will be further analysed in chapter 6, with a specific focus on the multicomponent behaviour observed for methanol and acetone. The physical significance of the additional peaks will be explored and the resultant data compared to the logarithmic average approach presented in this chapter. The phenomenological power law approach used in this chapter will also be further expanded on in chapter 7 in order to specifically address the underlying spin interactions that are causing the observed relaxation.

5.7 References

(1) Kimmich, R.; Anoardo, E. Field-Cycling NMR Relaxometry. *Prog. Nucl. Magn. Reson. Spectrosc.* **2004**, *44*, 257–320.

(2) Teng, C.; Hong, H.; Kiihne, S.; Bryant, R. G. Molecular Oxygen Spin–Lattice Relaxation in Solutions Measured by Proton Magnetic Relaxation Dispersion. *J. Mag. Res* **2001**, *34*, 31–34.

(3) Godefroy, S.; Korb, J.-P.; Fleury, M.; Bryant, R. G. Surface Nuclear Magnetic Relaxation and Dynamics of Water and Oil in Macroporous Media. *Phys. Rev. E* **2001**, *64*, 021605.

(4) Levitz, P. Random Flights in Confining Interfacial Systems Random Flights in Confining Interfacial Systems. *J. Phys. Condens. Matter* **2005**, *17*, S4059–S4074.

(5) Ward-Williams, J.; Korb, J.-P.; Gladden, L. F. Insights into Functionality-Specific Adsorption Dynamics and Stable Reaction Intermediates Using Fast Field Cycling NMR. *J. Phys. Chem. C* **2018**, *122*, 20271–20278.

(6) Kimmich, R. *NMR Tomography, Diffusometry, Relaxometry*; Springer-Verlag, 1999.

(7) Ferrante, G.; Sykora, S. Technical Aspects of Fast Field Cycling. *Adv. Inorg. Chem.* **2005**, *57*, 405–470.

(8) Singer, P. M.; Asthagiri, D.; Chapman, W. G.; Hirasaki, G. J. Molecular Dynamics Simulations of NMR Relaxation and Diffusion of Bulk Hydrocarbons and Water. *J. Magn. Reson.* **2017**, *277*, 15–24.

(9) Korb, J.-P. Multiscale Nuclear Magnetic Relaxation Dispersion of Complex Liquids in Bulk and Confinement. *Prog. Nucl. Magn. Reson. Spectrosc.* **2018**, *104*, 12–55.

(10) Meier, R.; Kruk, D.; Gmeiner, J.; Rössler, E. A. Intermolecular Relaxation in Glycerol as Revealed by Field Cycling ^{1}H NMR Relaxometry Dilution Experiments. *J. Chem. Phys.* **2012**, *136*, 34508.

(11) Korb, J.-P.; Whaley-Hodges, M.; Bryant, R. G. Translational Diffusion of Liquids at Surfaces of Microporous Materials: Theoretical Analysis of Field-Cycling Magnetic Relaxation Measurements. *Phys. Rev. E* **1997**, *56*, 1934–1945.

(12) Zavada, T.; Kimmich, R. The Anomalous Adsorbate Dynamics at Surfaces in Porous Media Studied by Nuclear Magnetic Resonance Methods. The Orientational Structure Factor and Lévy Walks. *J. Chem. Phys.* **1998**, *109*, 6929–6939.

(13) Korb, J. -P.; Levitz, P. E. Direct Probing of the Wettability of Plaster Pastes at the

Nanoscale by Proton Field Cycling Relaxometry. *AIP Conf. Proc.* **2008**, *1081*, 55–58.

(14) Steele, R. M.; Korb, J.-P.; Ferrante, G.; Bubici, S. New Applications and Perspectives of Fast Field Cycling NMR Relaxometry. *Magn. Reson. Chem.* **2015**, *54*, 502–509.

(15) Stapf, S.; Ren, X.; Talnishnikh, E.; Blümich, B. Spatial Distribution of Coke Residues in Porous Catalyst Pellets Analyzed by Field-Cycling Relaxometry and Parameter Imaging. *Magn. Reson. Imaging* **2005**, *23*, 383–386.

(16) Conte, P.; Loddo, V.; De Pasquale, C.; Marsala, V.; Alonzo, G.; Palmisano, L. Nature of Interactions at the Interface of Two Water-Saturated Commercial TiO_2 Polymorphs. *J. Phys. Chem. C* **2013**, *117*, 5269–5273.

(17) Chemmi, H.; Petit, D.; Levitz, P.; Denoyel, R.; Galarneau, A.; Korb, J.-P. Noninvasive Experimental Evidence of the Linear Pore Size Dependence of Water Diffusion in Nanoconfinement. *J. Phys. Chem. Lett.* **2016**, *7*, 393–398.

(18) Mitchell, J.; Broche, L. M.; Chandrasekera, T. C.; Lurie, D. J.; Gladden, L. F. Exploring Surface Interactions in Catalysts Using Low-Field Nuclear Magnetic Resonance. *J. Phys. Chem. C* **2013**, *117*, 17699–17706.

(19) Stapf, S.; Kimmich, R.; Seitter, R. O.; Maklakov, A. I.; Skirda, V. D. Proton and Deuteron Field-Cycling NMR Relaxometry of Liquids Confined in Porous Glasses. *Phys. Rev. Lett.* **1996**, *115*, 107–114.

(20) Korb, J. P.; Whaley Hodges, M.; Gobron, T.; Bryant, R. G. Anomalous Surface Diffusion of Water Compared to Aprotic Liquids in Nanopores. *Phys. Rev. E* **1999**, *60*, 3097–3106.

(21) Mattea, C.; Kimmich, R.; Ardelean, I.; Wonorahardjo, S.; Farrher, G. Molecular Exchange Dynamics in Partially Filled Microscale and Nanoscale Pores of Silica Glasses Studied by Field-Cycling Nuclear Magnetic Resonance Relaxometry. *J. Chem. Phys.* **2004**, *121*, 10648–10656.

(22) Korb, J. P.; Monteilhet, L.; McDonald, P. J.; Mitchell, J. Microstructure and Texture of Hydrated Cement-Based Materials: A Proton Field Cycling Relaxometry Approach. *Cem. Concr. Res.* **2007**, *37*, 295–302.

(23) Faux, D. A.; Mcdonald, P. J. Explicit Calculation of Nuclear-Magnetic-Resonance Relaxation Rates in Small Pores to Elucidate Molecular-Scale Fluid Dynamics. *Phys. Rev. E* **2017**, *95*, 033117.

(24) Korb, J. P.; Freiman, G.; Nicot, B.; Ligneul, P. Dynamical Surface Affinity of Diphasic Liquids as a Probe of Wettability of Multimodal Porous Media. *Phys. Rev. E* **2009**, *80*, 61601.

(25) Korb, J.; Nicot, B.; Bubici, S.; Ferrante, G. Dynamics and Wettability of Oil and Water in Oil Shales. *J. Phys. Chem. C* **2014**, *118*, 23212–23218.

(26) Korb, J. P.; Godefroy, S.; Fleury, M. Surface Nuclear Magnetic Relaxation and Dynamics of Water and Oil in Granular Packings and Rocks. *Magn. Reson. Imaging* **2003**, *21*, 193–199.

(27) Südland, N.; Zavada, T.; Su, N. Propagator Representation of Anomalous Diffusion : The Orientational Structure Factor Formalism in NMR. *Phys. Rev. E* **1999**, *60*, 1292–1298.

(28) Djemai, A.; Balan, E.; Morin, G.; Labbe, J. C.; Pierre, J. Behaviour of Paramagnetic Iron during the Thermal Transformations of Kaolinite. *J. Am. Ceram. Soc* **2001**, *84*, 1017–1024.

(29) Hollewand, M. P.; Gladden, L. F. Transport Heterogeneity in Porous pellets—I. PGSE NMR Studies. *Chem. Eng. Sci.* **1995**, *50*, 309–326.

(30) Butler, J. P.; Reeds, J. A.; Dawson, S. J. Estimating Solutions of First Kind Integral Equations with Nonnegative Constraints and Optimal Smoothing. *J. Numer. Anal.* **1981**, *18*, 381–397.

(31) Korb, J.; Ferrante, G.; Bubici, S.; Mallett, M. New Instrumental Platform for the Exploitation of the Field- Dependence of T_1 in Rock Core Analysis and Petroleum Fluids : Application to T_1-T_2 Correlation Maps. *Diffus. fundementals* **2014**, *22*, 1–7.

(32) Gossuin, Y.; Serhan, Z.; Sandiford, L.; Henrard, D.; Marquardsen, T.; de Rosales, R. T. M.; Sakellariou, D.; Ferrage, F. Sample Shuttling Relaxometry of Contrast Agents: NMRD Profiles above 1 T with a Single Device. *Appl. Magn. Reson.* **2016**, *47*, 237–246.

(33) Sato, T.; Hamada, Y.; Sumikawa, M.; Araki, S.; Yamamoto, H. Solubility of Oxygen in Organic Solvents and Calculation of the Hansen Solubility Parameters of Oxygen. *Ind. Eng. Chem. Res.* **2014**, *53*, 19331–19337.

(34) Korb, J.-P.; Vorapalawut, N.; Nicot, B.; Bryant, R. G. Relation and Correlation between NMR Relaxation Times, Diffusion Coefficients, and Viscosity of Heavy Crude Oils. *J. Phys. Chem. C* **2015**, *119*, 24439–24446.

(35) D'Agostino, C.; Mitchell, J.; Mantle, M. D.; Gladden, L. F. Interpretation of NMR Relaxation as a Tool for Characterising the Adsorption Strength of Liquids inside Porous Materials. *Chem. A Eur. J.* **2014**, *20*, 13009–13015.

(36) Reichardt, C. *Solvents and Solvent Effects in Organic Chemistry*; Wiley-VCH Publishers: Weinheim, 2003.

(37) Webster, C. E.; Drago, R. S.; Zerner, M. C.; Gaines, V. Molecular Dimensions for Adsorptives. *J. Am. Chem. Soc* **1998**, *120*, 5509–5516.

(38) Smallwood, I. M. *Handbook of Organic Solvent Properties*; Arnold, 1996.

(39) Wu, H.; Gong, Q.; Olson, D. H.; Li, J. Commensurate Adsorption of Hydrocarbons and Alcohols in Microporous Metal Organic Frameworks. *Chem. Rev.* **2012**, *112*, 836–868.

(40) Fripiat, J.; Cases, J.; Francois, M.; Letellier, M. Thermodynamic and Microdynamic Behavior of Water in Clay Suspensions and Gels. *J. Colloid Interface Sci.* **1982**, *89*, 378–400.

(41) Vecino, P. A.; Huang, Z.; Mitchell, J.; McGregor, J.; Daly, H.; Hardacre, C.; Thomson, J. M.; Gladden, L. F. Determining Adsorbate Configuration on Alumina Surfaces with ^{13}C Nuclear Magnetic Resonance Relaxation Time Analysis. *Phys. Chem. Chem. Phys.* **2015**, *17*, 20830–20839.

Chapter 6 : Multicomponent relaxation of liquids imbibed within γ-alumina

The work contained within this chapter forms part of the publication: Ward-Williams, J.; Korb, J.-P.; Gladden, L. F. Insights into Functionality-Specific Adsorption Dynamics and Stable Reaction Intermediates Using Fast Field Cycling NMR. *J. Phys. Chem. C* **2018**, *122*, 20271–20278.

Contents

6.1 Introduction

Chapter 5 demonstrated the use of FFC-NMR as a powerful tool for measuring the relative interaction strengths of several adsorbates imbibed within a catalytically relevant γ-alumina system. This approach was performed holistically, by taking the relaxation behaviour of each molecule as the logarithmic average of the R_1 distribution obtained at each field strength. By doing so the analysis of each dataset was simplified, but this approach prevented the exploitation of a key advantage of NMR – its chemical specificity. Different functional groups within an adsorbate may have very different interactions with the surface, leading to a range of relaxation behaviour. If these differences are sufficiently large it is possible to separate them out, and allow a more granular understanding of the physicochemical processes that are occurring at the catalyst surface.

In this chapter the data presented in chapter 5 for liquids adsorbed within γ-alumina are further explored. For each adsorbate the T_1 distributions are re-analysed at all field strengths and, as mentioned in chapter 5, for some adsorbates a second minor peak is observed. Further experiments are pursued to clarify the nature of the minor components and the implications of them on the adsorption behaviour are discussed.

6.2 Background and literature review

6.2.1 FFC-NMR studies of multicomponent relaxation in porous media

Fourier transform NMR spectroscopy has made the separation of multiple chemical environments trivial for almost all fixed field NMR machines.[1] In contrast, hardware limitations currently prohibit the acquisition of chemically (or spectroscopically) resolved fast field cycling experiments.[2] This is because the design of the electromagnet is optimised to allow rapid switching of the magnetic field, rather than achieving the necessary magnetic homogeneity and stability required for spectroscopic resolution. This leads to single component relaxation behaviour being observed in the vast majority of literature examples.[3–6] More complex behaviour has been observed for liquids imbibed within non-uniform porous media, where the complexity of the system leads to a continuous distribution of relaxation rates.[7,8] Separating the distribution out into

individual components is often too complicated, and the logarithmic average of the relaxation rate constant, $<R_1>$, is used to simplify the relaxation behaviour. This simplification removes the finer details of the adsorption process, but makes the relaxation behaviour more manageable. A formal modelling approach can still be meaningfully applied to the logarithmic average nuclear magnetic relaxation dispersion (NMRD) profiles if a single relaxation process is responsible for the relaxation distribution. Even in complex porous media, such as rock cores[9] and soils,[4] the relaxation processes are sufficiently homogenous that a representative average T_1 value is often used.

Separable multicomponent behaviour of liquids in porous media has been observed through previous field cycling experiments. This behaviour has been attributed to multi-modal pore sizes distributions,[9] and to the chemical separation of oil and water imbibed within rock cores.[10] In each case the additional information provided by separating out the signals improved the understanding of the physicochemical processes that were occurring. For instance, the separation of the oil and water signals allowed a realistic measurement of the wettability of oil (dodecane) to be measured when confined within a carbonate rock. Without the ability to separate the dodecane signal from the brine signal it would not have been possible to measure the rock under representative conditions (irreducible water saturation) and therefore the resultant wettability value may not have been informative.

Multicomponent behaviour may also be present in systems where it is not explicitly observed. In cases where the T_1 relaxation time constant of one of the environments is far shorter than the experimental switching time it will not be possible to detect any signal directly from the fast component. However, the relaxation of this environment may still influence the relaxation rates and populations of other environments. For example, in the specific case of water adsorbed within cement pastes, the rapidly relaxing signal from water tightly bound in the calcium silicate hydrate surface layer was not directly observable.[11,12] It did, however, influence the relaxation rate of water within the cement paste via a cross-relaxation mechanism described in eq. (6.1):[11]

$$R_1(\omega) = \begin{cases} FR_{1,\mathrm{sol}}/(1+F) = cst, & \text{for } \omega \leq \omega_c \\ R_{1,\mathrm{w}}(\omega), & \text{for } \omega \geq \omega_c \end{cases} \qquad (6.1)$$

where ω is the ^{1}H Larmor frequency, ω_c is a cut-off frequency, $R_{1,\mathrm{sol}}$ and $R_{1,\mathrm{w}}$ are the relaxation rates of the solid hydrates and water respectively, F is the population ratio between the two environments, and cst denotes a constant. This situation is analogous to the expected relaxation behaviour of liquids in mesoporous catalytic materials, where the fast relaxing component would represent either surface hydroxyls or chemisorbed water. It is therefore possible for the adsorbates to directly probe the relaxation rate of the solid as well as the solid-liquid interactions.

Greater resolution of multiple components can be obtained through more advanced FFC-NMR experiments. For example, multidimensional T_1-T_2 experiments have very recently been demonstrated using a fast field cycling relaxometer.[13] The addition of the T_2 domain allowed the separation of a physical mixture of porous glasses of different pore sizes imbibed with water, which was not possible through a conventional T_1 analysis.[13] Whilst the advantages of two dimensional experiments are clear, the experimental procedure is not simple to implement on a fast field cycling relaxometer as they are on a fixed field magnet. Time dependent fluctuations in the magnetic field strength and the short T_2* times observed for most samples limit the generality of this approach. As such, multidimensional FFC-NMR experiments are not pursued within this thesis.

6.2.2 Numerical methods for separating components in T_1 distributions

When the observed relaxation is comprised of a series of contributions from distinct magnetic environments (that are not averaged on the timescale of the experiment) the decay profile will deviate from a single exponential function. One of the most commonly used methodologies to extract the relaxation time constants from multicomponent relaxation data is to fit an exponential expression of the form:

$$M_z = \sum_n M_{0,n} \exp\left\{\frac{-\tau}{T_{1,n}}\right\}, \tag{6.2}$$

where M_z is the observed magnetization, n is the number of relaxation components that are expected in the sample, $M_{0,n}$ is the initial magnetization of the n^{th} component, $T_{1,n}$ is the relaxation time constant of the n^{th} environment, and τ is the experimental delay time. This method, however, is dependent on *a priori* knowledge of the value of n and is not well-suited to systems containing a distribution of relaxation time constants. To

mitigate against these issues a common alternative is to apply an inverse Laplace transformation in order to obtain a probability distribution function of T_1.[14] The observed NMR signal, $\underline{S}$, is decomposed into the kernel matrix describing the expected relaxation behaviour, $\underline{K}$, the true T_1 distribution, $\underline{F}$, and the experimental noise, $\underline{E}$:

$$\underline{S} = \underline{KF} + \underline{E}\,. \tag{6.3}$$

Due to the ill-conditioned nature of the exponential kernel matrix, the solution to this equation is non-trivial. The standard methodology for obtaining $\underline{F}$ begins by assuming it to be a smooth and continuous distribution. Tikhonov regularization can then be applied and the minimisation problem is expressed as:[15]

$$\underline{F} = \arg\min_{\underline{F}\geq 0}\left(\frac{\alpha}{2}\left\|\underline{KF} - \underline{S}\right\|_2^2 + \frac{1}{2}\left\|\underline{RF}\right\|_2^2\right), \tag{6.4}$$

where α is a regularization parameter and $\underline{R}$ is a matrix that acts upon $\underline{F}$ to give its second derivative. The regularization parameter is then optimised to strike a balance between the first (fidelity) and the second (penalty) terms. When properly optimised this method is robust and does not require *a priori* knowledge of the number of relaxation components within the system. The underlying assumption, however, is that the distribution is smooth and continuous. This may not reflect the true physical chemistry of the system and prevents the separation of close peaks (within a factor of 3).[16] In instances where $\underline{F}$ is known to be discrete, the regularization can be recalculated using the L_1 norm of the distribution as the penalty term:

$$\underline{F} = \arg\min_{\underline{F}\geq 0}\left(\frac{\alpha}{2}\left\|\underline{KF} - \underline{S}\right\|_2^2 + \left\|\underline{F}\right\|_1\right). \tag{6.5}$$

This alternative methodology has been successfully implemented for the quantitative separation of alkane binary liquid mixtures adsorbed in silica in instances where the relaxation rates differed by only 10%.[15]

6.3 Materials and methods

6.3.1 Materials

All materials mentioned in section 5.3.1 were used for the experiments presented within this chapter. In addition, ethanol, *n*-propanol, *iso*-propanol, *n*-butanol, butanone, pentan-3-one, disopropyl ketone and hexamethyl acetone were purchased from Alfa Aesar at a purity of >98%. Mesityl oxide was obtained from Sigma Aldrich at a purity of >90%. Deuterated and partially deuterated analogues of methanol were obtained from Fluorochem at a purity of >98%.

6.3.2 NMR methods

For a typical NMRD profile between 10 and 30 ^{1}H Larmor frequencies were analysed, logarithmically spaced between 10 kHz and 40 MHz. Switching times were set to 3 ms and a slewing rate of 12 MHz ms^{-1} were used as standard. A pre-polarized sequence was used for field strengths below 10 MHz and a non-polarized sequence was used for measurements above 10 MHz. For each T_1 experiment 32 delay times were used with relaxation delays that were logarithmically spaced between 1 ms and 6 x T_1. Unless otherwise stated, all analysis of the experiments was performed as outlined in section 5.3.2. For NMRD profiles displaying multiple peaks the relaxation rates and relative populations were calculated using a bilogarithmic fit. This was compared against a 1D inverse Laplace analysis and found to agree within error. In cases where the population of the minor component was stable across the frequency range the average population from each frequency was reported. For alcohols the population was not stable across all frequencies and as such the population was averaged over only the range of 0.1-1 MHz.

NMR spectroscopy experiments were performed on a Bruker Ascend 300 MHz spectrometer equipped with Micro 5 probe and a 5 mm ^{1}H/^{13}C coil. ^{1}H spectra were acquired in a single scan, and 4096 signal averages were used to measure the carbon spectra. Kinetic experiments were performed with a time resolution of 2 h per point for ^{13}C NMR. For all spectra, chemical shifts were referenced to the respective resonances of tetramethysilane.

6.4 Results

In this section a detailed analysis of the T_1 distribution recorded for each liquid imbibed within γ-alumina is presented. For each liquid that showed additional features in its T_1 distribution the robustness of these peaks was tested – both in terms of their relative size and T_1 value. To explore the generality of these additional feature, liquids containing similar chemical functionalities to the liquids that showed multicomponent behaviour were also imbibed within γ-alumina. This allowed an assignment of chemical origin of the multicomponent relaxation behaviour.

6.4.1 Identification of multicomponent relaxation behaviour

The T_1 distributions measured at 1 MHz for n-heptane, cyclohexane, toluene, THF, acetone, DMSO, methanol, and water imbibed within γ-alumina are shown in Figure 6.1. The data for *n*-heptane, cyclohexane, toluene, THF, DMSO, and water showed single component T_1 distributions, consistent with previous relaxation time analyses of these liquids in different porous media.[3,4,17–19] In contrast, the data for methanol and acetone clearly showed two T_1 components. For both acetone and methanol the minor relaxation component was associated with a T_1 time constant approximately 1-2 orders of magnitude smaller than the main component, with the population of the minor component being 12-20% of that of the major peak. The relative population of the minor environments was unaffected by the limits of the inverse Laplace transformation, and the T_1 values showed a strong dependence on the ^{1}H Larmor frequency. These observations suggested that the minor environment had a genuine physical origin and was not an artefact introduced during data processing. There appeared to be a peak present in the toluene T_1 distribution at approximately 10^{-2} s, but this was of very low intensity and not stable across the frequency range. Because of these observations the peak was likely to be a noise artefact rather than a physically meaningful feature. The remainder of this section will focus on the optimization of the acquisition parameters and the post processing techniques that are used to ensure that both the major and minor environment are well-characterised in terms of their relaxation rates and relative populations.

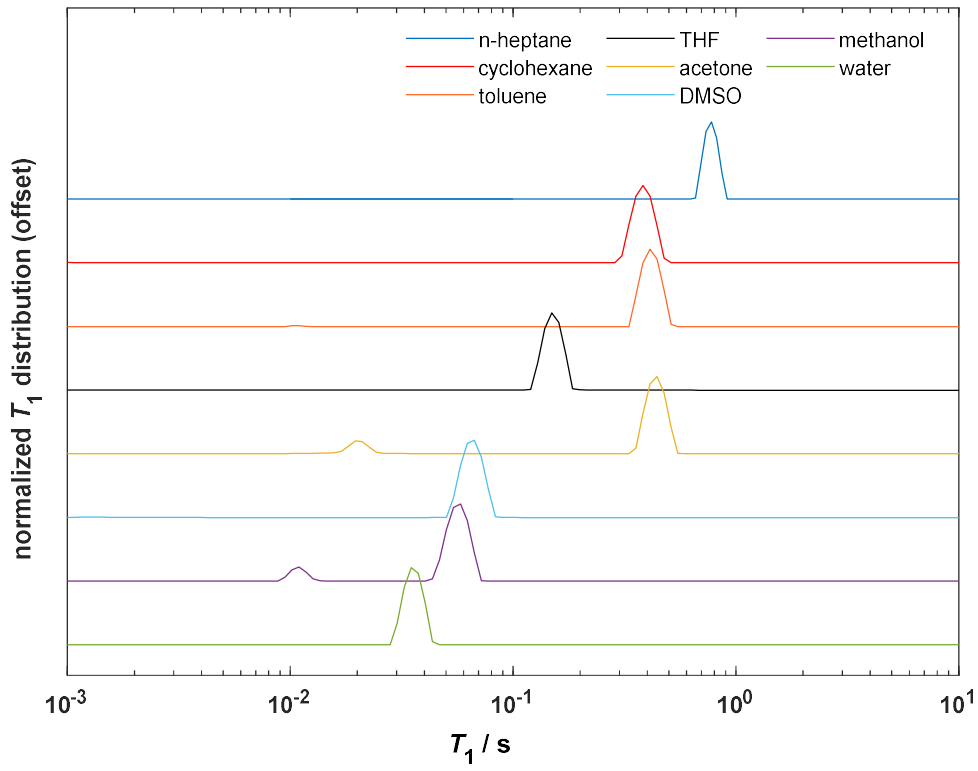

Figure 6.1: The T_1 distributions obtained at 1 MHz from an inverse Laplace transformation of several different organic liquids and water imbibed within γ-alumina.

The analysis of minor components, such as those observed for methanol and acetone, was experimentally challenging as FFC-NMR relaxation measurements provide no spectroscopic information to confirm the identity or validity of the peak. To ensure that the minor components were robust, both in terms of R_1 values and populations, the measurement was repeated with four scans to improve the SNR, and with 64 delay times in the T_1 domain to improve the sampling of the magnetisation decay. The results of these experiments are presented in Figure 6.2. The R_1 values of all components were consistent regardless of the SNR or sampling frequency, showing that neither of these parameters dominated the observed trends in the relaxation rate data. For both acetone and methanol the major component was more stable than the minor component. The largest errors in the R_1 values of methanol occurred at high frequencies, where the two peaks converge in terms of their relaxation rates.

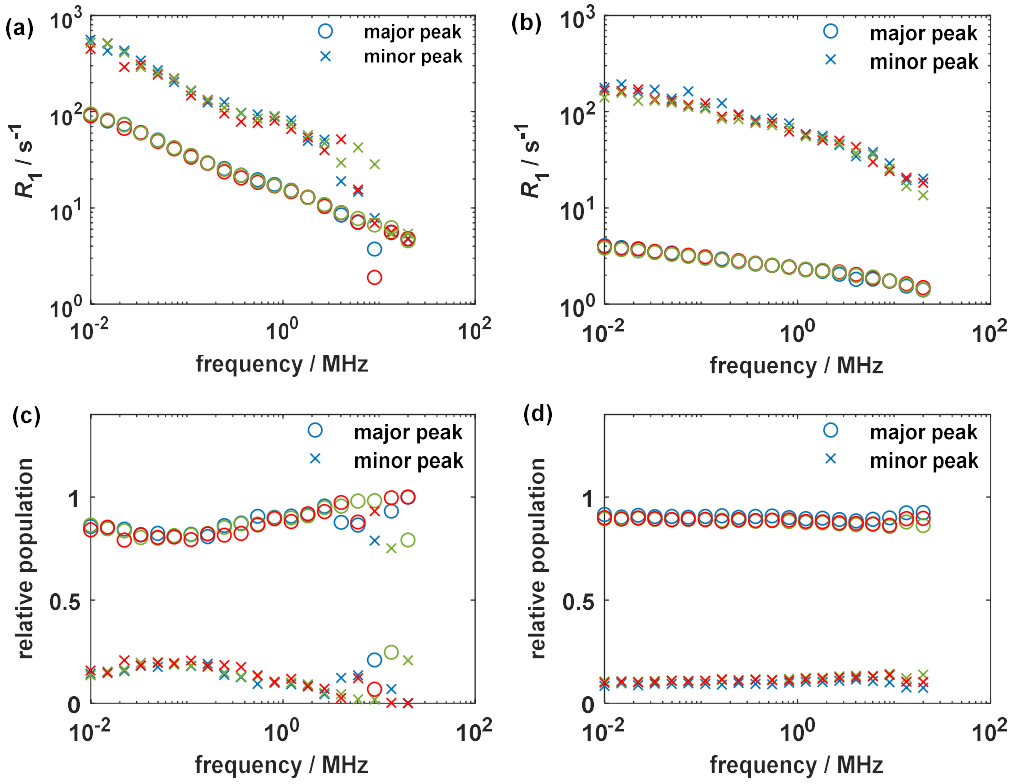

Figure 6.2: The (a-b) relaxation rates and (c-d) relative populations of (a and c) methanol and (b and d) acetone imbibed within γ-alumina. For both liquids a comparison is shown between the relaxation data acquired with 32 time delays and 1 scan (blue symbols), 64 time delays and 1 scan (red symbols), and 32 time delays and 4 scans (green symbol) on the same sample.

The relative populations showed a more complicated trend with respect to the ^{1}H Larmor frequency, as shown in Figure 6.2c-d. Under standard conditions (32 time delays and 1 scan) the relative population of the minor component of acetone was roughly stable at 13.5% at high fields and showed only a minor decrease to 11% at lower field strengths. The stability of the population indicated that this was a reliable measurement of the true population. For methanol, however, the population of the minor component was as low as 4% at high field strengths and rose to 19% at a frequency of 0.17 MHz. The relative population of the minor component then began to systematically decrease again at lower field strengths, and at 10 kHz the population of the minor component was below 14%. These trends were independent of the number of scans and the sampling frequency of the acquired data. Therefore the methanol measurements were not reflective of the true populations of the major and minor environments. Further experiments were explored to

optimise the sampling pattern as outlined in previous studies,[20] but no significant differences were noted in the resultant relaxation rates or populations.

The relaxation rate of the fast relaxing component of the methanol sample was seen to far exceed the inverse of the switching time. This suggests that this environment was relaxing significantly during the switching time (3 ms) and during the 1 ms minimum delay in the T_1 experiment. This led to an irrecoverable loss of signal that primarily affected the signal arising from the fast relaxing component, and led to an underestimation of its population. The problem was then compounded by the data normalization strategy, which assumed that the first experimental point was equal to the true initial magnetization, $M_{z,0}$, of the T_1 decay. To explore the effects of this initial signal loss and the normalization strategy two approaches were attempted. The first was to adjust the switching time for a methanol sample between 2 and 5 ms to minimise the signal loss of the minor component. The second was to improve the estimate of $M_{z,0}$ by fitting the raw data with a biexponential decay and extrapolating this back to time $t = 0$. The results of these experiments are presented in Figure 6.3.

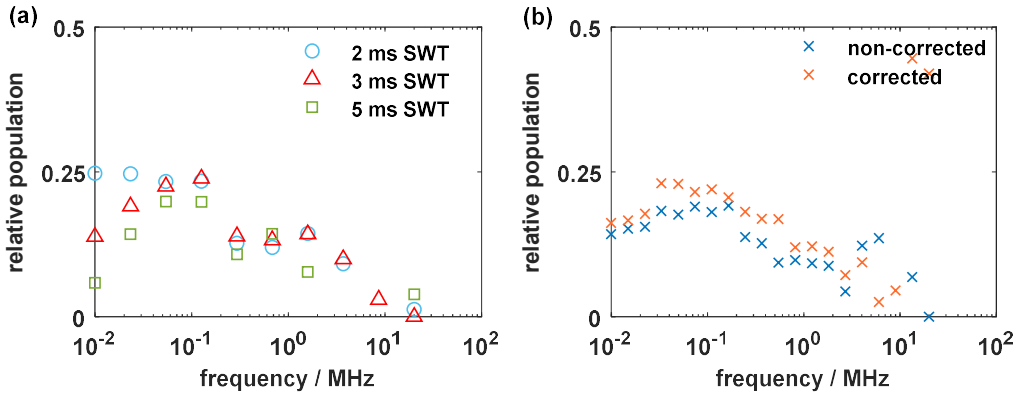

Figure 6.3: The relative population of the minor environment of methanol imbibed within γ-alumina (a) as a function of the switching time of the magnetic field (SWT) and (b) at a fixed value of SWT = 3ms and a slewing rate of 8 MHz ms^{-1}, with and without a normalization correction applied.

For all values of the switching time shown in Figure 6.3a, the relative size of the minor peak was similar above 0.1 MHz. Appreciable scatter was observed in the data, but a general increase was observed in the relative population of the minor environment as the field strength was decreased from 20 MHz to 0.1 MHz. For a switching time (SWT) of 2 ms a stable plateau was reached below 0.1 MHz, which corresponded to a relative

population of 25%. When the SWT was increased to 3 and 5 ms a systematic decrease of the relative population at low field occurred, and the population of the minor environment at 10 kHz fell to 14% and 6% respectively. A SWT of 1 ms was also explored, but the slewing rate was insufficient for the magnet to switch the field adiabatically.[2] The non-adiabatic switching resulted in a reduction in the SNR of the experiment, and the appearance of several additional peaks in the Laplace inversion. This made the data unreliable, and imposed a minimum switching time of 2 ms for FFC-NMR experiments. The normalization correction shown in Figure 6.3b resulted in an increase in the relative population of the minor component below 3 MHz. The difference was small, and the shape of the graph was preserved. This suggested that the data normalization strategy was not the dominant effect controlling the population of the minor component.

Optimisation of the acquisition parameters (primarily the switching time) resulted in a better estimate of the populations at low field strengths, but could not correct for the overlap of peaks seen at high field strengths. In order to improve this issue several processing techniques were explored. Exponential fittings, L_2, and L_1 inversions of the conventionally acquired methanol data are shown in Figure 6.4. All three methods appeared to be effective at separating out the relaxation behaviour below approximately 3 MHz. Above this value there were some noticeable differences. Forcing a biexponetial fitting generated unstable results as the values of R_1 converged, leading to significant scatter in the rate of both the fast and slow relaxing components. The L_2 inversion was more robust in terms of the major component, but failed to reliably identify the minor component when the difference in relaxation rates was below a factor of 3. Finally, the L_1 inversion appeared to be slightly more effective at separating peaks at high field strengths, but the difference between the methodologies was not significant enough for any particular method to be preferred.

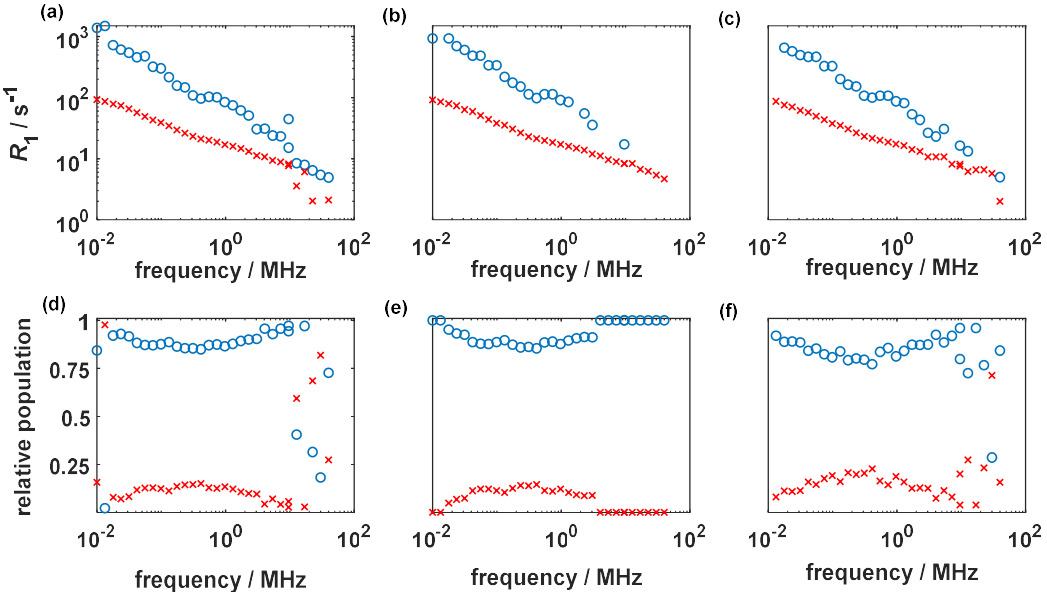

Figure 6.4: The NMRD profile of the two relaxation components of methanol imbibed within γ-alumina obtained using an (a) exponential, (b) L_2 inversion and (c) L_1 inversion. The relative populations of the two environments are also presented for the (d) exponential, (e) L_2 inversion and (f) L_1 inversion. Each NMRD profile is obtained from the same dataset, with a SWT of 3 ms and a slewing rate of 12 MHz ms^{-1}.

The dataset presented in Figure 6.4 is analogous to that presented in Figure 6.3a, however the slewing rate was faster for the former. As the slewing rate was faster the sample reached the relaxation field quicker, and was held at that field for the remainder of the switching time. This increased the effect of the switching times on the population of the minor environment and led to a greater underestimate at low field strengths. By using data with larger slewing rates (a less optimized procedure) the differences between the post-processing methodologies were expected to be clearer.

Regardless of which inversion method was used the relative population of the minor peak followed the same trend of initially increasing as the field strength was decreased to approximately 0.1-0.5 MHz. Thereafter, the relative population decreased as the field strength was further decreased. The exponential and L_2 data sets agreed very well below 3 MHz but, as was seen for the relaxation rates, the populations were not stable or reliable above this value. The L_1 inversion had a slightly higher population of the minor component (18.7%) and was more stable at high frequencies. Combining the back calculation method of $M_{z,0}$ shown in Figure 6.3 with the different inversion methods shown in Figure 6.4 resulted in a small increase in the population of the minor component

when analysed by an exponential or L_2 method. This resulted in all three inversion methodologies being almost identical for characterising methanol imbibed within γ-alumina. The L_2 and exponential methods will therefore be used throughout this chapter due to their greater robustness.

In summary, population estimates of 25% and 13% were obtained for the minor environments of methanol and acetone respectively. For methanol these values were highly sensitive to the acquisition parameters, and under standard conditions, showed the lowest error between 0.1-1 MHz. Under the extreme conditions of short switching times the population of the minor environment converged to 25% at low field strengths, which corresponded to the true population of the minor environment. For acetone the population was stable across the entire frequency range. The following sections will focus on the identification of the chemical origin of these peaks.

6.4.2 Methanol minor environment

For methanol the two peaks are likely associated with the two chemically distinct ^{1}H environments in methanol; as has previously been observed through high field NMR relaxometry of alcohols adsorbed onto metal oxide surfaces.[21] Spectral resolution was not possible for FFC-NMR experiments, but a series of partial deuteration experiments were performed to unambiguously assign the two methanol environments. Figure 6.5 shows the NMRD profiles and corresponding inverse Laplace transforms as a function of acquisition frequency for CH_3OH, CH_3OD and CD_3OH imbibed within γ-alumina. For each of the partially deuterated methanol adsorbates the two-component ^{1}H NMRD behaviour was reduced to a single-component decay. A comparison of the partially deuterated methanol and undeuterated methanol showed that the fast relaxing minor environment was consistent with the hydroxyl ^{1}H atoms, and the slow relaxing major environment was consistent with the alkyl ^{1}H atoms. The differences in relaxation rate between the undeuterated and partially deuterated samples were slightly larger than the sample to sample variation. This was expected however, as the relaxation behaviour was complicated by the introduction of ^{1}H-^{2}H and ^{2}H-^{2}H intramolecular couplings, but the effect was small and did not add ambiguity to the assignment of each relaxation environment.

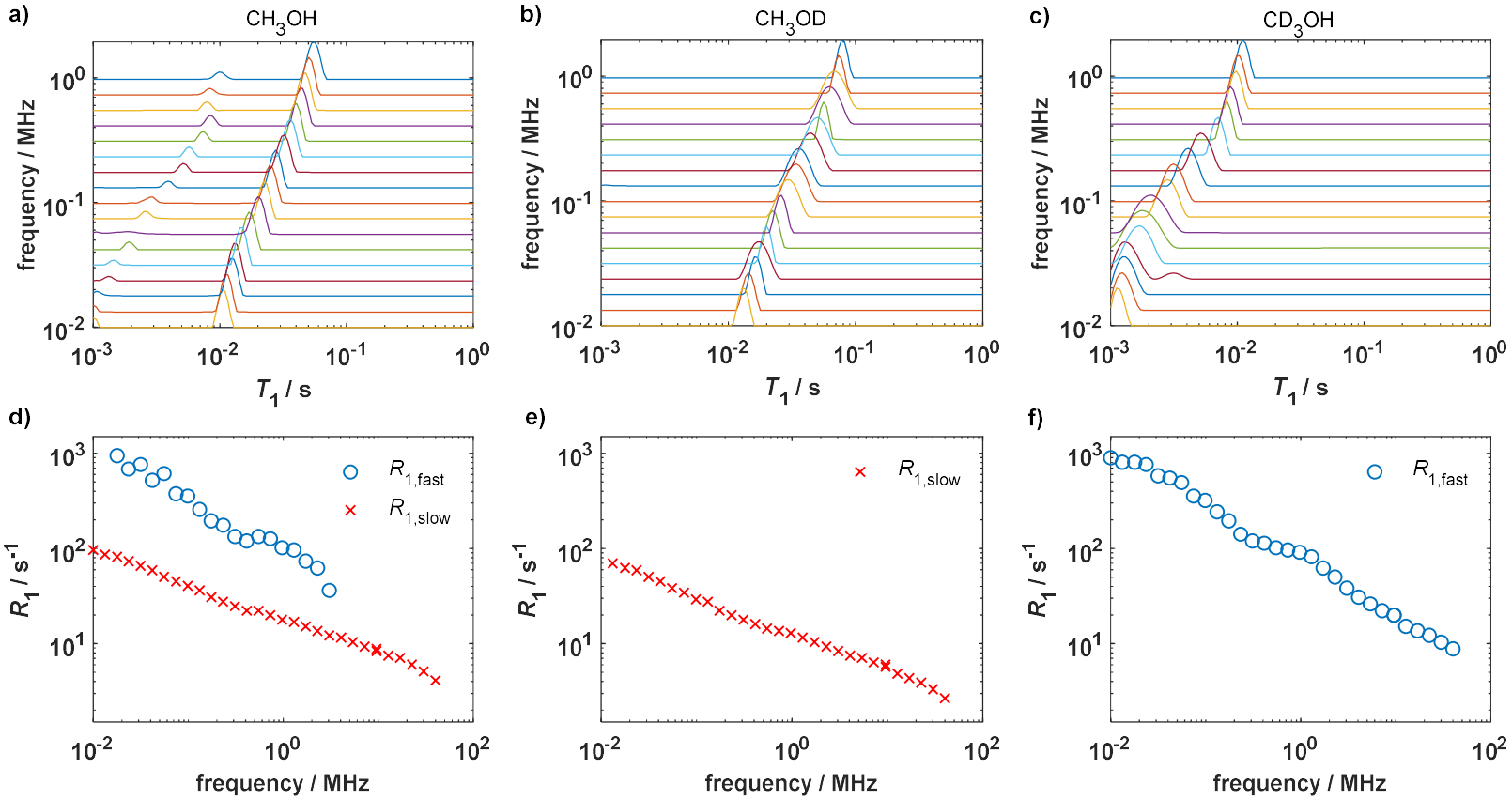

Figure 6.5: The (a-c) T_1 distributions recorded at a frequency values ≤1 MHz and (d-f) the NMRD profiles obtained from each peak in the T_1 distributions of partially deuterated analogues of methanol imbibed within γ-alumina. The imbibed fluids are (a and d) CH_3OH, (b and e) CH_3OD and (c and f) CD_3OH.

The assignment of the peaks to the O^{1}H and alkyl ^{1}H environments led to two observations. The first was that the relaxation rate of the hydroxyl and alkyl ^{1}H of methanol could be described by power laws of exponent -0.57 and -0.36 respectively as shown in Figure 6.6. A more effective relaxation pathway was active for the hydroxyl functionality, which demonstrated that relaxation effects can be functionality specific rather than controlled by the motions of molecules as a whole. The second observation was that the logarithmic average NMRD profile was almost identical to the profile obtained from the alkyl environment. The information about the hydroxyl group relaxation behaviour was lost through logarithmic averaging, and was only accessible from a more detailed analysis of the underlying T_1 distributions.

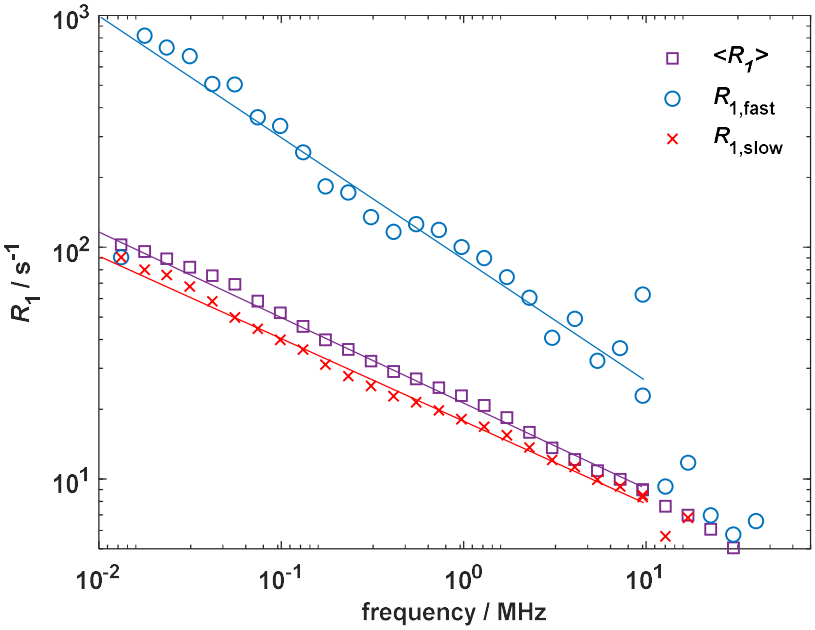

Figure 6.6: The NMRD profile of methanol imbibed within γ-alumina. The modal values of the fast and slow components extracted from the inverse Laplace transformation are compared to the logarithmic average of the distribution.

A final study was performed on a range of alcohols to explore the relative ratios of the two environments under standard measurement conditions (switching time of 3 ms and slewing rate of 12 MHz ms^{-1}, as outlined in section 6.3.2). The relative population of the minor environment observed for *n*- and *iso*-alcohols imbibed within γ-alumina is presented in Figure 6.7 alongside the expected values of the minor environment corresponding to the hydroxyl functionality. The expected decrease in population was not observed for the *n*-alcohols, and the population remained roughly constant between

11-13%. For methanol this represented an underestimate of 12% relative to the expectation value of 25%, but for the longer chain alcohols an overestimate of approximately 4% was observed. For the *iso*-alcohols the populations were underestimates of the true population for both C3 and C4 alcohols, and had a smaller relative population than the corresponding *n*-alcohols. The presence of a minor component for all of the tested alcohols corroborates the assignment of the two peaks being the hydroxyl and alkyl environments. However, the trends in the relative populations suggest that this is difficult to accurately measure when one or both components are fast relative to the switching time of the magnet.

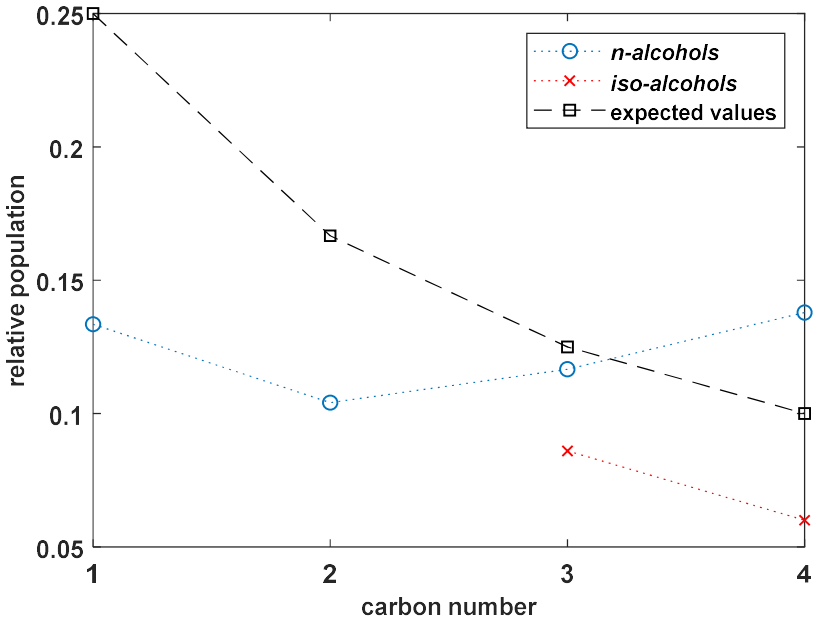

Figure 6.7: The relative populations of the minor environments of several different alcohols imbibed within γ-alumina. The population was calculated as the average value over the frequency range 0.1-1 MHz for reasons discussed in section 6.4.1.

Two component relaxation of alcohols imbibed within mesoporous media was a constant feature. Experiments were performed which showed that a second component was present for methanol imbibed within θ-alumina, silica of varying pore sizes, anatase titania, and calcium oxide. The data are not presented here as the identification and separation of the relaxation mechanisms and underlying molecular dynamics that is required to fully understand the relaxation behaviour of alcohols on different oxide supports is beyond the scope of this thesis.

6.4.3 Acetone minor environment

Figure 6.8 shows the T_1 distributions and corresponding NMRD profiles for acetone imbibed within γ-alumina. For this system the population of the minor environment was much more stable, varying only 3% across the entire frequency range. The stability of the population of this minor environment indicated a simpler relaxation process than that observed for methanol. For both environments the relaxation rates varied with a power law frequency dependence below 10 MHz, with evidence of a plateau at low field strengths for the minor relaxation environment.

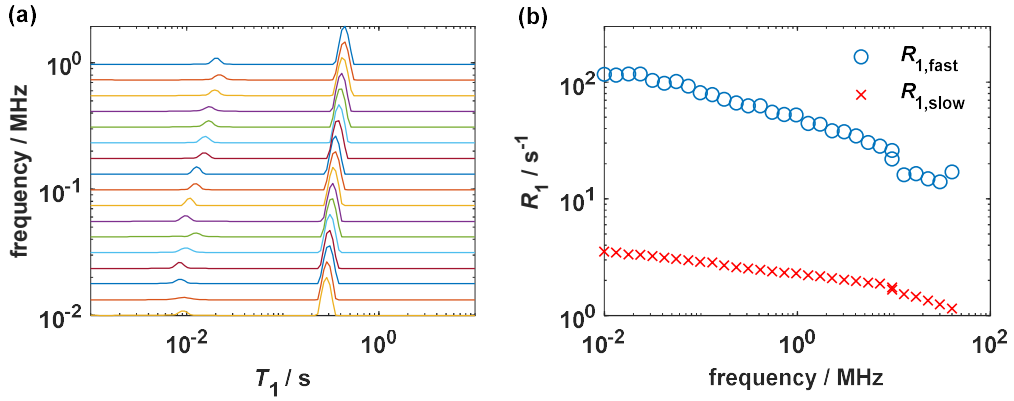

Figure 6.8: The (a) T_1 distributions of acetone imbibed within γ-alumina shown at each ^{1}H Larmor frequency below 1 MHz and the (b) corresponding NMRD profiles calculated from a biexponential fitting of the data.

A range of ketones of increasing size were imbibed within γ-alumina, and a minor environment was observed in all cases. The population of each minor environment is reported in Table 6.1. For acetone the minor environment was substantial, but the relative population quickly reduced as the size of the ketone increased. For pentan-3-one and hexamethylacetone the population of the minor component was sufficiently small that the data could also be fitted to a monoexponential function with a fitting error of <1%. This made the separation of genuine peaks from noise complex, and the presence of a minor component for these two samples imbibed within γ-alumina may have been an artefact generated by forcing a biexponential fit rather than evidence of two component relaxation.

Table 6.1: The relative populations of the minor environment obtained for a range of different ketones imbibed within γ-alumina.

Adsorbate	Population of minor environment / ^{1}H %
acetone	0.123 ± 0.003
butanone	0.044 ± 0.003
pentan-3-one	0.012 ± 0.002
diisoproylketone	0.042 ± 0.004
hexamethylacetone	0.022 ± 0.002

In contrast to methanol, it was not possible to chemically resolve the two methyl groups in acetone due to the symmetry of the molecule. Therefore an alternative explanation of the minor environment was required. The acid-base nature of γ-alumina and the moderate reactivity of acetone was consistent with an aldol condensation reaction taking place on the γ-alumina surface to form mesityl oxide, and therefore the second species that was observed could have been either mesityl oxide or an aldol intermediate. A schematic of this reaction scheme is shown in Figure 6.9.[22]

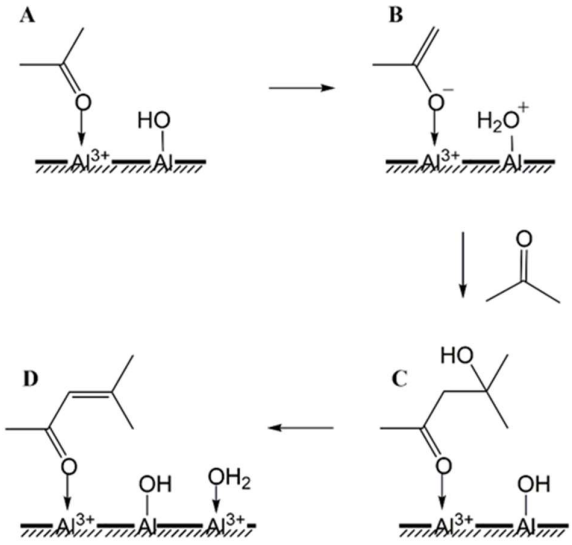

Figure 6.9: A reaction scheme for the formation of mesityl oxide from acetone over a γ-alumina surface via an aldol condensation reaction.[22] The scheme shows acetone (A) adsorbed on the hydroxylated alumina surface, an enolate intermediate (B) caused by deprotonation of acetone, a β-hydroxy ketone intermediate (C) formed by the attack of the enolate into a second equivalent of acetone, and the subsequent dehydration product, mesityl oxide (D). Species B and C can be considered as aldol intermediates, and this aldol reaction can be generalised to all aldehydes and ketones that possess α-hydrogens.

Figure 6.10 shows the ^{1}H spectra recorded over the course of 24 h from the initial point of imbibition in order to monitor the time dependence of any reaction that occurred. The initial data showed a single broad peak centred about a chemical shift of $\delta_{\mathrm{H}} = 2.05$ ppm, which was consistent with acetone adsorbed within a porous medium. Over the course of 24 h the intensity of this peak decreased and two other features became apparent. The first was a well-defined peak at $\delta_{\mathrm{H}} = 6.1$ ppm and the second was a shoulder peak, which appeared at a chemical shift of $\delta_{\mathrm{H}} = 0.9$ ppm. The time dependence of the ^{1}H spectra was consistent with a reaction taking place.

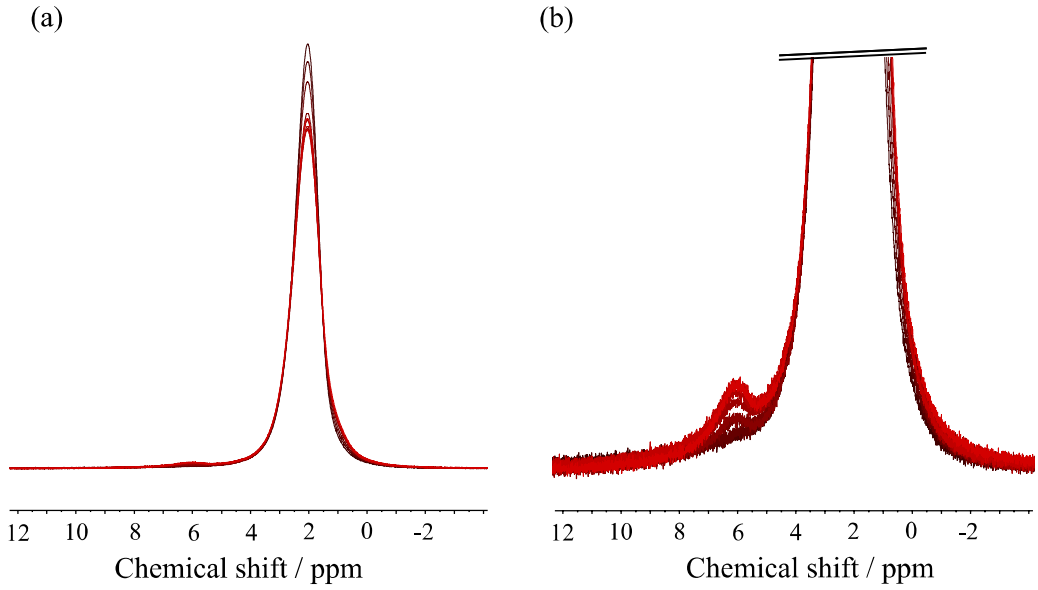

Figure 6.10: The ^{1}H NMR spectra of acetone imbibed within γ-alumina recorded over the first 24 hrs after imbibition. Spectra progress from black (0 h) to red (24 h) along a colour gradient with increasing time after imbibition. The (a) full spectra and (b) magnification of the spectra are shown to highlight all relevant features.

Due to the significant line broadening caused by internal gradient effects, it was not possible to perform a full structural analysis of the ^{1}H spectra. Instead, heteronuclear experiments were pursued to provide greater clarity. Figure 6.11 shows the ^{13}C NMR spectrum of acetone imbibed within γ-alumina every 2 h after initial imbibition. The low signal-to-noise ratio of this experiment meant that 4096 scans were required to achieve a reliable spectrum, and hence it was not possible to time resolve the data over shorter intervals. Each resonance in the ^{13}C spectra was assigned to a species in Figure 6.9 through a comparison with the literature.[23] Figure 6.11b shows that the peaks

corresponding to the intermediate (C) formed rapidly (within the first 2 h) and then did not change further. The peaks corresponding to mesityl oxide behaved very differently, and a clear growth in the peaks at $\delta_C = 125$ and 154 ppm was observed as a function of time. This indicated that a slow formation of mesityl oxide was occuring. This is very strong evidence that an aldol reaction was taking place on the alumina surface.

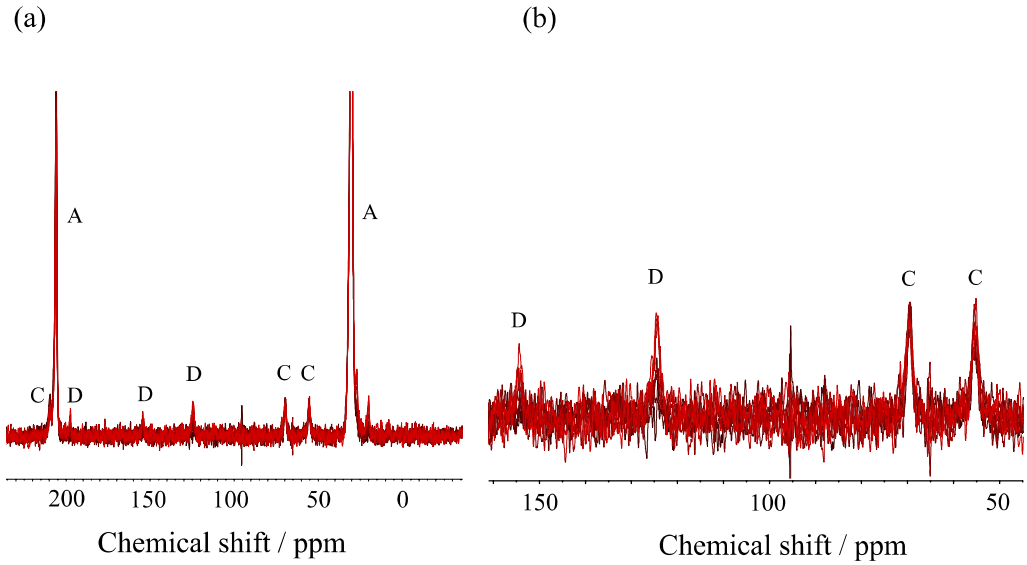

Figure 6.11: The ^{13}C NMR spectra of acetone imbibed within γ-alumina recorded over the first 16 hrs after imbibition. Spectra progress from black (0 h) to red (16 h) along a colour gradient with increasing time after imbibition. The (a) full spectra and (b) magnification of the spectra are shown to highlight all relevant features. Where possible, peaks in the ^{13}C NMR have been assigned to the relevant structures in Figure 6.9 through a comparison to literature values.[23]

To further investigate the influence of this second species on the relaxation behaviour of acetone, additional FFC-NMR experiments were performed using single-component mesityl oxide, and a 50:50 mol% mixture of mesityl oxide and acetone. The NMRD profiles for these two samples imbibed within γ-alumina are compared to acetone imbibed in γ-alumina and are shown in Figure 6.12. For acetone and the 50:50 mol% mixture of acetone and mesityl oxide imbibed within γ-alumina, the logarithmic average NMRD profiles were identical within experimental error, with a maximum relaxation rate of 5 s^{-1} at low field strengths. This was in contrast to single component mesityl oxide, which showed a maximum relaxation rate 3 times larger than both single component acetone and the mixture. Considering the inverse Laplace transformed data in Figure 6.12b it was clearly seen that the T_1 value of the major component in the distributions

does occurr at a smaller value of T_1 for mesityl oxide than for acetone, consistent with the dispersion profiles in Figure 6.12a. For all of the imbibed liquids a well-defined minor peak was present at about $T_1 = 10^{-2}$ s. For acetone this peak comprised ~12.3% of the relative population, 5.4% for mesityl oxide, and 9.8% for the mixture. As noted earlier, because of the finite switching time effects, this was an underestimate of the actual population, however, the longer T_1 times observed for the minor component of acetone (relative to the minor component of methanol) reduce this underestimate.

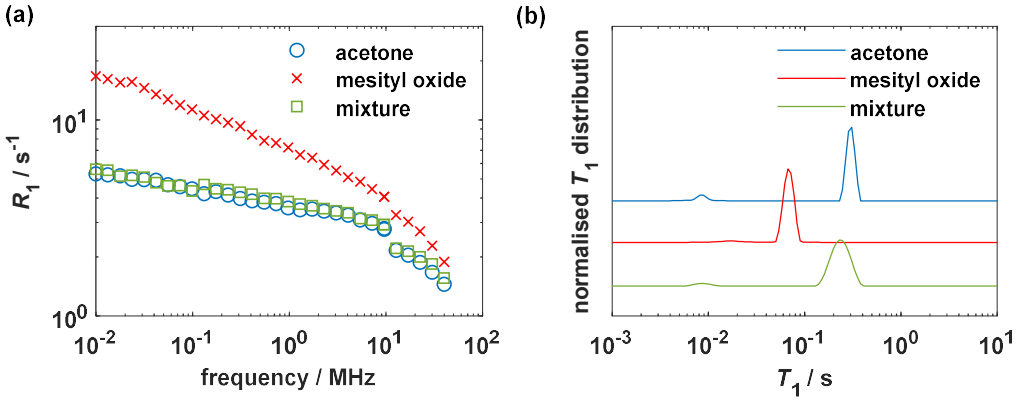

Figure 6.12: The (a) NMRD profiles and (b) inverse Laplace transformed data for acetone, mesityl oxide and a 50:50 mol% mixture of the two imbibed within γ-alumina. The inverse Laplace data was obtained at a ^{1}H Larmor frequency of 17 kHz.

6.5 Discussion

For both methanol and acetone all of the data presented in section 6.4 will be critically assessed in order to confirm the chemical origins of the observed minor environments. The implications of these minor environments on the relaxation behaviour of the two liquids will then be discussed.

6.5.1 Hydroxyl and alkyl group relaxation during alcohol adsorption

The comparison of partially deuterated and undeuterated analogues of methanol imbibed within γ-alumina provided convincing evidence that the major and minor relaxation environments observed in Figure 6.5 represented the alkyl and hydroxyl groups respectively. This assignment led to expected relative populations of 75% and 25% for the alkyl and hydroxyl groups respectively, due to the ratio of the ^{1}H atoms within

methanol. Under standard measurement conditions a significant underestimate of the population of the minor environment was observed, with a maximum relative population of 18% for the hydroxyl group. The low frequency behaviour was not stable, and indicated a loss of magnetization during the switching intervals. The loss of magnetization affected the fast relaxing hydroxyl environment more significantly than the slow relaxing alkyl environment, and reduced the apparent relative population of the hydroxyl group. At a sufficiently short SWT this effect was negated and the population of the hydroxyl tended to a constant value of 25%, which was consistent with the expected value. This confirmed the assignment of the two peaks to the two chemical functionalities of methanol.

Assignment of the two relaxation environments to the O^1H and alkyl ^1H environments showed that the hydroxyl group experienced more effective relaxation than the alkyl group. Commonly the relaxation behaviour of an adsorbate imbibed within a porous medium is controlled by the motions of the molecule as a whole,[24–27] rather than specific functionalities. However, the separation of multiple relaxation environments within the same molecule has not previously been demonstrated using FFC-NMR. It was likely that the chemical differences between these environments allowed different relaxation processes to occur. The key difference between the two environments being the ability of the methanol hydroxyl environment, OH_M, to exchange with the surface hydroxyl environment, OH_S as shown in Figure 6.13.

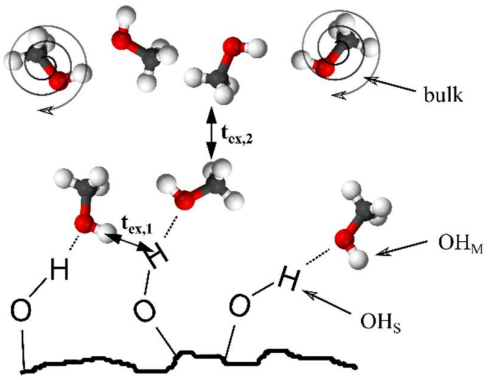

Figure 6.13: A schematic representation of the three different relaxation environments of exchangeable ^1H atoms. These can be classified as surface hydroxyls, OH_S, and methanol hydroxyls, OH_M. The OH_M can be further subdivided into hydroxyls on adsorbed methanol and hydroxyls in bulk methanol. Provided that $t_{ex,1}$ and $t_{ex,2} >> T_1$ all three environments will be in fast exchange.

The occurrence of an exchange process between the surface hydroxyls and the methanol hydroxyls was confirmed by the imbibition of methanol-d_4 within γ-alumina. The NMRD profile of imbibed methanol-d_4 was identical to methanol-d_3. The only source of ^{1}H atoms that could have been incorporated into methanol-d_4, and therefore detected by FFC-NMR, must have originated on the catalyst surface and been transferred to methanol through a rapid exchange process. The exchange process had two important consequences. The first was that the observed T_1 of the hydroxyl group became a weighted average of the OH_M T_1 and OH_S T_1 (which was significantly lower). This resulted in the NMRD profile of the methanol hydroxyl group showing a greater R_1 value than the alkyl group at all frequencies studied, and a greater dispersion across the frequency range. The second consequence of the exchange process was that the effective residence time of the OH_M species on the surface was altered relative to that of the alkyl group in methanol. This meant that the power law exponent of the NMRD profile of the hydroxyl group was no longer a reliable metric for measuring the interaction strength of methanol with the alumina surface. The hydroxyl group is therefore an exception to the observed correlation between the polarity of a molecule and its surface interaction strength, which was shown previously in Figure 5.9. As the molecular dynamics of the molecule were controlled by the interaction strength between methanol and the surface it would not be possible for one functionality to experience a greater residence time than the other without the possibility of exchange. The relaxation enhancement seen for OH_M imbibed within γ-alumina was instead a probe of the surface hydroxyl chemistry. As a consequence, it would be misleading to compare the relaxation behaviour of adsorbates with exchangeable ^{1}H atoms, such as water, to adsorbates that contain only non-exchangeable groups, such as DMSO.

By taking a logarithmic average of the methanol data the relaxation rate became a population weighted average of the methanol hydroxyl and alkyl relaxation environments. The enhanced relaxation of the hydroxyl environment increased the logarithmic average value of R_1 relative to that of the true R_1 of the alkyl group. If not correctly accounted for, this overestimate may be interpreted erroneously as a greater interaction strength. A power law exponent of 0.36 was obtained by fitting the relaxation rate of the alkyl environment using eq. (5.6). This value was only slightly lower than the value of 0.38 obtained from the logarithmic average NMRD data. As methanol had the largest ratio of hydroxyl ^{1}H atoms to alkyl ^{1}H atoms of all alcohols used within this study,

the difference between the logarithmic average and the relaxation rate of the alkyl environment would have been the greatest for this adsorbate. The effect was small for methanol, and it follows that it will also be small for larger alcohols. This meant that, to a good approximation, the logarithmic average NMRD profile of alcohols were equivalent to the relaxation rate of the alkyl environment, and were directly comparable to non-exchangeable adsorbates as a measure of interaction strength. This can be seen by the near coincidence of the logarithmic and slow component (alkyl) NMRD profiles of methanol imbibed within γ-alumina, which are shown in Figure 6.6.

6.5.2 Implications of stable reaction intermediates in ketone adsorption

The relaxometry and spectroscopy data presented in section 6.4.3 were consistent with the minor environment observed for acetone imbibed within γ-alumina being a stable reaction intermediate formed by an aldol reaction that occurred at the catalyst surface. The ^{13}C spectra shown in Figure 6.11 showed that the intermediate reached an equilibrium concentration shortly after imbibition. This allows the population trends shown in Table 6.1 for the intermediate to be used to support the occurrence of aldol chemistry. As the steric bulk of the ketone was increased the formation of the enolate intermediate, B, became less favourable, and therefore the equilibrium was shifted towards the starting materials. This reduced the population of the intermediate for larger ketones. In the extreme case of hexamethylacetone, the absence of α-hydrogens prevented aldol chemistry from occurring. This was consistent with the observed population of the minor environment being negligible within a reasonable degree of error in the data fitting. The presence of a very small peak (~1% relative population) was likely to be an artefact introduced by forcing a two-component model fit to the data, or the presence of low level impurities in the starting material.

Spectroscopic evidence presented in Figure 6.11 also supported the occurrence of aldol chemistry. Resonances ascribed to acetone (A), a β-hydroxy ketone intermediate (C), and the final product mesityl oxide (D), as referred to in Figure 6.9, were clearly resolved. No evidence of the enolate intermediate (B) was observed, however its existence (or an equivalent reaction intermediate) was implied by the formation of species C and D. The presence of multiple components in the pore space implied that a competitive adsorption process was occurring. It has been shown in Chapter 5 that the more polar compound would have greatest affinity for the alumina surface. As intermediate C contains a polar

hydroxyl functionality, it outcompeted acetone or mesityl oxide for surface binding sites, leading to the enhanced relaxation rate observed for the intermediate relative to the starting material. This confirms the assignment of the two environments present in acetone as the unreacted acetone and a stable reaction intermediate.

The effects of the aldol intermediate on the relaxation behaviour of acetone was most evident when the relaxation behaviour of single component acetone, and mesityl oxide was compared to a 50:50 mol% mixture imbibed within γ-alumina. The data is shown in Figure 6.12. The greater relaxation rate (and dispersion slope) shown by single component mesityl oxide imbibed within γ-alumina suggested that mesityl oxide had a stronger interaction with the surface than acetone. This result was surprising, because the aldol condensation of acetone to mesityl oxide is an established heterogeneous catalytic conversion.[22,28,29] The apparent stronger interaction of the product, mesityl oxide, than the reactant, acetone, with the γ-alumina surface would suggest that the catalyst would bind the product strongly. This would inhibit further conversion, or result in the formation of a wide array of by-products; such behaviour is not typical of this reaction. Further, the similarity of dispersion curves for acetone and the 50:50 mol.% mixture of mesityl oxide and acetone suggested that the mesityl oxide was characterised by a much weaker interaction with the surface when co-imbibed with acetone. Greater insights into the physicochemical effects leading to this unusual behaviour were found by examining the minor component of each T_1 profile. The steady-state concentration of the aldol intermediate was only 5% for mesityl oxide compared to 13% for acetone – likely due to mesityl oxide having been a poorer substrate for aldol reactions than acetone.[29] For the γ-alumina used within this study a composition fraction of ~16% would have been required to form a full monolayer coverage of the intermediate. This meant that even if the strongly interacting intermediate fully outcompeted the unreacted species for surface binding sites there were still surface sites available for the unreacted species to access. For mesityl oxide the remaining 95% of the signal from unreacted adsorbate had greater access to the surface than the unreacted adsorbate of acetone, which resulted in a much lower value of T_1 for the former. The T_1 distribution acquired for the 50:50 mol.% mixture of mesityl oxide and acetone also showed a major and minor peak. The T_1 value of the unreacted species was similar to that of the single component acetone data, which suggested that mesityl oxide was much less strongly interacting with the surface in the presence of acetone. A minor peak representing ~10% of the population was also

observed, which was consistent with the surface accessibility arguments presented above. The addition of the more reactive substrate, acetone, to the mesityl oxide system increased the concentration of aldol intermediates. As a result of the competitive adsorption process the T_1 of the major peak increased. Under these conditions the T_1, and hence the expected interaction with the γ- alumina surface, were very similar for acetone and mesityl oxide, and also essentially identical to that of single component acetone.

The competitive adsorption process observed for acetone imbibed within γ-alumina weakened the surface interaction of this adsorbate. This was seen in the phenomenological modelling of the data presented in chapter 5, which showed that acetone had a significantly weaker interaction with the surface than was predicted from its polarity. In contrast, the structurally similar adsorbate, DMSO, was unreactive under the measurement conditions, and showed a power law 3 times larger than acetone imbibed within γ-alumina. The reactivity of these two species was only evident from the T_1 distributions, and was not immediately clear from a logarithmic average analysis of the T_1 dispersion data. This demonstrates the importance of analysing all of the features contained within T_1 distributions when possible.

In summary, it was shown that by taking the logarithmic average dispersion data for single-component mesityl oxide and acetone, the competitive adsorption behaviour of the two species was not predicted. This meant that misinterpretations of the relative interaction strengths of the two species with a γ-alumina surface were likely. However, by comparing the data for the single-component acetone and mesityl oxide in the T_1-domain, there was clear evidence of the stable reaction intermediates present during single-component adsorption. These intermediates were characterised in terms of their relaxation rates and populations, which had a strong effect on the relaxation behaviour of the major relaxation environment. Therefore, the information gathered from the single component systems was sufficient to predict the behaviour of the binary system. The T_1 domain analysis was demonstrated to be a rapid and informative method for analysing FFC-NMR data. This approach is not limited to the formation of reaction intermediates and can theoretically be generalised to any form of *in situ* competitive adsorption processes, such as solvent effects[30,31] or water promotion effects.[32,33]

6.6 Conclusions

The FFC-NMR data acquired in chapter 5 were further analysed in the T_1 domain at each magnetic field strength. Doing so allowed the observation of a minor component in the T_1 distributions of methanol and acetone when imbibed within γ-alumina. These intermediates were assigned to functionality specific relaxation behaviour (hydroxyl and alkyl), and the presence of a stable reaction intermediate respectively. The minor peaks were characterised in terms of their reaction rates and relative populations. The relaxation rates and the population of the acetone minor environment were robust regardless of the acquisition parameters or processing techniques used. In contrast, the relative population of the methanol minor environment was optimised by minimising the switching times of the FFC-NMR experiment. At very short switching times the signal loss of the hydroxyl environment was minimised and relative populations of 25% and 75% were obtained for the hydroxyl and alkyl group of methanol respectively. For larger alcohols a more complex interaction occurred and the hydroxyl environment was no longer a quantitative measure of population.

By analysing the methanol and acetone data sets in the T_1 domain it was possible to answer several questions that may arise during the initial interpretation of the adsorption behaviour of these liquids. In the case of methanol the two component behaviour observed in the T_1 domain was dominated by the major component in the logarithmic average data presented in chapter 5. Therefore to a good approximation the data only represent the non-exchangeable ^{1}H atoms in this system, and were a reliable measure of interaction strength. For water the exchange effect was expected to be more dominant, and therefore the interpretation of this adsorbate requires further consideration.

For acetone, the observation of a stable adsorption intermediate altered the adsorption properties of acetone. In this case, the reaction intermediate was more strongly bound to the surface than acetone itself, and this prevented the unreacted acetone from interacting significantly with the surface. This justified why acetone had a much lower TOD and power law exponent than expected based on its polarity. This was confirmed through a comparison to DMSO, which has a similar structure and polarity, but was not capable of reacting to form the observed intermediate.

The subtle differences between exchangeable and non-exchangeable functionalities will be explored in greater detail in chapter 7 as a formal modelling approach is implemented to describe the observed relaxation behaviour for each adsorbate. Furthermore, the competitive adsorption behaviour seen for ketones imbibed within γ-alumina will be explored in a controlled manner for binary liquid mixtures in chapter 8. In this case two or three component behaviour is expected, and ability of FFC-NMR to characterise the populations and relaxation rates of these mixtures will be tested.

6.7 References

(1) Keeler, J. *Understanding NMR Spectroscopy*; John Wiley & Sons, 1999.

(2) Ferrante, G.; Sykora, S. Technical Aspects of Fast Field Cycling. *Adv. Inorg. Chem.* **2005**, *57*, 405–470.

(3) Mitchell, J.; Broche, L. M.; Chandrasekera, T. C.; Lurie, D. J.; Gladden, L. F. Exploring Surface Interactions in Catalysts Using Low-Field Nuclear Magnetic Resonance. *J. Phys. Chem. C* **2013**, *117*, 17699–17706.

(4) De Pasquale, C.; Marsala, V.; Berns, A. E.; Valagussa, M.; Pozzi, A.; Alonzo, G.; Conte, P. Fast Field Cycling NMR Relaxometry Characterization of Biochars Obtained from an Industrial Thermochemical Process. *J. Soils Sediments* **2012**, *12*, 1211–1221.

(5) Hsu, C.; Chen, Y.; Rana, B. S.; Kumar, R.; Sinha, A. K.; Hwang, D. W. Dynamics of Water in Hierarchical Mesoporous H-ZSM 5 by Fast Field-Cycling. *J. Phys. Chem. C* **2014**, *118*, 20481–20487.

(6) Zampetoulas, V.; Lurie, D. J.; Broche, L. M. Correction of Environmental Magnetic Fields for the Acquisition of Nuclear Magnetic Relaxation Dispersion Profiles below Earth's Field. *J. Magn. Reson.* **2017**, *282*, 38–46.

(7) Zhou, B.; Yang, P.; Ferrante, G.; Pasin, M.; Steele, R.; Bortolotti, V.; Korb, J.-P. Applying Fast-Field Cycling Nuclear Magnetic Relaxation to Petroleum Tight Sandstone Rocks. *Energy & Fuels* **2019**, *33*, 1016–1022.

(8) Korb, J.; Ferrante, G.; Bubici, S.; Mallett, M. New Instrumental Platform for the

Exploitation of the Field- Dependence of T1 in Rock Core Analysis and Petroleum Fluids : Application to T_1-T_2 Correlation Maps. *Diffus. fundementals* **2014**, *22*, 1–7.

(9) Korb, J. P.; Freiman, G.; Nicot, B.; Ligneul, P. Dynamical Surface Affinity of Diphasic Liquids as a Probe of Wettability of Multimodal Porous Media. *Phys. Rev. E* **2009**, *80*, 61601.

(10) Korb, J. P.; Godefroy, S.; Fleury, M. Surface Nuclear Magnetic Relaxation and Dynamics of Water and Oil in Granular Packings and Rocks. *Magn. Reson. Imaging* **2003**, *21*, 193–199.

(11) Barberon, F.; Korb, J.; Petit, D.; Morin, V.; Bermejo, E. Probing the Surface Area of a Cement-Based Material Ny Nuclear Magnetic Relaxation Dispersion. *Phys. Rev. Lett.* **2003**, *90*, 116103.

(12) Plassais, A.; Lequeux, N.; Petit, D.; Barberon, F.; Bresson, B. Microstructure Evolution of Hydrated Cement Pastes. *Phys. Rev. E* **2005**, 041401.

(13) Neudert, O.; Mattea, C.; Stapf, S. Application of CPMG Acquisition in Fast-Field-Cycling Relaxometry. *Microporous Mesoporous Mater.* **2018**, *269*, 103–108.

(14) Butler, J. P.; Reeds, J. A.; Dawson, S. J. Estimating Solutions of First Kind Integral Equations with Nonnegative Constraints and Optimal Smoothing. *J. Numer. Anal.* **1981**, *18*, 381–397.

(15) Reci, A.; Sederman, A. J.; Gladden, L. F. Obtaining Sparse Distributions in 2D Inverse Problems. *J. Magn. Reson.* **2017**, *281*, 188–198.

(16) Callaghan, P. T. *Translational Dynamics & Magnetic Resonance*; Oxford University Press, 2011.

(17) Korb, J. P. Nuclear Magnetic Relaxation of Liquids in Porous Media. *New J. Phys.* **2011**, *13*, 35016.

(18) Badea, C., Pop, A., Mattea, C. Stapf, S. Ardelean, I. The Effect of Curing Temperature on Early Hydration. *Appl. Magn. Reson.* **2014**, *45*, 1299–1309.

(19) Stapf, S.; Ren, X.; Talnishnikh, E.; Blümich, B. Spatial Distribution of Coke Residues in Porous Catalyst Pellets Analyzed by Field-Cycling Relaxometry and

Parameter Imaging. *Magn. Reson. Imaging* **2005**, *23*, 383–386.

(20) Reci, A.; Ainte, M. I.; Sederman, A. J.; Mantle, M. D.; Gladden, L. F. Optimising Sampling Patterns for Bi-Exponentially Decaying Signals. *Magn. Reson. Imaging* **2019**, *56*, 14–18.

(21) Stubner, B.; Knozinger, H.; Conard, J.; Fripiat J., J. Adsorption of Alcohols on Alumina. 2. Nuclear Magnetic Resonance Investigation. *J. Chem. Phys.* **1978**, *82*, 1811–1817.

(22) Zaki, M. I.; Hasan, M. A.; Pasupulety, L. Surface Chemistry of Acetone on Metal Oxides: IR Observation of Acetone Adsorption and Consequent Surface Reactions on Silica-Alumina versus Silica and Alumina. *Langmuir* **2000**, *16*, 430–436.

(23) Singhal, A.; Pai, M. R.; Rao, R.; Pillai, K. T.; Lieberwirth, I.; Tyagi, A. K. Copper (I) Oxide Nanocrystals – One Step Synthesis , Characterization , Formation Mechanism , and Photocatalytic Properties. *Eur. J. Inorg. Chem* **2013**, 2640–2651.

(24) Korb, J. P.; Whaley Hodges, M.; Gobron, T.; Bryant, R. G. Anomalous Surface Diffusion of Water Compared to Aprotic Liquids in Nanopores. *Phys. Rev. E* **1999**, *60*, 3097–3106.

(25) Chemmi, H.; Petit, D.; Levitz, P.; Denoyel, R.; Galarneau, A.; Korb, J.-P. Noninvasive Experimental Evidence of the Linear Pore Size Dependence of Water Diffusion in Nanoconfinement. *J. Phys. Chem. Lett.* **2016**, *7*, 393–398.

(26) Muncaci, S.; Mattea, C.; Stapf, S.; Ardelean, I. Frequency-Dependent NMR Relaxation of Liquids Confined inside Porous Media Containing an Increased Amount of Magnetic Impurities. *Magn. Reson. Chem.* **2013**, *51*, 123–128.

(27) Conte, P.; Loddo, V.; De Pasquale, C.; Marsala, V.; Alonzo, G.; Palmisano, L. Nature of Interactions at the Interface of Two Water-Saturated Commercial TiO_2 Polymorphs. *J. Phys. Chem. C* **2013**, *117*, 5269–5273.

(28) Hernández-Giménez, A. M.; Ruiz-Martínez, J.; Puértolas, B.; Pérez-Ramírez, J.; Bruijnincx, P. C. A.; Weckhuysen, B. M. Operando Spectroscopy of the Gas-Phase Aldol Condensation of Propanal over Solid Base Catalysts. *Top. Catal.* **2017**, *60*, 1522–1536.

(29) Gamman, J. J.; Jackson, S. D.; Wigzell, F. A. Synthesis of Methyl Isobutyl Ketone over Pd/MgO/SiO_2. *Ind. Eng. Chem. Res.* **2010**, *49*, 8439–8443.

(30) Sievers, C.; Noda, Y.; Qi, L.; Albuquerque, E. M.; Rioux, R. M.; Scott, S. L. Phenomena Affecting Catalytic Reactions at Solid–Liquid Interfaces. *ACS Catal.* **2016**, *6*, 8286–8307.

(31) D'Agostino, C.; Brett, G. L.; Miedziak, P. J.; Knight, D. W.; Hutchings, G. J.; Gladden, L. F.; Mantle, M. D. Understanding the Solvent Effect on the Catalytic Oxidation of 1,4-Butanediol in Methanol over Au/TiO_2 Catalyst: NMR Diffusion and Relaxation Studies. *Chem. Eur. J.* **2012**, *18*, 14426–14433.

(32) Davies, P. R. On the Role of Water in Heterogeneous Catalysis: A Tribute to Professor M. Wyn Roberts. *Top. Catal.* **2016**, *59*, 671–677.

(33) Hutchings, G. J. Promotion in Heterogeneous Catalysis : A Topic Requiring a New Approach? *Perspect. Catal.* **2001**, *75*, 1–12.

Chapter 7 : Surface dynamics of liquids imbibed within γ-alumina

Contents

7.1 Introduction

The results presented in chapter 5 showed a clear correlation between the solid-liquid interaction strength of several different liquids imbibed within γ-alumina and the slope of the corresponding NMRD profile. This was further built upon in chapter 6, where functionality specific adsorption dynamics and competitive adsorption processes were shown to contribute to the observed dispersion profiles. The sensitivity of the FFC-NMR technique to such a wide array of molecular dynamics showed that the NMRD profiles contained more information about the solid-liquid interactions than it was possible to obtain from the simple correlation. In this chapter, this additional information is explored through a formal modelling of the NMRD profile. For a subset of the liquids studied in chapter 5, the surface dynamics of the imbibed liquids was characterised through temperature dependent experiments. The temperature dependence of each adsorbate was combined with an analysis of all of the features present in the corresponding NMRD profiles, and the nature of the underlying chemical interactions. This information allowed the application of a suitable model to the NMRD profiles for a wide range of different liquids, and a quantitative assessment of their solid-liquid interaction strengths.

7.2 Background and literature review

7.2.1 Modelling approaches of FFC-NMR for porous media systems

In this section the main theories used to describe the relaxation behaviour of liquids imbibed within porous media are outlined. In each case an analysis of the underlying molecular dynamics is applied in order to obtain expressions for the surface relaxation rate, $R_{1,\mathrm{S}}$, or the spectral density functions that can be combined with the well-known relaxation equations for like and unlike spins respectively:

$$R_{1,\mathrm{S},II} = A[J(\omega_I) + 4J(2\omega_I)]\,, \tag{7.1}$$

$$R_{1,\mathrm{S},IS} = A[7J(\omega_S) + 3J(\omega_I)]\,, \tag{7.2}$$

where ω_I and ω_S refer to the proton and electron Larmor frequency respectively, and A is a constant. These expressions can then be combined with the two-phase fast exchange model to describe the observed relaxation behaviour, $R_{1,\mathrm{obs}}$, as:[1]

$$R_{1,\mathrm{obs}} = R_{1,\mathrm{B}} + p(R_{1,\mathrm{S}} - R_{1,\mathrm{B}}) \,, \tag{7.3}$$

where p is the population fraction of the adsorbed surface layer, and $R_{1,\mathrm{B}}$ is the bulk relaxation rate.

7.2.1.1 Fast molecular relaxation processes

Relaxation processes caused by fast molecular motions result in features of the nuclear magnetic relaxation dispersion (NMRD) profile at high field strengths. These fast motions include many translational or rotational processes, meaning that the physical origin of high field relaxation is often poorly defined. Many different sources of molecular motions have been cited as controlling the high field relaxation behaviour. For example, for liquids imbibed within porous media the high frequency dispersions can arise entirely from the bulk liquid. For liquids containing dissolved oxygen, which is a paramagnetic relaxation source, a simple Lorentzian spectral density can be assumed following the theory outlined previously,[2]

$$J(\omega) \propto \frac{\tau}{1 + (\omega_{\mathrm{S}}\tau)^2} \,, \tag{7.4}$$

where τ is an effective correlation time combining the electron spin-lattice relaxation time and the translational diffusion of the liquid, and ω_S is the electron Larmor frequency. The presence of molecular oxygen causes a dispersion in the NMRD profile of the bulk liquid at Larmor frequencies above 10 MHz. As the relaxation rate of liquids imbibed within porous media is a population weighted sum of the bulk and surface relaxation rates (eq. (7.3)), any relaxation process that has a frequency dependence in the bulk state will also show a frequency dependence when imbibed within a porous medium. Alternatively, other authors argue that the main source of the high field relaxation behaviour of liquids imbibed within porous media is due to fast local molecular reorientations.[3,4] As the reorientations are fast the relaxation dispersion is limited to a narrow high field region, and no further changes in R_1 occur at low field strengths. To satisfy such constraints the fast local processes are also described by a Lorentzian spectral density function,

analogous to eq. (7.4). This means that although the physical origin of the relaxation may be argued to be very different, the mathematical modelling of it is almost identical. These fast relaxation processes occur simultaneously with much slower processes, which will dominate the relaxation behaviour at low field strengths.

7.2.1.2 Korb model

In the model of Korb,[5] for transient (non-specific) surface binding in the presence of paramagnetic impurities, an intermolecular interaction occurs between the adsorbate (*I* spins) and any paramagnetic species (*S* spins) at the pore surface. The high gyromagnetic ratio of the unpaired electron ($\gamma_S = 658\gamma_I$) means that fluctuations of the *I*-*S* dipolar interaction lead to highly efficient relaxation. Due to the efficacy of paramagnetic relaxation this process has been shown to be the dominant relaxation mechanism for liquids imbibed in porous media when only 36 ppm of ferric ions (Fe^{3+}) were present as paramagnetic impurities.[6] Typically this relaxation mechanism is accompanied by a restriction of the geometrical freedom of the molecule due to surface binding. The restriction leads to a slow decay of the correlation function, and more frequent *I*-*S* re-encounters[7] as shown in Figure 7.1. The adsorbate explores the pore surface in a series of jumps with a characteristic hopping time, τ_m. Eventually, after many jumps, the adsorbate will escape from the surface and lose correlation.[5] This escape process is characterised by a correlation time of surface residence, τ_s. The ratio of τ_s/τ_m describes the average number of jumps an adsorbate undertakes before leaving the surface, and has been used as a surface affinity metric, analogous to T_1/T_2 ratios and rock wettability indices.[8]

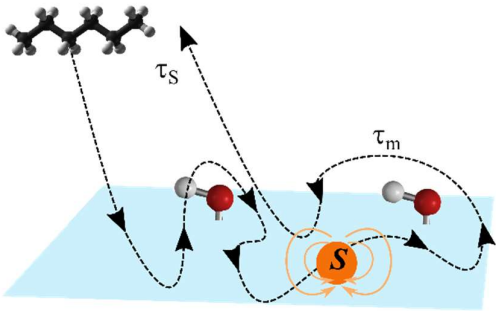

Figure 7.1: A schematic representation of the Korb model of NMR relaxation based on the transient binding of adsorbates in the presence of paramagnetic surface impurities. Fluctuations of the *I*-*S* dipolar interaction are modulated by a surface hopping mechanism, characterised by a hopping time, τ_m, and a surface residence time, τ_S.

In the case of a quasi-two dimensional diffusion, the spectral density for this process can be explicitly calculated:[5]

$$J(\omega) = \frac{3\pi\sigma_S}{20d^2\delta'^2}\tau_{\mathrm{m}}\ln\left[\frac{1+\omega^2\tau_{\mathrm{m}}^2}{\tau_{\mathrm{m}}^2/\tau_{\mathrm{S}}^2+\omega^2\tau_{\mathrm{m}}^2}\right], \tag{7.5}$$

which results in an observed relaxation of the form:[5]

$$\frac{1}{T_{1,\mathrm{obs}}} = \frac{1}{T_{1,\mathrm{bulk}}} + \left(\frac{\mu_0}{4\pi}\right)^2 \frac{N_S}{N}\frac{\pi\sigma_S(\gamma_{\mathrm{I}}\gamma_{\mathrm{S}}\hbar)^2 S(S+1)}{15d^2\delta'^2}$$
$$\tau_{\mathrm{m}}\left(3\ln\left[\frac{1+\omega_I^2\tau_{\mathrm{m}}^2}{\tau_{\mathrm{m}}^2/\tau_{\mathrm{S}}^2+\omega_I^2\tau_{\mathrm{m}}^2}\right] + 7\ln\left[\frac{1+\omega_S^2\tau_{\mathrm{m}}^2}{\tau_{\mathrm{m}}^2/\tau_{\mathrm{S}}^2+\omega_S^2\tau_{\mathrm{m}}^2}\right]\right). \tag{7.6}$$

For these expressions μ_0 is the vacuum permittivity constant, $N_S/N = \lambda S/V_{\mathrm{P}}$ is the ratio of molecules at the pore surface to the total number of molecules, λ is the thickness of the adsorbed surface layer, S is the specific surface area, V_{P} is the pore volume, σ_S is the density of paramagnetic impurities on the surface, γ_{I} and γ_{S} are the gyromagnetic ratios of the ^{1}H spin and unpaired electron respectively, S is the spin of the paramagnetic impurity, d is the molecular diameter, δ' is an effective distance of minimal approach between the I and S spins, τ_{m} is the surface correlation time between jumps, and τ_{s} is the surface residence correlation time. This model will be referred to herein as the Korb model. The distinctive feature of this relaxation mechanism is a bilogarithmic frequency dependence, which physically manifests itself as two straight lines in the semi-logarithmic plot of frequency against relaxation rate, with a gradient ratio of 10:3. This behaviour has previously been observed for oil in rock cores,[8] water in cement pastes,[9] and a range of polar liquids imbibed within silica.[6] The exact form of the relaxation model has been evaluated for a range of porous media systems based on small variations in the initial assumptions.[5,7,8,10] In most cases the bilogarithmic frequency dependence is preserved, as shown in Figure 7.2, but depending on the values of τ_{S} and τ_{m} it can be difficult to identify this feature.[11]

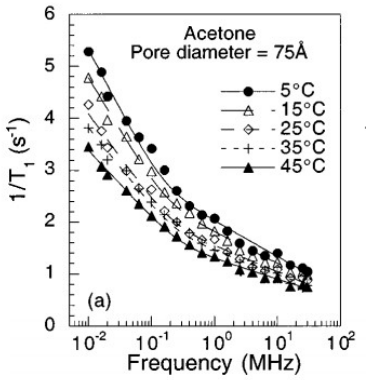

Figure 7.2: The NMRD profiles measured for acetone imbibed within a porous glass with an average pore size of 7.5 nm. In the semilogarithmic plotting of the data, the bilogarithmic frequency dependence of $1/T_1$ can be seen as two straight lines in the frequency dependence of $1/T_1$. Reproduced from et al.[6]

7.2.1.3 Reorientations mediated by translational diffusion

In the case of strong and directional binding at the pore surface, the intramolecular relaxation of liquids imbibed within porous media is often cited as being caused by a modulation of the rotational dipolar (or quadrupolar if applicable) coupling over very long timescales.[3,12–14] These slow molecular motions are achieved through an intermittent binding process, in which the adsorbate binds to the surface for an average time, τ_A, before desorbing into the bulk, and undergoing a bulk excursion of average time, τ_B, before returning to the surface. This bulk mediated surface diffusion (BMSD)[15] process can occur many times before the correlation function decays fully, and is shown schematically in Figure 7.3a. This process occurs many orders of magnitude slower than the rotation of bulk liquids, but is almost universally observed. The persistence of the correlation function can then be justified through a directional binding of the liquid at the pore surface. For strongly interacting species, the surface will impose a preferential orientation of binding upon the liquid, thereby restricting the degree of rotational freedom available to the molecule. Through a series of bulk excursions the molecule will move to different binding sites within the pore space leading to a slow loss of correlation. In the presence of pore curvature or surface roughness this relaxation process will be enhanced, and the correlation function will decay through a process known as reorientations mediated through translational diffusion (RMTD),[12] as is shown in Figure 7.3b.

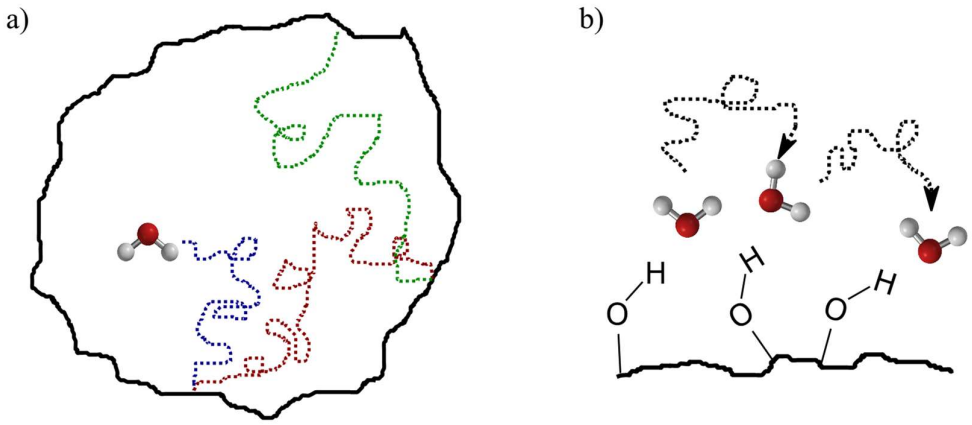

Figure 7.3: Schematic diagrams showing a) bulk mediated surface diffusion, and b) reorientations mediated by translational diffusion.

Following the formalisms introduced for relaxation due to a purely RMTD process the relaxation behaviour can be defined as: [3,16]

$$R_{1,S} \propto b\Gamma(1-\chi)c^{-(1-\chi)}\omega_H{}^{\chi}\,, \tag{7.7}$$

where b and c are constants, Γ is the gamma function, ω_H is the ^{1}H Larmor frequency, and χ is a constant describing the fractal surface dimensionality. A power law frequency dependence of the relaxation rate on the Larmor frequency is expected from eq. (7.7). The power law exponent has previously been shown to depend only on the geometry of the surface and its roughness, rather than the differences in the solid-liquid interaction strength.[17] This was demonstrated for several different polar liquids imbibed within the same porous glass, the NMRD profiles of which all showed the same value of χ.[17] However, systems where this is not the case have also been demonstrated in the literature. Different power law exponents have been reported for water and DMSO imbibed within alumina,[18] and for water and heptane imbibed within carbon xerogels.[19] The differences in the exponent were either not discussed in detail, or related to the "effective surface roughness" experienced by the adsorbate. This latter concept implies that the surface adsorption properties also contribute to the magnitude of the power law exponent, as well as the pore geometry and roughness.

Recently other groups have explored alternative strategies for modelling the RMTD processes. Following the approach of Levitz,[20] an alternative methodology is to consider the probability distributions associated with the adsorption, Ψ_{A}, and bulk relocations, Ψ_{R}. The introduction of Ψ_{A} allows the relaxation model to be sensitive to the average adsorption time, τ_{A}, unlike the RMTD approach. During surface binding the adsorbate will experience magnetic noise that induces relaxation, but not during the bulk excursions. The general form of the spectral density function, $J(\omega)$, can be expressed as:

$$J(\omega) = \frac{2}{\tau_{\mathrm{A}}\omega^2}\,\mathrm{Re}\left[\frac{\left(1-\widetilde{\Psi}_{\mathrm{A}}(\omega)\right)\left(1-\widetilde{\Psi}_{\mathrm{R}}(\omega)\right)}{1-\widetilde{\Psi}_{\mathrm{A}}(\omega)\widetilde{\Psi}_{\mathrm{R}}(\omega)}\right], \tag{7.8}$$

where the tilde accent denotes the Fourier transform of the respective probability distribution functions. This expression has only been evaluated for a few geometries,[14,20,21] in which the relocation statistics showed an algebraic tail at long times, which allowed closed form expressions of the spectral density function to be obtained. In the case of porous confinement the algebraic tail is often suppressed by an exponential cut-off,[13,14] which complicates the analysis. However the spectral density function in the case of a planar surface has been applied to study the water dynamics within spherical silica pores with a diameter of 10-14 nm.[22] In this case the spectral density function reduces to:[14]

$$J(\omega) = \left[\omega_{\mathrm{A}}\left(\sqrt{\frac{\omega}{\omega_{\mathrm{A}}}} + \frac{\omega}{\omega_{\mathrm{A}}} + \frac{1}{2}\left(\frac{\omega}{\omega_{\mathrm{A}}}\right)^{3/2}\right)\right]^{-1}, \tag{7.9}$$

$$\omega_{\mathrm{A}} = \frac{\delta^2}{2D\tau_{\mathrm{A}}^2}, \tag{7.10}$$

where ω_{A} is characteristic frequency which is a function of the distance of the adsorbate from the surface, δ, the bulk diffusion coefficient, D, and the average adsorption time of the adsorbate at the pore surface, τ_{A}. This expression suggests that the apparent power law relaxation behaviour will shift from an exponent of -0.5 in the weak adsorption limit (small values of τ_{A}) to -1.5 in the strong adsorption limit (large values of τ_{A}). Although not formally a power law between these limits, an increase in the magnitude of an

apparent power law exponent would be expected as the strength of the surface interaction increased.

7.2.1.4 Protic model

Protic species are defined as molecules containing readily exchangeable ^{1}H atoms, and include many common liquids such as water, alcohols and amines. These exchangeable ^{1}H atoms are almost exclusively found as part of a functionality that will participate in the formation of hydrogen bonds. When protic liquids are imbibed within a porous medium that contains exchangeable surface hydroxyl groups, the relaxation behaviour of the solid becomes coupled to that of the liquid. At the pore surface a highly structured hydrogen bond network is established, which allows the rapid transfer of magnetization, either through a direct material exchange (^{1}H exchange) as is shown in Figure 7.4, or via cross-relaxation effects. The latter is analogous to the exchange-mediated orientational randomization (EMOR) model of relaxation proposed for proteins.[23] Over the timescale of the experiment the surface magnetization is further averaged across the entire pore space in accordance with the two-phase fast exchange model, which transfers the surface relaxation to the observed magnetization.

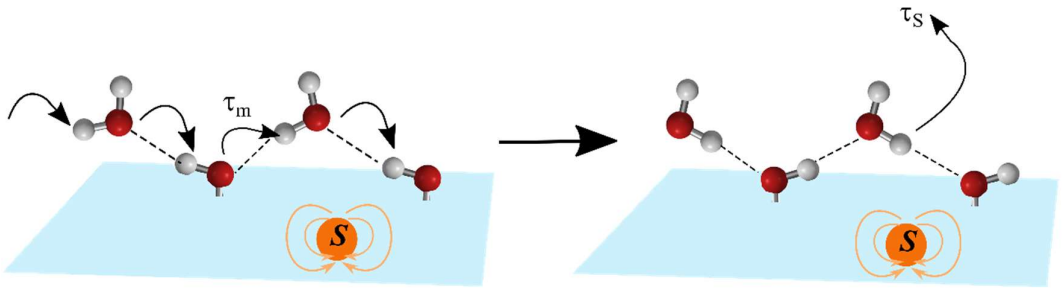

Figure 7.4: A schematic diagram showing the coupling of the solid hydroxyl ^{1}H protons and the ^{1}H protons within the surface layer. Dashed lines represent the hydrogen bond network and curly arrows represent a possible exchange mechanism with a characteristic hopping time, τ_m, which is interrupted by exchange to the bulk after a residence time, τ_S. The hydrogen bond network and molecular exchange average the effects of *I-S* correlations at the pore surface across all exchangeable functionalities within pore space.

In the presence of paramagnetic impurities, the hydroxyl groups at the pore surface experience *I-S* correlations that persist for very long timescales.[6,24] This long *I-S* correlation has been shown to cause a strong dispersion for water imbibed within a porous glass.[6] A power law exponent of -0.5 was observed for the water relaxation behaviour

with respect to the ^{1}H Larmor frequency, which showed that the motion of spins at the surface followed a 1 dimensional diffusive process. For water in silica glasses, a power law exponent of -0.5 has commonly been observed for a range of different relaxation processes,[6,25] however for many other porous media the value of the power law is distorted by competing effects.[18,19] To allow the protic model to be applicable to NMRD data that showed a power law dependence of the relaxation rate on the Larmor frequency with an exponent of $\chi \neq 0.5$, a correlation function that tended to a power law of variable exponent at long times was required. Assuming an independence of two different relaxation processes: a surface diffusion of correlation time, τ_{m}, and a finite time of residence at surface, τ_{S} (>>τ_{m}), the pairwise dipolar correlation function, $G(\tau)$ can be expressed as:[26]

$$G(\tau) = \frac{\exp\left(-\frac{|\tau|}{\tau_{\mathrm{s}}}\right)}{\left(\frac{|\tau|}{\tau_{\mathrm{m}}}\right)^{1-\chi}}, \qquad 0 < \chi < 1, \tag{7.11}$$

where χ is the power law exponent. The corresponding spectral density of $G(\tau)$ is the cosine Fourier transform of the correlation function:[26]

$$J(\omega_i) = 2\,\frac{{\tau_{\mathrm{m}}}^{1-\chi}{\tau_{\mathrm{s}}}^{\chi}\Gamma(\chi)}{(1+{\omega_i}^2{\tau_{\mathrm{s}}}^2)^{\chi/2}}\cos[\chi\mathrm{ArcTan}(\omega_i\tau_{\mathrm{s}})], \qquad i = I \text{ or } S. \tag{7.12}$$

The gamma function is denoted as $\Gamma(\chi)$ and ω_i=2πν_i. In the limit that $\omega_i\tau_{\mathrm{s}} \ll 1$ the spectral density function reduces to the frequency independent plateau,

$$J(\omega_i) = 2\,{\tau_{\mathrm{m}}}^{1-\chi}{\tau_{\mathrm{s}}}^{\chi}\Gamma(\chi). \tag{7.13}$$

In the opposing limit that $\omega_i\tau_{\mathrm{s}} \gg 1$ the spectral density follows a power law frequency dependence,

$$J(\omega_i) = 2\,\frac{{\tau_{\mathrm{m}}}^{1-\chi}\Gamma(\chi)}{{\omega_i}^{\chi}}\cos\left[\chi\frac{\pi}{2}\right], \qquad i = I \text{ or } S. \tag{7.14}$$

Physically eq. (7.12) describes the surface motion of an exchangeable hydroxyl ^{1}H atom, diffusing at the pore surface. In the presence of paramagnetic impurities at the pore surface the geometric confinement due to hydrogen bonding leads to an increase in the number and duration of *I*-*S* reencounters, causing an efficient relaxation process. After a characteristic time, τ_{S}, the hydroxyl ^{1}H atom escapes the hydrogen bond network and

loses correlation. An important distinction arises between the protic case and the other models that have been discussed in this section, which is that the protic model is dominated only by the hydroxyl functionality of the adsorbed molecule coupling to the surface hydroxyls. The relaxation rate is functionality specific rather than governed by the motions of the entire molecule, in contrast to the RMTD and Korb models.

7.2.1.5 Electron paramagnetic relaxation effects

Electron paramagnetic relaxation (EPR) effects arise due to the direct interaction between paramagnetic species and ^{1}H atoms on molecules bound to the paramagnetic centre. The close proximity of the paramagnetic species and ^{1}H atoms allows the electron relaxation of the paramagnetic species to be transferred to the ^{1}H atoms, and then to the remainder of the imbibed liquid through chemical exchange. The resultant relaxation enhancement is observed as an increase in the relaxation rate which occurs over a small range of high magnetic field strengths.[5] Figure 7.5 shows the effect of the EPR enhancement for water imbibed within white cement pastes, which was centred about a magnetic field strength of 50-60 MHz.[27] The EPR behaviour occurred concurrently with a 2D surface relaxation process that was modelled by a Korb expression. Only at high field strengths did the EPR effect control the observed relaxation behaviour.

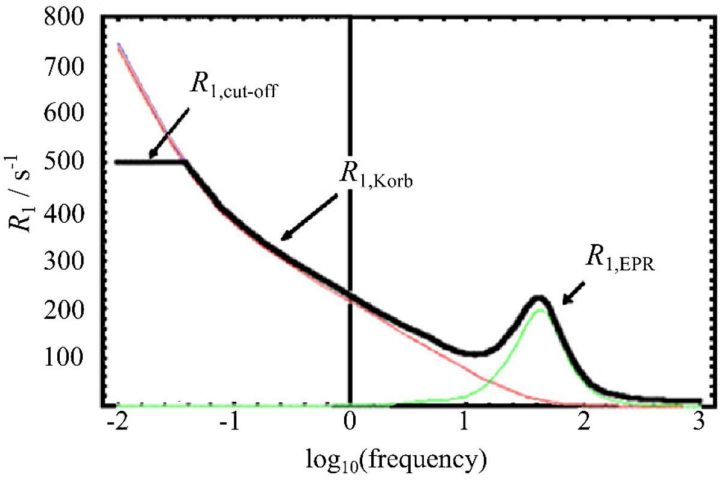

Figure 7.5: The NMRD profile of water imbibed within white cement (black). The observed NMRD profile has been decomposed into contributions from the electronic paramagnetic relaxation, $R_{1,\text{EPR}}$ (green), a Korb model component, $R_{1,\text{Korb}}$ (red), and a cut-off frequency, $R_{1,\text{cut}-\text{o}}$. Modified from Korb et al.[27]

The relaxation enhancement, $R_{1,\mathrm{EPR}}$, can be modelled as a Lorentzian function:[9]

$$R_{1,\mathrm{EPR}} = \frac{8n\varepsilon^2}{{r_{I-S}}^6}\tau_\mathrm{c}\left[\frac{7}{1+\omega_S^2\tau_\mathrm{c}^2}+\frac{3}{1+\omega_I^2\tau_\mathrm{c}^2}\right], \tag{7.15}$$

where n is the number of molecules in the coordination sphere of the paramagnetic species, ε is the molecular size, r_{I-S} is the distance of minimal approach between the I and S spins, and ${\tau_\mathrm{c}}^{-1} = {\tau_\mathrm{ex}}^{-1} + T_{1,\mathrm{elec}}^{-1}$. The exchange time, τ_ex, defines the residency time of molecule in the coordination sphere of the paramagnetic species, and the electron relaxation time, $T_{1,\mathrm{elec}} \ll \tau_\mathrm{ex}$, is given by:

$$\frac{1}{T_{1,\mathrm{elec}}} = H_S^2\tau_\mathrm{V}\left[\frac{1}{1+\omega_S^2\tau_\mathrm{v}^2}+\frac{4}{1+4\omega_S^2\tau_\mathrm{v}^2}\right], \tag{7.16}$$

where H_S^2 describes the intensity of the electron spin fluctuations and τ_v describes the timescale of the fluctuations.

7.2.2 Temperature dependent relaxation

The temperature dependent relaxation properties of simple bulk liquids are well known from BPP theory (section 2.5.3). According to this theory an increase in the temperature will increase the rate of molecular tumbling, and reduce the rotational correlation time, τ_c. Depending on the rate of molecular tumbling of the sample the increase in temperature can lead to a decrease (A), no change (B), or an increase (C) in the relaxation rate as shown in Figure 7.6. For small molecules in their bulk liquid form the molecular motions are sufficiently fast ($\tau_\mathrm{c} \approx 10^{-12}$ s) that an increase in temperature causes a reduction in the relaxation rate. This behaviour will be referred to herein as a normal temperature dependence.

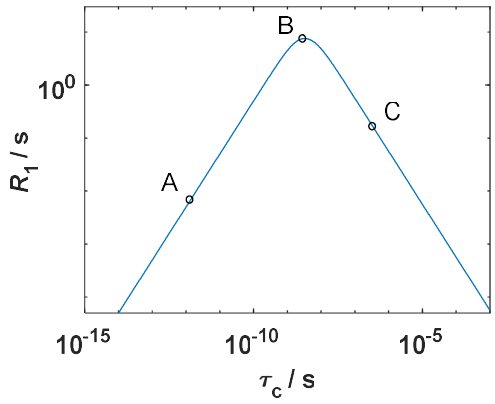

Figure 7.6: The relaxation time constant as a function of the molecular correlation time, τ_c, according to BPP theory. Values of $A = 10^9$ s^{-2} and $\omega_0 = 10^7$ rad s^{-1} were chosen to represent values commonly encountered within the literature. Bulk liquid correlation times are on the order of $\tau_c = 10^{-12}$ s.

For liquids imbibed within porous media the temperature dependence is more complex to predict. For example, the relaxation rate of acetone within porous silica has been observed to decrease as the temperature increased, whilst water in the same silica showed an increase in its relaxation rate at low field strengths as the temperature increased.[6] Other examples showed similar behaviour for water and oil in granular packings,[28] or temperature independent relaxation behaviour in porous media.[3,29] The variation in the temperature dependent relaxation behaviour reflects the wide array of motional regimes experienced by liquids at the pore surface. As such, variable temperature experiments are an effective method to differentiate between the surface relaxation processes, and allow the assignment of a suitable model to describe the underlying molecular motions.

The temperature dependence of the theories presented in section 7.2.1 to describe the relaxation behaviour of liquids imbibed in porous media will now be discussed. In the case of transient diffusion in the presence of paramagnetic impurities (Korb model) the relaxation behaviour has been shown to decrease with increasing temperature across the entire frequency range.[6] The activation energy for the process can be calculated from an Arrhenius analysis at each field strength.

$$\mathrm{Ln}(R_1) = \mathrm{Ln}(A) - \frac{E_a}{RT}, \tag{7.17}$$

where A is the pre-exponential factor, E_a is the activation energy of diffusion, and R is the gas constant. For acetone imbibed within the porous glass the measured value of E_a agreed well with the expected value for acetone self-diffusion at all field strengths.[5]

For reorientations mediated by translational diffusion (RMTD) the temperature dependence of the relaxation behaviour only contributes to the diffusion process during bulk excursions. This process weakly depends on the temperature at low field strengths[12,25] as shown for DMSO in Bioran glass in Figure 7.7a, but may be accompanied by stronger temperature dependencies at higher field strengths due to fast molecular processes.

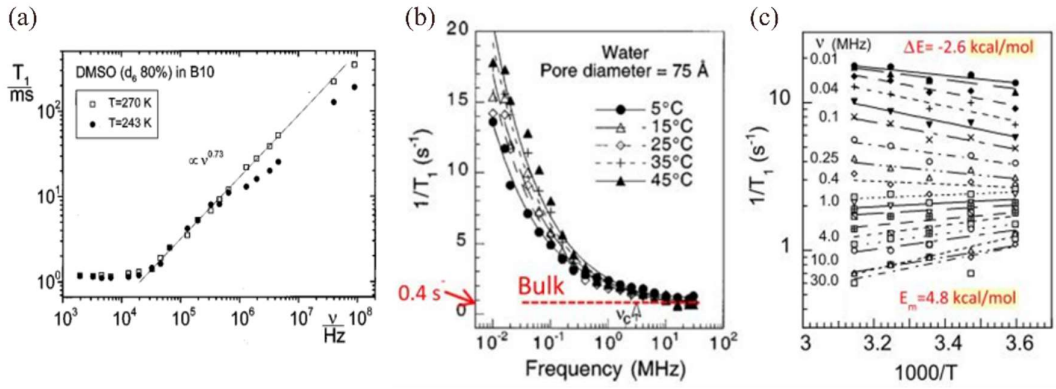

Figure 7.7: The (a) NMRD profile of 80% d_6-DMSO in Bioran glass measured at 243 and 270 K, reproduced from Zavada et al.[3] The (b) NMRD profile of water imbibed within a silica glass,[6] and (c) the corresponding Arrhenius plot. Reproduced from Korb et al.[6]

In the case of polar protic species (protic model) a normal temperature dependence was observed at high field strengths. However, the temperature dependence inverted at low field strengths as shown in Figure 7.7b-c. The inversion of the activation energy was justified by an activated process modulating the relaxation behaviour, namely surface diffusion in the presence of strong hydrogen bonds. At high field strengths the experiments were sensitive to the properties of the bulk fluid, and hence probed the activation energy of self-diffusion of the bulk liquid. At low frequencies the experiments were sensitive to the surface dynamics, and the observed activation energies tended to $\Delta E = -(E_{\mathrm{a,surf}} - E_{\mathrm{a,bulk}})$, where $E_{\mathrm{a,surf}}$ was approximately equal to the energy of a hydrogen bond.[5,6]

The clear difference in the temperature dependence of different relaxation mechanisms makes variable temperature experiments a robust technique for identifying the underlying molecular dynamics of liquids imbibed within porous media.

7.3 Materials and methods

7.3.1 Materials

All materials used within this section were obtained from Alfa Aesar and Fluorochem at a purity of >98%. The BET and BJH analysis of γ-alumina gave a surface area of 206 m^2 g^{-1} and an average pore size of 9 nm. Gravimetric measurements showed the alumina to have pore volume of 0.65 cm^3 g^{-1} and ESR measurements showed the presence of 7 ppm of Fe^{3+} impurities (see appendix 1). Further details about the materials used can be found in section 5.3.1.

7.3.2 Sample preparation

Two classes of samples were prepared; those which had liquid inside the pellets only (imbibed) and those which had liquid both inside and outside of the pellets (immersed). Imbibed samples were prepared by drying the γ-alumina pellets for 12 h at 120 °C. The pellets were then soaked in the desired liquid for 12 h, and the extra pellet fluid was removed by drying the sample on filter paper shortly before the NMR measurement. This process left only the liquid imbibed within the alumina. The preparation methodology was identical for the immersed samples, except the final drying step was removed and liquid immersed γ-alumina samples were obtained.

7.3.3 FFC-NMR methods

FFC-NMR experiments were performed on a Stelar Spinmaster Duo relaxometer. For each NMRD profile between 10 and 30 ^1H Larmor frequencies were analysed, logarithmically spaced between 10 kHz and 40 MHz. A pre-polarized sequence was used for field strengths below 10 MHz, and a non-polarized sequence was used for measurements above 10 MHz. For each T_1 experiment 32 delay times were used with relaxation delays that were logarithmically spaced between 1 ms and 6 x T_1. M_z^0 was estimated as the observed magnetisation after 1 ms of relaxation delay and M_z^∞ was taken as the average of magnitude measured after the longest two relaxation delays. In all cases

only a single scan was required to achieve a good SNR unless otherwise specified. The sample temperature was controlled with liquid nitrogen and a compressed air heating system, which was calibrated against an external thermocouple. After each temperature change the sample was left for 30 minutes to allow for thermal equilibration. The raw FFC-NMR data were renormalized such that the signal in each dataset decayed from 1 to 0.[12] Unless otherwise stated the T_1 distribution at each field strength was obtained via an inverse Laplace transformation using Tikhonov regularization.[30] The relative intensity of each peak was extracted directly from the regularisation. The data were also fitted to a mono or multiexponential function using NNLS regression for comparison.

7.3.4 Temperature calibration

A two-fold calibration of the temperature was carried out to ensure that the applied temperature was consistent with the sample temperature for all measurements. In the first stage a thermocouple within a sample tube was placed inside the magnet, and the measured temperature was compared to the temperature set point. For sample temperatures between 20-125 °C the temperatures were consistent to within ∓ 1 °C up to temperatures of 85 °C, and ∓ 2 °C in the range 85-125 °C. When the liquid nitrogen cooling system was used to reach temperatures from 5-15 °C a constant offset of -10 °C was observed. This offset was consistent to within ∓ 1 °C and therefore was a calibration error associated with the hardware, which could be trivially adjusted for. The second stage of temperature verification was to monitor the relaxation behaviour of a bulk water sample over the temperature range 5-65 °C (the data for which are shown in section 7.4.1). Arrhenius behaviour was observed over this range, confirming the accuracy of the temperature controller.

7.3.5 Molecular modelling

Atomic distances were computed for methanol, DMSO and THF using Jmol molecular modelling software (open-source, http://jmol.sourceforge.net/). For each liquid, the structure was optimised using an inbuilt energy minimisation algorithm. The algorithm was iterated several times, and from three different initial structures to ensure that a global energy minimum was achieved. The distance between each pair of ^{1}H atoms was measured for the optimized structure.

7.4 Results

The temperature dependence of the relaxation rate constant, R_1, for liquids imbibed within porous media is principally controlled by the molecular motions occurring within the sample. However, the relaxation rate will also be affected by physical and chemical changes of the sample that occur at higher temperatures. This includes changes in the pore filling factor due to material loss, or irreversible changes in surface chemistry. These effects must be separated from the true relaxation effects in order to understand the temperature dependence of each liquid imbibed within γ-alumina. In this section the temperature dependence of a bulk water sample is explored in order to establish a normal temperature dependence of the relaxation behaviour. This is then compared to the relaxation behaviour of γ-alumina immersed in 5 different liquids; doing so allows changes in the sample as a function of time to be explored and corrected for. Finally, the temperature dependent relaxation behaviour of the immersed samples is compared to that of the same liquids imbibed within γ-alumina.

7.4.1 Bulk water relaxation

Figure 7.8 shows the Arrhenius plots obtained from the bulk water NMRD profiles recorded over the temperature range 5-65 °C. The relaxation data were measured at 5 frequencies, logarithmically spaced from 10 kHz to 7.5 MHz. At each temperature the relaxation rate was independent of the frequency, as previously observed.[5,12] This resulted in all five Arrhenius plots being identical. The relaxation rate showed a strong temperature dependence – with the relaxation rate decreasing as the temperature was increased. This temperature dependence was expected,[31] and was indicative of a relaxation process dominated by self-diffusion or rotational motion. The activation energy of the diffusive process was obtained from the slope of the Arrhenius plot at each frequency, and was found to be 17.2∓0.4 kJ mol^{-1}. This value was consistent with previously reported activation energies for water self-diffusion.[31,32] The temperature range was not further explored, as the temperature dependence of the water relaxation rate was known to show non-Arrhenius behaviour over larger observation ranges.

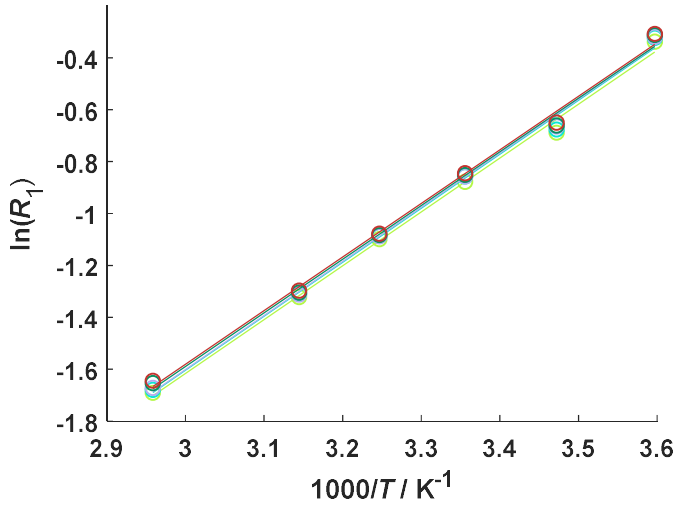

Figure 7.8: Arrhenius plots for bulk water measured between 5-65 °C. For each temperature 5 different frequencies from 10 kHz-7.5 MHz were measured. No frequency dispersion was observed for the bulk liquid over this range, resulting in all 5 profiles overlapping.

7.4.2 γ-alumina immersed in liquids

7.4.2.1 Comparison of immersed and imbibed samples

For immersed γ-alumina samples both intra- and extra-pellet fluid were present. The rate of molecular exchange between these environments was not sufficient for each spin to sample both environments on the timescale of the NMR measurement, which resulted in multiexponential relaxation profiles as demonstrated in Figure 7.9. This was significantly different to the monoexponential relaxation observed for imbibed liquids, where only intra-pellet fluid was present, and full spatial averaging was possible within the pore space.

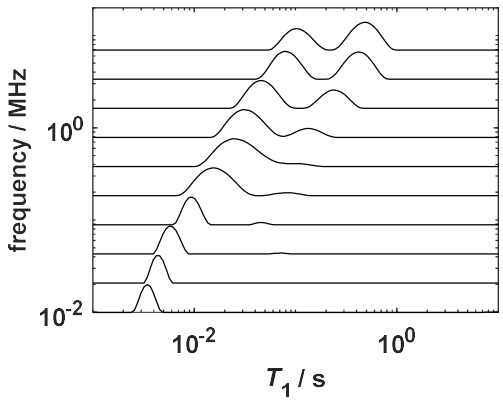

Figure 7.9: The T_1 distributions of γ-alumina immersed in water measured at magnetic field strengths from 10 kHz to 7.5 MHz.

Two broad relaxation features were observed in the T_1 distributions recorded at high frequencies, but only one sharp feature was present at low frequencies. The two peaks in the distributions obtained at 7.5 MHz were assigned to an intra-particle fluid and a bulk-type fluid, which give relaxation times of 104 ms and 510 ms respectively. The intra-pellet fluid followed an identical frequency dependence to that of the imbibed liquid, but the bulk-type fluid was significantly different to the bulk liquid relaxation behaviour. A clear frequency dependence of the bulk-type fluid was observed, and the high field relaxation rate was 4 times smaller than that of bulk water. This indicated that a partial exchange between the inter- and intra-pellet fluid was occurring. The exchange had little effect on the observed relaxation rate of the intra-particle fluid, but did increase the relaxation rate of the inter particle (bulk-like) fluid above the true bulk liquid value.

As the frequency was decreased the relaxation rate of the fast relaxing component increased. This meant that it was necessary to reduce the time delays used to sample the magnetization decay at each field strength. This had two important effects; firstly it improved the accuracy of the measurement of the fast relaxing environment. The second effect was that the slow relaxing environment was biased against, by measuring the decay over a sufficiently short time period that no decay of the slow relaxing environment occurred. This reduced the effective magnitude of the slow relaxing component until it was no longer present at low field strengths, as shown in Figure 7.9. By weighting out the slow relaxing component the inversion became monoexponential rather than biexponential. This reduced the uncertainty in the values of T_1 that were estimated from the Laplace inversion, and reduced the width of the peaks in the T_1 distributions. The

measured relaxation rate at low field strengths was therefore equivalent to only that of the imbibed liquids. A comparison of the NMRD profiles for imbibed and immersed samples of cyclohexane, DMSO and water within γ-alumina is presented in Figure 7.10. As explained above, the relaxation rate of water imbibed within γ-alumina and water-immersed γ-alumina samples converged at low field strengths. For more slowly relaxing samples the convergence was less complete, however all immersed samples showed enhanced relaxation relative to their respective bulk liquids. This showed that the immersed liquid samples were sensitive to the surface relaxation behaviour, and could be used to probe the temperature dependent trends that occurred in the imbibed liquids. By doing so it was possible to remove the effect of liquid being expelled from the pores at high temperatures as a complicating factor in the explanation of the temperature dependent relaxation behaviour.

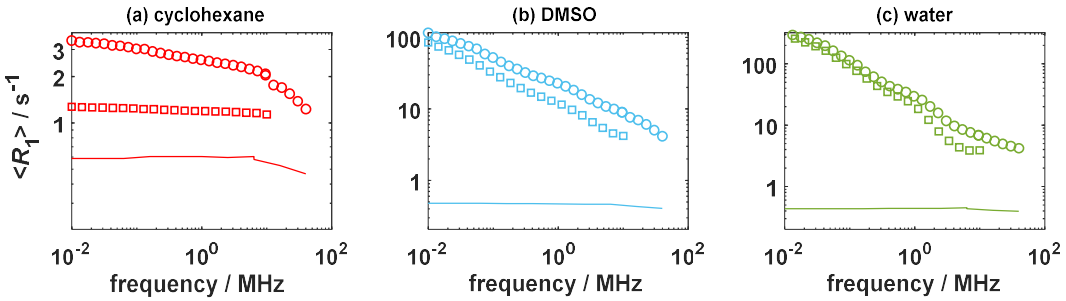

Figure 7.10: The NMRD profiles of (a) cyclohexane, (b) DMSO, and (c) water, imbibed within γ-alumina (○), liquid immersed γ-alumina samples (□), and as a bulk liquid (-).

7.4.2.2 Heating profiles and sample variation

The complexity of porous media samples meant that many possible physical or structural changes may have occurred during the heating process. To decouple these changes from the temperature dependent effects of molecular motions, it was necessary to investigate whether the heating profile led to irreversible changes in the sample. DMSO was chosen as the probe molecule for this study as it had the highest boiling point of all adsorbates, and would not complicate the analysis with rehydroxylation effects that may have occurred for water. Two temperature sampling methodologies were explored; heating the sample up progressively to a maximum temperature, and starting at the highest temperature point and cooling the sample progressively. Figure 7.11a shows the NMRD profiles of DMSO obtained at 25 °C after heating the sample to 65, 85, 105 and 125 °C.

A clear systematic increase in the relaxation rate was observed, meaning that physical changes were occurring within the sample as it was heated. Figure 7.11b shows the NMRD profile at 25 °C after initially heating the sample to 125 °C and then the same NMRD profile after acquiring data from 105-35 °C. By acquiring the NMRD profiles in a descending fashion all irreversible changes in the sample occurred during the first heating interval. As a result, the sample did not change further throughout the experiments. Using a decreasing temperature ramp allowed a more reliable comparison of the temperature dependent data, as changes in the sample over time could be excluded from the interpretation. Repeat temperature cycling to 125 °C did not further change the NMRD profiles obtained at 25 °C. This showed that the irreversible changes that occurred upon heating happened within the thermal equilibration period (30 min), and that a decreasing temperature ramp was a robust method for measuring the temperature dependence of the relaxation rate.

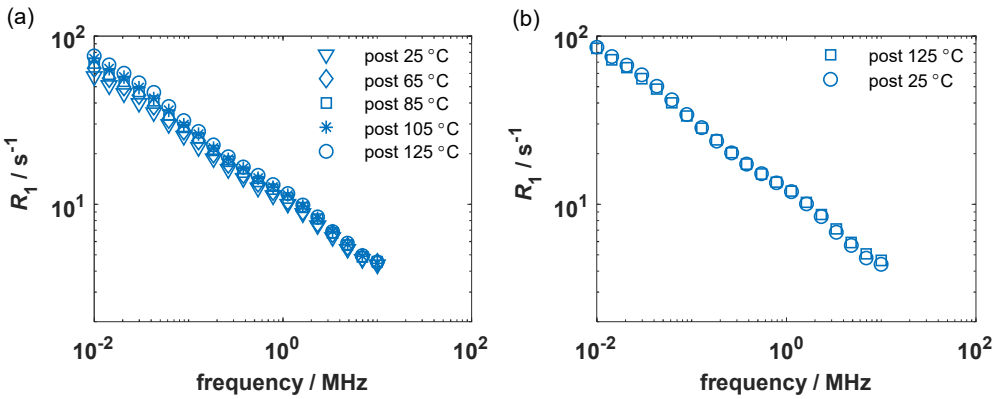

Figure 7.11: The NMRD profiles of γ-alumina immersed in DMSO obtained at 25 °C during temperature cycling. The temperature was varied in (a) an increasing fashion and (b) a decreasing fashion to demonstrate any irreversible changes that occurred within the sample as a result of heating.

7.4.2.3 Liquid immersed γ-alumina results

The temperature dependent NMRD profiles of water, methanol, DMSO, THF, and cyclohexane obtained from liquid immersed γ-alumina samples are shown in Figure 7.12, and the corresponding Arrhenius plots are presented in Figure 7.13. As shown in the previous section, the low field data were the most representative of the intra-pellet liquid, and hence the surface adsorption behaviour. To focus in on these effects and avoid any ambiguity from high field bulk-type effects, only the low field data is shown (<0.5 MHz).

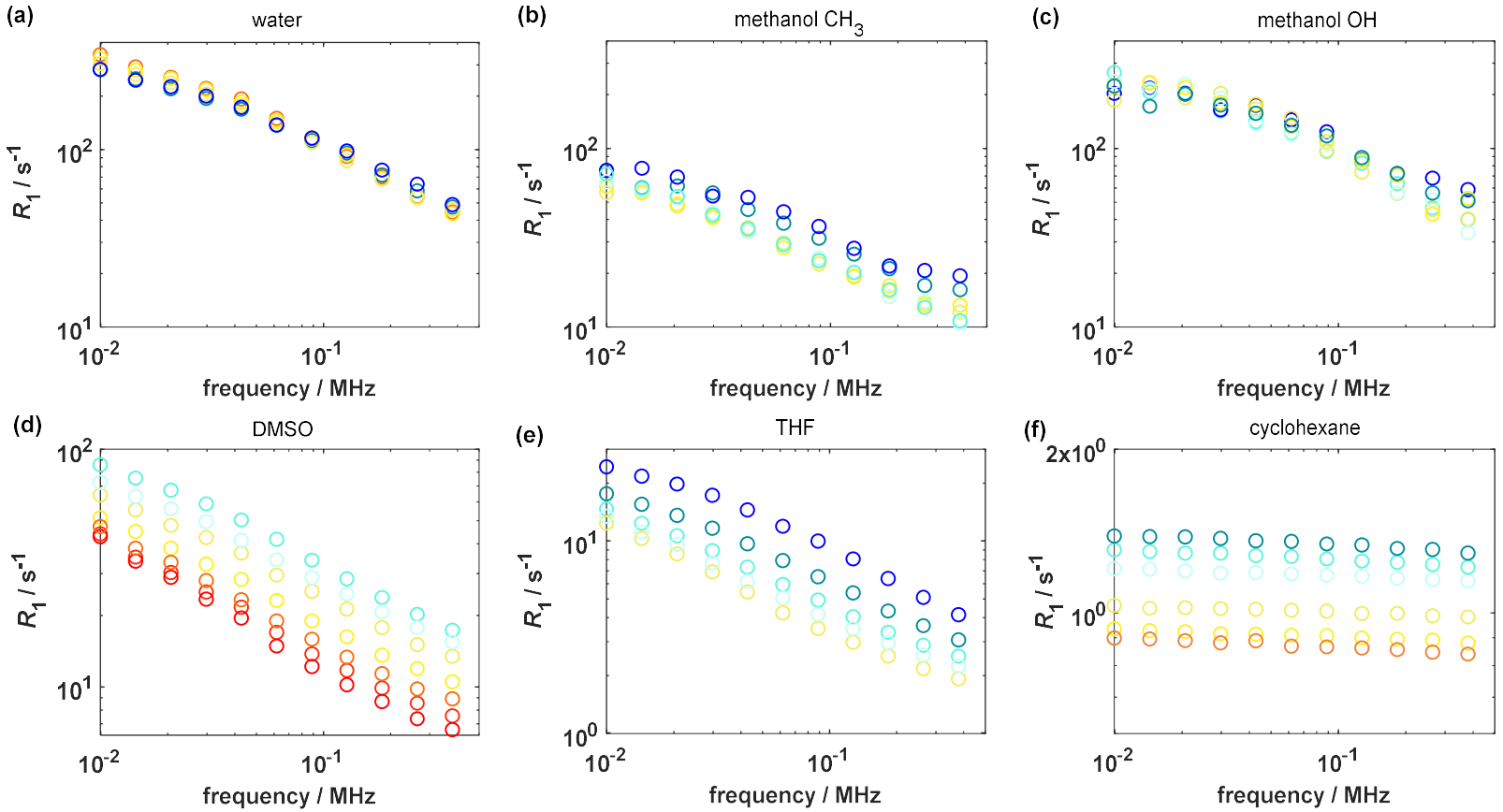

Figure 7.12: The temperature dependent low field relaxation of behaviour of γ-alumina immersed in (a) water, (b-c) methanol, (d) DMSO, (e) THF, and (f) cyclohexane. For methanol the relaxation behaviour is resolved into (b) that of the methyl group and (c) that of the hydroxyl group. Relaxation rates at temperatures of 5(○), 15(○), 25(○), 35(○), 45(○), 65(○), 85(○), 105(○), and 125 °C (○) were measured depending on the freezing and boiling points of each liquid.

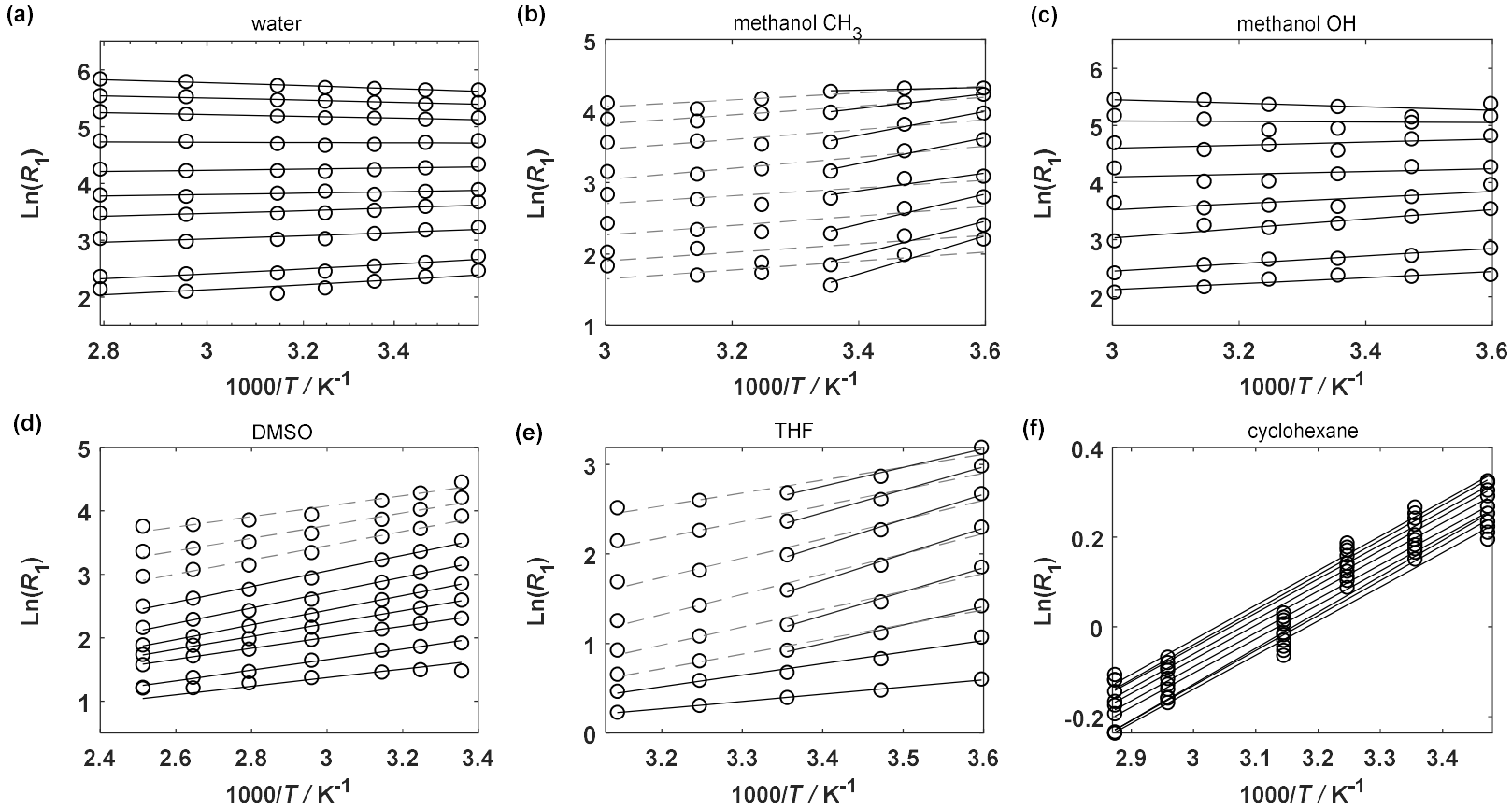

Figure 7.13: Arrhenius plots for the temperature dependent relaxation behaviour of γ-alumina immersed in (a) water, (b-c) methanol, (d) DMSO, (e) THF, and (f) cyclohexane. For methanol the relaxation behaviour is resolved into (b) that of the methyl group and (c) that of the hydroxyl group. Arrhenius fits are represented by solid lines. In cases where a single Arrhenius fit was not valid due to the curvature of the data the Arrhenius fit over the whole dataset is shown (dashed line) and the low temperature data are fitted independently (solid line).

A wide range of relaxation behaviour was observed, which varied depending on the adsorbate, frequency and temperature at which the experiment was performed. Figure 7.12a shows that for water imbibed within γ-alumina a clear inverse temperature dependence of the relaxation rate was observed at low field strengths, with a crossover from a normal temperature to the inverse behaviour occurring at a ^{1}H Larmor frequency of 0.09 MHz. Similar behaviour was also observed for the hydroxyl group of methanol, with an inversion of the temperature dependence of the relaxation rate occurring at low frequencies. These two environments showed the highest relaxation rates of all NMRD profiles, but the magnitude of the relaxation rate was lower for the methanol hydroxyl group than for water at low frequencies. The inverse temperature dependence was not observed for the alkyl group of methanol, indicating that the observed relaxation was functionality specific rather than molecule specific. For the alkyl group of methanol a normal temperature dependence was observed until approximately 25 °C. Thereafter, the relaxation rate became weakly dependent on the temperature. The dataset for methanol-immersed γ-alumina was complicated relative to the other liquids studied herein as the separation of the hydroxyl and alkyl environments of imbibed methanol, and the inter-pellet fluid required the separation of three components. The degree of resolution from the inverse Laplace transformation was not sufficient to fully resolve all components. This made the results more sensitive to noise than the inverse Laplace transformation of the other fluids, which required only two components to be separated. The level of noise did not prevent a qualitative assessment of the system, but did limit a fully quantitative analysis.

To further clarify the nature of the low field temperature dependence of the relaxation rates of the two chemical functionalities within methanol, samples of d_1- and d_3-methanol were prepared. This deuterated out the hydroxyl and methyl groups respectively, and simplified the numerical inversion. The results of these experiments are shown in Figure 7.14. The relaxation rates of these analogues have previously been shown to be representative of the two functionalities of methanol (section 6.4.2). For the alkyl group Figure 7.14a showed that a normal temperature dependence was observed down to values of $1000/T = 3.22$ (37 °C). For higher temperatures the relaxation rate showed no further changes, reaching a plateau at $R_1 = 58$ s^{-1}. In contrast, Figure 7.14b shows γ-alumina immersed in d_3-methanol, which demonstrated very different temperature behaviour. The change in R_1 was much smaller, and in the opposite direction

to that of the methyl group. The molecular interactions and surface binding strengths were identical for γ-alumina immersed in d_0, d_1- and d_3-methanol. If both functionalities relaxed via the same mechanism then they would obey similar temperature dependencies. As this is not the case it is clear that different functionalities within the same molecule can relax via different mechanisms. Figure 7.14c shows the NMRD profiles of CD_3OH imbibed within γ-alumina obtained at 5 and 60 °C. The hydroxyl functionality demonstrated an inversion in the temperature dependence at low frequencies, with an inversion frequency of ~0.08 MHz. The inversion frequency was identical to the value observed for water imbibed within γ-alumina, despite significantly different liquid-surface interactions occurring.

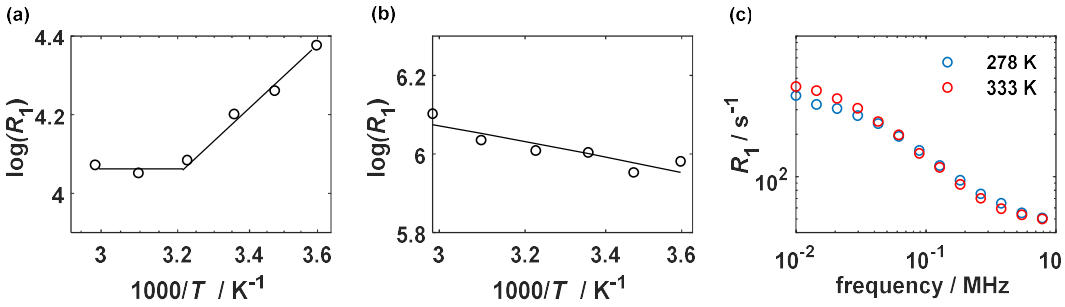

Figure 7.14: The Arrhenius plots of γ-alumina immersed in (a) d_1-methanol (CH_3OD) and (b) d_3-methanol (CD_3OH). The (c) low field section of the NMRD profile of CD_3OH imbibed within γ-alumina at 278 K and 333K. Solid lines represent a guide to the eye.

For γ-alumina immersed in DMSO, R_1 decreased as the temperature increased at all field strengths for temperatures below 85 °C. At 85-125 °C the low field section of the profiles began to converge in the same manner as the alkyl environment of methanol. Similar behaviour was noted for alumina immersed in THF, however, for the less viscous liquid the convergence began at much lower temperatures (~25 °C). The final dataset, γ-alumina immersed in cyclohexane, showed no convergence at any temperature studied. There was a small discontinuity in the profiles between 35-45 °C, but this did not result in any high temperature convergence of the data.

The analysis of the NMRD profiles was formalised in terms of an Arrhenius analysis, the results of which are shown in Figure 7.13. A clear inversion of the temperature dependence of water and the hydroxyl group of methanol were observed, with both reaching apparent activation energies of -2.1 kJ mol^{-1}. For the alkyl group of methanol the trends in the relaxation behaviour were more difficult to separate from the

experimental noise. There was evidence of a plateau at high temperatures, and a much steeper, linear region at low temperatures. The low temperature data showed an apparent activation energy of 12.1 kJ mol^{-1}. Similar behaviour was observed in the case of the DMSO and THF samples, which showed curvature in the NMRD profiles at high temperatures. Activation energies estimated from only the low temperature region were 12.1 and 22.6 kJ mol^{-1} respectively. Finally, cyclohexane showed a highly stable activation energy of 6.3 kJ mol^{-1} despite the discontinuity observed between 35-45 °C. All values of the activation energy were within a factor of 2 of the bulk activation energies of self-diffusion for each liquid, with the exception of THF and water. At low frequencies, the latter was 8 times smaller than the bulk value and negative.

7.4.3 Liquids imbibed within γ-alumina

Figure 7.15 and Figure 7.16 show almost identical trends in the relaxation behaviour for imbibed liquids compared to the immersed samples. This demonstrated that both types of sample were representative of the relaxation behaviour occurring within porous confinement. In the case of imbibed liquids it was possible to extend the analysis up to much higher field strengths without the behaviour of the extra-pellet fluid obscuring any trends in the relaxation data. For water imbibed within γ-alumina the variation in the relaxation rate as a function of frequency was small, with a maximum variation of 25%. At high frequencies a decrease in the relaxation rate was observed with increasing temperature. This behaviour inverted at low frequencies and the relaxation rate began to increase with increasing temperature. As with the immersed case, the point of inversion occurred at 0.09 MHz. The activation energies for this process changed from 3.1 kJ mol^{-1} at high field strengths to -1.8 kJ mol^{-1} at low field strengths. For methanol the absence of inter-pellet fluid simplified the separation of the relaxation behaviour from a three component problem to a two component problem. This reduced the uncertainty in the relaxation rate of each component. The alkyl group showed a strong decrease in the relaxation rate as the temperature was increased, obeying Arrhenius behaviour ($E_a = 10.5$ kJ mol^{-1}) over the entire temperature range at high field strengths. For the lowest three field strengths a curvature was present in the Arrhenius plots, with the data tending towards a constant value at high temperatures. The hydroxyl group showed a much weaker temperature dependence than the alkyl group, with evidence of an inversion of the relaxation rate at low field strengths.

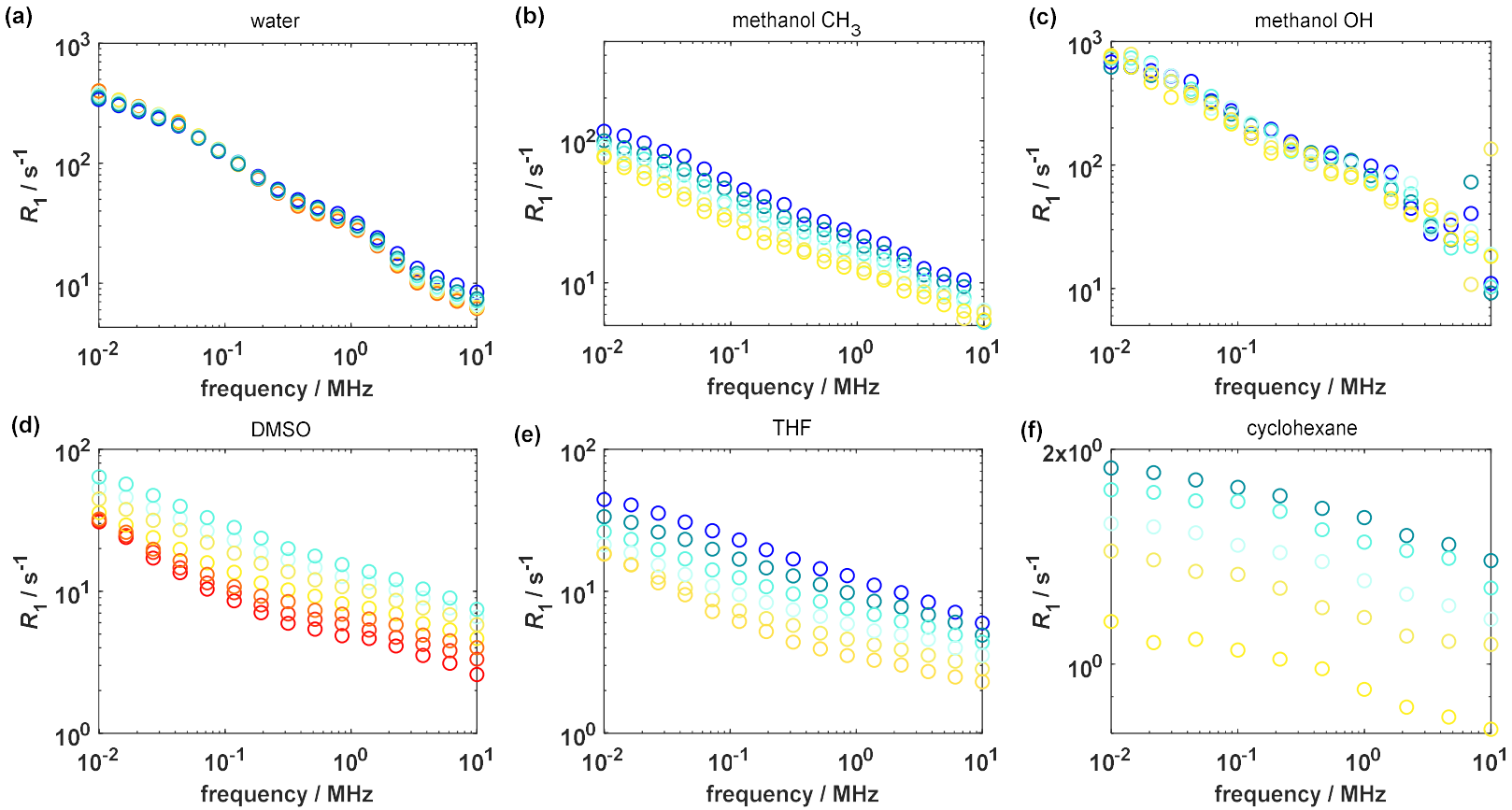

Figure 7.15: The temperature dependent low field relaxation of behaviour of (a) water, (b-c) methanol, (d) DMSO, (e) THF, and (f) cyclohexane imbibed within γ-alumina. For methanol the relaxation behaviour is resolved into (b) that of the methyl group and (c) that of the hydroxyl group. Relaxation rates at temperatures of 5(○), 15(○), 25(○), 35(○), 45(○), 65(○), 85(○), 105(○), and 125 °C (○) were measured depending on the freezing and boiling points of each liquid.

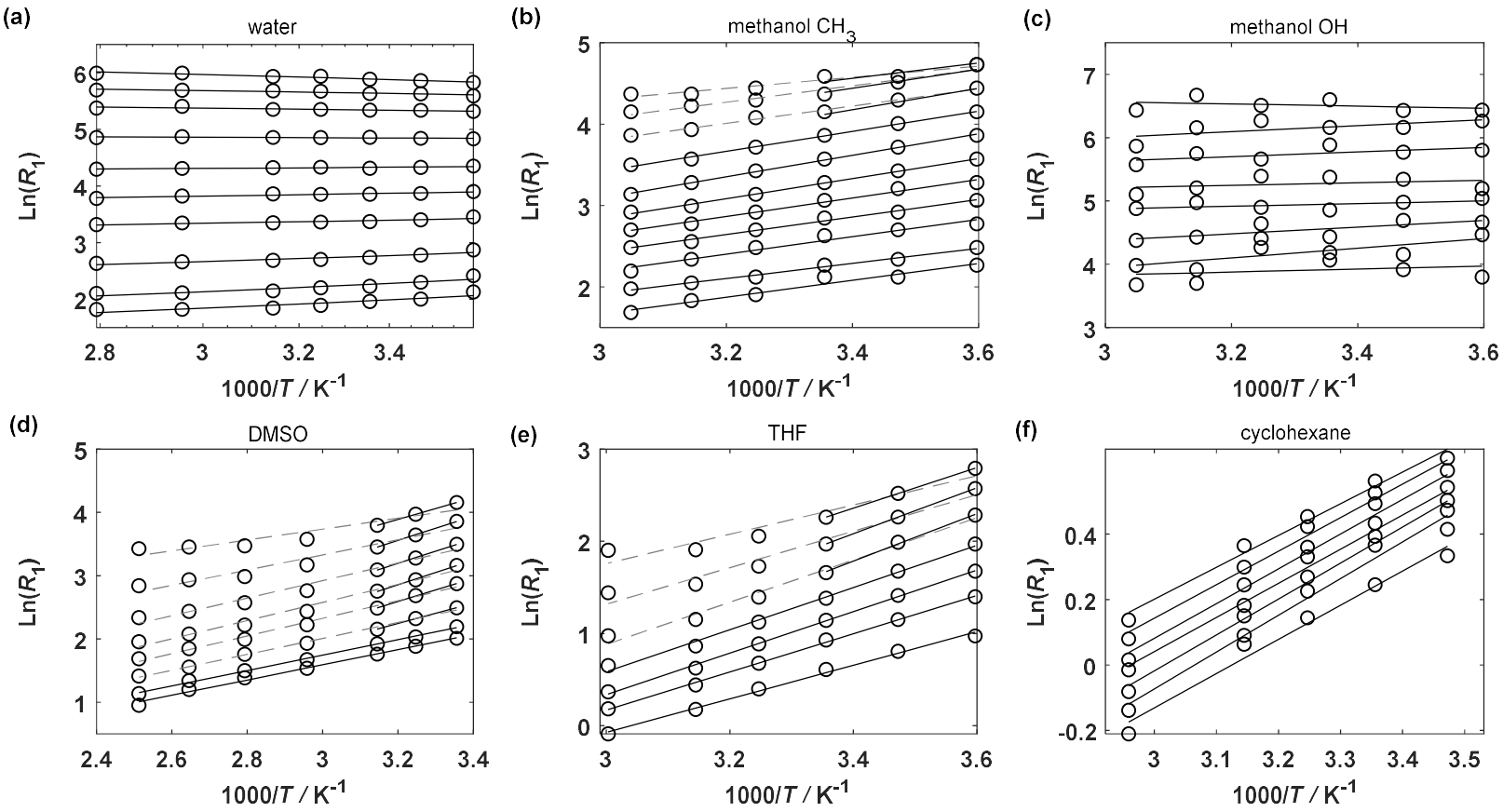

Figure 7.16: Arrhenius plots for the temperature dependent relaxation behaviour of (a) water, (b-c) methanol, (d) DMSO, (e) THF, and (f) cyclohexane imbibed within γ-alumina. For methanol the relaxation behaviour is resolved into (b) that of the methyl group and (c) that of the hydroxyl group. Arrhenius fits are represented by solid lines. In cases where a single Arrhenius fit was not valid due to the curvature of the data the Arrhenius fit over the whole dataset is shown (dashed line) and the low temperature data is fit independently (solid line).

For DMSO and THF a noticeable curvature was present in the low field relaxation data, with both species showing a plateau in their relaxation rate at higher temperatures. The low temperature behaviour followed normal diffusive processes with activation energies of 15.5 and 20.1 kJ mol^{-1} respectively. For THF and methanol the degree of curvature was less pronounced for the imbibed case relative to the immersed alumina. Due to the order in which the experiments were performed (highest temperatures to lowest temperatures) the pore filling decreased over the course of the variable temperature experiments. As the pore filling decreased, the relaxation rate increased despite the surface interactions remaining unchanged.[33] This effect opposed the levelling off of the relaxation data previously seen for high temperature relaxation data for THF, DMSO and the alkyl group of methanol, resulting in a linear Arrhenius behaviour being evident over a larger temperature range for imbibed samples compared to immersed samples.

Cyclohexane imbibed within γ-alumina showed linear Arrhenius behaviour across the entire temperature range. The linear Arrhenius behaviour occurred for both alumina immersed in cyclohexane and cyclohexane imbibed in γ-alumina. The activation energy for imbibed cyclohexane was 8.8 kJ mol^{-1}, slightly higher than that of the immersed sample, which was 6.3 kJ mol^{-1}.

7.5 Modelling of the relaxation of liquids imbibed within γ-alumina

In this section the adsorbates studied in section 7.4 are grouped based on their temperature dependent relaxation behaviour into non-polar, polar aprotic and polar protic adsorbates. The differing regimes of temperature dependent relaxation behaviour that were observed in section 7.4.3 are used to justify the choice of mathematical models that are fitted to the NMRD profiles of the liquids imbibed within γ-alumina. By grouping adsorbates based on the type of intermolecular interactions that are formed at the surface, all of the data presented in Figure 5.3 are modelled.

7.5.1 Non-polar liquids

Two features were observed in the NMRD profiles of non-polar species imbibed within γ-alumina, a sharp increase in the relaxation rate from 40-10 MHz, and a logarithmic increase in the relaxation rate below 10 MHz. For non-polar liquids (*n*-heptane,

cyclohexane and toluene) imbibed within γ-alumina a transient bonding was expected at the pore surface, which was consistent with a Korb model of relaxation. The non-polar adsorbates contained a greater concentration of dissolved oxygen than the polar liquids, which was shown in chapter 5 to cause a high field dispersion in the NMRD profile. These observations allowed the data to be fitted with a Korb model in the presence of dissolved oxygen (eqs. (7.2)-(7.4) & (7.6)). The results of the fitting are presented in Figure 7.17. The model was also applied to acetone which, despite being polar, showed a weak surface binding. The weak interaction was a direct result of the competitive adsorption process taking place at the catalyst surface, as shown in section 6.4.3. The stable reaction intermediate that formed from acetone was able to outcompete unreacted acetone for surface binding sites. This led to a reduced surface accessibility for acetone, and a weakening of the surface interaction strength. The reduced surface accessibility was estimated by subtracting the relative population of the intermediate from the relative surface population $\left({}^{N_S}/_{N} = {}^{\delta S}/_{V_P} - 0.13\right)$.

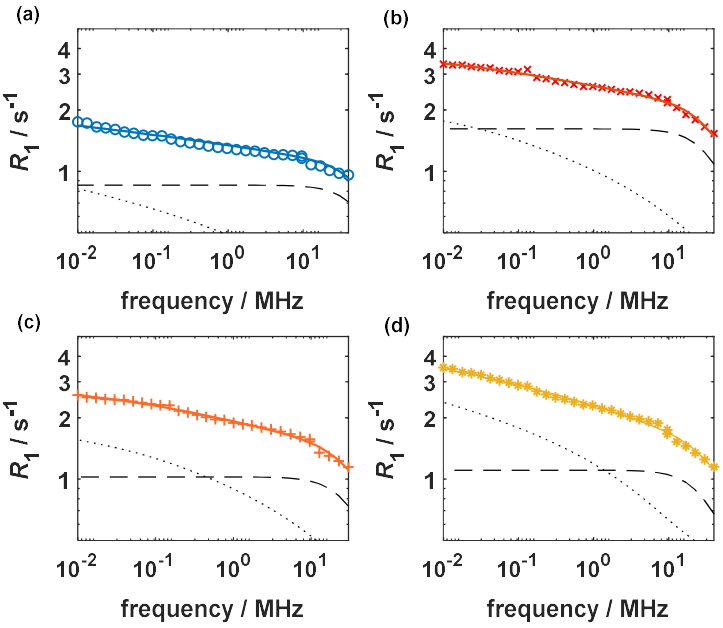

Figure 7.17: The NMRD profiles of (a) n-heptane, (b) cyclohexane, (c) toluene, and (d) acetone imbibed within γ-alumina. For each liquid the best fits obtained from eqs. (7.2)-(7.4) & (7.6) are shown (-) and decomposed into the oxygen contribution (- -), and the Korb model contribution (···).

For all four adsorbates excellent fits were obtained from eqs. (7.2)-(7.4) & (7.6). The calculated parameters are presented in Table 7.1, and the fitting parameters are presented in Table 7.2. The prefactor for the Korb model, A_{Korb} was defined as:

$$A_{\mathrm{Korb}} = \left(\frac{\mu_0}{4\pi}\right)^2 \frac{\pi\sigma_S(\gamma_I\gamma_S\hbar)^2 S(S+1)}{15d^2\delta'^2}, \tag{7.18}$$

and was calculated explicitly for each adsorbate rather than varied as a fitting parameter. For heptane, cyclohexane and acetone the contribution of molecular oxygen to the relaxation rate was similar, with all adsorbates showing a plateau in the oxygen contribution at $R_1 \sim$ 0.9-1.8 s^{-1}. The largest plateau of 1.8 s^{-1} was observed for cyclohexane. The contribution of the Korb model to the relaxation rate was the greatest for acetone, then similar for cyclohexane and toluene, and smallest for heptane. This ordering agreed well with the values of τ_{m}, which were used to rank the relative solid-liquid interactions strengths. The modelling showed highly variable values of τ_{S}, with some implausible values obtained. The sensitivity of the modelling to this parameter was tested by varying τ_{S} over several orders of magnitude, which resulted in no change in the fit for $\tau_{\mathrm{S}} > 16$ μs. This was because τ_{S} was larger than the limit that could be measured by FFC-NMR over the frequency range of 10 kHz-40 MHz (~10 μs). The insensitivity of the model to τ_{S} was further justified by an absence of a plateau in the NMRD profiles.

Table 7.1: The calculated parameters used for the fits shown in Figure 7.17. Values of d were taken from previous FFC-NMR modelling work for consistency,[5,34] ${}^{N_{\mathrm{S}}}/_{N} = {}^{\delta S}/_{V_{\mathrm{P}}}$, and A_{Korb} values were calculated from eq. (7.18).

Adsorbate	$\boldsymbol{d = \delta'}$ **/ Å**	$\boldsymbol{N_S/N}$	$\boldsymbol{A_{\mathrm{Korb}}}$**/ 10^9 s^{-2}**
n-heptane	6.0	0.19	7.4
cyclohexane	6.2	0.20	6.3
Toluene	6.0	0.19	4.3
acetone	6.1	0.04	6.7

For the Lorentzian contribution, the values of A_{Lor} were largest for heptane and cyclohexane, which contained the highest concentration of dissolved oxygen. This trend was consistent with the behaviour observed for bulk liquids in section 5.4.1. In contrast, the correlation times for relaxation in the presence of molecular oxygen, τ, were between

5.8-8.6 ps for all adsorbates excluding heptane ($\tau = 2.4$ ps). The values of τ followed a similar trend to the values τ_m, however the trend was less well-defined for τ.

Table 7.2: The fitting parameters obtained for the fits shown in Figure 7.17. The surface residence time, τ_S, is not shown as this value exceeded the maximum value that could be probed over the frequency range of the experiment.

Adsorbate	τ_m / ps	A_{Lor} / 10^9 s^{-2}	τ / ps
n-heptane	2.9	33.8	2.4
cyclohexane	7.1	28.4	5.8
Toluene	9.7	15.9	6.8
acetone	55.9	15.5	8.6

7.5.2 Polar aprotic liquids

For polar aprotic liquids (THF, DMSO, and the alkyl environment of methanol) two relaxation features were observed; a high frequency Lorentzian term and a power law term at low field strengths. For polar species capable of forming hydrogen bonds with the surface, strong and directional bonding was expected. This was consistent with an RMTD mechanism of relaxation. For consistency with the modelling of the non-polar adsorbates the high field Lorentzian term has been assigned to an interaction with molecular oxygen. As discussed in section 7.2.1.1, other possible physical origins may exist for this relaxation process, but they did not change the form of the spectral density function. These observations allowed the NMRD profiles of the polar aprotic adsorbates to be fitted with eqs. (7.1)-(7.4) and (7.9)-(7.10). The results of the fitting are presented in Figure 7.18. Methanol is a protic molecule, however, it was shown in chapter 6 that the alkyl and hydroxyl functionalities gave rise to different relaxation behaviour. The hydroxyl environment formed hydrogen bonds with the surface and the hydroxyl ^{1}H atom was readily exchangeable, however the alkyl environment was not. The differences in the surface chemistry controlled the relaxation rate of each functionality. As there was no evidence of intramolecular cross relaxation between the two environments, the non-exchangeable alkyl ^{1}H environment of methanol was modelled with an RMTD model in the presence of oxygen.

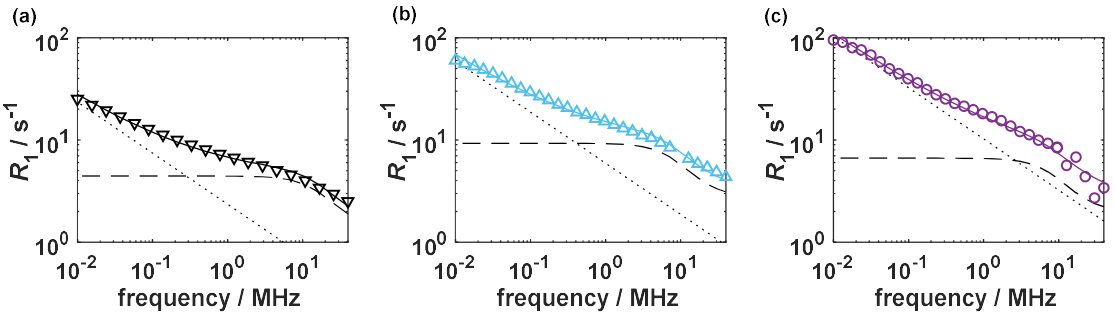

Figure 7.18: The NMRD profiles of (a) THF, (b) DMSO, and (c) the alkyl environment of methanol imbibed within γ-alumina. For each liquid the best fits obtained from eqs. (7.1)-(7.4) & (7.9)-(7.10) are shown (-) and decomposed into the Lorentzian contribution (- -), and the RMTD model contribution (···).

For all three liquids imbibed within γ-alumina, good fits to the experimental data were obtained. The physical parameters used in the fitting of the data in Figure 7.18 are listed in Table 7.3, and the fitting parameters are listed in Table 7.4. The prefactor for the RMTD model of relaxation, A_{RMTD}, was fixed for all adsorbates at 1×10^{9} s^{-2}. For all three liquids imbibed within γ-alumina the high field relaxation mechanism showed a greater relaxation rate for the polar aprotic liquids than was observed for the non-polar species. This resulted in values of τ that were 2-10 times larger for the polar aprotic liquids than the non-polar species, which was indicative of a stronger interaction of the polar species at the surface.

When considering the contribution of the RMTD mechanism to the relaxation behaviour, the surface adsorption correlation time, τ_{A}, can be considered as a direct measurement of the solid-liquid interaction strength. The values of τ_{A} obtained from the modelling showed that methanol and DMSO had very similar interaction strengths with the surface. Both, however, were more strongly interacting with the surface than THF.

Table 7.3: The calculated parameters used for the fits shown in Figure 7.18. Values of d were taken from previous FFC-NMR modelling work for consistency where possible,[5,34] $N_{\mathrm{S}}/N = \delta S/V_{\mathrm{P}}$, and A_{RMTD} was set to $1x10^{9}$ s^{-2}.

Adsorbate	δ / Å	D / 10^{-9} m^2 s^{-1}	N_S/N	A_{RMTD}/ 10^{9} s^{-2}
THF	6.3	2.84	0.20	1
DMSO	7.1	0.73	0.23	1
Methanol	3.6	2.41	0.11	1

Table 7.4: The fitting parameters obtained for the fits shown in Figure 7.18.

Adsorbate	τ_A / ps	A_{Lor}/ 10^9	τ/ ps
THF	10.0	34.4	12.9
DMSO	51.0	36.2	25.7
Methanol	48.7	27.7	25.3

7.5.2.1 Estimation of A_{RMTD}

In this section the effect of A_{RMTD} on the value of τ_A is explored. At low field strengths the RMTD contribution to the relaxation behaviour tended to a power law of exponent $\chi = -0.5$. This indicated that $\omega \ll \omega_A$. In this limit the RMTD component of the relaxation rate reduced to:

$$R_{1,obs} = R_{1,HF} + \frac{N_S}{N} A_{RMTD} {\omega_A}^{-1} \left[\left(\frac{\omega}{\omega_A} \right)^{-1/2} + 4 \left(\frac{2\omega}{\omega_A} \right)^{-1/2} \right], \quad (7.19)$$

where $R_{1,HF}$ is the high field relaxation rate. This expression could be further rearranged, and combined with eq. (7.10) to give:

$$R_{1,obs} = R_{1,HF} + \frac{N_s}{N} A_{RMTD} \frac{\sqrt{2D}\tau_A}{\delta} \left[\omega^{-1/2} + 4(2\omega)^{-1/2} \right]. \quad (7.20)$$

From eq. (7.20) it is clear that the observed relaxation rate depended on the combined parameter $A_{RMTD}\tau_A$. These two parameters were correlated and therefore it was necessary to explicitly calculate A_{RMTD} in order to obtain absolute values of τ_A from a direct fitting of the data.

The prefactor A_{RMTD} is given by the dipolar energy of the system, ω_d^2,[5]

$$A_{RMTD} = \omega_d^2 = \left(\frac{\gamma_I^2 \hbar}{r^3} \right)^2, \quad (7.21)$$

where r is the effective ^{1}H-^{1}H distance of the intramolecular dipolar interaction. The only variable that changed between adsorbates was the effective distance, r. For a two spin system, such as water, r is equal to the distance between the ^{1}H atoms. However, for a multispin system A_{RMTD} must be calculated by summing all of the dipolar interactions

between each pair of adsorbates (at a distance r_{ij}) and normalizing the value by the number of protons present, n_{p}.

$$A_{\mathrm{RMTD}} = \frac{\gamma_{\mathrm{I}}^4 \hbar^2}{n_{\mathrm{p}}} \sum \frac{1}{{r_{ij}}^6}. \tag{7.22}$$

An energy minimization was performed in Jmol to optimise the structure of each polar aprotic liquid. From these structures the corrected values of A_{RMTD} were calculated according to eq. (7.22), and the fitting of the data in Figure 7.18 was repeated. For methanol the interactions with the hydroxyl group were excluded. The results of the fitting are listed in Table 7.5. The relative results of the fitting were almost identical to those obtained when $A_{\mathrm{RMTD}} = 1\mathrm{x}10^9$. The τ_{A} values of DMSO and methanol were identical to one another within error, once again making it impossible to rank the interaction strength of these liquids. THF showed a lower value of τ_{A}, though this was now only a factor of 3 smaller than the value obtained for methanol and DMSO, rather than a factor of 5 as previously observed. The relative information was similar between the two fitting procedures, however the absolute values of τ_{A} were smaller when A_{RMTD} was explicitly calculated. The absolute values obtained from this method were smaller than bulk correlation times.[35] This suggested that whilst the relative measurements were robust, the modelling approach did not allow the extraction of absolute correlation times.

Table 7.5: The calculated values of the effective internuclear distance, r, and A_{RMTD}, and the fitting parameters obtained for the fits shown in Figure 7.18.

Adsorbate	r / Å	A_{RMTD} /10^{10} s^{-2}	τ_{A} / ps	A_{Lor}/ 10^9 s^{-2}	τ / ps
THF	2.31	1.0	1.0	34.2	13.0
DMSO	2.06	1.7	3.0	35.3	26.3
Methanol	1.96	1.8	2.7	25.4	26.2

7.5.3 Polar protic liquids

For polar protic liquids (water and the hydroxyl environment of methanol) three relaxation features were observed; a power law frequency behaviour which spanned the majority of the frequency range, the onset of a plateau of the relaxation rate at low frequencies, and a localized increase in the relaxation rate at $\omega/2\pi = 1.5$ MHz. For polar protic liquids, hydrogen bonding between the surface and the imbibed liquid would have resulted in an RMTD type relaxation process, as was observed for polar aprotic

adsorbates. However, the exchangeability of the protic functionalities interrupted the RMTD process, and transferred the magnetisation of the surface hydroxyls (i.e. the solid) to that of the adsorbate. The protic exchange mechanism allowed the NMRD data to be modelled as a surface diffusive process of hopping time, τ_m, and a surface residency time, τ_S, given by eq. (7.11). The local increase in the relaxation rate at 1.5 MHz was ascribed to an electronic paramagnetic relaxation effect as described in section 7.2.1.5. The close proximity of the paramagnetic species and ^{1}H atoms allowed the electron relaxation of the paramagnetic species to be transferred to the ^{1}H atoms, and then to the remainder of the imbibed liquid through chemical exchange. Finally, the power law relaxation behaviour of the protic liquids imbibed within γ-alumina extended to high frequencies. There was no evidence of a high field Lorentzian process, as was seen for non-polar and polar aprotic adsorbates.

Based on the observations made from inspection of the NMRD profiles, the protic data were fitted with eq. (7.2), (7.3), (7.12), (7.15), and (7.16). The results of the fitting are presented in Figure 7.19. For comparison, the NMRD profiles of the hydroxyl group of methanol are shown for CH_3OH (Figure 7.19b) and CD_3OH (Figure 7.19c) imbibed within γ-alumina. In the undeuterated case the presence of a dominant ^{1}H signal from the alkyl group increased the error in the estimation of the hydroxyl relaxation rate from the numerical inversions. The increased error was particularly evident at high field strengths, where the T_1 values of the alkyl and hydroxyl environments were similar. For the partially deuterated analogue (CD_3OH) the alkyl signal was no longer present, and the monoexponential relaxation behaviour was measured with a higher degree of accuracy.

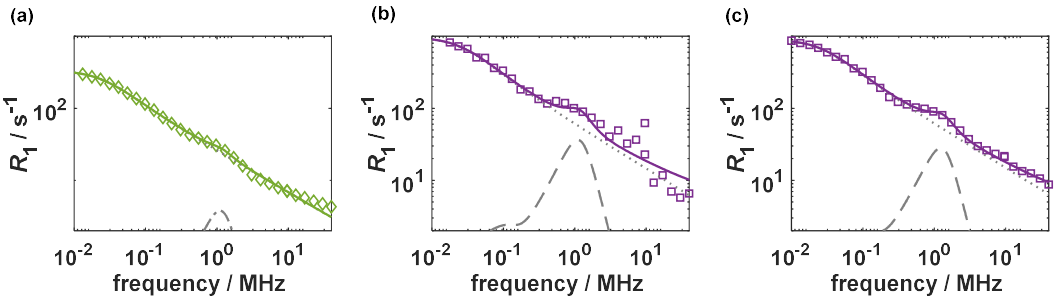

Figure 7.19: The NMRD profiles of (a) water, (b) the hydroxyl group of CH_3OH, and (c) CD_3OH imbibed within γ-alumina. For each liquid the best fits obtained from eqs.(7.2), (7.3), (7.12), (7.15), and (7.16) are shown (-) and decomposed into the EPR contribution (- -), and the protic model contribution (···).

For all three liquids imbibed within γ-alumina excellent fits to the experimental data were obtained. The prefactor, A_{prot}, was set to 1x10^9 s^{-2} for all samples for comparison, and the parameters obtained from the fitting are listed in Table 7.6. The value of χ and τ_{S} were the most robust parameters from the fitting, as these described the steepness of the NMRD profile and the onset of the plateau respectively. Remarkably, for all three samples imbibed within γ-alumina almost identical values of χ and τ_{S} were obtained. Greater variations were seen in the values of τ_{m} and $R_{1,\mathrm{B}}$, however these parameters were sensitive to experimental noise. According to eq. (7.12) the value of τ_{m} was estimated from the prefactor term, ${\tau_m}^{1-\chi} \approx {\tau_m}^{0.4}$. This resulted in the error in $\tau_m$being significant even for good fits of the experimental data. Furthermore, τ_{m} will be correlated with A_{prot} and therefore interpreting trends in τ_{m} is difficult without a prior knowledge of A_{prot}. It was noted however that τ_{m} was almost identical for the hydroxyl groups of CH_3OH and CD_3OH imbibed within γ-alumina.

Table 7.6: The fitting parameters obtained for the fits shown in Figure 7.19.

Adsorbate	χ	τ_S / µs	τ_m / ps	$R_{1,\mathrm{B}}$ / s^{-1}	H_{v} / 10^{17} s^{-2}	τ_{v} / ns	A_{EPR} / 10^9 s^{-2}
Water	0.57	5.9	31	0.0	1.8	1.7	0.02
CH_3OH hydroxyl group	0.62	5.7	174	3.1	1.6	1.6	0.18
CD_3OH hydroxyl group	0.61	5.4	187	4.0	1.8	1.2	0.15

7.6 Discussion

In this section the temperature dependent relaxation behaviour of the different liquids imbibed within γ-alumina is used to justify the choice of model used to explain the observed relaxation behaviour. The implications that the modelling process has on the physicochemical conclusions that can be drawn from the NMRD profiles of each adsorbate are then discussed.

7.6.1 Relaxation of non-polar species

Cyclohexane was a typical non-polar adsorbate that showed a weak interaction with the surface. This was confirmed by the shallow dispersion profile and the small relaxation rate at low field strengths that was observed for cyclohexane imbibed within γ-alumina. The relaxation rate decreased as the temperature was increased over the entire temperature range, with an associated activation energy of 6.3 and 8.8 kJ mol^{-1} for the immersed and imbibed experiments respectively. This value was consistent with temperature dependent relaxation measurements of dodecane in a range of rock cores and silica packings,[28] and only slightly lower than the measured activation energies of bulk diffusion observed for cyclohexane (13.0 kJ mol^{-1})[36] and dodecane (10.9 kJ mol^{-1}).[28] The decrease in the apparent activation energy upon adsorption was expected in the presence of a weak, but non-zero, surface interaction strength. The presence of 7 ppm of Fe^{3+} was observed by ESR (see appendix 1), which dominated the relaxation behaviour of the sample due to the large gyromagnetic ratio of the unpaired electrons ($\gamma_S = 658\gamma_I$). Based on these observations, a Korb model was used to describe the low frequency relaxation behaviour.

At high field strengths a Lorentzian feature was observed, which was identical in shape to the dispersion behaviour observed for bulk liquids. For bulk liquids the dissolved oxygen content controlled the relaxation rate of this feature. As the non-polar liquids had large oxygen solubilities it followed that a Lorentzian feature was expected for the non-polar imbibed liquids. Figure 7.17 shows that the contribution from molecular oxygen was larger for the adsorbed species than it was for bulk liquids (section 5.4.1). At the pore surface, the oxygen-solvent complexes formed in solution experienced a restricted rotation due to the presence of the pore surface. The restriction increased the rotational correlation time of the complex and increased the contribution to the NMRD profile from molecular oxygen. This was consistent with cyclohexane having the largest contribution from molecular oxygen, as this liquid was highly viscous and had the greatest oxygen solubility of the non-polar liquids used within this study.

By extension, the other non-polar species explored within this work (heptane and toluene) were expected to obey a similar temperature dependence, and were therefore fitted with a Korb model and an oxygen contribution. For acetone an aldol reaction occurred, which generated a strongly interacting intermediate as shown in section 6.4.3.

The competitive adsorption process resulted in acetone being outcompeted for surface binding sites, and thus it was only weakly interacting with the surface. The temperature dependence of acetone adsorption could not be measured without influencing the equilibrium position of the aldol reaction. It was assumed that the molecular dynamics of the weakly interacting acetone could be well described by a Korb model with an oxygen contribution. The absolute values of the correlation times for each liquid were only slightly larger than those of the respective bulk liquids,[35] which was consistent with a weak surface interaction for all adsorbates. The surface hopping correlation times, τ_{m}, described the rate of translational diffusion of the molecule across the surface, and this metric was a good indicator of the solid-liquid interaction strength. The τ_{m} values obtained from the data fitting ranked the solid-liquid surface interaction as acetone > toluene > cyclohexane > heptane. This ordering was consistent with the relative polarities of the liquids given by Reichardt analysis (Table 5.3). However, for toluene and cyclohexane the reported values of τ_{m} were within a factor of 1.4. This meant that it was not possible to definitely rank these molecules, despite there having been a large difference in their respective polarities. In contrast, the separation between heptane and cyclohexane was much clearer, despite these molecules having the same polarity. This means that for weakly interacting species geometric or steric effects may also contribute to the binding strength and relaxation behaviour.

7.6.2 Relaxation of polar aprotic species

THF, DMSO and methanol were all polar adsorbates that bound to the surface by acting as hydrogen bond acceptors. This binding process led to strong and directional intermolecular interactions, which was corroborated by steep NMRD profiles, and a high relaxation rate at low field strengths for each liquid imbibed within γ-alumina. At high field strengths the relaxation rate of the imbibed liquid decreased as the temperature increased. From this region activation energies of 21.8, 13.8 and 11.3 kJ mol^{-1} were obtained for THF, DMSO and methanol respectively. For DMSO and methanol these values were comparable to their bulk activation energy of self-diffusion.[36,37] In contrast, the measured activation energy of the relaxation rate of THF imbibed within γ-alumina was 4 times larger than the activation energy of self-diffusion.[38] This suggested that for DMSO and methanol the high field relaxation behaviour was dominated by a simple diffusive process, but for THF imbibed within γ-alumina a more complex surface

interaction occurred. Despite the strong temperature dependence observed for THF, the high field data could still be well represented by a Lorentzian spectral density function.

At low field strengths, the relaxation rate of each liquid imbibed within γ-alumina increased as the temperature was increased, before reaching a temperature independent plateau. For THF and methanol imbibed within γ-alumina the NMRD profile became temperature independent for $T > 35$ °C, whereas DMSO showed a temperature dependence up to $\sim T = 65$ °C. The transition between two temperature dependent regimes implied a superposition of the Lorentzian process with an RMTD mechanism. The magnitude of the Lorentzian feature was largest for DMSO, which was consistent with the low field plateau occurring at the highest temperature for this adsorbate. At higher temperatures and low field strengths the contribution of the Lorentzian process to the total relaxation rate was negligible, and the temperature dependence reflected the weak dependence of the RMTD mechanism.

In contrast to the intermolecular Korb model of relaxation (I-S interactions), the RMTD model is controlled by an intramolecular relaxation process (I-I interactions). For non-polar species the Korb model dominated the relaxation of the adsorbate, however for polar aprotic liquids the RMTD mechanism was most effective. The difference in the dominant relaxation mechanism was caused by the hydrogen bond acceptor properties of the polar aprotic liquids, as shown schematically in Figure 7.20. The polar aprotic liquids formed directional bonds on the surface, which held the ^{1}H spins of the adsorbate (I spins) away from the paramagnetic impurities on the pore surface (S spins). The strength of the intermolecular interaction depends strongly on the distance between the spins, r, and is proportional to r^{-3}. This meant that the increased magnitude of r caused by the hydrogen bonding greatly reduced the efficacy of the intermolecular relaxation pathway for the polar aprotic species. Furthermore, the directionality of the binding prevented the rapid loss of rotational correlation, and made an intramolecular RMTD mechanism of relaxation effective at low field strengths. For non-polar species there was no directionality imposed upon the surface binding, allowing a short distance of closest approach between the spins of the adsorbate and the paramagnetic impurities on the pore surface (Figure 7.20a).

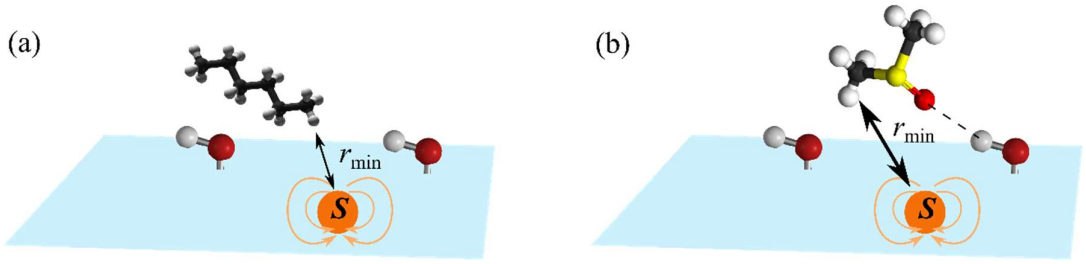

Figure 7.20: Schematic diagrams of the distance of closest approach, r_{min}, between a fixed paramagnetic impurity on the pore surface and the spins of an (a) non-polar and (b) polar aprotic adsorbate.

The surface adsorption times, τ_A, described the residence time of the adsorbate on the surface between successive bulk excursions. Therefore this metric was expected to be a good indicator of surface interaction strength. For methanol and DMSO the values of τ_A were identical, despite methanol being more polar than DMSO. Polarity was therefore not the only factor affecting the surface binding, and the greater Lewis basicity of DMSO[39] may have resulted in similar binding strengths for the two adsorbates. Both DMSO and methanol showed a greater interaction strength than THF when imbibed within γ-alumina. The absolute values of the τ_A were orders of magnitude smaller than those previously obtained,[5,22] and the τ_A values obtained after an explicit calculation of the prefactor were shorter than bulk correlation times. This discrepancy can be justified by the form of the spectral density function that was applied for the RMTD mechanism. To obtain a closed form expression that allowed the fitting of the NMRD profile an infinite planar surface was assumed. This simplification does not accurately represent the pores of the γ-alumina, which were far more geometrically complex. The geometry of the pore and local surface curvature have a strong effect on the observed relaxation rate.[13,40] Molecular dynamics simulations have shown that these effects are exacerbated for strongly adsorbed species,[13] which was expected for polar liquids imbibed within γ-alumina. Theoretical expressions have been proposed to account for the effects of geometry and surface roughness, however these approaches required a detailed knowledge of the probability distributions for molecular adsorption and relocations within the bulk pore space. The latter, in particular, has so far only been solved for a limited range of pore geometries and the effect of confinement has been argued to further complicate the modelling by suppressing the tail of the associated probability distributions.[13] This complicates the application of RMTD models that explicitly

consider the pore geometry and makes them applicable only in cases where extensive physical and theoretical characterisation of the porous medium has been undertaken. Instead, by imposing a planar geometry upon all adsorbates imbibed within the same γ-alumina it was possible to measure the relative solid-liquid interaction strength of each liquid with minimal prior knowledge. The fitting was repeated without the inclusion of the high field Lorentzian term, in order to explore the effect that this component has on the relative values of τ_A. Although the quality of the fitting was poorer for all adsorbates, there were negligible changes in the relative values of τ_A.

7.6.3 Relaxation of polar protic species

Water and methanol are polar protic adsorbates, which bond to the surface through a strong and directional hydrogen bond network. The exchange of the protic functionalities with the surface hydroxyl groups interrupted the RMTD relaxation mechanism that occurred for polar adsorbates. This reduced the distance of closest approach between the I and S spins to the length of the surface hydroxyl functionality, as shown in Figure 7.21. As the distance between the I and S spins was reduced, the intermolecular interaction dominated the relaxation rate, in contrast to the relaxation of the polar aprotic adsorbates.

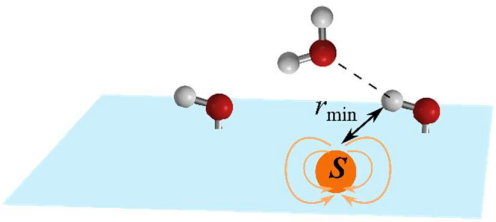

Figure 7.21: A schematic diagram of the distance of closest approach, r_{min}, between a fixed paramagnetic impurity on the pore surface and the spins of polar protic adsorbate. As the surface hydroxyls are able to exchange with protic functionalities, the distance between the paramagnetic impurity and the surface hydroxyl is the distance of closest approach.

The importance of the exchange mechanism was demonstrated by the temperature dependent relaxation behaviour observed for protic adsorbates. The inversion of the temperature dependence at low field strengths was indicative of an activated diffusion process dominating the relaxation behaviour. The apparent activation energy at low field strengths has been shown to be the difference between the difference between the activation energy of bulk diffusion (E_a~ −20.1 kJ mol^{-1}) and the activation energy for

diffusion on the surface ($E_{\mathrm{m}}\sim -31.0$ kJ mol^{-1}).[6] This resulted in an apparent activation energy of ($E_{\mathrm{a}} - E_{\mathrm{m}}$)$\sim$10.9 kJ mol^{-1} for water in a silica glass.[6] This value was larger in magnitude than the value obtained for water and methanol imbibed within γ-alumina (1.8 kJ mol^{-1}). For the experiments reported within this chapter, the frequency at which the temperature dependence inverted was also much lower than that observed for the silica glass. The slope was still changing at the lowest frequency points, and therefore even lower fields would be required to estimate E_{m} accurately for liquids imbibed within γ-alumina. The position of the inversion was of particular interest for the protic liquids imbibed within γ-alumina, as it remained constant for both water and methanol at a frequency of 0.07-0.09 MHz. This implied that the temperature dependence, and hence the relaxation rate, did not strongly depend on the interaction between the imbibed liquid and the surface. Instead the relaxation was dominated by the relaxation of the surface hydroxyl groups.

The results of the modelling showed very similar values of χ, τ_{S}, and $R_{1,\mathrm{B}}$ for water, CH_3OH and CD_3OH. This was consistent with a surface relaxation process that was constant for all three adsorbates. The renormalized NMRD profiles of water and CD_3OH imbibed within γ-alumina are shown in Figure 7.22. The renormalization confirmed that the molecular dynamics that dominated the relaxation behaviour were identical for these adsorbates. As the interaction strength of water with the surface was not be identical to that of methanol with the surface, the NMRD profiles were insensitive to the surface interaction strength. Instead, the exchangeability of the protic functionalities allowed the measurements to probe the surface relaxation rate directly. Further to the coincidence of the NMRD profiles, the presence of an electronic paramagnetic relaxation (EPR) enhancement between 0.5-3 MHz strongly supported the presence of a hydrogen bond network at the catalyst surface. This is because EPR enhancements are a through space interaction which are only observed in systems where the ^{1}H spins being measured are capable of binding directly to the paramagnetic impurity. For the hydroxyl ^{1}H atoms of methanol the EPR enhancement was observed, but for the alkyl ^{1}H atoms it was not. This meant that the molecule was bound to the surface through the hydroxyl group and therefore hydrogen bonding was occurring.

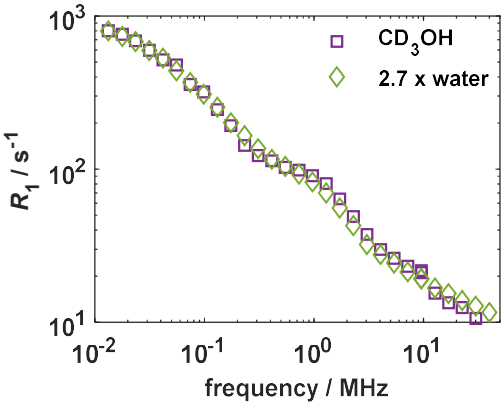

Figure 7.22: The NMRD profile of CD_3OH and water imbibed within γ-alumina. The water NMRD profile has been multiplied by a factor of 2.7 to show that the two NMRD profiles are controlled by the same dynamic process.

7.6.3.1 Scaling factors for methanol and water NMRD profiles

The surface relaxation process dominating the relaxation behaviour of protic liquids imbibed within γ-alumina was shown to be identical for methanol and water. As a result of the uniform surface relaxation process, the observed relaxation rate can be expressed as:

$$R_{1,\mathrm{obs}} = R_{1,\mathrm{B}} + \frac{N_\mathrm{S}}{N} R_{1,\mathrm{S}}\,, \tag{7.23}$$

where $\frac{N_\mathrm{S}}{N}$ is the ratio of spins involved in the surface hydrogen bond network, and N is the total number of spins within the pore space. The scaling process used to generate Figure 7.22 showed that $\frac{N_\mathrm{S}}{N}$ was 2.7 times larger for methanol than for water. The geometric arguments presented in section 5.5.2.3 can be used to estimate the number of spins within a single adsorbed layer for methanol and water:

$$N_\mathrm{S} = N_\mathrm{ads} + N_\mathrm{Surf}\,, \tag{7.24}$$

where N_ads is the number of exchangeable functionalities present in the adsorbed surface layer, and N_Surf is the number of surface hydroxyl groups. As the surface hydroxyl groups are exchangeable, these must be included in the N_S term. If the number of surface hydroxyl groups is larger than the number of molecules that can fit within the surface layer, N_ads is given as:

$$N_{\mathrm{ads}} = \frac{S_p \lambda m N_{\mathrm{A}} n_p}{V_{\mathrm{m}}}, \tag{7.25}$$

where S_{P} is the surface area, λ is the thickness of the surface layer, m is the sample mass, N_A is Avogadros constant, n_p is the number of exchangeable protons per molecule, and V_{m} is the pore volume. However, if the number of surface hydroxyl groups is lower than the number of molecules that can occupy a single surface layer, N_{ads} is given as:

$$N_{\mathrm{ads}} = \alpha_{\mathrm{OH}} S_{\mathrm{P}} m n_p, \tag{7.26}$$

where α_{OH} is the surface hydroxyl density of the porous material. The value of α_{OH} is rarely known *a priori*, but is important in the analysis of the adsorption properties and catalytic behaviour of porous materials. Using the formalisms outlined within this section the difference in scaling of the NMRD profiles of CD_3OH and water can be justified by a γ-alumina surface with $\alpha_{\mathrm{OH}} = 5.6$ nm^{-2}. This value is consistent with other measurements reported in the literature for the surface hydroxyl density of γ-alumina.[41] The arguments presented in this section show that the observed difference in the magnitude of the NMRD profiles of water and methanol imbibed within γ-alumina was due to a population scaling factor. Furthermore, the size of this scaling factor could be used to further characterise the porous surface and provide information about the density of surface hydroxyl functionalities.

7.7 Conclusions

A protocol was developed to allow the separation of the temperature dependent relaxation behaviour of several different liquids imbibed within γ-alumina from the physicochemical changes in the sample caused by heating. By measuring the samples with a descending temperature profile an accurate measurement of the temperature dependence was achieved for γ-alumina immersed in each liquid. A comparison of the liquid-immersed and imbibed liquid samples showed the same temperature dependence for both types of sample. The variable temperature experiments could be separated into three classes of adsorbate; those that showed a decrease in R_1 as the temperature increased at all field strengths, those that showed no temperature dependence at low field strengths,

and those that showed an increase in R_1 as the temperature increased at low field strengths. These temperature dependencies could be assigned to non-polar, polar aprotic, and polar protic molecules respectively.

For non-polar liquids imbibed within γ-alumina, a Korb model of relaxation combined with a Lorentzian term for the contribution of dissolved oxygen provided an excellent fit to the NMRD profiles. This highlighted the transient nature of the bonding at the pore surface. The resultant correlation times allowed a clear ordering of the solid-liquid interaction strength, given as acetone > toluene ≈ cyclohexane > heptane. The absolute values of the correlation times were slightly larger than bulk correlation times, and were all consistent with a weak surface interaction strength.

For polar aprotic liquids imbibed within γ-alumina a RMTD model combined with a Lorentzian term for the contribution of dissolved oxygen provided a good fit to the NMRD profiles. This showed that strong and directional hydrogen bonds were formed at the pore surface, and once again an ordering of the interaction strength of the adsorbates was possible, with methanol ≈ DMSO > THF. However, the absolute correlation times obtained from the fitting of the RMTD model were unphysical. The application of the model assumed an infinite planar surface, and was not applicable to the alumina studied herein. This resulted in the correlation times obtained from these experiments giving a relative ranking of the solid-liquid interaction strength, but not absolute values.

Finally, the protic liquids imbibed in γ-alumina were insensitive to the solid-liquid interaction strength. An exchange mechanism occurred between the surface hydroxyl groups and the protic functionalities of the adsorbates. The exchange allowed magnetization transfer between the two environments. As a result, the relaxation behaviour of the solid dominated the NMRD profile. A relaxation mechanism assuming a surface diffusive process of the ^{1}H hydroxyl species, with a cut-off at long times, provided an excellent fit to the data. This model was combined with an electronic paramagnetic enhancement that controlled the relaxation rate over a narrow range of high frequency values. The fitting parameters obtained from this modelling approach showed that the NMRD profiles of water, CH_3OH, and CD_3OH imbibed within γ-alumina were controlled by the same molecular dynamics process. As water and methanol did not have the same interaction strength with the surface it was evident that the NMRD profiles of each imbibed liquid were only sensitive to the relaxation behaviour of the solid. A

renormalization of the NMRD profiles of water and CD_3OH imbibed within γ-alumina showed a constant ratio between the two of 2.7. This factor could be justified in terms of the difference in the ratio of spins at the surface and the total number of spins present for each adsorbate. Based on a detailed characterisation of the pore, the difference of 2.7 corresponded to a surface hydroxyl density of 5.6 nm^{-2}.

Despite all of the liquids studied herein being imbibed in the same γ-alumina sample, a wide array of different relaxation behaviour was observed. The type of behaviour was controlled by the solid-liquid interactions, and in the case of non-polar and polar aprotic liquids the NMRD profiles could be used to quantify the solid-liquid interaction strength. In contrast, the NMRD profiles of protic liquids allowed a direct characterisation of the properties of the solid. Given that water is an often used adsorbate for NMRD studies, these results imply that great care must be taken when interpreting the NMRD profile of water imbibed in mesoporous oxides, and particularly when comparing water to other adsorbates.

7.8 References

(1) Brownstein, K., R.; Tarr, C., E. Spin-Lattice Relaxation in a System Governed by Diffusion. *J. Magn. Reson.* **1977**, *26*, 17–24.

(2) Teng, C.; Hong, H.; Kiihne, S.; Bryant, R. G. Molecular Oxygen Spin–Lattice Relaxation in Solutions Measured by Proton Magnetic Relaxation Dispersion. *J. Mag. Res* **2001**, *34*, 31–34.

(3) Zavada, T.; Kimmich, R. The Anomalous Adsorbate Dynamics at Surfaces in Porous Media Studied by Nuclear Magnetic Resonance Methods. the Orientational Structure Factor and Lévy Walks. *J. Chem. Phys.* **1998**, *109*, 6929–6939.

(4) Martini, F.; Borsacchi, S.; Geppi, M.; Forte, C.; Calucci, L. Hydration of MgO-Based Cement: Water Dynamics by ^1H Fast Field-Cycling NMR Relaxometry. *J. Phys. Chem. C* **2017**, *121*, 26851–26859.

(5) Korb, J.-P. Multiscale Nuclear Magnetic Relaxation Dispersion of Complex Liquids in Bulk and Confinement. *Prog. Nucl. Magn. Reson. Spectrosc.* **2018**, *104*,

12–55.

(6) Korb, J. P.; Whaley Hodges, M.; Gobron, T.; Bryant, R. G. Anomalous Surface Diffusion of Water Compared to Aprotic Liquids in Nanopores. *Phys. Rev. E* **1999**, *60*, 3097–3106.

(7) Korb, J.-P.; Whaley-Hodges, M.; Bryant, R. G. Translational Diffusion of Liquids at Surfaces of Microporous Materials: Theoretical Analysis of Field-Cycling Magnetic Relaxation Measurements. *Phys. Rev. E* **1997**, *56*, 1934–1945.

(8) Korb, J. P.; Freiman, G.; Nicot, B.; Ligneul, P. Dynamical Surface Affinity of Diphasic Liquids as a Probe of Wettability of Multimodal Porous Media. *Phys. Rev. E* **2009**, *80*, 61601.

(9) Barberon, F.; Korb, J.; Petit, D.; Morin, V.; Bermejo, E. Probing the Surface Area of a Cement-Based Material By Nuclear Magnetic Relaxation Dispersion. *Phys. Rev. Lett.* **2003**, *90*, 116103.

(10) Muncaci, S.; Mattea, C.; Stapf, S.; Ardelean, I. Frequency-Dependent NMR Relaxation of Liquids Confined inside Porous Media Containing an Increased Amount of Magnetic Impurities. *Magn. Reson. Chem.* **2013**, *51*, 123–128.

(11) Korb, J. P.; Louis-Joseph, A.; Benamsili, L. Probing Structure and Dynamics of Bulk and Confined Crude Oils by Multiscale NMR Spectroscopy, Diffusometry, and Relaxometry. *J. Phys. Chem. B* **2013**, *117*, 7002–7014.

(12) Kimmich, R.; Anoardo, E. Field-Cycling NMR Relaxometry. *Prog. Nucl. Magn. Reson. Spectrosc.* **2004**, *44*, 257–320.

(13) Levitz, P. Probing Interfacial Dynamics of Water in Confined Nanoporous Systems by NMRD. *Mol. Phys.* **2018**, *117*, 952-959.

(14) Levitz, P.; Bonnaud, P. A.; Cazade, P.-A.; Pellenq, R. J.-M.; Coasne, B. Molecular Intermittent Dynamics of Interfacial Water: Probing Adsorption and Bulk Confinement. *Soft Matter* **2013**, *9*, 8654–8663.

(15) Oleg V. Bychuk; Ben O'Shaughnessy. Anomalous Diffusion of Surface-Active Species at Liquid-Fluid and Liquid-Solid Interfaces. *J. Phys. II Fr.* **1994**, *4*, 1135–1156.

(16) Kimmich, R.; Fatkullin, N. Progress in Nuclear Magnetic Resonance Spectroscopy Self-Diffusion Studies by Intra- and Inter-Molecular Spin-Lattice Relaxometry Using Field-Cycling : Liquids , Plastic Crystals , Porous Media , and Polymer Segments. *Prog. Nucl. Magn. Reson. Spectrosc.* **2017**, *101*, 18–50.

(17) Stapf, S.; Kimmich, R.; Seitter, R. O.; Maklakov, A. I.; Skirda, V. D. Proton and Deuteron Field-Cycling NMR Relaxometry of Liquids Confined in Porous Glasses. *Phys. Rev. Lett.* **1996**, *115*, 107–114.

(18) Stapf, S.; Ren, X.; Talnishnikh, E.; Blümich, B. Spatial Distribution of Coke Residues in Porous Catalyst Pellets Analyzed by Field-Cycling Relaxometry and Parameter Imaging. *Magn. Reson. Imaging* **2005**, *23*, 383–386.

(19) Cadar, C.; Ardelean, I. Surface Influence on the Rotational and Translational Dynamics of Molecules Confined inside a Mesoporous Carbon Xerogel. *Magn. Reson. Chem. 57*, 829-835.

(20) Levitz, P. Random Flights in Confining Interfacial Systems Random Flights in Confining Interfacial Systems. *J. Phys. Condens. Matter* **2005**, *17*, S4059.

(21) Levitz, P.; Zinsmeister, M.; Davidson, P.; Constantin, D.; Poncelet, O. Intermittent Brownian Dynamics over a Rigid Strand: Heavily Tailed Relocation Statistics in a Simple Geometry. *Phys. Rev. E* **2008**, *78*, 30102.

(22) Chemmi, H.; Petit, D.; Levitz, P.; Denoyel, R.; Galarneau, A.; Korb, J.-P. Noninvasive Experimental Evidence of the Linear Pore Size Dependence of Water Diffusion in Nanoconfinement. *J. Phys. Chem. Lett.* **2016**, *7*, 393–398.

(23) Halle, B. Molecular Theory of Field-Dependent Proton Spin-Lattice Relaxation in Tissue. *Magn. Reson. Med.* **2006**, *56*, 60–72.

(24) Korb, J.-P. Surface Dynamics of Liquids in Porous Media. *Magn. Reson. Imaging* **2001**, *19*, 363–368.

(25) Südland, N.; Zavada, T.; Su, N. Propagator Representation of Anomalous Diffusion : The Orientational Structure Factor Formalism in NMR. *Phys. Rev. E* **1999**, *60*, 1292–1298.

(26) Korb, J.; Diakova, G.; Bryant, R. G.; Korb, J. Paramagnetic Relaxation of Protons

in Rotationally Immobilized Proteins Paramagnetic Relaxation of Protons in Rotationally Immobilized Proteins. *J. Chem. Phys.* **2006**, *124*, 134910.

(27) Korb, J. P.; Monteilhet, L.; McDonald, P. J.; Mitchell, J. Microstructure and Texture of Hydrated Cement-Based Materials: A Proton Field Cycling Relaxometry Approach. *Cem. Concr. Res.* **2007**, *37*, 295–302.

(28) Godefroy, S.; Fleury, M.; Deflandre, F.; Korb, J. P. Temperature Effect on NMR Surface Relaxation in Rocks for Well Logging Applications. *J. Phys. Chem. B* **2002**, *106*, 11183–11190.

(29) Latour, L. L.; Kleinberg, R. L.; Sezginer, A. Nuclear Magnetic Resonance Properties of Rocks at Elevated Temperatures. *J Colloid Interface Sci* **1992**, *150*, 535–548.

(30) Butler, J. P.; Reeds, J. A.; Dawson, S. J. Estimating Solutions of First Kind Integral Equations with Nonnegative Constraints and Optimal Smoothing. *J. Numer. Anal.* **1981**, *18*, 381–397.

(31) Krynicki, K. Proton Spin-Lattice Relaxation in Pure Water between 0 °C and 100 °C. *Physica* **1966**, *32*, 167–178.

(32) Krauss, C. J.; Spinks, J. W. T. Temperature Coefficients for Self-Diffusion in Solution. *Can. J. Chem.* **1954**, *32*, 71–78.

(33) Mattea, C.; Kimmich, R.; Ardelean, I.; Wonorahardjo, S.; Farrher, G. Molecular Exchange Dynamics in Partially Filled Microscale and Nanoscale Pores of Silica Glasses Studied by Field-Cycling Nuclear Magnetic Resonance Relaxometry. *J. Chem. Phys.* **2004**, *121*, 10648–10656.

(34) Webster, C. E.; Drago, R. S.; Zerner, M. C.; Gaines, V. Molecular Dimensions for Adsorptives. *J. Am. Chem. Soc* **1998**, *120*, 5509–5516.

(35) Singer, P. M.; Asthagiri, D.; Chapman, W. G.; Hirasaki, G. J. Molecular Dynamics Simulations of NMR Relaxation and Diffusion of Bulk Hydrocarbons and Water. *J. Magn. Reson.* **2017**, *277*, 15–24.

(36) Holz, M.; Heil, S. R.; Sacco, A. Temperature-Dependent Self-Diffusion Coefficients of Water and Six Selected Molecular Liquids for Calibration in

Accurate ^{1}H NMR PFG Measurements. *Phys. Chem. Chem. Phys.* **2000**, *2*, 4740–4742.

(37) Tyn, M. T. Temperature and Concentration Dependence of Liquid Phase Diffusion Coefficients (Thesis), Loughborough University, 1974.

(38) Tan, R.-R.; Shen, X.; Hu, L.; Zhang, F.-S. Liquid-to-Glass Transition of Tetrahydrofuran and 2-Methyltetrahydrofuran. *Chinese Phys. B* **2012**, *21*, 86402.

(39) Brown, I. D. Structural Chemistry and Solvent Properties of Dimethylsulfoxide. *J. Solution Chem.* **1987**, *16*, 205–224.

(40) *Field-Cycling NMR Relaxometry*; Kimmich, R., Ed.; New Developments in NMR; The Royal Society of Chemistry, 2019.

(41) Digne, M.; Sautet, P.; Raybaud, P.; Euzen, P.; Toulhoat, H. Hydroxyl Groups on γ-Alumina Surfaces: A DFT Study. *J. Catal.* **2002**, *211*, 1–5.

Chapter 8 : Binary liquid mixtures imbibed within γ-alumina

The work contained within this chapter forms part of the publication: Ward-Williams, J.; Gladden, L. F. Insights into Adsorption Behaviour of Binary Liquid Mixtures in Porous Media Using Fast Field Cycling NMR. *Magn. Reson. Imaging* **2019***, 56,* 57–62.

Contents

8.1 Introduction

The multicomponent relaxation behaviour of liquids imbibed within γ-alumina was observed for acetone and methanol in chapter 6. The ability of FFC-NMR to resolve minor components in the T_1 distributions allowed a degree of chemical resolution to be obtained that was not normally possible through FFC-NMR experiments. In each case the physical origin of the peak was identified and used to enhance the overall understanding of the system. In this chapter the interaction strengths of samples that are expected to give multicomponent relaxation will be explored using FFC-NMR and compared to a conventional T_1/T_2 approach. These samples consist of binary liquid mixtures of cyclohexane:THF (non-polar:polar) and THF:methanol (polar:polar) imbibed within a γ-alumina catalyst over a wide range of compositions. The relaxation rate data will be analysed to explore the relative influences of surface dynamics and surface accessibility on the observed relaxation rates.

8.2 Background and literature review

8.2.1 Applications and limitations of NMR methods for studying binary liquid adsorption

Single-component liquids imbibed within porous media at full and partial saturation have been widely reported within the literature using NMR techniques,[1–4] but comparatively few studies exist for liquid mixtures.[2,5–9] The focus of existing studies of binary liquid mixtures has often been centred on displacement experiments, where a single fluid is imbibed within a porous medium before a second fluid is added to displace the first. These include cryoporometry measurements of the water displacement of decane in silicas,[6] and time resolved T_1/T_2 measurements of water and *iso*-propanol displacements in Ru/Al_2O_3 catalysts.[2] Depending on the sample preparation methodology, displacement experiments allow both kinetic and thermodynamic measurements of the surface adsorption behaviour. Fixed field NMR measurements are often sufficiently fast to monitor the dynamics of these coadsorption problems, but variable field techniques are much slower. For example, FFC-NMR experiments can take several hours to record a full profile, and thus far FFC-NMR has only been used to monitor the kinetics of cement

drying over the course of a 100 h period.[10] If fixed field measurements provide sufficient information then these measurements are more applicable to rapidly changing systems.

The spectroscopic separation of peaks is an advantage commonly exploited for fixed field NMR experiments. This allows each component within the binary liquid mixture to be treated separately, and hence the dynamics of each component can be independently characterised. Chemical resolution of peaks within the binary liquid mixture is often simpler for fixed field measurements due to the high homogeneity of the field. In contrast, field cycling magnets are optimised to allow a rapid switch in the magnitude of the field at the expense of the homogeneity of the field, which results in linewidths of kHz-MHz, and makes the spectroscopic separation of peaks impossible. Multiple environments can be separated using inverse Laplace transformations or multi-exponential fits, provided that the difference in the relaxation rate of each environment is sufficiently large (as was demonstrated in chapter 6). The complexity of the porous medium may result in a distribution of relaxation environments and prevent clear chemical resolution.[11] A simple γ-alumina catalyst support was selected for this work as it had a uniform structure and mono-modal pore size distribution. This maximised the possibility of separating out relaxation environments.

NMR is a well suited technique for analysing complex dynamics within porous media. For cases of simple relaxation behaviour a fixed field approach benefits from an easier characterisation of the peaks and significant time savings. When the interpretation obtained from a fixed field approach is ambiguous, the enhanced clarity obtained from FFC-NMR experiments make it a powerful tool for monitoring equilibrium adsorption problems or slow displacements.

8.2.2 Non-NMR methods for studying binary liquid adsorption

The application of neutron scattering and infrared spectroscopy has been highly successful at characterising the intraparticle adsorption behaviour of liquids in porous media.[12–14] In the case of an ordered SBA-15 nanoporous silica imbibed with a miscible mixture of *tert*-butanol and toluene, a strong microphase separation was observed.[12] The polar species, *tert*-butanol (TBA), preferentially adsorbed at the porous surface forming a shell of almost pure TBA and a core that was deficient in TBA, and therefore rich in toluene. For binary systems such a microphase separation is well known.[12,15] The separation ranges from full to only partial demixing, and is shown schematically in Figure

8.1. Theoretically, the extent of this microphase separation depends both on the liquid properties and those of the porous medium itself, making it difficult to predict. Experimentally, however, the degree of microphase separation is often large – with TBA strongly outcompeting toluene for surface sites in the previous example.[12]

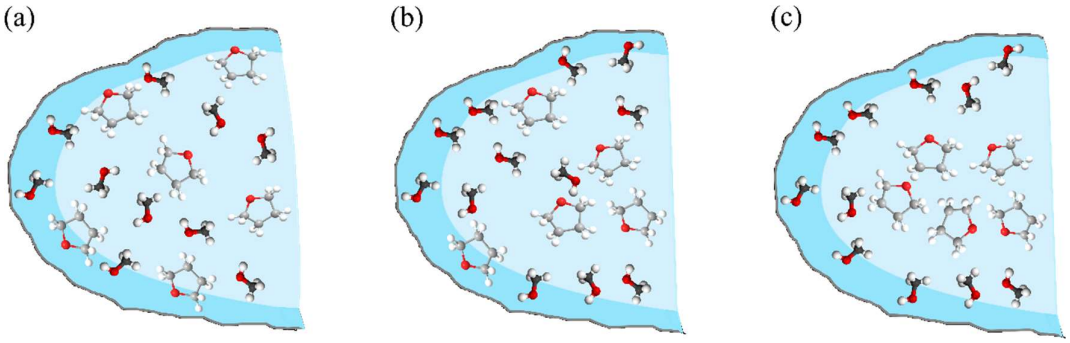

Figure 8.1: A schematic diagram showing (a) no demixing, (b) partial demixing, and (c) full demixing of a THF:methanol binary liquid system.

Whilst neutron scattering and infrared techniques have thus far not provided any dynamical information about the two components in the binary liquid mixture they have provided important structural information to describe the liquid ordering within porous media. The generality of this microphase separation at hydrophilic surfaces implies that it can occur for binary liquid mixtures imbibed within γ-alumina. Determining the degree of demixing is important in understanding the liquid structuring within the pore space and the relative surface interactions of each species.

8.2.3 Relaxation theory for multicomponent adsorption

To achieve maximum generality the treatment of a multicomponent liquid system can be broken down into a separate treatment of each of the constituent liquids. In doing so an N liquid system can be thought of as N examples of partially filled pores. Within this chapter all work is shown for the specific case that $N = 2$, and the relaxation theory required to describe the T_1 relaxation behaviour of liquids in partially filled pores will be proposed, and extended to T_1/T_2 measurements.

8.2.3.1 Relaxation measurements of partially filled pores

The influence of the surface-adsorbate interaction strength has been discussed in detail in the preceding chapters, but this is not the only factor influencing the observed relaxation rate. The degree of pore filling also contributes to the observed relaxation

behaviour,[1] which is justified in terms of the two-phase fast exchange model schematically shown in Figure 8.2.

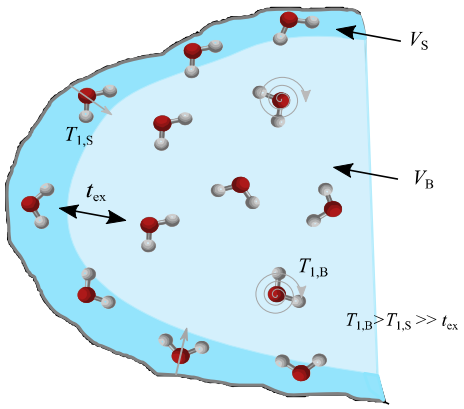

Figure 8.2: A schematic representation of the two-phase fast exchange model of relaxation. The relaxation rates of molecules in the adsorbed phase and the bulk pore space are denoted as $T_{1,S}$ and $T_{1,B}$ respectively. The different molecular motions experienced by the bulk and surface molecules are denoted by spirals and straight arrows respectively. Provided that the exchange time, t_{ex}, is much smaller than the $T_{1,S}$ and $T_{1,B}$ then the observed relaxation becomes a population weighted average of the two environments.

In a partially filled pore the liquid will preferentially occupy the surface volume layer, V_S, rather than filling the bulk pore space, V_B. As the two environments are in fast exchange the observed relaxation rate will be a population weighted average of the surface and bulk relaxation rates. The preferential surface adsorption shifts the weighted average towards the surface relaxation rate, and results in larger observed relaxation rates at smaller values of the filling factor, f. This situation has been considered elsewhere for the limiting cases where the molecular exchange time, t_{ex}, is slower or faster than the molecular correlation times, τ_c.[1] In these limits the observed relaxation rate can be expressed as:

$$\frac{1}{T_{1,obs}} = \frac{1}{T_{1,B}} + \left(\frac{\lambda S}{V}.\frac{1}{f}\right)^2 \left(\frac{1}{T_{1,S}} - \frac{1}{T_{1,B}}\right) \qquad \text{for } \tau_c \ll t_{ex}\,, \tag{8.1}$$

$$\frac{1}{T_{1,obs}} = \frac{1}{T_{1,B}} + \frac{\lambda S}{V}.\frac{1}{f}\left(\frac{1}{T_{1,S}} - \frac{1}{T_{1,B}}\right) \qquad \text{for } \tau_c \gg t_{ex}\,, \tag{8.2}$$

where S/V is the surface to volume ratio of the porous medium, and the labels S, B and obs are used to denote contributions from the surface, bulk and the observed relaxation

rates respectively. Only in the case of cyclohexane imbibed within a 4 nm porous glass was the fast correlation time limit observed (eq. (8.1)). For water in a 4 mm porous glass, and both cyclohexane and water imbibed within a larger porous support, the slow correlation time limit was observed (eq. (8.2)). Assuming that no interspecies relaxation occurs, this method can be used to understand multicomponent adsorption.

8.2.3.2 T_1 measurements of multicomponent liquid mixtures

For the case of multicomponent miscible liquid mixtures adsorbed in γ-alumina a new model is proposed based on the relaxation behaviour of liquids in partially filled pores. The relaxation of component i within a mixture is given as the generalization of eq. (8.1):

$$\frac{1}{T_{1,\mathrm{obs},i}} \approx \frac{1}{T_{1,\mathrm{B},i}} + \frac{V_{\mathrm{S},i}}{V} \cdot \frac{1}{f_i}\left(\frac{1}{T_{1,\mathrm{S},i}}\right), \quad \text{where } \frac{1}{T_{1,\mathrm{S},i}} \gg \frac{1}{T_{1,\mathrm{B},i}}. \tag{8.3}$$

As the population of the surface layer will depend on the adsorption properties of the solid and the imbibed species, the term λS in eq. (8.2) has been replaced with the adsorbed surface layer volume, $V_{\mathrm{S},}$. The label S identifies the molecules influenced by the surface and not just the molecules in the monolayer adjacent to the surface. The analogous expression derived from eq. (8.1) occurs in the fast correlation time limit.

Eq. (8.3) shows that the observed relaxation rate will vary with the composition of each component in the mixture, even if the surface relaxation rates (and hence the surface dynamics leading to relaxation) remain fundamentally unchanged. It is therefore important to know the composition of the fluid inside the pores, and hence the value of f_i for each component. If a microphase separation occurs at the pore surface this will alter the composition of the surface layer relative to the bulk pore composition. This results in the measured composition of the liquid imbibed within the γ-alumina not necessarily being equivalent to the composition of the liquid that the porous medium was initially immersed in. Instead, the true molar composition (of the adsorbed and bulk pore volumes combined) can be measured directly with FFC-NMR from the populations obtained from a multi-exponential fit. Normalizing these values by the number of protons per molecule, $n_{\mathrm{p},}$, gives a molar fraction, $f_{m,i}$, which can be converted into the volume fraction, f_i, used in eq. (8.3):

$$f_i \equiv \frac{f_{\mathrm{m},i} V_{\mathrm{m},i}}{\sum_{\mathrm{k}} f_{\mathrm{m},k} V_{\mathrm{m},k}}, \tag{8.4}$$

where $V_{\mathrm{m},i}$ is the molar volume of species i. In the limit that all molar volumes are assumed to be equal then eq. (8.4) can be simplified to:

$$f_i \equiv \frac{f_{\mathrm{m},i}}{\sum_k f_{\mathrm{m},k}}. \tag{8.5}$$

The validity of eq. (8.5) will depend on the nature of the system under investigation and will be commented on further in section 8.5.2. The theory outlined in this section allows NMR relaxation experiments to be used to characterise each component in an N-component liquid mixture both in terms of their relaxation times and their relative filling factors. This allows an important decoupling of these parameters, which may have otherwise led to an erroneous interpretation.

8.2.3.3 T_1-T_2 measurements of multicomponent liquid mixtures

Eq. (8.3) is valid for T_2 measurements as well as T_1 measurements, provided that no additional relaxation mechanisms are active that may distort the value of T_2.[16] By rearranging eq. (8.3) and taking the ratio of T_1/T_2 it is possible to isolate the surface relaxation ratio:

$$\frac{\frac{1}{T_{1,\mathrm{obs},i}} - \frac{1}{T_{1,\mathrm{B},i}}}{\frac{1}{T_{2,\mathrm{obs},i}} - \frac{1}{T_{2,\mathrm{B},i}}} = \frac{T_{2,\mathrm{S},i}}{T_{1,\mathrm{S},i}}. \tag{8.6}$$

This can be further simplified in the limit that $\frac{1}{T_{1,\mathrm{obs},i}} \gg \frac{1}{T_{1,\mathrm{B},i}}$ and $\frac{1}{T_{2,\mathrm{obs},i}} \gg \frac{1}{T_{2,\mathrm{B},i}}$:

$$\frac{T_{2,\mathrm{obs},i}}{T_{1,\mathrm{obs},i}} = \frac{T_{2,\mathrm{S},i}}{T_{1,\mathrm{S},i}}. \tag{8.7}$$

By taking the ratio of T_1/T_2 the dependence of the relaxation data on the pore size, filling factor, and volume of the adsorbed surface layer are cancelled out. This means that the relaxation behaviour of a T_1/T_2 measurement depends only on the surface dynamics. If no changes in the surface dynamics occur as a function of composition then the T_1/T_2

ratio will remain constant. Any structural information can still be accessed through the individual T_1 and T_2 measurements.

8.3 Materials and methods

8.3.1 Materials

Methanol, tetrahydrofuran (THF, with 250 ppm BHT stabiliser) and cyclohexane were obtained from Alfa Aesar with a purity of >99%. The polarities of these liquids are 0.76, 0.21 and 0.01 respectively relative to the polarity of water.[17] Methanol-d_1 was purchased from Fluorochem Ltd with an isotopic enrichment of >99%. The γ-alumina catalyst was obtained from Alfa Aesar in the form of ⅛″ diameter cylindrical extrudates with typical lengths of ⅛ - ¼″.

For both fixed field and FFC-NMR experiments the samples were prepared by drying the alumina for 12 h at 120 °C and then soaking the alumina for a further 12 h in a liquid mixture of known composition. Extra-pellet liquid was removed by pouring the sample onto filter paper and lightly drying the outer surface. To avoid any loss of imbibed material through evaporation the sample was prepared immediately before analysis. The relative composition of the liquid imbibed within the pore space was calculated from the signal intensities of the observed relaxation environments. This procedure was applied to the T_1 values measured at each field, and the average value was taken from the 20 measured field values for each mixture.

8.3.2 NMR methods

FFC-NMR experiments were performed as outlined in section 5.3.2. For each nuclear magnetic relaxation dispersion (NMRD) profile 20 ^{1}H Larmor frequencies were analysed, logarithmically spaced between 10 kHz and 40 MHz. Each experiment consisted of 64 logarithmically spaced delay times from 1 ms to 5.5 s (~5 × $T_{1,max}$). The T_1 distribution at each field strength was obtained through an inverse Laplace transformation using Tikhonov regularisation. The data were then separately fitted with a bi- or tri-exponential function depending on whether the O^{1}H signal was of sufficient intensity to be robustly characterised. The reported relaxation rates and relative populations are those extracted from the multi-exponential fits.

T_1/T_2 measurements were performed on a Magritek 43 MHz spectrometer. Samples prepared as above were loaded into the magnet in 5 mm outer diameter NMR tubes. 32 T_1 delay times between 1 ms and 6 s were used, and 2048 echoes were recorded with an echo spacing of 1 ms. The data were analysed using a 2D inverse Laplace transformation with Tikhonov regularisation. Relaxation rates are reported as the modal values and the logarithmic averages of the peaks corresponding to each component of the mixture. The relative populations are calculated from the integrals of each relaxation environment.

8.4 Results

In this section binary liquid mixtures of cyclohexane:THF (non-polar:polar) and THF:methanol (polar:polar) imbibed within a γ-alumina catalyst were characterised in terms of their relaxation rates and relative populations using FFC-NMR and T_1/T_2 analyses.

8.4.1 Chemical assignment of the binary liquid mixtures

Figure 8.3 shows the T_1 distributions obtained from an inverse Laplace transformation of the relaxation rate data acquired at field strengths between 10 and 57 kHz using FFC-NMR. At each field strength the T_1 distributions are shown for single-component liquids and both binary liquid mixtures imbibed within γ-alumina. A single relaxation environment was observed for cyclohexane and THF imbibed within γ-alumina, whilst two peaks were seen for methanol. The latter observation was consistent with a difference in the O^1H and alkyl ^1H relaxation rates of alcohols imbibed within γ-alumina, as demonstrated in chapter 6. For the case of binary liquid mixtures imbibed within γ-alumina, the peaks in the T_1 distributions were well resolved and the number of environments present was equal to the sum of the number of relaxation environments in the respective single component liquids. In short, two peaks were present for cyclohexane:THF mixtures and three peaks were present for THF:methanol. A comparison of the relaxation behaviour of each single component species imbibed within γ-alumina to the relaxation behaviour of the binary liquid mixtures imbibed in γ-alumina allowed a chemical assignment of each peak in the T_1 distributions as shown in Figure 8.3. The assignment was further corroborated by the measured populations of each

component of the binary liquid mixtures within the pores, which were similar to the composition of the liquid that the samples were immersed in originally.

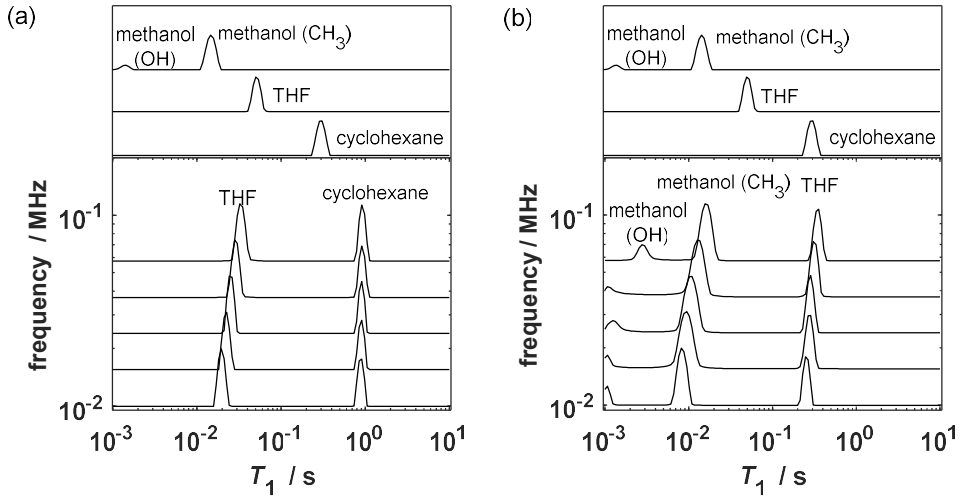

Figure 8.3: The T_1 distributions obtained between 10-57 kHz for binary liquid mixtures of (a) cyclohexane:THF and (b) THF:methanol imbibed within γ-alumina. In both cases the single component T_1 distributions are shown above the binary liquid mixture data for comparison. Initial liquid compositions were 50:50 mol % for the cyclohexane:THF mixture, and 20:80 mol % for the THF:methanol mixture.

The low relative signal intensity of the methanol O^{1}H functionality resulted in the relaxation rate of this environment being highly sensitive to noise. Furthermore, the discussion in section 6.4.1 demonstrated the poor reliability of the measurement of the population of the hydroxyl environment. In contrast, the methanol alkyl ^{1}H environment appeared much more robust in terms of population and relaxation rate. As such, the relaxation of methanol herein will be assumed to be that of the alkyl ^{1}H environment only for all FFC-NMR experiments.

Figure 8.4 shows the analogous T_1-T_2 distributions for single component and binary mixtures of methanol, THF and cyclohexane imbibed within γ-alumina. In each case the relaxation environments appeared as well-defined features that were fully separable. The methanol hydroxyl environment was only detected for the single component system imbibed within γ-alumina. This is because the T_2 relaxation time of the hydroxyl environment was too short to allow detection in all compositions of the binary liquid mixture that were studied. Once again the chemical assignment of relaxation

environments was performed through a comparison of the binary liquid mixture relaxation data to the single-component systems.

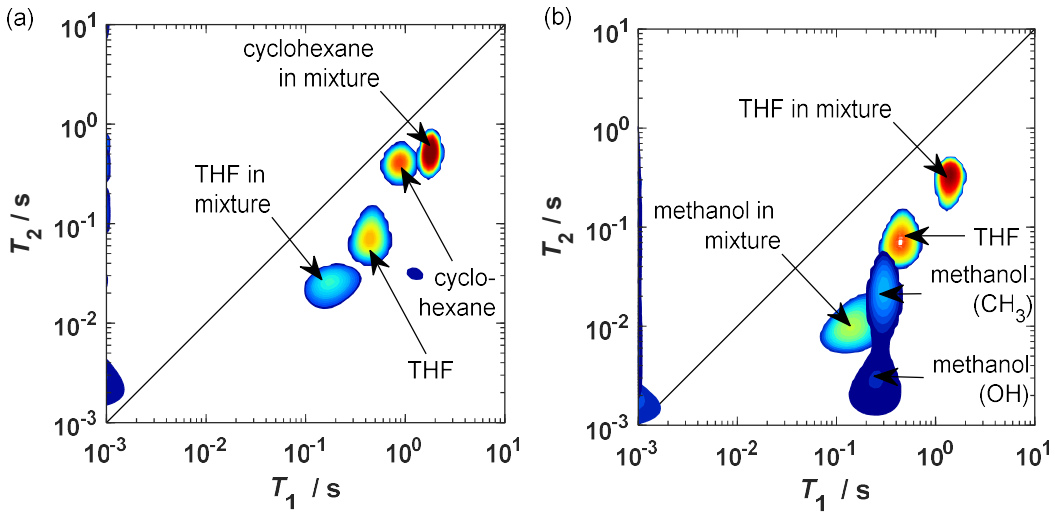

Figure 8.4: Typical T_1-T_2 correlation plots for binary liquid mixtures of (a) cyclohexane:THF and (b) THF:methanol, imbibed within γ-alumina. For each correlation plot the single component adsorption data have been included for comparison.

Several artefacts were observed in the T_1-T_2 correlation plots of the imbibed liquids. The most prevalent artefact was a series of peaks that occurred with a T_1 value of 1 ms for both binary liquid mixtures. These peaks had T_1/T_2 ratios much lower than 1, and were therefore not interpreted as having a genuine physical origin. Instead, these peaks were caused by an incomplete inversion of the magnetisation.[18,19] Achieving a full inversion of each peak within a mixture was not trivial experimentally, but the kernel function used to describe the magnetisation decay in the numerical inversion required a full inversion. Small deviations between the experimental and theoretical conditions led to the observed artefacts. A further minor artefact was observed inconsistently in the T_1-T_2 correlation plots at realistic values of T_1 and T_2. An example of this feature is shown in Figure 8.4a at values of $T_1 = 1.29$ s and $T_2 = 31$ ms. As this feature was not consistent across all experiments and only accounted for <2 % of the overall magnetisation it was excluded from the analysis of the binary liquid mixture.

8.4.2 Measurements of relative populations

The composition of the liquids prior to imbibition, and the measured intra-particle compositions from FFC-NMR and fixed-field T_1-T_2 measurements are shown in Table

8.1 for all compositions of the binary liquid mixtures. In all experiments the intra-particle liquid composition was similar to the composition of the liquid in which it was immersed. A moderate increase in the intra-particle concentration of the more polar component was observed for each imbibed mixture relative to the bulk liquid, which was consistent with a preferential adsorption of the more polar component for each binary liquid mixture. Separate samples were prepared for the fixed field and FFC experiments several months apart. Despite this the measured intra-particle populations generally differed by less than 5% and no measurement differed by more than 10%. This confirmed that FFC-NMR is a quantitative measure of composition for binary liquid mixtures. Further experiments, beyond the scope of this thesis, are required to define the precision of these population measurements.

Table 8.1: The compositions of the binary liquid mixtures used to soak the pellets (initial mixture) and the intra-particle compositions measured by FFC-NMR and fixed field T_1-T_2 measurements for mixtures of cyclohexane:THF and THF:methanol imbibed within γ-alumina.

Cyclohexane:THF composition / mol %			**THF:methanol composition / mol %**		
Initial mixture	**FFC intra-particle**	**T_1-T_2 intra-particle**	**Initial mixture**	**FFC intra-particle**	**T_1-T_2 intra-particle**
35:65	34:66	30:70	20:80	17:83	18:82
50:50	45:55	44:56	40:60	33:67	37:63
66:34	62:38	58:42	66:34	59:41	65:35
75:25	71:29	66:34	75:25	67:33	77:23
80:20	75:25	71:29	80:20	73:27	80:20

8.4.3 FFC-NMR results

Figure 8.5 shows the NMRD profiles of each component in a series of cyclohexane:THF and THF:methanol mixtures imbibed within γ-alumina. Common trends were observed for the two binary mixtures, with the relaxation rate of the more polar component increasing (relative to its single component relaxation rate) as the mole fraction of it was decreased. The increase depended strongly on the composition. In contrast, the relaxation rate of the less polar component decreased as the mole fraction of the species decreased. A large change in the relaxation rate when compared to the single component data was observed, however, once a small amount of the more polar component was present in the binary liquid mixture, the relaxation rate of the less polar component became weakly

dependent on the composition. The use of THF as a common component in both binary liquid mixtures demonstrated that these observations were related to the ability of the adsorbates to access the surface in a competitive adsorption process, rather than an intrinsic behaviour of specific liquids under confinement.

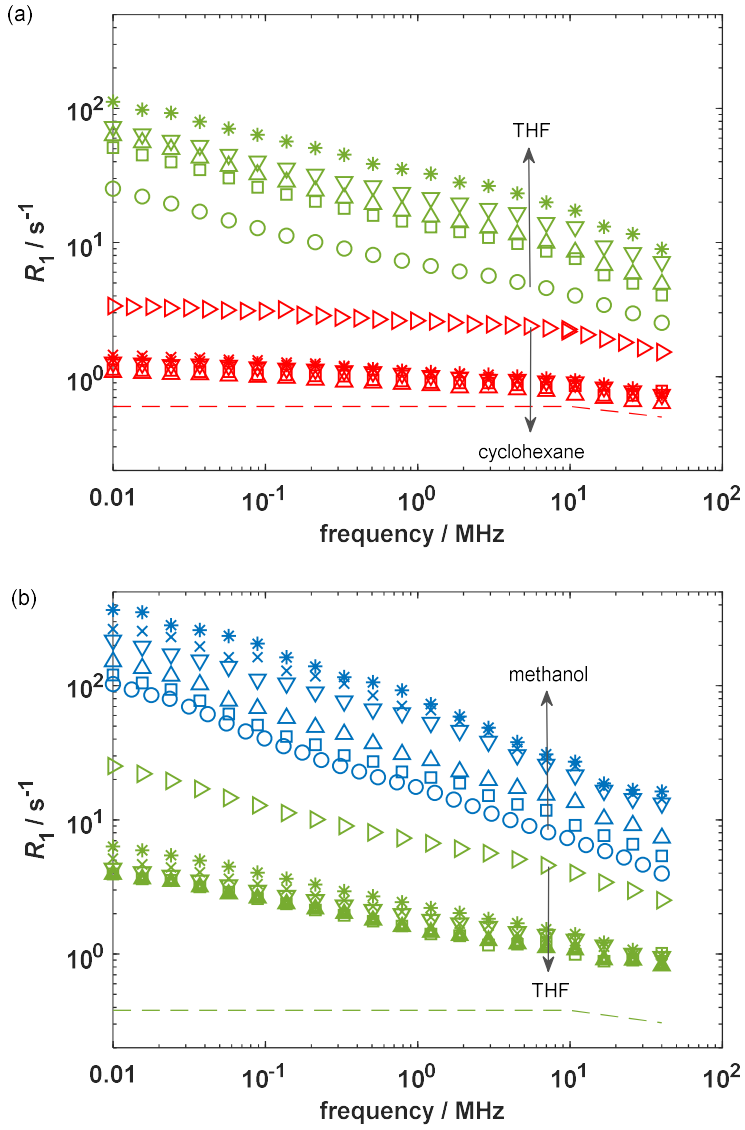

Figure 8.5: The NMRD profiles of a mixture of (a) cyclohexane:THF at intra-pellet compositions of 0:100 (○), 34:66 (□), 45:55 (△), 62:38 (▽), 71:29 (×), 75:25 (∗) and 100:0 (▷) mol %, and (b) THF:methanol at compositions of 0:100 (○), 17:83 (□), 33:67 (△), 59:41 (▽), 67:33 (×), 73:27 (∗) and 100:0 (▷) mol % imbibed within γ-alumina. For additional clarity the symbols are coloured red (cyclohexane), green (THF), and blue (methanol). Dashed lines represent the bulk liquid values for (a) cyclohexane and (b) THF i.e. in the absence of γ-alumina. The arrows indicate the trend in the NMRD profiles with decrease in concentration of each species.

To separate the effects of composition (surface accessibility) from the molecular motions (surface interaction) the data in Figure 8.5 were renormalized to form master curves.[20–22] Figure 8.6 shows the normalized master curves obtained by dividing each NMRD profile by the R_1 value obtained at 10 kHz, which is valid in the limit that $R_{1,\mathrm{obs},i} \gg R_{1,\mathrm{B},i}$ (eq. (8.3)).

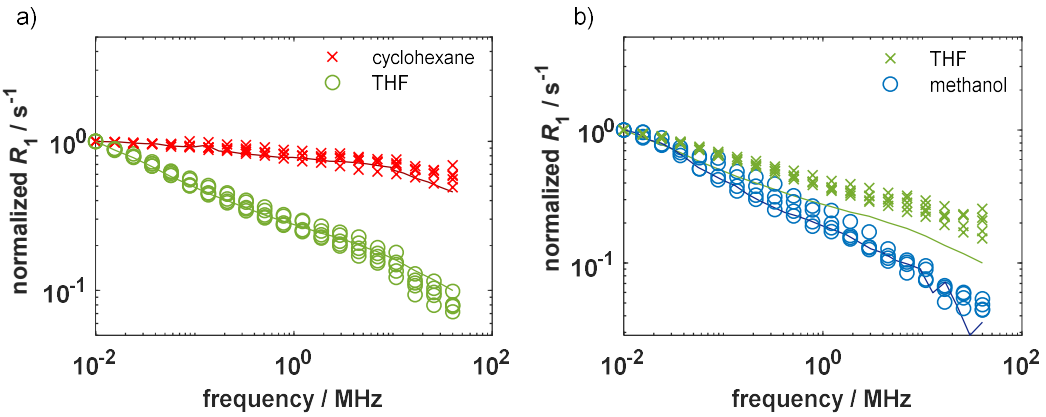

Figure 8.6: The renormalized NMRD profiles for of the data shown in Figure 8.5. The data are separated into (a) cyclohexane:THF, and (b) THF:methanol mixtures imbibed within γ-alumina. For additional clarity the symbols are coloured red (cyclohexane), green (THF), and blue (methanol). The solid lines represent relaxation rates of the single-component liquids imbibed within the same γ-alumina catalyst. No clear trend was seen between deviations from the renormalized lines and composition. Therefore each species is represented by a single symbol regardless of the composition of the binary liquid mixture, unlike in Figure 8.5.

For the cyclohexane:THF binary liquid mixtures imbibed within γ-alumina the NMRD profile of each component was renormalized to a single master curve regardless of the intra-particle composition. The single component profiles of THF and cyclohexane imbibed within γ-alumina were renormalized in the same manner, and the single component NMRD profiles were identical to the NMRD profiles obtained from the binary liquid mixture. The master curves could be phenomenologically described by a power law of exponent -0.26 and -0.05 for THF and cyclohexane respectively. This showed that for the cyclohexane:THF binary liquid system there was no change in the molecular dynamics of each liquid between single or binary adsorption, nor as a function of the binary composition. The same process was applied to the THF:methanol binary liquid system, and again the NMRD profiles of each component in the mixture could be renormalized to a single master curve for all compositions. The power law frequency

dependencies of the THF and methanol master curves were -0.20 and -0.38 respectively. In contrast to the cyclohexane:THF binary system, only the exponent of the strongly interacting species, methanol, was identical to its normalized single component data. For the weakly interacting species, THF, a change in the exponent of the power law was observed from -0.26 to -0.20. This was consistent with a weakening of the THF-surface interaction in the presence of methanol. The effect of the competitive adsorption in the binary liquid mixture was clearly visible in the renormalized THF:methanol profiles. The transient adsorption for single component cyclohexane was weak, and therefore no significant change was observed in the renormalized NMRD profiles of cyclohexane in the presence of THF.

In summary, for both binary liquid mixtures studied herein each component could be renormalized to a single master curve. For each species in the cyclohexane:THF binary liquid mixture, and methanol in the THF:methanol binary liquid mixture, the relaxation rate of the single component liquid imbibed within γ-alumina was consistent with the normalized data, which showed that no change in the surface interaction had occurred. For THF in the THF:methanol binary liquid mixture, however, a reduction in the slope of the NMRD profile relative to the single component system was observed, which was consistent with a reduced surface interaction. The resultant NMRD profile was much steeper than that of bulk THF, indicating some degree of surface interaction remained for THF even in the presence of methanol.

8.4.4 T_1-T_2 results

Figure 8.7 shows the T_1-T_2 correlation plots obtained from a series of binary liquid mixtures of cyclohexane:THF and THF:methanol at variable compositions. Considering first the cyclohexane:THF binary liquid mixture, the values of T_1 and T_2 of THF decreased as the mole fraction of THF in the binary mixture was decreased. As both relaxation time constants decreased concurrently the THF peak maintained a constant T_1/T_2 ratio of 6.4 across the composition range. This value indicated a moderate surface interaction. Furthermore, as the T_1/T_2 ratio was constant, no change in the surface interaction occurred across the composition range, as predicted by eq. (8.7). For cyclohexane the peak shifted to higher T_1 and T_2 values in the presence of even a small amount of THF. After the initial shift of this peak it became independent of the composition and remained at a T_1/T_2 ratio of 2.5. The lower T_1/T_2 ratio of cyclohexane

relative to that of THF in the binary liquid mixtures imbibed within γ-alumina was consistent with a preferential interaction of THF with the surface.

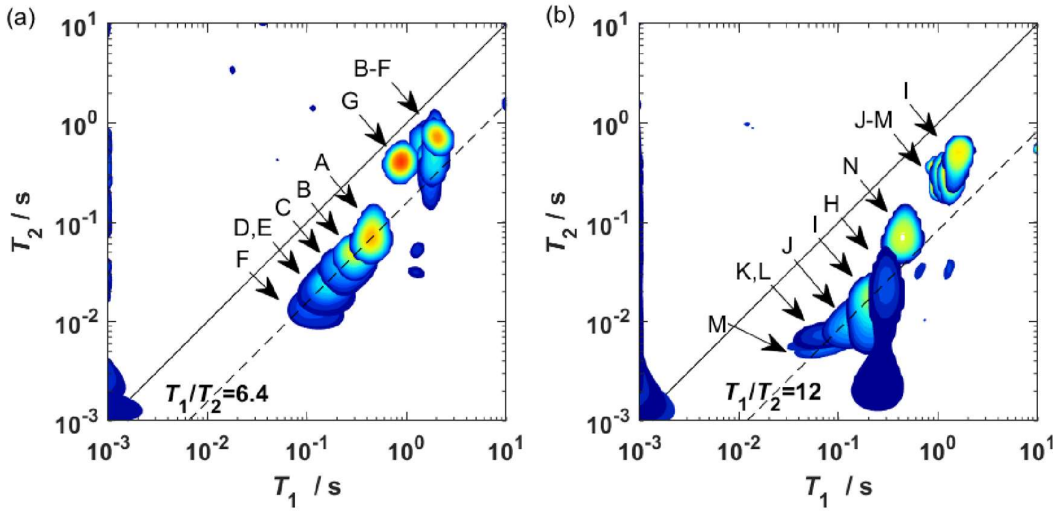

Figure 8.7: T_1-T_2 correlation plots for mixtures of (a) cyclohexane:THF and (b) THF:methanol binary liquid mixtures imbibed within γ-alumina at a range of compositions. Compositions for the cyclohexane:THF binary liquid mixture were (A) 0:100, (B) 30:70, (C) 44:56, (D) 58:42, (E) 66:34, (F) 71:29 and (G) 100:0. Compositions for the THF:methanol binary liquid mixture were (H) 0:100, (I) 18:82, (J) 37:63, (K) 65:35, (L)77:23, (M) 80:20 and (N) 100:0.

Similar trends were observed for the methanol:THF binary liquid mixture imbibed within γ-alumina. For the more polar component, methanol, the individual T_1 and T_2 values decreased as the composition of this component was decreased in the binary liquid mixture. Unlike THF in the cyclohexane:THF binary (Figure 8.7a) the methanol peak was much more distorted in shape. For single component methanol imbibed within γ-alumina (H) two regions were clearly observed with similar T_1 values but different T_2 values. The relative populations of the two environments were measured as 76% for the slow relaxing component and 24% for the fast relaxing component. This result was consistent with the fast relaxing environment being that of the hydroxyl environment and the slow relaxing environment being that of the methanol alkyl group (the expected ratio being 25% and 75% respectively). For binary liquid mixtures containing higher mole fractions of methanol (I and J) a broadening of the features was observed in the T_2 domain. Through a comparison of these features with the single component methanol data it was likely that the broadening resulted from the presence of the hydroxyl protons, which relaxed close to the time limits limit of the experimental acquisition and numerical

inversion. The distorted shape of the methanol peak meant that it was not immediately obvious if the T_1/T_2 ratio remained constant, however an approximate ratio of 12 described the system well. This was consistent with a strong methanol-surface interaction. For THF in the methanol:THF mixture a significant increase in the T_1 and T_2 values was observed relative to the single component data (N). After the initial increase in the relaxation time constants the relaxation behaviour became independent of composition. The T_1/T_2 ratio was measured as approximately 3, which suggested a weaker surface interaction than methanol.

To allow a quantitative analysis of the results the modal values and logarithmic averages of the data presented in Figure 8.7 are shown in Figure 8.8. The data were insensitive to the size of the integration region used to capture each peak, and were therefore not affected by noise artefacts. As the measurement error was small the experimental error became dominated by sample-to-sample variations. The magnitude of this error was assumed to be 10% for individual T_1 and T_2 measurements based on the results in section 4.4.1, and 20% for T_1/T_2 ratios. Sample-to-sample variation will affect T_1 and T_2 in a similar manner, resulting in the errors being correlated. This meant that the 20% error was a conservative estimate.

For the cyclohexane:THF binary liquid mixture imbibed within γ-alumina, shown in Figure 8.8a-c, no clear trend was observed in the modal or logarithmic average T_1/T_2 ratio of either species. This is in contrast to the individual T_1 and T_2 values, which showed strong trends. For cyclohexane the T_1 and T_2 values increases by a factor of 2 and 1.8 respectively at the lowest concentration studied relative to the relaxation time constant of the single component cyclohexane. The most significant change in relaxation time constants was observed between the pure component and the binary liquid mixture containing the smallest mole fraction of THF ($f_{\text{cyclohexane}} = 0.71$). For THF in the binary liquid mixtures the maximum decrease in the T_1 and T_2 time constants relative to single component THF imbibed within γ-alumina were factors of 3.8 and 5.2 respectively. For the THF:methanol binary liquid mixture almost identical trends were observed. In this binary liquid mixture the maximum change in T_1 and T_2 times were decreases by a factor of 7.1 and 3.7 for THF and increases by a factor of 4.4 and 4.4 for methanol respectively.

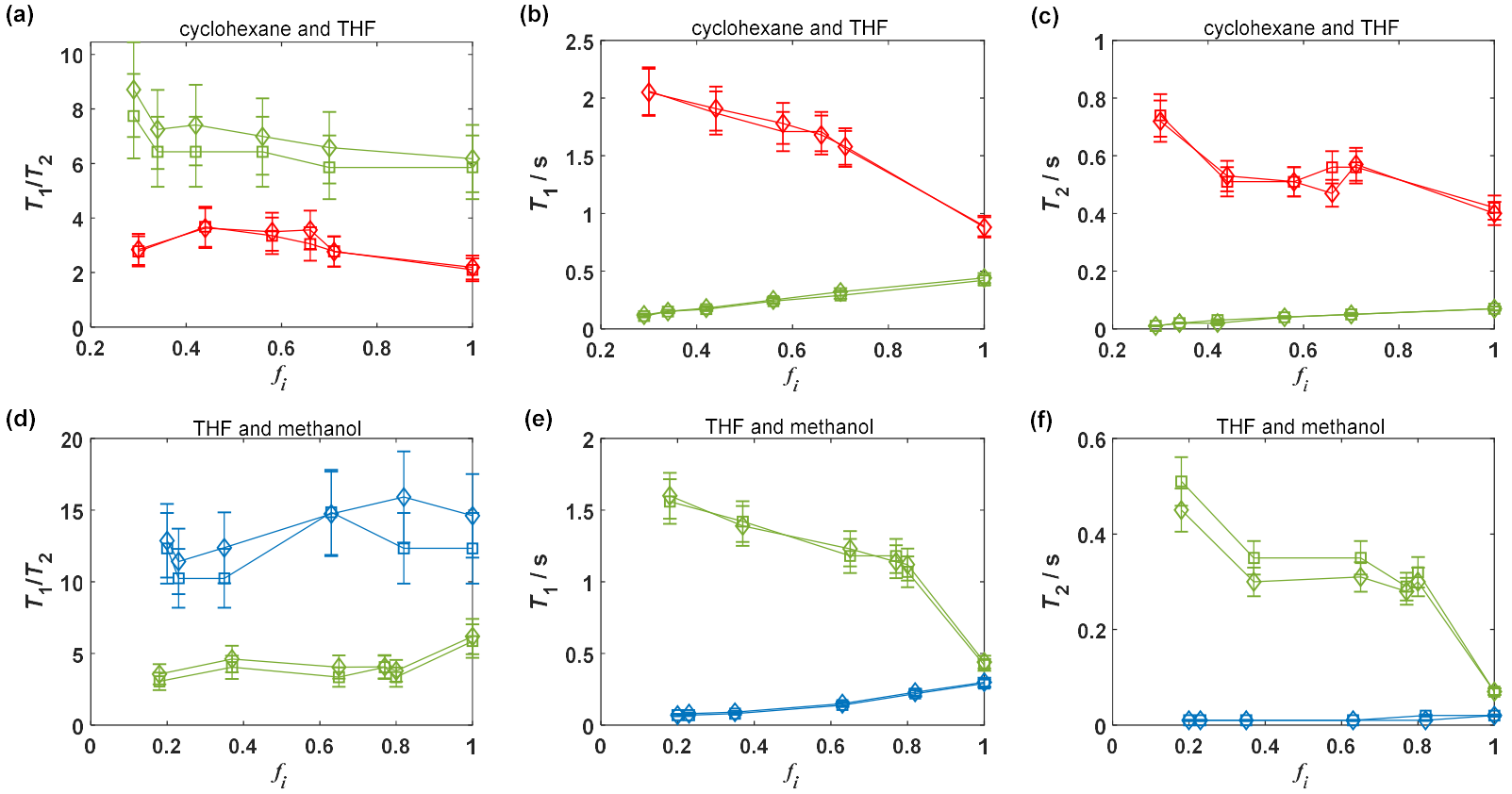

Figure 8.8: The relaxation data measured at 43 MHz for binary liquid mixtures of (a-c) cyclohexane:THF and (d-f) THF:methanol at a range of compositions. For each binary liquid mixture the composition is given as the mole fraction, f_i, where i = cyclohexane (red), THF (green) or methanol (blue). Square markers represent the logarithmic average of the data presented in Figure 8.7 and diamond markers represent the modal value. For each binary liquid mixture the dependence of the (a and d) T_1/T_2 ratio, (b and e) T_1 time constant and (c and f) T_2 time constant on the composition are shown.

8.5 Discussion

The sensitivity of FFC-NMR to the surface accessibility (Figure 8.5) and the surface interaction (Figure 8.6 and Figure 8.8a and d) of each component of liquid mixtures imbibed within γ-alumina has been demonstrated. In this section this information will be used to describe the competitive adsorption processes taking place within the pore space and the implications this has on the liquid structuring. The relative advantages and disadvantages of FFC-NMR and fixed field T_1-T_2 analyses for measuring this phenomenon are discussed. The assumption of uniform molar volumes are then tested and a correction based on true molar volumes is applied.

8.5.1 Liquid structuring within porous media

8.5.1.1 Interpretation of fast field cycling data

In the presence of cyclohexane, THF outcompeted the non-polar cyclohexane coadsorbate, and preferentially bound to the surface. This led to a microphase separation, and an increase in the surface volume fraction of THF compared to the composition of the bulk pore fluid. The increased surface volume resulted in an increase of the relaxation rate of THF in accordance with eq. (8.3). For cyclohexane the competitive adsorption process led to a small surface volume fraction of cyclohexane in the mixture, and the relaxation rate tended to a constant value in accordance with eq. (8.3) in the limit that $V_{S,i} \rightarrow 0$. The same trends were observed for the methanol:THF mixture. In this latter mixture, however, the weakly interacting species, THF, showed a clear frequency dependence. This proved that even though the THF was outcompeted for surface binding sites its surface accessibility was non-negligible.

The occurrence of competitive adsorption was clear from the trends in the FFC-NMR data, but the extent of demixing was not immediately obvious. In both binary liquid mixtures the strongly interacting component showed no difference in its renormalized relaxation behaviour between the single component adsorption and all binary mixture compositions. This suggested that the surface interactions did not change significantly between single and binary component adsorption for the strongly interacting species, and was indicative of a full demixing occurring. In this extreme the surface volume fraction of the strongly interacting species would become constant, provided that there is enough

of the strong adsorbent to form a full surface monolayer. In this limit eq. (8.3) reduces to:

$$\frac{1}{T_{1,\mathrm{obs,i}}} \approx \frac{1}{f_i} \cdot \frac{V_{S,i}}{V}\left(\frac{1}{T_{1,S,i}}\right), \quad \text{where } \frac{1}{T_{1,\mathrm{obs},i}} \gg \frac{1}{T_{1,B,i}}. \tag{8.8}$$

For a full microphase separation the surface volume term of the strong adsorbent, $V_{S,}$, is constant at one monolayer thickness. The pore volume, V, is a fixed property of the porous medium, and the surface dynamics of the adsorbate do not change as a function of composition for a given field strength according to Figure 8.6. This means that the only variable that affects $1/T_{1,\mathrm{obs},i}$ is $1/f_i$. A linear relationship between these parameters is predicted at each field strength in the case of full demixing, and was shown experimentally in Figure 8.9b and d.

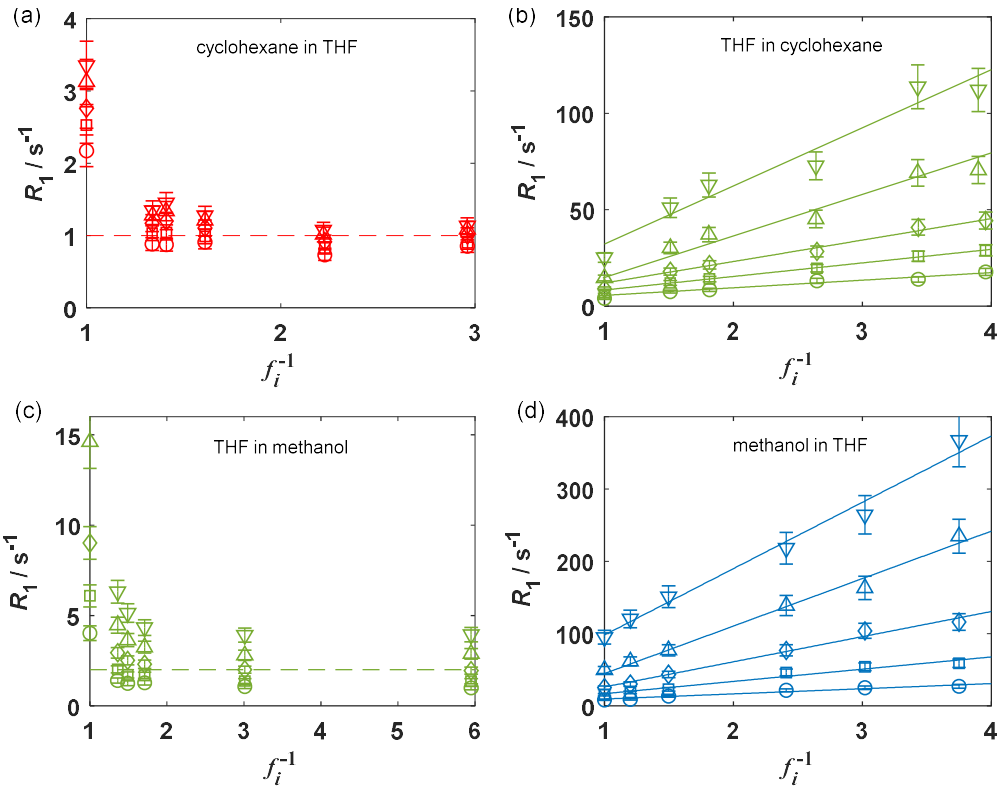

Figure 8.9: The relaxation rates of each component in a binary liquid mixture plotted against the inverse of the filling factor, f_i, for mixtures of (a-b) cyclohexane:THF and (c-d) THF:methanol. For (a and c) the weakly interacting species in each mixture a constant residual value of R_1 is shown by the dashed line. For the (b and d) strongly interacting species linear fits were performed at each field strength and are represented by solid lines.

In the same limit of full demixing the term $V_{S,i} \rightarrow 0$ for the weakly interacting species, and eq. (8.3) reduces to:

$$\frac{1}{T_{1,\mathrm{obs},i}} \approx \frac{1}{T_{1,\mathrm{B},i}}. \tag{8.9}$$

This equation suggests that there will be a significant decrease in the observed relaxation rate of the weakly interacting species in the presence of the strongly interacting species. For all compositions of the binary liquid mixture the relaxation rate of the weakly interacting species is not expected to vary significantly. This was shown experimentally in the data acquired for cyclohexane in the presence of THF, and THF in the presence of methanol in Figure 8.9a and c.

The experimentally observed case of full demixing was expected for the cyclohexane:THF binary liquid mixture imbibed within γ-alumina, as neutron scattering studies of similar non-polar:polar binaries demonstrated full demixing behaviour.[12] The demixing behaviour has been shown to be more complex for polar-polar binary liquid mixtures, and previous workers have reported contrasting predictions of the extent of demixing. Studies of water-ethanol mixtures imbibed within mesoporous silica showed a composition dependent microphase separation behaviour, which only resulted in full demixing when the ethanol mole fraction was between $0.3 - 0.45$.[23] In contrast, computational studies of water and ethanol in alumina slit pores showed a much stronger microphase separation across the full composition range,[24] which was consistent with the experimental results presented herein. The FFC-NMR methodology presented within this chapter allowed an experimental measurement of the liquid structuring phenomenon within porous media, and can be applied to a range of complex liquid mixtures.

8.5.1.2 A comparison of FFC-NMR with T_1-T_2 measurements

An analysis of the liquid structuring through a more conventional high field T_1-T_2 approach was also possible. The T_1/T_2 ratio itself contained no structural information as this was cancelled out. The ratio therefore acts only as a measurement of surface interaction. The individual relaxation time constants, however, still contain structural information, which could be accessed using the approach outlined in section 8.5.1.1. Figure 8.10 shows the relationship between $1/f_i$ and the fixed field T_1 and T_2 measurements for both binary liquid mixtures imbibed within γ-alumina.

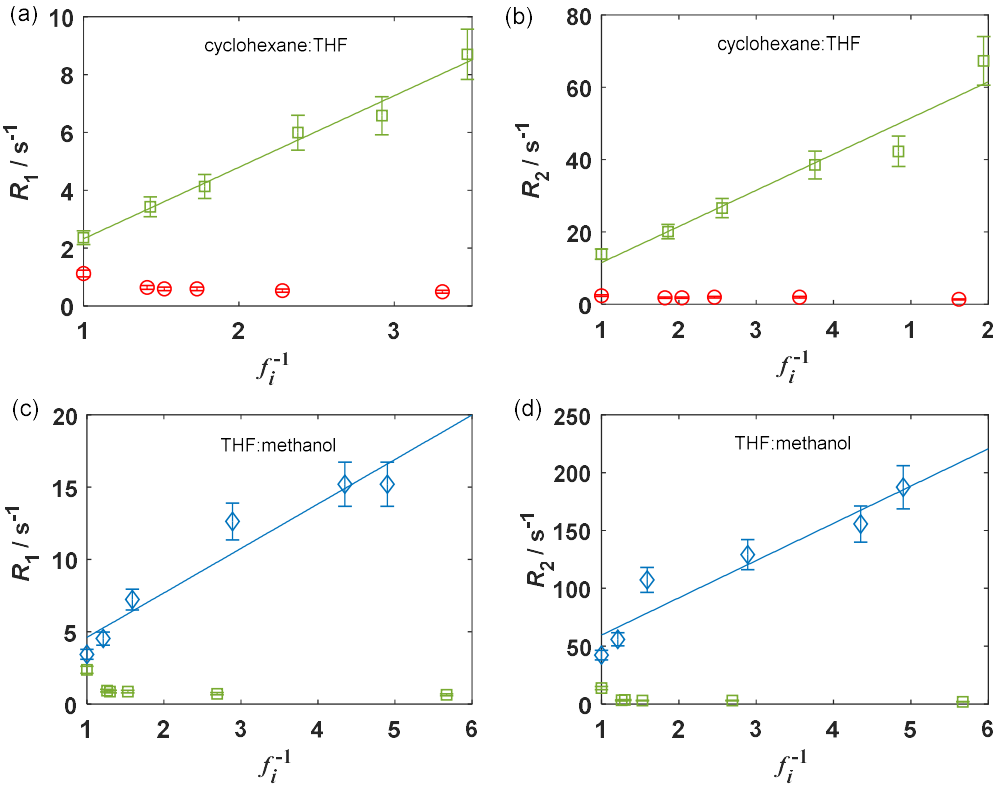

Figure 8.10: The relaxation rates of each component in a binary liquid mixture plotted against the inverse of the filling factor, f_i, for mixtures of (a-b) cyclohexane:THF and (c-d) THF:methanol. Cylcohexane (red), THF (green), and methanol (blue) are coloured for further clarity. Experiments were performed at 43 MHz and the change in (a and c) T_1 and (b and d) T_2 as a function of composition was monitored. For the strongly interacting component in each system a linear fit was applied as described by eq. (8.8).

For the cyclohexane:THF binary liquid mixture a clear linear relationship was seen for the R_1 and R_2 values of THF with respect to f_i^{-1}. This linear relationship is consistent with a microphase separation occurring at the pore surface, as previously evidenced by FFC-NMR. This result can be obtained using fixed field NMR in approximately a tenth of the time required to carry out the equivalent fast field cycling experiments. Furthermore, fixed field experiments can be performed on a conventional benchtop spectrometer, and therefore can be combined with chemical shift resolution, spatial resolution, or diffusion weighting to further understand the system. Performing these experiments using FFC-NMR would be slower and preclude the above advantages. This means that for simple systems the most effective characterisation technique is fixed field relaxometry. In contrast the THF:methanol binary showed a curvature in the R_1 time constant as a function of f_i^{-1}, and a possible sigmoidal dependence of R_2. This prevented

the clear assignment of a microphase separation from a fixed field T_1-T_2 measurement despite the phenomenon having been demonstrated by FFC-NMR. The deviation from linearity may have arisen due to changes in the viscosity or the relaxation rate of the hydroxyl group not being fully separated from that of the alkyl group. Additionally, more complex spin interactions such as spin rotation,[25] internal gradient effects,[16,26] and *J*-couplings[27] cannot be discounted. The ability of FFC-NMR to exclusively probe slow molecular processes allows this technique to isolate relaxation caused by surface diffusion, and remove any ambiguity from the characterisation of the system. The threshold of complexity before which an FFC-NMR analysis is required appears relatively low, with a binary mixture of small molecules (methanol:THF) not being well-described by a fixed field approach. Systems reflective of industrially relevant problems are likely to be far more complex. Reaction mixtures within solid catalysts will contain reactants, intermediates and products (as well as by-products). Rock cores will contain oil with a distribution of hydrocarbon chain lengths, aromatics, resins and impurities, as well as water. Even adsorbents used in separations purposes will be exposed to two (or normally many more) components. The enhanced clarity that FFC-NMR offers for complex systems is required to fully understand these processes and to avoid any misinterpretation that could occur based on fixed field T_1-T_2 data.

8.5.2 Size effects in binary liquid adsorption

The arguments presented in section 8.5.1 make the assumption that the molar volume, V_m, of each adsorbate is equal. Whilst this is a reasonable assumption for the cyclohexane:THF binary liquid mixture ($V_m = 109$ and 82 $cm^3\ mol^{-1}$ respectively) it requires further validation for the THF:methanol binary liquid mixture ($V_m = 82$ and 41 $cm^3\ mol^{-1}$ respectively). The true volume fractions of each component within the mixture can be calculated using eq. (8.4). The relaxation behaviour of the weakly interacting species in each binary liquid mixture was shown to be independent of the composition. Therefore the adjustment in composition values will have little effect on the interpretation of the data. The strongly interacting species, however, showed a clear dependency on the composition. Figure 8.11 shows the original and volume corrected data for the strongly interacting component in each mixture measured at 10 kHz using FFC-NMR, and at 43 MHz using fixed field measurements.

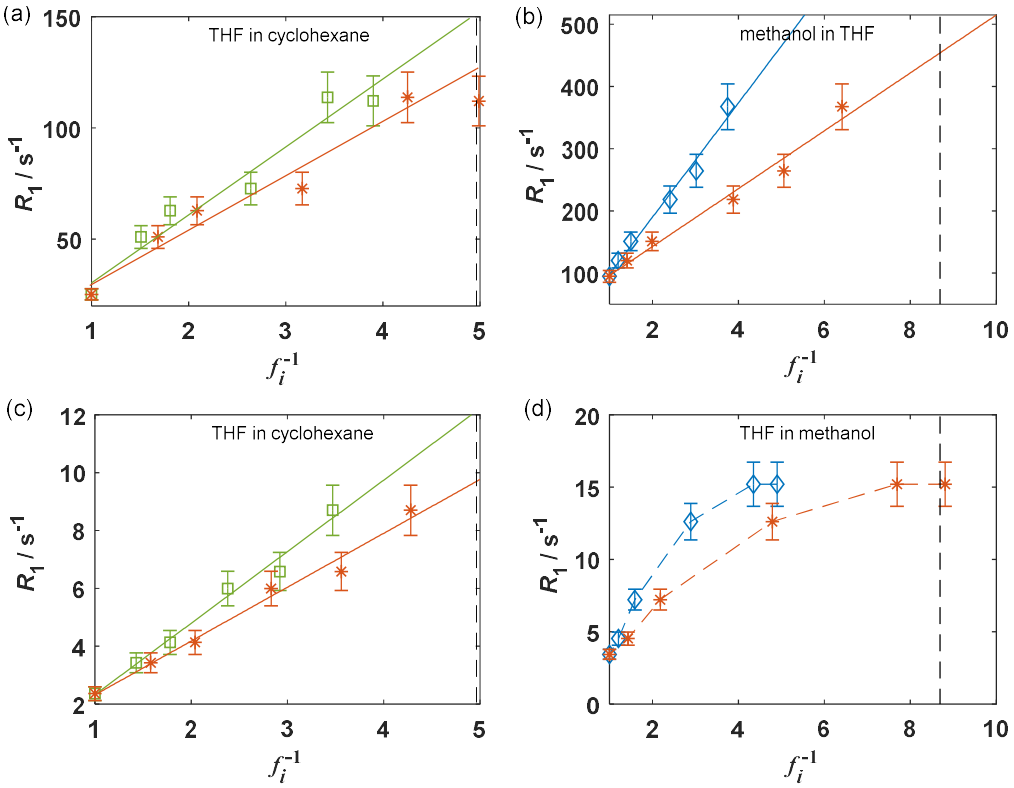

Figure 8.11: A comparison between the non-volume corrected (green and blue) and volume corrected (orange) R_1 values obtained for the strongly interacting components in binary liquid mixtures of (a and c) cyclohexane:THF and (b and d) THF:methanol. The data were obtained at (a-b) a field of 10 kHz using FFC-NMR and at (c-d) a fixed field of 43 MHz. Dashed lines show the values of f_i^{-1}corresping to a single monolayer coverage of the polar species.

For THF in cyclohexane there was a small variation in the compositions after volume adjustment. For both FFC-NMR and fixed field measurements the linearity of the relaxation behaviour was preserved for f_i^{-1} values between 1 and 4.2. This was consistent with the microphase separation discussed previously. Above this value there was evidence of a plateau in the FFC-NMR data, which was consistent with the quantity of THF within the pore space being less than the volume of a single monolayer. In this limit the surface volume term, $V_{S,THF}$, is no longer a constant and becomes dependent on the filling factor, f_{THF}. These dependencies cancel out in eq. (8.8) and the observed relaxation rate will become population independent. The observed relaxation rate will then tend to the true surface relaxation rate. For the γ-alumina system studied herein (with a measured surface area $S_{BET} = 206$ m^2 g^{-1} and a pore volume, $V_P = 0.65$ cm^3 g^{-1}), a single monolayer coverage of THF corresponds to $f_i^{-1} = 5.0$. This value agrees well

with the position of the observed plateau in the FFC-NMR data. Finally, the slope of the straight line shown in Figure 8.11a and c can be used to estimate the surface relaxation rate using eq. (8.8). Assuming a full monolayer coverage of THF the values of $T_{1,S}$ were 124 and 9.5 s^{-1} for the relaxation experiments carried out at using FFC-NMR (10 kHz) and fixed field NMR (43 MHz) respectively. These calculated values are only slightly larger (~10%) than the experimentally measured values for $f_i^{-1} > 4$, which were expected to approximate the true surface relaxation rate. The self-consistency of the modelling approach with the experimentally measurable quantities further validated this model. In addition, the ability to estimate surface relaxation rates from the slope of the linear fitting allows the direct measurement of surface relaxation rates even for mixtures that show composition dependent miscibility and demixing.

For methanol in THF a more significant deviation was observed in the values of f_i^{-1} after the volume correction was applied. The FFC-NMR data could still be well-described using the linear modelling, but even after the volume correction was applied the fixed field data showed a clear curvature. For methanol a single monolayer corresponded to $f_i^{-1} = 8.8$. In the fixed field data there is strong evidence for this plateau, though the relaxation rate reaching this plateau does not explain the curvature in the data at lower values of f_i^{-1}. This means that fixed field relaxometry provides an ambiguous measurement of the liquid structuring of THF and methanol binary liquid mixtures imbibed within γ-alumina. The FFC-NMR data was more robust and predicted a surface relaxation rate of 408 s^{-1} at 10 kHz. This value is only slightly larger (~11%) than the highest experimentally observed value of 367 s^{-1} and the theoretically predicted value for sub-monolayer coverages of 376 s^{-1}. Without applying the appropriate volume correction a surface relaxation rate of 664 s^{-1} was obtained, which was erroneous as this value was almost twice as large as the experimentally measured values corresponding to surface relaxation rates.

In summary, Table 8.2 shows the extracted values of the pore volume, V, surface layer volume, V_S, and the surface relaxation rate, $R_{1,S}$, for the each of the strongly interacting species in the binary liquid mixtures. If any two of these variables are known, the gradient of the lines shown in Figure 8.11 can be used to estimate the third parameter.

Table 8.2: The pore volume, V, surface layer volume, V_S, and the surface relaxation rate, $R_{1,S}$, of the strongly interacting species in the binary liquid mixtures. Pore volumes were estimated gravimetrically, surface layers were calculated following the arguments outlined in section 5.5.2.3, and surface relaxation rates were estimated as the experimentally measured surface relaxation rate corresponding to the lowest mole fraction of the strongly interacting species. All extracted parameters were extracted from the fast field cycling data measured at 10 kHz.

Mixture	V / $cm^3\ g^{-1}$ **(measured)**	V_S / $cm^3\ g^{-1}$ **(measured)**	$R_{1,S}$ / s^{-1} **(measured)**	V / $cm^3\ g^{-1}$ **(extracted)**	V_S / $cm^3\ g^{-1}$ **(extracted)**	$R_{1,S}$ / s^{-1} **(extracted)**
THF in Cyclo-hexane	0.65	0.13	114	0.59	0.14	126
Methanol in THF	0.65	0.07	367	0.59	0.08	408

For the binary liquid mixtures studied herein the volume correction made no difference to whether or not a linear model was applicable (and hence whether a full microphase separation was observed). It did, however, have a significant effect on the quantitative application of the modelling and the prediction of surface relaxation rates. This effect was most pronounced for the THF:methanol binary liquid mixture, where the difference in molar volumes between the two species is a factor of 2. For cases where the surface-to-volume ratio is known the quantitative analysis confirms the liquid structuring phenomenon. When the volume of the surface layer is unknown this methodology can be used to estimate the NMR affected surface volume. This means that it can be used to experimentally solve complex, and often debated, problems within material science. These include the thickness of the NMR affected surface layer[28,29] and, in size restrictive materials such as zeolites, whether or not a molecule can access specific cavities.[30,31]

8.6 Conclusion

FFC-NMR and fixed field T_1-T_2 studies of binary liquid mixtures imbibed within γ-alumina are reported. Laplace inversion of the data into the T_1 or T_1-T_2 domain allowed the discrimination of the two chemical species in each binary system. For the FFC-NMR experiments the NMRD profiles of each component directly revealed the species which had a greater interaction with the γ-alumina surface. Renormalisation of the NMRD

profiles showed the uniform molecular dynamics across the composition range. Furthermore, plotting the relaxation rates as a function of overall intra-particle composition allowed a modified two phase fast exchange model to be fitted. A linear relationship between the relaxation rate and the inverse of the filling factor demonstrated that a microphase separation was occurring, leading to a shell comprising almost completely of the strongly interacting component at the pore surface and a core rich in the weakly interacting component. For the case of cyclohexane in THF the microphase separation led to no apparent change in the surface dynamics of cyclohexane relative to the single component adsorption, as both situations are described by weak adsorbate-surface interactions. In contrast, THF showed a clear weakening of the adsorbate-surface interaction in the presence of methanol, as shown by the decrease in the apparent power law describing the relaxation behaviour from -0.26 to -0.2.

Consistent results were obtained using a T_1-T_2 analysis of the binary liquid mixtures. For each mixture the strongly interacting species were defined by a higher T_1/T_2 ratio relative to the weakly interacting species. The insensitivity to the T_1/T_2 ratio to the composition demonstrated that the molecular motions of each species did not change across this range. Further insight into the liquid structuring within the porous medium was possible for the cyclohexane:THF binary mixture. Despite the ratio of T_1/T_2 remaining constant, the individual relaxation rates showed a linear trend with the inverse of the filling factor. This confirmed that a microphase separation was occurring. For the THF:methanol binary liquid mixture a clear curvature was observed for the relaxation data. As the microphase separation was shown to occur in this system by FFC-NMR the high field data was distorted by the presence of additional relaxation processes that were not accounted for fully. This means that whilst fixed field relaxation measurements are much faster than FFC-NMR experiments the relaxation data can be misleading.

A volume adjustment was applied to the population terms allowing a fully quantitative application of the modelling. Predictions of the surface relaxation rate from the modelling were consistent to within 11% of the measured values for the FFC-NMR data of both binary liquid mixtures. This confirmed the validity of the modelling approach proposed, and allows it to be used to predict surface relaxation rates or effective surface-to-volume ratios when these quantities are not known.

8.7 References

(1) Mattea, C.; Kimmich, R.; Ardelean, I.; Wonorahardjo, S.; Farrher, G. Molecular Exchange Dynamics in Partially Filled Microscale and Nanoscale Pores of Silica Glasses Studied by Field-Cycling Nuclear Magnetic Resonance Relaxometry. *J. Chem. Phys.* **2004**, *121*, 10648–10656.

(2) Weber, D.; Mitchell, J.; McGregor, J.; Gladden, L. F. Comparing Strengths of Surface Interactions for Reactants and Solvents in Porous Catalysts Using Two-Dimensional NMR Relaxation Correlations. *J. Phys. Chem. C* **2009**, *113*, 6610–6615.

(3) Vecino, P. A.; Huang, Z.; Mitchell, J.; McGregor, J.; Daly, H.; Hardacre, C.; Thomson, J. M.; Gladden, L. F. Determining Adsorbate Configuration on Alumina Surfaces with ^{13}C Nuclear Magnetic Resonance Relaxation Time Analysis. *Phys. Chem. Chem. Phys.* **2015**, *17*, 20830–20839.

(4) D'Agostino, C.; Mitchell, J.; Mantle, M. D.; Gladden, L. F. Interpretation of NMR Relaxation as a Tool for Characterising the Adsorption Strength of Liquids inside Porous Materials. *Chem. A Eur. J.* **2014**, *20*, 13009–13015.

(5) Alnaimi, S. M.; Mitchell, J.; Strange, J. H.; Webber, J. B. W. Binary Liquid Mixtures in Porous Solids. *J. Chem. Phys* **2004**, *120*, 2075–2077.

(6) Mitchell, J.; Stark, S. C.; Strange, J. H. Probing Surface Interactions by Combining NMR Cryoporometry and NMR Relaxometry. *J. Phys. D Appl. Phys.* **2005**, *38*, 1950–1958.

(7) Korb, J. P.; Freiman, G.; Nicot, B.; Ligneul, P. Dynamical Surface Affinity of Diphasic Liquids as a Probe of Wettability of Multimodal Porous Media. *Phys. Rev. E* **2009**, *80*, 61601.

(8) Freed, D. E. Dependence on Chain Length of NMR Relaxation Times in Mixtures of Alkanes *J. Chem. Phys.* **2007**, *126*, 174502.

(9) Reci, A.; Ainte, M. I.; Sederman, A. J.; Mantle, M. D.; Gladden, L. F. Optimising Sampling Patterns for Bi-Exponentially Decaying Signals. *Magn. Reson. Imaging* **2019**, *56*, 14–18.

(10) Korb, J. P.; Monteilhet, L.; McDonald, P. J.; Mitchell, J. Microstructure and Texture of Hydrated Cement-Based Materials: A Proton Field Cycling Relaxometry Approach. *Cem. Concr. Res.* **2007**, *37*, 295–302.

(11) Fleury, M.; Romero-Sarmiento, M. Characterization of Shales Using T_1-T_2 NMR Maps. *J. Pet. Sci. Eng.* **2016**, *137*, 55–62.

(12) Mhanna, R.; Razzak, A.; Hamid, A.; Dutta, S.; Lefort, R.; Noirez, L.; Frick, B.; Morineau, D. More Room for Microphase Separation : An Extended Study on Binary Liquids Confined in SBA-15 Cylindrical Pores. *J. Chem. Educ.* **2017**, *146*, 24501.

(13) Barnette, A. L.; Kim, S. H. Coadsorption of N -Propanol and Water on SiO_2 : Study of Thickness, Composition, and Structure of Binary Adsorbate Layer Using Attenuated Total Reflection Infrared (ATR-IR) and Sum Frequency Generation (SFG) Vibration Spectroscopy. *J. Phys. Chem. C* **2012**, *116*, 9909–9916.

(14) Yang, Z.; Li, Q.; Hua, R.; Gray, M. R.; Chou, K. C. Competitive Adsorption of Toluene and *n*-Alkanes at Binary Solution / Silica Interfaces. *J. Phys. Chem. C* **2009**, *113*, 20355–20359.

(15) Hellweg, T.; Schemmel, S.; Rother, G.; Brûlet, A.; Eckerlebe, H.; Findenegg, G. H. De-Mixing Dynamics of a Binary Liquid System in a Controlled-Pore Glass. *Eur. Phys. J. E* **2003**, *12*, 1–4.

(16) Mitchell, J.; Chandrasekera, T. C.; Gladden, L. F. Obtaining True Transverse Relaxation Time Distributions in High-Field NMR Measurements of Saturated Porous Media: Removing the Influence of Internal Gradients. *J. Chem. Phys.* **2010**, *132*, 1–10.

(17) Reichardt, C. *Solvents and Solvent Effects in Organic Chemistry*; Wiley-VCH, 2003.

(18) Robertson, C. I. Characterising Adsorption and Mass Transfer in Porous Media (Doctoral Thesis)., 2018.

(19) Claridge, T. D. W. Chapter 5 - Introducing Two-Dimensional and Pulsed Field Gradient NMR. In *High-Resolution NMR Techniques in Organic Chemistry*. Elsevier, 2016; pp 171–202.

(20) Plassais, A.; Lequeux, N.; Petit, D.; Barberon, F.; Bresson, B. Microstructure Evolution of Hydrated Cement Pastes. *Phys. Rev. E* **2005**, 041401.

(21) Barberon, F.; Korb, J.; Petit, D.; Morin, V.; Bermejo, E. Probing the Surface Area of a Cement-Based Material by Nuclear Magnetic Relaxation Dispersion. *Phys. Rev. Lett.* **2003**, *90*, 116103.

(22) Korb, J.; Nicot, B.; Ligneul, P. presented at the 24th Symposium of the Society of Core Analysts, Halifax, 2010.

(23) Muthulakshmi, T.; Dutta, D.; Maheshwari, P.; Pujari, P. K. Evidence for Confinement Induced Phase Separation in Ethanol-Water Mixture: A Positron Annihilation Study. *J. Phys. Condens. Matter* **2017**, *30*, 25001.

(24) Phan, A.; Cole, D. R.; Striolo, A. Preferential Adsorption from Liquid Water–Ethanol Mixtures in Alumina Pores. *Langmuir* **2014**, *30*, 8066–8077.

(25) Farrar, T. C.; Becker, E. D. Chapter 4 - Relaxation Mechanisms. In *Pulse and Fourier Transform NMR.* Academic Press, 1971; pp 46–65.

(26) Mitchell, J.; Chandrasekera, T. C.; Gladden, L. F. A General Approach to T_2 Measurements in the Presence of Internal Gradients. *Microporous Mesoporous Mater.* **2013**, *178*, 20–22.

(27) Aguilar, J. A.; Nilsson, M.; Bodenhausen, G.; Morris, G. A. Spin Echo NMR Spectra without J Modulation. *Chem. Commun.* **2012**, *48*, 811–813.

(28) Mitchell, J.; Gladden, L. F.; Chandrasekera, T. C.; Fordham, E. J. Low-Field Permanent Magnets for Industrial Process and Quality Control. *Prog. Nucl. Magn. Reson. Spectrosc.* **2014**, *76*, 1–60.

(29) Muncaci, S.; Mattea, C.; Stapf, S.; Ardelean, I. Frequency-Dependent NMR Relaxation of Liquids Confined inside Porous Media Containing an Increased Amount of Magnetic Impurities. *Magn. Reson. Chem.* **2013**, *51*, 123–128.

(30) Jae, J.; Tompsett, G. A.; Foster, A. J.; Hammond, K. D.; Auerbach, S. M.; Lobo, R. F.; Huber, G. W. Investigation into the Shape Selectivity of Zeolite Catalysts for Biomass Conversion. *J. Catal.* **2011**, *279*, 257–268.

(31) Hendriks, F. C.; Valencia, D.; Bruijnincx, P. C. A.; Weckhuysen, B. M. Zeolite

Molecular Accessibility and Host–guest Interactions Studied by Adsorption of Organic Probes of Tunable Size. *Phys. Chem. Chem. Phys.* **2017**, *19*, 1857–1867.

Chapter 9 : Conclusions and further work

Contents

9.1 Conclusions

The principal objective of this thesis was to develop NMR relaxometry techniques that can be applied to study the adsorption behaviour of liquids imbibed within catalytically relevant porous materials. Both fixed and variable field NMR relaxation measurements were used to measure the adsorption behaviour of a wide range of different liquids imbibed within a typical catalyst support, γ-alumina. Systematic experimental studies were used to clarify the conditions under which fixed field measurements were robust. When fixed field measurements were no longer accurate, or further information was desired about the adsorption process, fast field cycling (FFC) NMR was demonstrated to be a robust alternative. The distinct advantage of FFC-NMR is that it probes the relaxation behaviour over a range of long molecular timescales, and can disambiguate the mechanisms leading to relaxation. An often cited disadvantage of FFC-NMR is that it lacks spectral resolution, and therefore structural characterisation of complex multicomponent samples is not possible. Within this thesis it is shown that chemical resolution can be obtained directly from FFC-NMR relaxation data, and that further structural information about the adsorption process is also accessible. This chemical resolution was used to demonstrate subtle structuring effects such as functionality specific adsorption and microphase separations within the pore space. The methodologies and results presented within this thesis show NMR relaxation experiments to be highly informative for the study of simple and complex liquid systems imbibed within porous catalytic materials. A more detailed summary of the main results will now be presented.

In chapter 4 the applicability of fixed field $T_{1,B}/T_{1,pore}$ and $e_{surf} = -T_2/T_1$ ratios was tested for a wide range of liquids imbibed within γ-alumina. These liquids ranged from non-polar to highly polar, and represented many of the key chemical functionalities used in catalysis. For rigid molecules the $T_{1,B}/T_{1,pore}$ ratio showed an excellent correlation with the adsorbate polarity, which was taken to be a measure of the solid-liquid interaction strength. For e_{surf} the correlation was poorer, and unsaturated molecules showed uncharacteristically strong surface interactions. Internal gradient corrections were unable to account for the scatter in the data relative to the $T_{1,B}/T_{1,pore}$ measurement.

A range of linear *n*-alkanes and *n*-alcohols were also imbibed within γ-alumina. These molecules were classed as flexible molecules, as they possessed significant potential for

internal rotations. The trends for each homologous series were different when measured with $T_{1,B}/T_{1,pore}$ ratios and the e_{surf} parameter, which indicated a clear limitation of the fixed field relaxation approach. Within each homologous series the trends in the e_{surf} parameter were consistent with the previous studies. When compared to the rigid molecules, however, an unphysical ordering of the solid-liquid interaction strengths was obtained. The erroneous nature of the ordering was further confirmed by a series of displacement experiments monitored by ^{1}H spectroscopy. The $T_{1,B}/T_{1,pore}$ and e_{surf} measurements were shown to not be quantitative when comparing rigid and flexible molecules imbibed within γ-alumina.

Chapter 5 introduced the fast field cycling NMR technique, and explored the applicability of FFC-NMR as an alternative to fixed field relaxation analysis. A full comparison of the relaxation dispersion data for bulk liquids, and liquids imbibed within γ-alumina was presented. Strong differences in the relaxation behaviour were observed for all liquids when compared to their respective bulk liquids. For all of the imbibed liquids a dispersion persisted from a measurement frequency of 40 MHz down to 10 kHz, which indicated that slow molecular dynamics were dominating the relaxation behaviour. A phenomenological power law model was fitted to the data, and the power law exponent, β, was used to rank the solid-liquid interaction strength of each liquid. With the exception of acetone, which showed multicomponent relaxation behaviour, the value of β trended well with the polarity of each molecule. FFC-NMR allowed a more reasonable ordering of the solid-liquid interaction strength than was obtained from a fixed field analysis.

Chapter 6 built upon the results presented in chapter 5 by exploring the multicomponent relaxation behaviour that was observed for methanol and acetone imbibed within γ-alumina. In the case of methanol a series of partial deuteration experiments were performed to unambiguously characterise the two environments as the alkyl group and the hydroxyl group of methanol respectively. The two chemical environments differed due to the exchangeability of the hydroxyl group with the surface hydroxyl groups. It was therefore possible to probe functionality specific relaxation behaviour for methanol, and this behaviour was also observed for a range of alcohols imbibed within γ-alumina. For acetone the minor environment was shown to be a stable reaction intermediate, formed during an aldol reaction at the catalyst surface. This was confirmed through ^{13}C NMR experiments, which showed clear evidence of a β-hydroxy ketone intermediate

and the aldol product. The intermediate was more polar than acetone and outcompeted acetone for surface binding sites. This led to a competitive adsorption process, which weakened the surface interaction of acetone. The competitive adsorption was used to explain why acetone was far more weakly interacting than other polar species such as DMSO and THF imbibed within γ-alumina. By identifying the origin of the minor component present when methanol and acetone were imbibed within γ-alumina, a more granular understanding of the adsorption behaviour was achieved.

Chapter 7 completes the analysis of the NMRD profiles shown in chapter 5 by applying a detailed quantitative analysis of the underlying molecular dynamics. A series of temperature dependent experiments were used to clarify the relaxation mechanism that occurred for water, methanol, DMSO, THF, and cyclohexane imbibed within γ-alumina. For each liquid a formal modelling procedure was applied, and correlation times that described the dynamics of the molecules at the surface were extracted. The ordering of the solid-liquid interaction strength predicted by inspection of the NMRD profiles was consistent with the values of the surface correlation times. For molecules bearing non-exchangeable functionalities the NMRD profiles were shown to be controlled by the differences in the type and strength of the solid-liquid interactions. For molecules bearing exchangeable functionalities, however, the relaxation behaviour was controlled by the surface hydroxyl groups of the solid. For γ-alumina it was therefore not possible to measure the interaction strength of water using FFC-NMR. The results showed that great care must be taken when interpreting the NMRD behaviour of water imbibed within mesoporous materials, especially given that water is a commonly used liquid in adsorption studies.

Finally, chapter 8 explored the competitive adsorption behaviour introduced in chapter 6 in greater detail. A series of binary liquid mixtures of cyclohexane:THF and THF:methanol at varying mixture compositions were imbibed within γ-alumina. The relaxation rate of the more strongly interacting component increased as its composition in the binary decreased. The opposite trend was observed for the less strongly interacting species. Renormalization of the NMRD profiles of each component in the binary liquid mixture showed that although the absolute relaxation rates changed, the shape of the NMRD profile did not. This meant that for each component in each binary liquid mixture a single surface dynamic process occurred that was independent of the binary liquid

mixture composition. The only exception to this was the surface adsorption behaviour of THF, which was shown to be severely weakened in the presence of even a small amount of methanol. Fitting the data to a rearrangement of the two-phase fast exchange model showed that both binary liquid mixtures demonstrated a microphase separation. A shell of the more polar species bound preferentially to the alumina surface, which left a bulk pore space rich in the less polar species. From this modelling the surface relaxation rate, pore volume, and adsorbed surface volume were extracted. A comparison between the modelling parameters and experimental measurements showed a difference of approximately 10%. An identical analysis was attempted using fixed field T_1/T_2 measurements at 43 MHz. Good agreement between the FFC-NMR and fixed field data was observed for the cyclohexane:THF binary liquid mixtures, but inconsistent results were obtained from the THF:methanol binary liquid mixtures. The FFC-NMR data had shown the occurrence of a microphase separation for both binary liquid mixtures, and therefore the high field relaxation behaviour of the THF:methanol system was controlled by factors other than just the adsorption. This resulted in ambiguous or misleading information at fixed field strengths when compared to FFC-NMR.

9.2 Further work

9.2.1 Application of FFC-NMR to catalytic materials

The work presented in chapters 5-8 established a strong theoretical and methodological understanding of the adsorption of liquids imbibed within γ-alumina. A natural extension to this work would be to study similar trends within other catalyst support materials and metal-loaded catalysts. Previous studies have already begun to explore the FFC-NMR relaxation behaviour of catalytic materials, but have only presented a few cases of single component adsorption.[1,2] The technique has great potential to be applied to the study of adsorption problems of direct catalytic interest. This may include optimization of the catalyst synthesis procedure by relating process changes to the adsorption properties of the final catalyst, or by studying dynamic processes such as competitive adsorption or catalyst poisoning *in situ*.

9.2.2 Conversion of FFC-NMR correlation times to diffusion coefficients

In chapter 7 modelling approaches were used to extract motional correlation times from FFC-NMR data. These motional correlation times have previously been converted into diffusion coefficients[3,4] however the values are never directly compared to other experimental techniques. Moreover, there is debate in the literature over the magnitude of these motional correlation times – with authors disagreeing by several orders of magnitude.[5,6] A comparison of the diffusion coefficients obtained from FFC-NMR with those obtained from pulsed field gradient (PFG) NMR will allow the quantitative nature of FFC-NMR diffusion coefficients to be tested. This is of particular interest for liquids in porous systems, where the surface diffusion coefficient is rarely obtained directly with PFG-NMR, and short T_2* times may prevent measurements from being performed. In these cases, FFC-NMR may be a more reliable alternative for the determination of quantitative surface diffusion coefficients.

9.2.3 Understanding catalytically relevant binary liquid mixtures

The model proposed in chapter 8 for the interpretation of binary liquid mixtures imbibed within porous media contains information about both the liquid structuring and the liquid dynamics within the pore space. In chapter 8 the model was only tested for two simplistic binary liquid mixtures, which showed a microphase separation across the entire composition range. There is great scope to extend this work to systems where more complex temperature dependent or concentration dependent phase behaviour is expected. The limits of the model can also be explored for sub-monolayer coverages of the strongly interacting species. At these extreme conditions the effects of cooperative and competitive binding can be explored in the context of industrial processes such as catalytic promotion or the fine tuning of separations processes.

9.2.4 Screening tools for rapid assessment and kinetic measurements

Whilst it has been argued within this thesis that FFC-NMR provides clear advantages to fixed field NMR relaxation measurement in terms of clarity of the relaxation process, it is a far more time consuming measurement. For time limited samples, such as those exhibiting fast kinetic processes or high-throughput experimentation, acquiring a full NMRD profile is not a reasonable approach. Instead, the acquisition of the relaxation rate at a few low frequencies can be sufficient to monitor or screen the adsorption behaviour

of liquids in porous media. This technique would be particularly useful in applications where a full NMRD profile of a similar system has previously been performed and therefore the relaxation behaviour is known.

9.3 References

(1) Mitchell, J.; Broche, L. M.; Chandrasekera, T. C.; Lurie, D. J.; Gladden, L. F. Exploring Surface Interactions in Catalysts Using Low-Field Nuclear Magnetic Resonance. *J. Phys. Chem. C* **2013**, *117*, 17699–17706.

(2) Stapf, S.; Ren, X.; Talnishnikh, E.; Blümich, B. Spatial Distribution of Coke Residues in Porous Catalyst Pellets Analyzed by Field-Cycling Relaxometry and Parameter Imaging. *Magn. Reson. Imaging* **2005**, *23*, 383–386.

(3) Korb, J.-P.; Whaley Hodges, M.; Gobron, T.; Bryant, R. G. Anomalous Surface Diffusion of Water Compared to Aprotic Liquids in Nanopores. *Phys. Rev. E* **1999**, *60*, 3097–3106.

(4) Chemmi, H.; Petit, D.; Levitz, P.; Denoyel, R.; Galarneau, A.; Korb, J.-P. Noninvasive Experimental Evidence of the Linear Pore Size Dependence of Water Diffusion in Nanoconfinement. *J. Phys. Chem. Lett.* **2016**, *7*, 393–398.

(5) Faux, D. A.; Cachia, S. H. P.; McDonald, P. J.; Bhatt, J. S.; Howlett, N. C.; Churakov, S. V. Model for the Interpretation of Nuclear Magnetic Resonance Relaxometry of Hydrated Porous Silicate Materials. *Phys. Rev. E.* **2015**, *91*, 032311.

(6) Faux, D. A.; Mcdonald, P. J. Explicit Calculation of Nuclear-Magnetic-Resonance Relaxation Rates in Small Pores to Elucidate Molecular-Scale Fluid Dynamics. *Phys. Rev. E* **2017**, *95*, 033117.

Appendix 1: Material characterisation

Contents

A1.1 Introduction

Additional characterisation of γ-alumina was performed using standard characterisation techniques, and this data was used to support the conclusions drawn in the main body of this thesis. Nitrogen Brunauer–Emmett–Teller (BET) and Barrett, Joyner, and Halenda (BJH) measurements were performed by Zlatko Sarajevic, and the data interpretation was performed as part of this thesis. Pore volume and electron spin resonance (ESR) measurements were both measured and interpreted as part of this thesis. For each of these techniques the key experimental details are presented, and the characterisation data is discussed.

A1.2 BET/BJH measurements

BET nitrogen adsorption measurements are a standard technique for the determination of the surface area in mesoporous and some microporous materials.[1] The adsorption theory extends upon Langmuir theory by allowing the possibility of multilayer adsorption. The relationship between the pressure, p, the saturation pressure, p_0, and the adsorbed gas quantity, v, is given as:[1]

$$\frac{1}{v[p_0/p-1]} = \frac{c-1}{v_m c}\left(\frac{p}{p_0}\right) + \frac{1}{v_m c}, \tag{A1.1}$$

where c is the BET constant and v_m is the monolayer adsorbed gas quantity. A graphical determination of the adsorption isotherm data allows the isolation of the gradient, A, and the intercept, I:

$$A = \frac{c-1}{v_m c}, \tag{A1.2}$$

$$I = \frac{1}{v_m c}. \tag{A1.3}$$

The specific surface area of the material can be defined as:

$$S_{\mathrm{P}} = \frac{1}{A + I}\frac{Ns}{Vm}, \tag{A1.4}$$

where N is Avogadro's constant, s is the cross-sectional area of nitrogen, V is the molar volume of nitrogen, and m is the mass of the sample.

Nitrogen adsorption analysis was performed using a Micromeritics TriStar 3000 automated gas adsorption analyser and each measurement was repeated in triplicate. Figure A1.1 shows the BET surface area plot for γ-alumina. A strong linear trend was observed for the data in the region $0.05 < p/p_0 < 0.2$, which gave a surface area of 206 ± 2 m^2 g^{-1}.

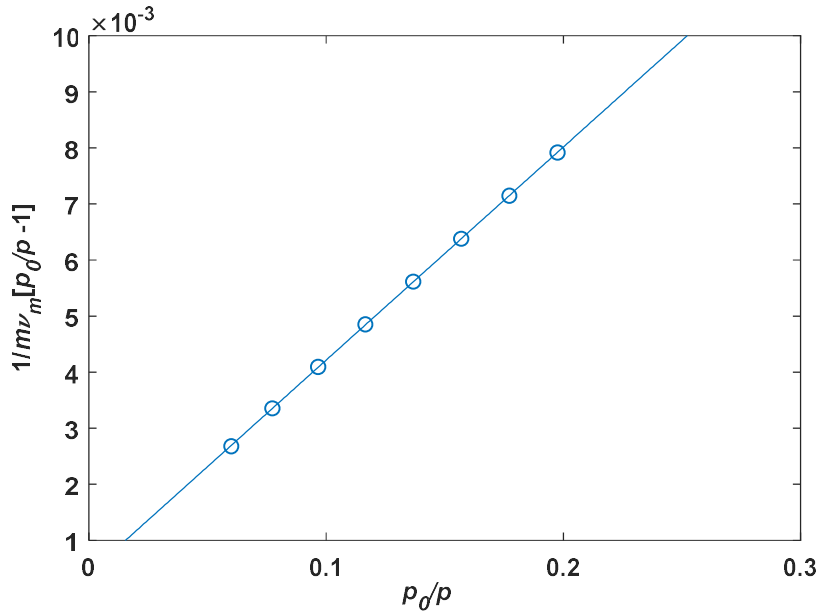

Figure A1.1: The BET surface area plot measured for γ-alumina in the region $0.05 < p/p_0 < 0.2$.

An analogous surface adsorption methodology, the Barrett, Joyner, and Halenda (BJH) approach, was used to determine the approximate pore size of γ-alumina.[2] The adsorption isotherm, shown in Figure A1.2a, showed a small hysteresis at high values of p/p_0, meaning that the adsorption and desorption pore size distributions were unequal. This difference is typically accounted for by the presence of capillary condensation in mesopores, which affects the adsorption isotherm rather than the desorption isotherm. The desorption isotherm was used to generate a pore size distribution, shown in Figure A1.2b.

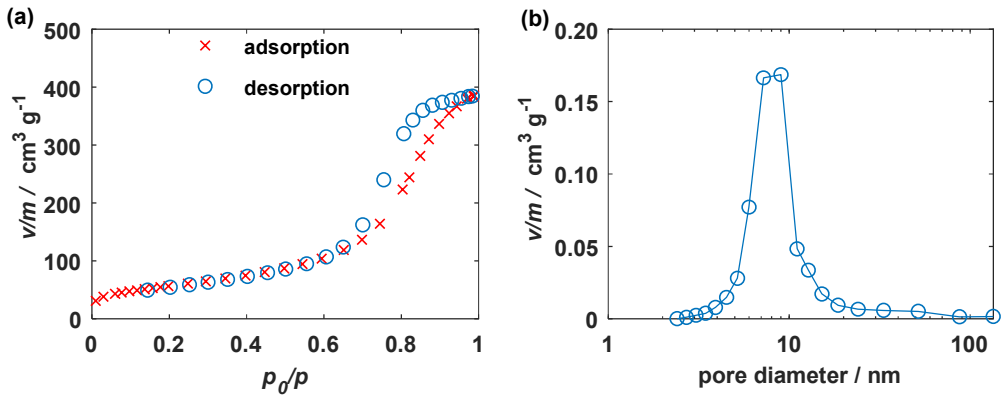

Figure A1.2: The (a) nitrogen adsorption and desorption isotherms, and (b) BJH pores size distribution obtained for γ-alumina.

The pore size distribution was monomodal, and centred about an average pore value of 9 nm. This was typical of a uniform mesoporous material. The BJH methodology has been widely criticised when applied to microporous systems, and the minimum pore size that the technique is applicable to has been argued to be as high as 7.5 nm.[3] Due to the contentious nature of this measurement for small mesoporous systems, the BJH derived pore diameter was not directly used in any calculations within this thesis, and is instead reported for reference.

A1.3 Pore volume measurements

Two measurements techniques were used to estimate the pore volume of the sample; the N_2 adsorption isotherm shown in Figure A1.2a, and gravimetric methods. For the nitrogen adsorption experiments the total volume of adsorbed gas, $V_{\max}$, and the sample mass, m, were used to calculate the pore volume, V_P:

$$V_P = \frac{V_{\max}}{m}. \tag{A1.5}$$

For a p/p_0 value of 0.99 a pore volume of 0.60 $cm^3\ g^{-1}$ was obtained. This was compared to gravimetric methods, in which the value of $V_{\max}$ was measured as the difference in mass between dry γ-alumina, and the alumina after being soaked overnight in water. The gravimetric results are shown in Table A1.1.

Table A1.1: The gravimetric measurements used to determine the pore volume of γ-alumina. The imbibing fluid was water, and had a density of 1 g cm^{-3}.

sample	dry mass / g	water mass / g	pore volume / cm^3 g^{-1}
1	0.88	0.57	0.65
2	1.06	0.70	0.66
3	0.91	0.57	0.63

The pore volume from the gravimetric method was measured as 0.65 cm^3 g^{-1}. This value was slightly larger than the value of 0.60 cm^3 g^{-1} obtained from the nitrogen adsorption isotherm. This small difference suggests that macroporous regions may exist within the sample alongside the observed mesopores. These pores were not observed by nitrogen adsorption measurements, but would be detected gravimetrically. It is also worth noting that the pore volume specified by the manufacturer ranged from 0.57-0.67 cm^3 g^{-1}, and both measurements were within the expected range. It was therefore not possible to rule out sample-to-sample variation within the batch, even though each pore volume measurement was performed in triplicate. To account for all fluid within the pore space, the gravimetric value of $V_P = 0.65$ cm^3 g^{-1} was used throughout this thesis.

A1.4 ESR measurements

Electron spin resonance (ESR) is analogous to NMR spectroscopy in many regards. An external magnetic field is applied to a sample to cause the splitting of otherwise degenerate energy levels, and the transitions between these levels are caused by the external application of electromagnetic radiation.[4] The key difference is that NMR measures transitions between energy levels of spin active nuclei, and ESR measures transitions between energy levels of unpaired electrons. The latter corresponds to much larger energy gap, and is therefore probed by microwave radiation rather than radiofrequency pulses. Typically in an ESR experiment the microwave frequency is held constant and the strength of the applied magnetic field is varied. When the frequency corresponds to the energy gap between energy levels absorption occurs. The absorption frequency and lineshape can be used to interpret the local environment of the electron.[4]

Electron spin resonance (ESR) measurements were performed on a Bruker E500 X-band spectrometer with an ER 4122SHQE cavity at a microwave frequency of 9.385 GHz. The external magnetic field was modulated at 100 kHz. A sample of 34 mg was loaded in a 3 mm inner diameter ESR tube inside an Oxford Instruments ESR900 cryostat with a temperature stability better than 0.1 K. Figure A1.3 shows the background measurement, the measurement of γ-alumina, and the difference spectrum of γ-alumina and the background.

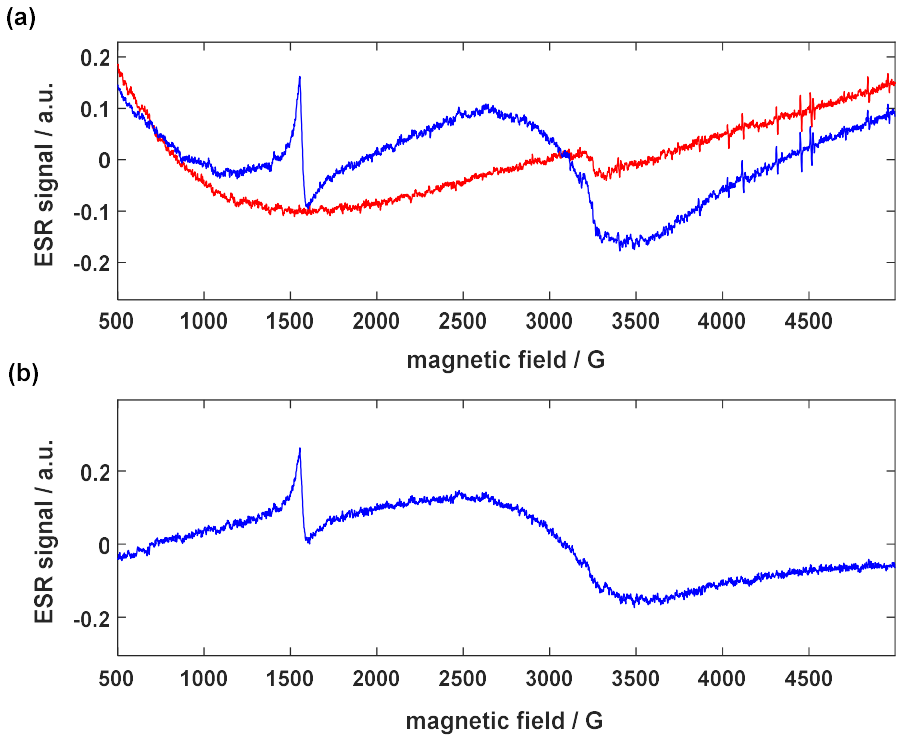

Figure A1.3: The (a) ESR measurements of γ-alumina (blue) and the background (red), and (b) the difference spectrum of γ-alumina and the background.

Two features were observed for γ-alumina, a sharp paramagnetic resonance at 1600 G ascribed to Fe^{3+} and a small broad feature centred about 3400 G which has previously been ascribed to superparamagnetic Fe^{3+} clusters within the framework.[5] The NMR relaxation between paramagnetic species and ^{1}H spins at the pore surface is expected to be proportional to r^{-3}, where r is the distance between the ^{1}H spin and the paramagnetic species. As the superparamagnetic clusters were not near to the surface they were not considered as relaxation sources within this work. The sharp feature at 1600 G, however, was taken to be due to a surface iron species. This feature was quantified by comparison

to a reference sample, and gave a spin density of $\sigma_S = 2.4 \times 10^{16}$ spins g^{-1}. The value can be converted into ppm using the expression:

$$\sigma_S \,/\, ppm = \frac{M_w \times \sigma_S \,/\, spins\ g^{-1}}{N_A}. \qquad \text{(A1.6)}$$

Where M_w is the molecular weight of the iron species and N_A is Avogadro's constant. This gave a mass fraction of paramagnetic species of 6 ppm.

A1.5 References

(1) Brunauer, S.; Emmett, P. H.; Teller, E. Adsorption of Gases in Multimolecular Layers. *J. Am. Chem. Soc.* **1938**, *60*, 309–319.

(2) Barrett, E. P.; Joyner, L. G.; Halenda, P. P. The Determination of Pore Volume and Area Distributions in Porous Substances. I. Computations from Nitrogen Isotherms. *J. Am. Chem. Soc.* **1951**, *73*, 373–380.

(3) Sing, K. The Use of Nitrogen Adsorption for the Characterisation of Porous Materials. *Colloids Surfaces A Physicochem. Eng. Asp.* **2001**, *187–188*, 3–9.

(4) Weil, J. A.; Bolton, J. R. Basic Principles of Paramagnetic Resonance. In *Electron Paramagnetic Resonance*; John Wiley & Sons, Ltd, 2006; pp 1–35.

(5) Djemai, A.; Balan, E.; Morin, G.; Labbe, J. C.; Pierre, J. Behaviour of Paramagnetic Iron during the Thermal Transformations of Kaolinite. *J. Am. Ceram. Soc* **2001**, *84*, 1017–1024.